University of Sheffield

CONTROL OF PERMANENT MAGNET SYNCHRONOUS MACHINES WITH SMALL DC-LINK CAPACITOR

Jun Yan

A thesis submitted for the degree of Doctor of Philosophy

Department of Electronic and Electrical Engineering

University of Sheffield

Mappin Street, Sheffield, S1 3JD, UK

15 August 2024

ABSTRACT

This thesis focuses on the control of permanent magnet synchronous machine (PMSM) drive systems with small dc-link capacitor.

In small dc-link capacitor-based PMSM drive systems, the dc-link voltage is subject to fluctuations, and thus, real-time accurate dc-link voltage information is critical. This thesis firstly analyses the challenges posed by dc-link voltage sensor faults, which can lead to significant measurement errors and compromise control accuracy, and then proposes a robust dc-link voltage observer to ensure accurate voltage estimation.

The thesis further investigates the influence of dc-link voltage fluctuation on high-speed sensorless control methods, particularly the extended electromotive force (EEMF)-based method. The results indicate that the dc-link voltage fluctuation can induce the harmonics in the estimated rotor position error, and deteriorate the system stability. A back-EMF harmonic suppression method is proposed to eliminate these rotor position error harmonics and enhance the performance of the EEMF-based sensorless control strategy.

For zero and low-speed sensorless control methods, conventional methods often require the injection of additional voltage signals to extract the rotor position information. However, in small dc-link capacitor-based PMSM systems, the fluctuating dc-link voltage can easily lead to insufficient voltage conditions, which can worsen the sensorless control performance or even lead to the failure of conventional high-frequency signal injection (HFSI)-based sensorless control methods. Two novel sensorless control methods are developed, leveraging inherent current harmonics resulted from the dc-link voltage fluctuation, to accurately determine the rotor position without the need for HFSI. Furthermore, a magnetic polarity detection method which utilizes the inherent current harmonics is also proposed to improve the accuracy and reliability of small dc-link capacitor-based PMSM drive systems under heavy load conditions.

Finally, the thesis analyzes the energy backflow phenomenon in small dc-link capacitor-based PMSM drive systems. This is particularly prevalent at high speeds and under heavy loads, when the amplitude of back-EMF may exceed the minimum dc-link voltage, threatening the system stability and efficiency. Furthermore, the limitations of conventional flux-weakening (FW) control methods under fluctuating dc-link voltage conditions are analyzed. An optimized FW control strategy is proposed to eliminate the energy backflow and further improve the overall system performance.

ACKNOWLEDGEMENTS

I would like to express my deepest gratitude to my supervisor, Prof. Z. Q. Zhu. His invaluable guidance, constructive support, and generous encouragement over the past four years have been instrumental in my PhD journey and will undoubtedly continue to inspire me in the future. I am truly grateful for the privilege of being his PhD student.

I am also grateful to Dr. Wenqiang Chu, whose recommendation provided me with the opportunity to pursue this PhD journey. His support has been a key factor in the development of my professional career.

I would also like to express my gratitude to Dr. Ximeng Wu, Dr. Bo Shuang, Dr. Bo Shao, Dr. Luocheng Yan and Dr. Lei Xu for their constructive advice and technical support. Special thanks also go to Dr. Yinzhao Zheng, Dr. Dong Xiang, Mr. Yang Chen, Dr. Yan Jia, and Mr. Zhitong Ran, who began this journey together with me. We have shared many experiences together, especially during the challenging years of the pandemic. I am also thankful to my colleagues and friends at the Electrical Machines and Drives Group, whose collaboration and discussions have provided both inspiration and motivation for me. I am particularly thankful to Dr. Ji Qi, Mr. Hai Xu, and Mr. Qiang Wei for their friendship during this journey.

Finally, and importantly, I am deeply grateful to my parents and especially my uncle for their financial support and unwavering encouragement. I will never take their generosity for granted. I am also grateful to my wife, Rongrong Ding, whose sacrifices and loving companionship have been invaluable. Her love for me is beyond any words. I also want to express my gratitude to our cat, "Potato", whose playful presence and companionship have brightened my days and brought joy to my life since he joined our family.

CONTENT

LIST OF SYMBOLS

Symbol	Explanation of Symbol	Units
$A_{d,k}$, $A_{q,k}$	Equivalent amplitudes of estimated dq-axis back-EMF	V
$A^e_{d,k}$, $A^e_{q,k}$,	Equivalent amplitudes of the kth harmonic of the estimated dq-axis back-EMFs with the dc-link voltage measurement error	V
B	Damping coefficient	N·m·s/rad
C_{dc}	DC-Link capacitance	μF
C_{str}	Stray loss coefficient	W/(r/min)^2
$E_{OFF,D}$	Turn-OFF energy losses of diode due to reverse recovery current	J
$E_{ON,I}$, $E_{OFF,I}$	Turn-ON and turn-OFF energy losses of IGBT	J
E_a, E_b, E_c	Three-phase stator back-EMF	V
$\hat{E}_d$, $\hat{E}_q$	dq-axis back-EMFs in estimated synchronous reference frame	V
$\hat{E}^e_d$, $\hat{E}^e_q$	dq-axis back-EMFs with dc-link voltage measurement error	V
E_{ex}	Extended back-EMF	V
I_{hf}	High frequency carrier current vector	A
I_f	Fundamental current	A
I_n	Amplitude of negative high frequency carrier current	A
I_p	Amplitude of positive high frequency carrier current	A
i_{damp}	Damping current	A
i_a, i_b, i_c	Three-phase stator currents	A
i_{cap}	Current flowing through capacitor	A
$i^*_{d,e}$	Resulting d-axis reference current	A

i_d, i_q	dq-axis stator currents in synchronous reference frame	A
i_d^*	Reference d-axis current	A
i_{dh}, i_{qh}	dq-axis high frequency current in synchronous reference frame	A
i_{dc}	DC-Link current	A
i_g	Grid side current	A
i_g^*	Ideal grid current	A
i_{max}	Maximum stator current	A
i_{nrms}	RMS value of the nth harmonic of grid side current	A
i_s	Stator current	A
i_α, i_β	$\alpha\beta$-axis stator currents in stationary reference frame	A
$i_{\alpha h}, i_{\beta h}$	$\alpha\beta$-axis high frequency currents in stationary reference frame	A
$\hat{i}_{d,0}, \hat{i}_{q,0}$	Amplitudes of dc component of estimated dq-axis currents	A
$\hat{i}_{d,k}, \hat{i}_{q,k}$	Amplitudes of the kth order harmonic of estimated dq-axis currents	A
$\hat{i}_d, \hat{i}_q$	dq-axis stator currents in estimated synchronous reference frame	A
$\hat{i}_{dh,100\cdot k}, \hat{i}_{qh,100\cdot k}$	dq-axis high frequency dq-axis currents with $100 \cdot k$ Hz	A
$\hat{i}^d_{dh,100\cdot k}, \hat{i}^q_{dh,100\cdot k}$	Demodulated d-axis currents by phase angle of d- and q-axis voltages	A
$\hat{i}_{dh,sat}, \hat{i}_{qh,sat}$	dq-axis induced currents considering magnetic saturation	A
$\hat{i}_{dh}, \hat{i}_{qh}$	dq-axis high frequency currents in the estimated synchronous reference frame	A
$\hat{i}_d^m, \hat{i}_q^m$	Estimated dq-axis currents with dc-link voltage measurement error	A

$\hat{i}_{qh,100\cdot k}^{d}$, $\hat{i}_{qh,100\cdot k}^{q}$	Demodulated q-axis currents by phase angle of *d- and q*-axis voltages	A
K_h,	Hysteresis loss coefficient	
K_e	eddy current coefficient	
$K_{dc,id}$, $K_{dc,iq}$	Gain variations of dq-axis currents with dc-link voltage measurement error	
K_{dc}	Sampling times in one voltage harmonic period	
K_{delay}	Delayed sampling times	
k_{dc}	Gain variation of dc-link voltage sensor	
L_{aa}, L_{bb}, L_{cc}	Three-phase self-inductances	mH
L_{dh}, L_{qh}	dq-axis high frequency incremental self-inductances in synchronous reference frame	mH
L_d^{nom}	Nominal value of d-axis inductance	mH
L_{dqh}, L_{qdh}	dq-axis high frequency incremental mutual-inductances in the synchronous reference frame	mH
L_g	Grid side inductance	mH
L_n	Negative sequence inductance	mH
L_p	Positive sequence inductance	mH
L_q^{nom}	Nominal value of q-axis inductance	mH
L_s	Stator inductance	mH
L_{s0}	DC components of self-inductance	mH
L_{s2}	DC components of self-inductance	mH
L_{sa}	Average value of dq-axis inductances	mH
L_{sd}	Differential value of dq-axis inductances	mH
$L_{\alpha\alpha}$, $L_{\beta\beta}$	Self-inductance in stationary reference frame	mH
$L_{\alpha\beta}$	Inductance matrix of $\alpha\beta$-axis	mH

$M_{ab}, M_{ba}, M_{ac}, M_{ca}, M_{bc}, M_{ba}$	Three-phase mutual- inductances	mH
M_{s0}	Second order harmonic components of mutual-inductance	mH
M_{s2}	Second order harmonic components of mutual-inductance	mH
$M_{\alpha\beta}, M_{\beta\alpha}$	Mutual-inductances in stationary reference frame	mH
m	Modulation index	
n_p	Number of pole pairs	
P_{damp}	Damping power	W
$P_{\text{inv}}^{R_s^{\text{nom}}}$	Inverter power with nominal value of stator resistance	W
$P_{\text{inv}}^{\text{ref}}$	Actual inverter power	W
$P_{cu}, P_{ir}, P_{st}, P_{sw}, P_{co}$	Copper losses, iron losses, stray losses, switching losses and conduction losses	W
P_{dc}	DC-Link capacitor power	W
P_g	Grid input power	W
P_g^*	Ideal grid input power	W
$P_{inv}^{L_d^{nom}}$	Inverter power with nominal value of d-axis inductance	W
$P_{inv}^{L_q^{nom}}$	Inverter power with nominal value of q-axis inductance	W
$P_{inv}^{\varphi_f^{nom}}$	Inverter power with nominal value of flux linkage	W
$P_{inv}^{\omega_{eac}}$	Inverter power considering the estimated speed harmonics	W
P_{inv}	Inverter output power	W
P_{inv}^*	Ideal inverter output power	W
P_{inv}^{cal}	Calculated inverter output power	W

P_{loss}	Power loss	W
R_{damp}	Damping resistance	Ω
R_g	Grid side resistance	Ω
R_{inv}	Inverter equivalent input resistance	Ω
R_s	Stator phase resistance	Ω
R_s^{nom}	Nominal value of stator resistance	Ω
$S_{\mathrm{a}}, S_{\mathrm{b}}, S_{\mathrm{c}}$	Switch status of three above IGBTs	
$T(\theta_r)$	Transform matrix from stationary reference frame to synchronous reference frame	
$T^{-1}(\theta_r)$	Transform matrix from synchronous reference frame to estimated synchronous reference frame	
T_L	Load torque	Nm
T_e	Electromagnetic torque	Nm
t_d	Delayed time caused by LPF	s
$t_{discharge}$	Discharging time of capacitor	s
U_0	Initial voltage during capacitor discharge process	V
U_g	Amplitude of grid voltage	V
$u_{\mathrm{dc,offset}}$	DC offset of dc-link voltage sensor	V
u_{hf}	Amplitude of injected high frequency voltage signal	V
u_{EMF}	Amplitude of back-EMF	V
u_a, u_b, u_c	Three-phase stator voltages	V
u_{cap}	Voltage of dc-link capacitor	V
u_d, u_q	Stator voltages in synchronous reference frame	V
$u_{dh,100\cdot k}$, $u_{qh,100\cdot k}$	High frequency dq-axis voltages with $100 \cdot k$ Hz	V

u_{dh}, u_{qh}	dq-axis high frequency voltages in synchronous reference frame	V
$u_{dc,0}$, $u_{dc,k}$	Average value and the kth order harmonic of fluctuating dc-link voltage	V
u_{dc}	DC-Link voltage	V
$u_{dc}^{delay\_comp}$	Reconstructed dc-link voltage	V
u_{dc}^{m}, u_{dc}^{a}	Measured and actual dc-link voltage	V
u_g	Grid voltage	V
u_{max}	Maximum stator voltage can be applied to motor	V
u_s^*	Amplitude of stator voltage	V
u_α, u_β	$\alpha\beta$-axis stator voltages in stationary reference frame	V
$u_{\alpha h}$, $u_{\beta h}$	$\alpha\beta$-axis high frequency voltage in stationary reference frame	V
$\hat{u}_{d,0}$, $\hat{u}_{q,0}$	Amplitudes of dc component of estimated dq-axis voltages	V
$\hat{u}_{d,k}$, $\hat{u}_{q,k}$	Amplitudes of the kth order harmonic of estimated dq-axis voltages	V
$\hat{u}_d$, $\hat{u}_q$	dq -axis stator voltage in estimated synchronous reference frame	V
$\hat{u}_{dh}$, $\hat{u}_{qh}$	dq-axis high frequency voltage in estimated synchronous reference frame	V
$\hat{u}_{dc,0}$	Amplitude of dc component of estimated dc-link voltage	V
$\hat{u}_{dc,k}$	Amplitude of the kth order harmonic of estimated dc-link voltage	V
$\tilde{u}_{dc}$	Small-signal variation of dc-link voltage	V
$\hat{u}_d^m$, $\hat{u}_q^m$	Estimated dq-axis voltages with dc-link voltage measurement error	V

$\hat{v}_{dh}$	Injected square wave voltage	V
δ_{skin}	Skin depth	mm
θ_d	Conduction angle of diode in rectifier	Degree
θ_g	Phase angle of grid	Degree
θ_m	Cross-coupling angle	Degree
θ_r	Rotor electrical angle	Degree
$\varphi_{d_{100\cdot k}}$, $\varphi_{q_{100\cdot k}}$	Phase angles of *dq*-axis voltages with $100 \cdot k$ Hz	Degree
$\varphi_{d,k,A}$, $\varphi_{q,k,A}$	Equivalent phases of estimated *dq*-axis back-EMFs	Degree
$\varphi^e_{d,k,A}$, $\varphi^e_{q,k,A}$	Equivalent phases of the *k*th harmonic of estimated *dq*-axis back-EMFs with dc-link voltage measurement error	Degree
$\varphi^i_{d,k}$, $\varphi^i_{q,k}$	Phases of the *k*th order harmonic of estimated *dq*-axis currents	Degree
$\varphi^u_{d,k}$, $\varphi^u_{q,k}$	Phases of the *k*th order harmonic of estimated *dq*-axis voltages	Degree
$\varphi_{dc,k}$	Phase angle of fluctuating dc-link voltage	Degree
φ_a	Active flux-linkage	Wb
φ_a, φ_b, φ_c	Flux linkages of three-phase windings	Wb
φ_d, φ_q	*dq*-axis flux-linkages in synchronous reference frame	Wb
φ_f^{nom}	Nominal value of flux linkage	Wb
$\varphi_{k,\theta}$	Phase of the *k*th order harmonic of estimated position error	Degree
$\varphi^e_{k,\theta}$	Phase of the *k*th harmonic of estimated position error with dc-link voltage measurement error	Degree
$\varphi_{k,\omega}$	Phase of the *k*th order harmonic of estimated speed error	Degree
$\varphi_{m\alpha}$, $\varphi_{m\beta}$	$\alpha\beta$-axis PM excitation flux-linkage in stationary reference frame	Wb

φ_α, φ_β	$\alpha\beta$-axis flux-linkages in stationary reference frame	Wb
ψ_f	PM flux-linkage	Wb
$\Delta i_{d,0}$, $\Delta i_{q,0}$	DC offsets of dq-axis currents with dc-link voltage measurement error	A
$\Delta u_{d,0}$, $\Delta u_{q,0}$	DC offsets of dq-axis voltages with dc-link voltage measurement error	V
$\Delta u_{dc}^{\Delta\omega_e}$	Estimated dc-link voltage error due to estimated speed harmonics	V
$\Delta\theta_{r,0}$	Amplitude of dc component of estimated position error	Degree
$\Delta\theta_{r,k}$	Amplitude of the kth order harmonic of estimated position error	Degree
$\Delta\theta_r$	Estimated position error	Degree
ΔT	Half cycle of injected square wave voltage signal	
ΔL	Differential values of dq-axis inductances	mH
J	Moment of inertia	kg·m²
p	Derivative operator	
$\Delta\theta_{r,0}^e$	Amplitude of dc component of estimated position error with dc-link voltage measurement error	Degree
$\Delta\theta_{r,k}^e$	Amplitude of kth order harmonic of estimated position error with dc-link voltage measurement error	Degree
$\Delta\omega_e$	Estimated speed error	rad/s
ΣL	Average values of dq-axis inductances	mH
γ	Current phase angle between stator current and d-axis current	Degree
δ	Phase difference between grid voltage and current	Degree
μ	Gain coefficient of notch filter	
μ	Permeability of conductor	H/m

ρ	Resistivity of conductor	Ω·m
τ	Time constant of capacitor discharge process	s
φ	Turn-off angle of diode in rectifier	Degree
$\widehat{\omega}_{e,0}$	Amplitude of dc component of estimated speed	rad/s
$\widehat{\omega}_{e,k}$	Amplitude of the *k*th order harmonic of estimated speed	rad/s
$\widehat{\omega}_e$	Estimated speed	rad/s
ω_{hf}	Frequency of injected high frequency voltage signal	Hz
ω_{res}	LC resonance frequency	Hz
ω_{base}	Base speed	rad/s
ω_c	Center frequency of notch filter	Hz
ω_e	Electrical rotor speed	rad/s
ω_g	Grid frequency	Hz
ω_m	Mechanical rotor speed	rad/s
ΔL_d, ΔL_q	Difference between actual value and nominal value of *dq*-axis inductance	mH
$\Delta P_{inv}^{\Delta R_s}$	Power calculation due to resistance changes	W
ΔR_s	Difference between actual and nominal values of stator resistance	Ω
$\Delta\theta_r^e$	Estimated position error with dc-link voltage measurement error	Degree
$\Delta\varphi_f$	Difference between actual value and nominal value of flux linkage	Wb

LIST OF ABBREVIATIONS

AC	Alternate current
Back-EMF	Back electromotive force
BLAC	Brushless AC
BLDC	Brushless DC
BPF	Band pass filter
CPL	Constant power load
DC	Direct current
EEMF	Extended electromotive force
EMI	Electromagnetic interference
EVs	Electric vehicles
FB-FW	Feedback flux weakening
FEA	Finite element analysis
FF-FW	Feedforward flux weakening
FOC	Field-oriented control
FTC	Fault-tolerant control
FW	Flux weakening
GD	Gradient descent
HF	High frequency
HFSI	High frequency signal injection
IPMSM	Interior permanent magnet synchronous machine
LC	Inductor-capacitor
LMS	Least mean square
LPF	Low pass filter
MPC	Model predictive control

MTPA	Maximum torque per ampere
MTPV	Maximum torque per voltage
Non-SSOA	Non-safe sensorless operation area
PF	Power factor
PFC	Power factor correction
PIR	Proportional integral resonance
PLL	Phase-locked loop
PM	Permanent magnet
PMSM	Permanent magnet synchronous machine
PWM	Pulse width modulation
Quasi-PIR	Quasi-proportional integral resonant
SMO	Sliding mode observer
SNR	Signal-to-noise ratio
SPMSM	Surface permanent magnet synchronous machine
SRFF	Synchronous reference frame filter
SSOA	Safe sensorless operation area
SVPWM	Space vector pulse width modulation
THD	Total harmonic distortion
UCG	Uncontrolled generation
VFDs	Variable-frequency drives
VSI	Voltage source inverter

CHAPTER 1

GENERAL INTRODUCTION

Permanent magnet synchronous machines (PMSMs) have been extensively used in industrial and domestic applications due to high efficiency, high torque density, and excellent control performance [ZHU07] [WAN20A] [ZHU23]. Conventional PMSM drive systems typically rely on large-volume capacitors to stabilize the dc-link voltage and maintain steady motor operation. However, these large-volume dc-link capacitors have some obvious disadvantages, including large size, heavy weight, high cost, and low reliability. Besides, the constant dc-link voltage maintained by large-volume capacitors can cause input current distortion, and reduce power factor (PF). Therefore, conventional PMSM drive systems require additional power factor correction (PFC) circuits to improve power quality, but this further increases the cost and complexity of the system, thereby reducing overall reliability [WAN20B].

Consequently, the small-volume dc-link capacitor-based PMSM drive systems have been extensively studied for their cost-effectiveness, compactness, and extended lifespan, especially in domestic appliances where precise control is not essential [WAN20B]. Furthermore, due to the use of small dc-link capacitors and the omission of PFC circuits, the dc-link voltage fluctuation increases the conduction angle of the grid side diode rectifier, which can be further optimized to improve the PF by developing appropriate control strategies [ZHA19A]. Therefore, replacing large-volume dc-link capacitors with smaller volume dc-link capacitors not only improves system reliability but also reduces the overall size and cost of the drive system. However, the reduction in capacitance to 1/50 or 1/100 of the original value significantly decreases the energy storage capacity, which leads to difficulties in maintaining a stable dc-link voltage. As a result, the dc-link voltage fluctuates at twice the grid frequency, posing considerable challenges for the control of the PMSM drive systems [ZHA19A] [WAN20B].

Therefore, this thesis will focus on the influence of dc-link voltage fluctuation on PMSM drive systems and propose various suppression strategies to mitigate these effects. This chapter first introduces the main PMSM topologies, modelling, and basic control strategies. Then, it reviews the current research status of PMSM drive systems based on small dc-link capacitors. At the end of this chapter, the research scope and contributions of this thesis are highlighted.

1.1 PM Machines

1.1.1 PM machine Topologies

The PM machines can be classified into brushless DC (BLDC) machines and brushless AC (BLAC) machines based on their back electromotive force (back-EMF) waveform and current excitation method. BLDC machines operate with a trapezoidal back-EMF and are driven by square wave currents. In contrast, BLAC machines operate with a sinusoidal back-EMF and are driven by sinusoidal currents as shown in Fig. 1.1.

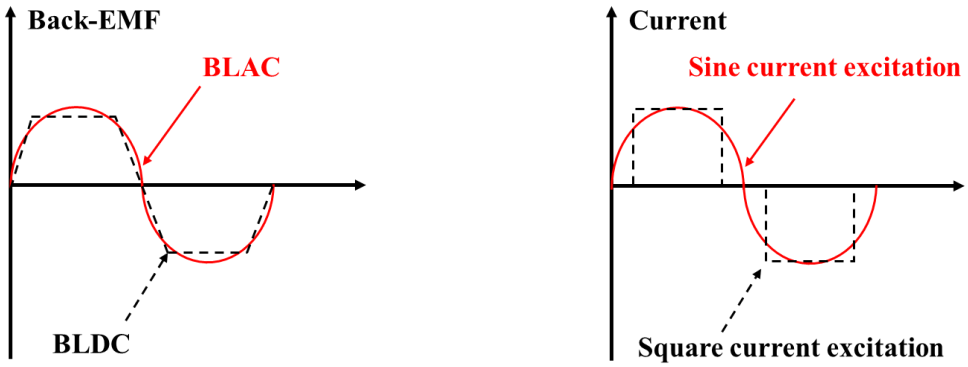

(a) Back-EMF (b) Current excitation

Fig. 1.1. BLDC and BLAC machines. (a) Back-EMF. (b) Current excitation.

BLAC machines can be further divided based on the placement of permanent magnet (PM). They are categorized into configurations whether the PMs are on the rotor or the PMs are on the stator. In configurations with PMs on the stator, the PMs are placed around the stator, which simplifies cooling and maintenance. However, this configuration is less common in high-performance applications due to limitations in magnetic flux interaction [CHU13].

In the most commonly used configurations with PMs on the rotor, they are classified into two types based on rotor PM construction: surface PMSM (SPMSM) and interior PMSM (IPMSM). SPMSMs feature PM mounted directly on the surface of the rotor, simplifying the manufacturing process and resulting in a robust motor structure that provides high efficiency and precise control. The surface-mounted PM in SPMSMs is typically arranged in a cylindrical pattern around the rotor, which allows for a uniform magnetic field and smooth operation. However, these exposed PMs are more susceptible to mechanical damage and thermal stresses, which can limit performance at higher speeds and in demanding environments. Meanwhile, IPMSMs have PMs embedded within the rotor, offering better mechanical protection and the

capability to generate additional reluctance torque due to salient-pole rotor structure. This configuration enhances the performance in high-speed applications and maintains high efficiency across a wide range of operating speeds. The internal placement of the PM in IPMSMs also improves thermal performance and reduces the risk of demagnetization, making them particularly suitable for applications such as electric vehicles where a broad speed range and high torque are essential.

For topologies with PMs on the rotor, they can be further divided into four types, namely surface-mounted, surface-inset, interior-radial, and interior-circumferential [CHU13], as shown in Fig. 1.2. The classification of PM machines is shown in Fig. 1.3.

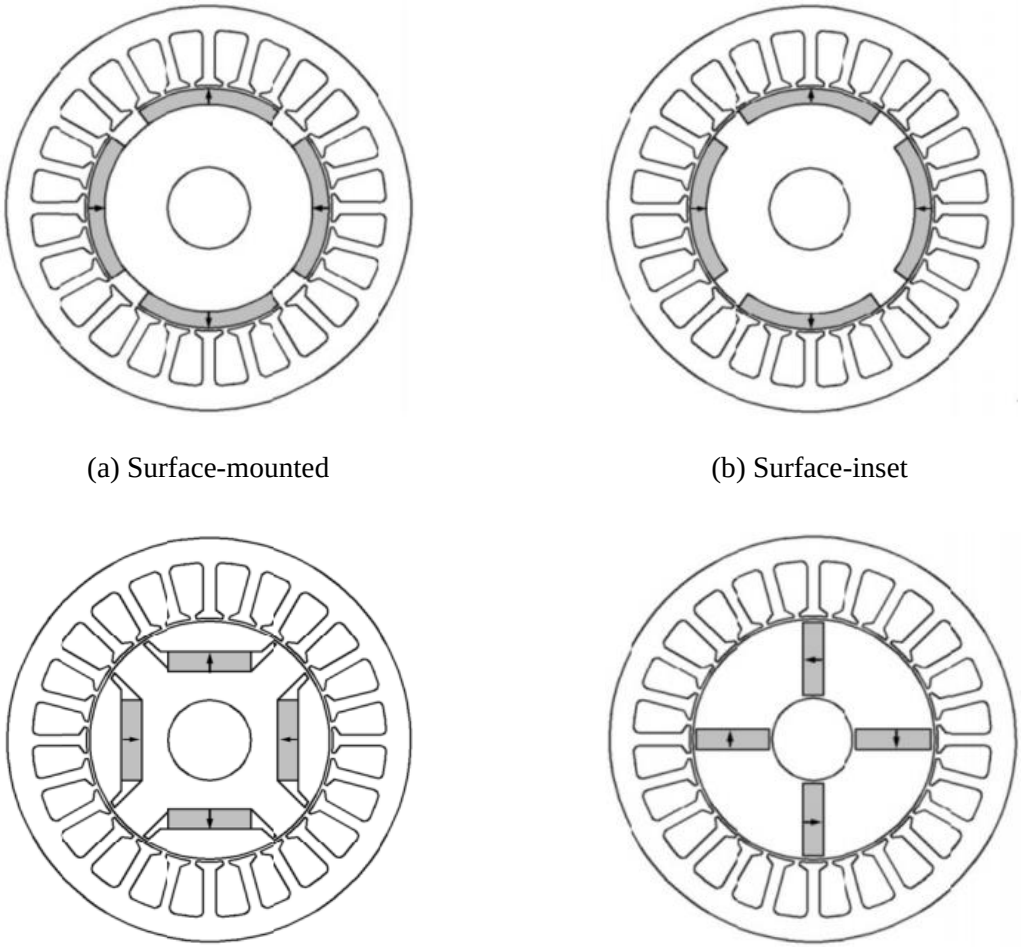

(a) Surface-mounted (b) Surface-inset

(c) Interior-radial (d) Interior-circumferential

Fig. 1.2. Typical rotor structures of brushless PM synchronous machines [CHU13]. (a) Surface mounted. (b) Surface-inset. (c) Interior-radial. (d) Interior-circumferential.

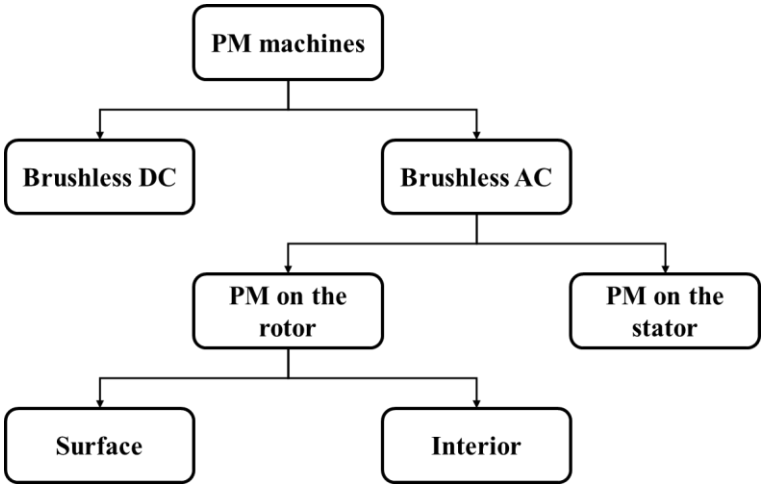

Fig. 1.3. Classification of PM machines.

1.1.2 Modelling of PM Machines

For the single three-phase PMSM, mathematical modelling is important for implementing various control strategies. To simplify the analysis, the following assumptions are made [WAN20B]:

- The three-phase stator windings are symmetrically distributed in space, and the discrete properties of their structure are ignored. Consequently, the armature reaction magnetomotive force generated by the stator windings in the air gap is sinusoidal, and the induced back-EMF is also a sinusoidal wave;
- The internal permeability of the PMs is consistent with that of air, resulting in a sinusoidal distribution of the EMF produced in the air gap;
- Iron losses, thermal effects, and magnetic saturation effects are neglected. The rotor permeability is considered infinitely constant;
- The influence of temperature and load effect on the PM machine parameters is disregarded, and there is no damper winding on the rotor.

These assumptions simplify the modelling of PM machines in different reference frames, such as the ABC reference frame [ERT94], the stationary reference frame (αβ0) [HU98], and the synchronous reference frame (dq0) [CHE03]. The relationship of these three reference frames is shown in Fig. 1.4.

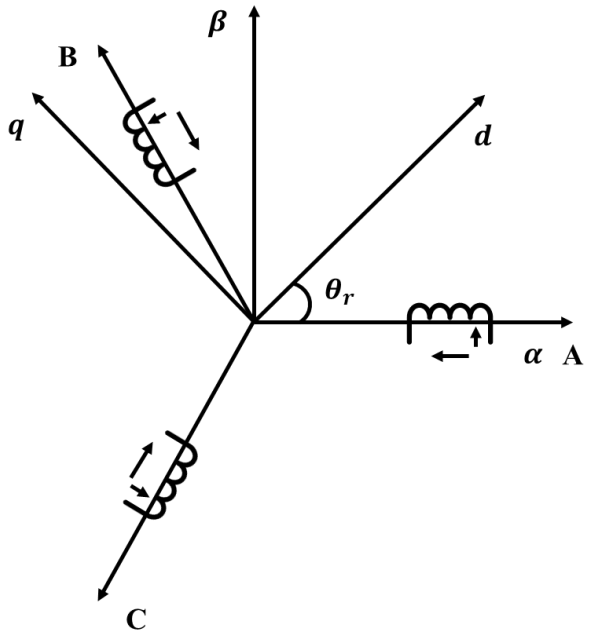

Fig. 1.4. Relationship between ABC, stationary, and synchronous reference frame.

A. Model in ABC reference frame

The symmetrical single three-phase ABC reference frame shown in Fig. 1.4 is a mathematical model directly abstracted from the physical model of the PMSMs.

The three-phase voltage equation is shown as

$$\begin{bmatrix} u_a \\ u_b \\ u_c \end{bmatrix} = \begin{bmatrix} R_s & 0 & 0 \\ 0 & R_s & 0 \\ 0 & 0 & R_s \end{bmatrix} \begin{bmatrix} i_a \\ i_b \\ i_c \end{bmatrix} + p \begin{bmatrix} \varphi_a \\ \varphi_b \\ \varphi_c \end{bmatrix} \tag{1.1}$$

where u_a, u_b, u_c are the three-phase stator voltages, R_s is the phase resistance, i_a, i_b, i_c are the three-phase stator currents, p is the derivative operator, φ_a, φ_b, φ_c are the flux linkages of three-phase winding.

The three-phase flux linkage can be expressed by

$$\begin{bmatrix} \varphi_a \\ \varphi_b \\ \varphi_c \end{bmatrix} = \begin{bmatrix} L_{aa} & M_{ab} & M_{ac} \\ M_{ba} & L_{bb} & M_{bc} \\ M_{ca} & M_{cb} & L_{cc} \end{bmatrix} \begin{bmatrix} i_a \\ i_b \\ i_c \end{bmatrix} + \psi_f \begin{bmatrix} \cos\theta_r \\ \cos(\theta_r - \frac{2}{3}\pi) \\ \cos(\theta_r + \frac{2}{3}\pi) \end{bmatrix} \tag{1.2}$$

where $M_{ab} = M_{ba}$, $M_{ac} = M_{ca}$, $M_{bc} = M_{cb}$ are the mutual inductance between the three-phase windings, L_{aa}, L_{bb}, L_{cc} are the self-inductance of each winding, ψ_f is the PM flux-linkage, and θ_r is the rotor electrical angle.

$$\begin{cases} L_{aa} = L_{s0} - L_{s2}\cos 2\theta_r \\ L_{bb} = L_{s0} - L_{s2}\cos 2(\theta_r - \frac{2}{3}\pi) \\ L_{cc}L_{s0} - L_{s2}\cos 2(\theta_r + \frac{2}{3}\pi) \end{cases} \tag{1.3}$$

$$\begin{cases} M_{ab} = M_{ba} = -M_{s0} + M_{s2}\cos 2(\theta_r + \frac{2}{3}\pi) \\ M_{ac} = M_{ca} = -M_{s0} + M_{s2}\cos 2\theta_r \\ M_{bc} = M_{cb} = -M_{s0} + M_{s2}\cos 2(\theta_r - \frac{2}{3}\pi) \end{cases} \tag{1.4}$$

where L_{s0} , L_{s2} , M_{s0} and M_{s2} are the dc components and the second order harmonic components of self-inductance and mutual inductance, respectively. It is worth mentioning that there is no second-order harmonic component in the non-salient machines (SPMSMs), that is, $L_{s2} = M_{s2} = 0$.

B. Model in stationary reference frame

From (1.1) to (1.4), the mathematical model of IPMSMs in the ABC reference frame is very complicated from the control perspective. Therefore, the motor model is usually transformed into the stationary frame. According to the phase magnitude invariance method, the Clarke transformation matrix and inverse Clarke transformation matrix are shown as

$$T_{abc-\alpha\beta0} = \frac{2}{3}\begin{bmatrix} 1 & -\frac{1}{2} & -\frac{1}{2} \\ 0 & \frac{\sqrt{3}}{2} & -\frac{\sqrt{3}}{2} \\ \frac{1}{2} & \frac{1}{2} & \frac{1}{2} \end{bmatrix} \tag{1.5}$$

$$T_{\alpha\beta0-abc} = \begin{bmatrix} 1 & 0 & 1 \\ -\frac{1}{2} & \frac{\sqrt{3}}{2} & 1 \\ -\frac{1}{2} & -\frac{\sqrt{3}}{2} & 1 \end{bmatrix} \tag{1.6}$$

After transformation, the voltage and flux-linkage in the stationary reference frame can be presented as

$$\begin{bmatrix} u_\alpha \\ u_\beta \end{bmatrix} = \begin{bmatrix} R_s & 0 \\ 0 & R_s \end{bmatrix}\begin{bmatrix} i_\alpha \\ i_\beta \end{bmatrix} + p\begin{bmatrix} \varphi_\alpha \\ \varphi_\beta \end{bmatrix} \tag{1.7}$$

$$\begin{bmatrix}\varphi_\alpha\\ \varphi_\beta\end{bmatrix}=\begin{bmatrix}L_{\alpha\alpha} & M_{\alpha\beta}\\ M_{\beta\alpha} & L_{\beta\beta}\end{bmatrix}\begin{bmatrix}i_\alpha\\ i_\beta\end{bmatrix}+\varphi_f\begin{bmatrix}\cos\theta_r\\ \sin\theta_r\end{bmatrix} \tag{1.8}$$

$$L_{\alpha\beta}=\begin{bmatrix}L_{\alpha\alpha} & M_{\alpha\beta}\\ M_{\beta\alpha} & L_{\beta\beta}\end{bmatrix}=\begin{bmatrix}\Sigma L+\Delta L\cos(2\theta_r) & \Delta L\sin(2\theta_r)\\ \Delta L\sin(2\theta_r) & \Sigma L-\Delta L\cos(2\theta_r)\end{bmatrix} \tag{1.9}$$

$$\Sigma L=\frac{L_d+L_q}{2}\quad \Delta L=\frac{L_d-L_q}{2} \tag{1.10}$$

where u_α, u_β, i_α, i_β, φ_α, φ_β, $L_{\alpha\alpha}$, $L_{\beta\beta}$, $M_{\alpha\beta}$, and $M_{\beta\alpha}$ are the stator voltages, currents, flux-linkages, self- and mutual- inductances in the stationary reference frame, respectively. $L_{\alpha\beta}$ is the inductance matrix of $\alpha\beta$-axis, ΣL and ΔL are the average and differential values of *dq*-axis inductances, L_d, and L_q are the equivalent inductances in the *dq*-axis.

C. Model in synchronous reference frame

From (1.8) and (1.9), the inductances in the stationary reference frame are still periodically determined by the real-time rotor position information. For decoupling the *dq*-axis and simplifying control algorithms, the Park transformation is typically used to transform the variables in the stationary reference frame to the synchronous reference frame. The Park transformation matrix and inverse Park transformation matrix are expressed as

$$T_{\alpha\beta-dq}=\begin{bmatrix}\cos\theta_r & \sin\theta_r\\ -\sin\theta_r & \cos\theta_r\end{bmatrix} \tag{1.11}$$

$$T_{dq-\alpha\beta}=\begin{bmatrix}\cos\theta_r & -\sin\theta_r\\ \sin\theta_r & \cos\theta_r\end{bmatrix} \tag{1.12}$$

After Park transformation, the *dq*-axis voltage can be presented as

$$\begin{bmatrix}u_d\\ u_q\end{bmatrix}=\begin{bmatrix}R_s & 0\\ 0 & R_s\end{bmatrix}\begin{bmatrix}i_d\\ i_q\end{bmatrix}+p\begin{bmatrix}\varphi_d\\ \varphi_q\end{bmatrix}+\omega_e\begin{bmatrix}-\varphi_q\\ \varphi_d\end{bmatrix} \tag{1.13}$$

$$\begin{bmatrix}\varphi_d\\ \varphi_q\end{bmatrix}=\begin{bmatrix}L_d & 0\\ 0 & L_q\end{bmatrix}\begin{bmatrix}i_d\\ i_q\end{bmatrix}+\varphi_f\begin{bmatrix}1\\ 0\end{bmatrix} \tag{1.14}$$

where u_d, u_q, i_d, i_q, φ_d, and φ_q represent the *dq*-axis stator voltages, currents and flux-linkages in the synchronous reference frame, respectively ω_e is the electrical rotor speed. Specifically, for a non-salient machine, i.e. SPMSM, $L_d=L_q=L_s$. From (1.14), the inductances of SPMSM in the synchronous reference frame is constant and no longer determined by the rotor position.

The electromagnetic torque in the synchronous reference frame can be presented by

$$T_e = \frac{3}{2} n_p [\varphi_f i_q + (L_d - L_q) i_d i_q] \tag{1.15}$$

where T_e is the electromagnetic torque, n_p is the number of pole pairs.

The eletromechanical dynamic characteristics can be expressed as

$$T_e - T_L - B\omega_m = J \frac{d\omega_m}{dt} \tag{1.16}$$

where T_L is the load torque, B is the damping coefficient, ω_m is the mechanical rotor speed, and J is the moment of inertia.

1.2 Field-Oriented Control

Field-oriented control (FOC), also known as vector control, is an AC motor control theory proposed by F. Blaschke of Siemens in 1971. The basic concept of this theory is to simulate the FOC of a DC motor by decomposing the stator current of an AC motor into two components: the excitation component, which aligns with the rotor magnetic flux, and the torque component, which is orthogonal to the magnetic flux. By decoupling the excitation and torque components, the control strategy becomes more simplified, thereby enabling precise speed and torque control of AC motors. The block diagram of FOC is shown in Fig. 1.5.

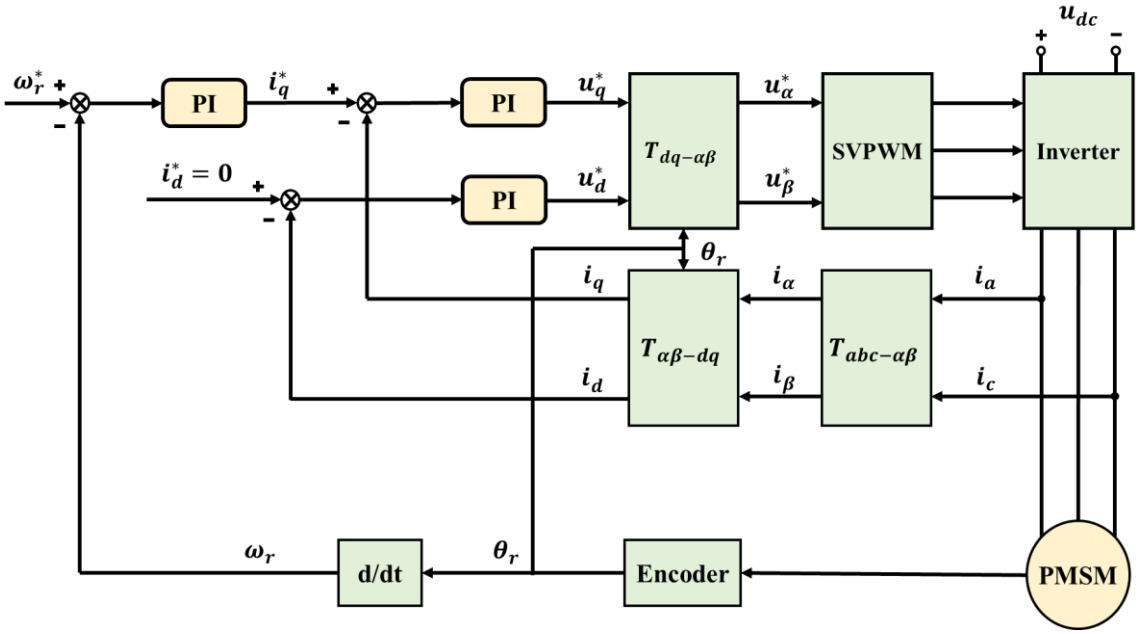

Fig. 1.5. Block diagram of FOC with $i_d = 0$ control.

The commonly used methods in FOC include $i_d = 0$ control, maximum torque per ampere

(MTPA) control, flux weakening (FW) control, and sensorless control.

- i_d =0 control strategy simplifies control algorithms by nullifying the *d*-axis current;
- MTPA control strategy optimizes torque output by dynamically adjusting i_d and i_q to achieve maximum torque for a given current magnitude;
- FW control strategy extends the speed range of the machine by increasing i_d at high speeds, although at the cost of decreased torque capability;
- Sensorless control strategy eliminates the need for physical position sensors by estimating rotor position and speed from terminal voltages and currents, thereby saving costs and enhancing reliability.

These strategies are crucial for customizing PMSM performance across various applications, balancing efficiency, torque generation, speed range, and system cost-effectiveness.

1.2.1 $i_d = 0$ Control

The block diagram of $i_d = 0$ control is shown in Fig. 1.5. From (1.13) and (1.14), it can be seen that when the *d*-axis current is 0, the stator current vector coincides with the *q*-axis current direction, and the PM flux linkage coincides with the *d*-axis, thus, this control method is also called rotor flux linkage oriented control. The magnetic reluctance torque generated by the asymmetry of the *dq*-axis in the electromagnetic torque is 0, and only the torque generated by the PM remains. Therefore, the magnitude of the electromagnetic torque can only be controlled by controlling the *q*-axis current. The electromagnetic torque equation is shown in (1.15), which greatly reduces the control complexity of the motor by $i_d = 0$. Especially in the SPMSM, the *q*-axis and the *d*-axis are symmetrical, the magnetic reluctance torque becomes 0, and the control is simpler. However, for IPMSM, the magnetic reluctance torque is not fully utilized, and it is difficult for the motor to run above the rated speed, thus, this strategy is not suitable for applications with a wide speed regulation range.

1.2.2 MPTA Control

As mentioned, with the $i_d = 0$ control strategy, the electromagnetic torque generated by the motor is not maximized for the IPMSM drives under the same stator current. The saliency effect, due to the specific magnet position, results in a higher *q*-axis inductance compared to the *d*-axis. Consequently, from (1.15), both *d*-axis and *q*-axis currents contribute to electromagnetic torque production. To ensure high efficiency and maximum torque in IPMSM drive systems, the MTPA control strategy is proposed to determine the optimal *d*-axis and *q*-

axis currents, thereby achieving the required torque with minimal current.

Assuming that the phase angle between the stator current i_s and the d-axis current i_d denoted as γ. The stator current vector is decoupled in the dq-axis reference frame, as shown in Fig. 1.6.

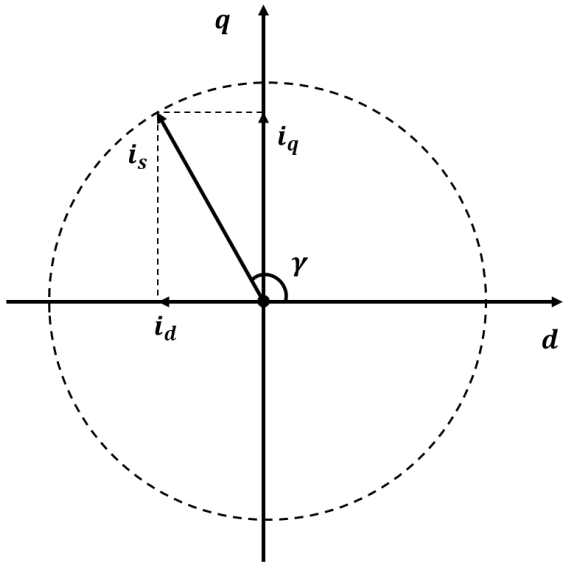

Fig. 1.6. Decoupling of stator current vector.

The relationship between the stator current and the dq-axis currents is derived as

$$\begin{cases} i_d = i_s \cos\gamma \\ i_q = i_s \sin\gamma \end{cases} \tag{1.17}$$

Therefore, the electromagnetic torque can be expressed as

$$T_e = \frac{3}{2} n_p \varphi_f i_s \sin\gamma + \frac{3}{4} n_p \left(L_d - L_q\right) i_s^2 \sin 2\gamma \tag{1.18}$$

According to the MTPA control principle, which states that the same stator current generates the maximum electromagnetic torque, assuming the stator current is constant, the partial derivative of the electromagnetic torque with respect to the angle γ can be obtained as follows.

$$\frac{\partial T_e}{\partial \gamma} = \frac{3}{4} n_p \left(L_d - L_q\right) i_s (2\cos^2\gamma - 1) + \varphi_f \cos\gamma = 0 \tag{1.19}$$

Therefore

$$\cos\gamma = \frac{-\varphi_f + \sqrt{\varphi_f^2 + 8(L_d - L_q)^2 i_s^2}}{4(L_d - L_q) i_s} \tag{1.20}$$

Therefore, the *dq*-axis current can be expressed as

$$i_d = \frac{-\varphi_f + \sqrt{\varphi_f^2 + 8(L_d - L_q)^2 i_s^2}}{4(L_d - L_q)} \tag{1.21}$$

$$i_q = \sqrt{i_s^2 - i_d^2} \tag{1.22}$$

The relationship between the torque (electromagnetic torque, PM torque, and reluctance torque) and γ can be plotted as shown in Fig. 1.7. The PM torque reaches its maximum when the γ is 90°. The electromagnetic torque initially increases and then decreases between 90° and 180°, reaching its maximum value at an angle of MTPA. The torque generated by the PM decreases continuously as the angle increases. The reluctance torque is maximized when γ is 135°.

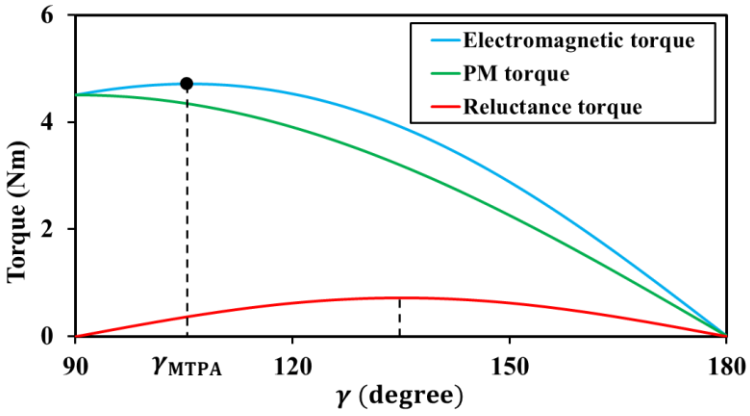

Fig. 1.7. Relationship between torque and current angle.

The speed at which the machine is operated in the MTPA mode is called the base speed. Up to the base speed, the speed region is called the constant torque region, and above the base speed, the region is called the FW region. The base speed of IPMSM can be expressed by

$$\omega_{base} = \frac{u_{max}}{\sqrt{\left(L_d i_d + \Psi_f\right)^2 + \left(L_q i_q\right)^2}} \tag{1.23}$$

1.2.3 FW Control

A. Principle of FW control

When the motor runs below the base speed, the current capacity of the inverter is the main limitation. In this case, the MTPA control is the better choice. However, when the motor runs above the base speed, the voltage capacity of the inverter becomes the main limitation. To obtain a wider speed regulation range, a negative *d*-axis current is used to generate demagnetization flux. This demagnetization flux offsets some of the opposite flux provided by the PMs, reduces the effective air gap flux, and widens the speed range of the IPMSM. In this case, the maximum current and dc-link voltage need to be considered simultaneously to prevent overcurrent and voltage saturation. The IPMSM is affected by the following constraints during operation.

$$i_s^2 = i_d^2 + i_q^2 < i_{max}^2 \tag{1.24}$$

$$u_s = \sqrt{u_d^2 + u_q^2} \le u_{max} = \frac{u_{dc}}{\sqrt{3}} \tag{1.25}$$

According to (1.13), (1.14) and (1.25), if the motor speed is high enough and the stator resistance voltage drop is small enough, then the voltage drop by the stator resistance can be neglected. Hence, (1.25) can be approximated as

$$(L_d i_d + \varphi_f)^2 + (L_q i_q)^2 \le \frac{u_{max}^2}{\omega_e^2} \tag{1.26}$$

Fig. 1.8 shows the operating characteristics of an IPMSM under FW control. The red curve outlines the motor's trajectory through three control stages: MTPA control, FW control, and maximum torque per voltage (MTPV) control.

The MTPA control is the first stage to optimize torque output for a given current. As illustrated in Fig. 1.8, the red trajectory initially follows the MTPA curve from point O to point A, maximizing torque by appropriately distributing the *d*-axis and *q*-axis currents until the current limit circle. This stage is predominantly effective in low to medium-speed ranges. As the motor speed increases beyond point A where the voltage limit becomes significant, the control strategy transitions to the FW stage. This is represented in Fig. 1.8 by the red curve diverging from point A to point B. In this phase, the *d*-axis current is adjusted to a negative value, which effectively reduces the back-EMF. This reduction in back-EMF is crucial for allowing the

motor to operate at higher speeds within the given voltage limits. Although current limitations still apply, the voltage limit becomes the dominant factor affecting the motor's performance. At very high speeds, the motor reaches the maximum voltage limit, necessitating a shift to the MTPV control stage. This stage is depicted in Fig. 1.8 as the red curve from point B to point C. The MTPV strategy focuses on maximizing speed under voltage limitations by optimizing the *d*-axis and *q*-axis current distributions. The primary objective here is to maintain motor operation within the voltage limit while achieving the highest possible speed, thus extending the operational range of the motor.

It is worth mentioning that the presence or absence of MTPV control in the tested prototype can be attributed to the specific motor parameters. For the test prototype in this thesis, $\frac{\varphi_f}{L_d}$ equal to 6.25, which is less than the current limit of 10 A. Thus, the center of the voltage limit ellipse is located inside the current limit circle as shown in Fig. 1.8. Therefore, the MTPV control can be implemented to optimize the motor performance within the voltage limit, allowing the motor to achieve higher speeds by appropriately adjusting the current vector.

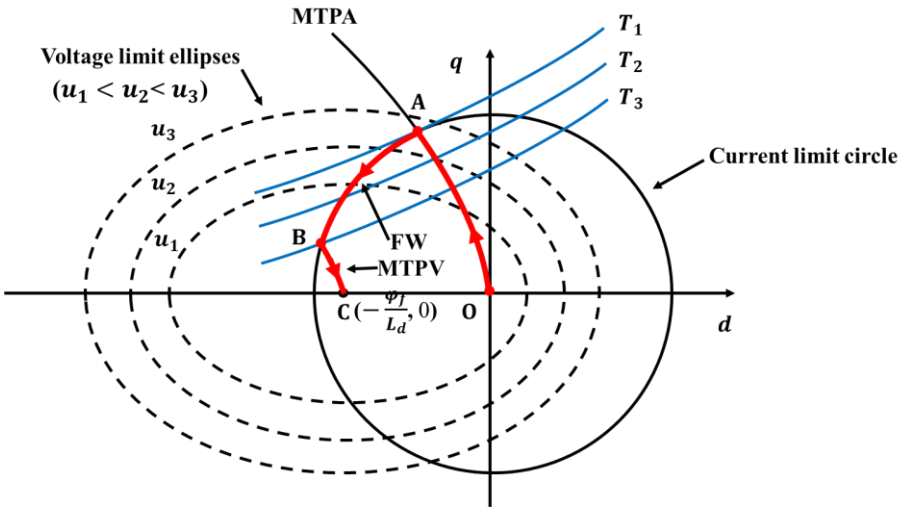

Fig. 1.8. Operating characteristics of an IPMSM under FW control.

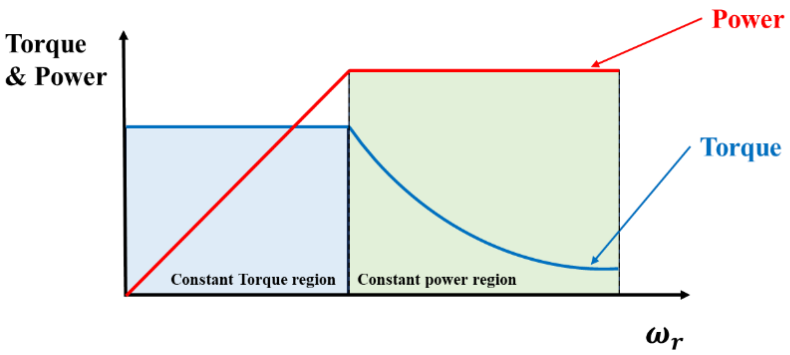

Fig. 1.9. Typical torque/speed and power/speed characteristic curves.

B. Control strategies of FW control

Based on the ways to develop the *d*- and *q*-axis currents, the FW control methods can be classified into three categories: feedforward control, feedback control, and hybrid control. This section provides an overview of conventional FW control strategies, including feedforward and feedback methods.

- **Feedforward control**

The concept of feedforward FW (FF-FW) control was first introduced by Morimoto et al. [MOR90] [MOR94]. FF-FWC methods are typically model-based FW control methods, relying on the mathematical model of PMSMs and the dc-link voltage. The reference *d*- and *q*-axis current vectors can be obtained by online calculation [MOR90] [MOR94] or offline lookup table [SHI04].

According to Fig. 1.8, in the FF-FWC stage which is curve "AB", the machine operates on the intersection point of the voltage limit ellipse and current limit circle. Hence, ignoring the resistance voltage drop, the reference *d*- and *q*-axis current can be obtained by

$$i_d = \frac{-\varphi_f + \sqrt{(\frac{u_{max}}{\omega_e})^2 - (L_q i_q)^2}}{L_d} \tag{1.27}$$

$$i_q = \sqrt{i_s^2 - i_d^2} \tag{1.28}$$

FF-FWC methods are highly dependent on accurate motor parameters and operating conditions but offer good stability and transient responses. These strategies ensure that the motor operates within the voltage and current limits, thereby preventing saturation and instability. The block diagram of FF-FWC methods is shown in Fig. 1.10.

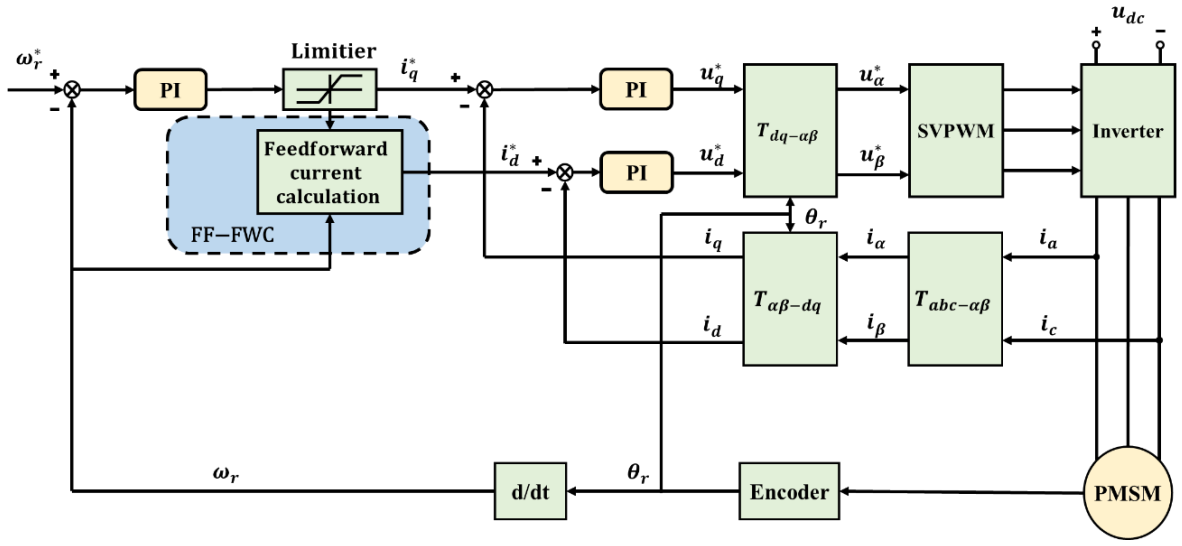

Fig. 1.10. Block diagram of FF-FWC method.

- **Feedback control**

The feedback FW (FB-FW) method employs a voltage feedback controller to adjust the current commands. Initially proposed for SPMSMs in [SON96] and later adapted for IPMSMs in [KIM97], the voltage FB-FW method is characterized by its closed-loop structure, providing robustness against parameter variations. This method can automatically achieve FW control without the need for decision trees. According to [BOL14], FB-FW control can be divided into two methods: adjusting the *d*-axis reference current [SON96] [KIM97] [BIA01] [WAI01] [JUN14] [BOZ17] [HUO22B] [WAN23] and modifying the current lead angle [DEN19] [BOL14]. The typical block diagram of the voltage magnitude FB-FW control based on *d*-axis current control is shown in Fig. 1.11.

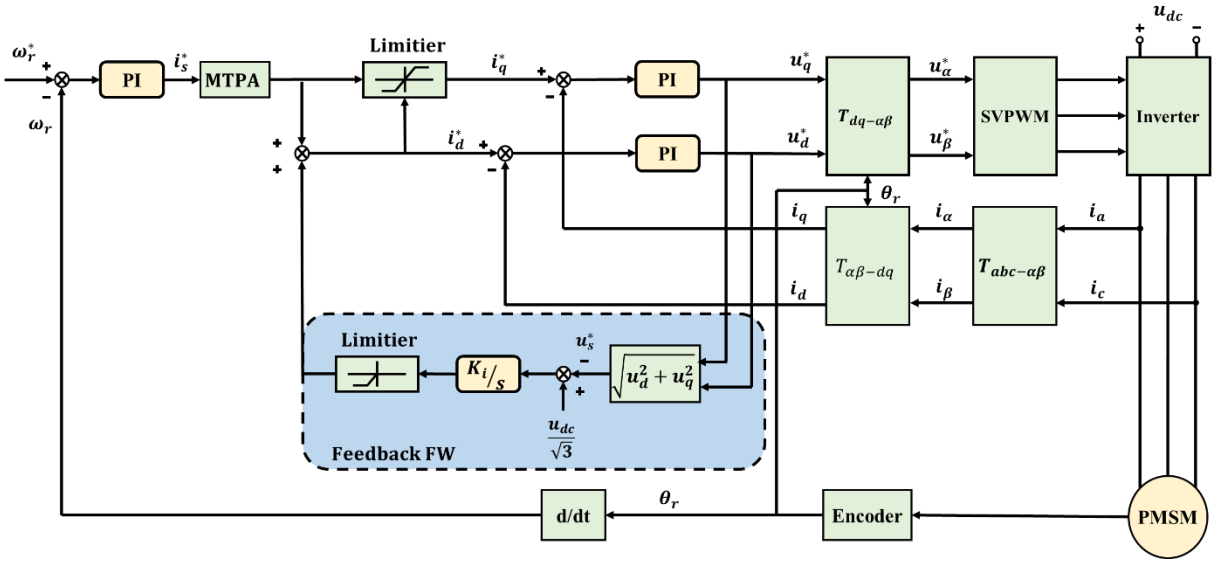

Fig. 1.11. Block diagram of the FB-FW control based on *d*-axis current control.

TABLE 1.1

COMPARISON OF FF-FW AND FB-FW CONTROL [WAN19A]

	FF-FW Control	**FB-FW Control**
Control strategy	Direct calculation based on motor model	Real-time adjustment based on PI controller
Implementation complexity	Low	High
Static performance	Medium	High
Dynamic performance	High	Medium
Adaptability	Low	High
Tuning requirements	Low	High
Stability	Medium	Medium
Parameter sensitivity	Yes	No

1.2.4 Sensorless Control

The development of sensorless control techniques for PMSMs has attracted significant attention in recent years due to their advantages in reducing system cost, increasing reliability, and enhancing robustness against harsh environmental conditions. Sensorless control can achieve high performance while mitigating mechanical wear and environmental issues by eliminating the need for physical position and speed sensors. Sensorless control techniques can be generally categorized into fundamental model-based methods and saliency-based methods. Fundamental model-based methods rely on mathematical models of the motor to estimate the rotor position. These methods are effective but can be compromised by parameter variations due to temperature changes and magnetic saturation. Saliency-based sensorless control methods involve injecting high-frequency (HF) signals into the motor windings and analyzing the resulting HF current response to determine the rotor position. These methods exploit the anisotropic properties of the motor and can provide accurate rotor position estimation, especially at zero and low-speed ranges where back-EMF is weak. A brief classification of sensorless control techniques for PMSMs is shown in Fig. 1.12.

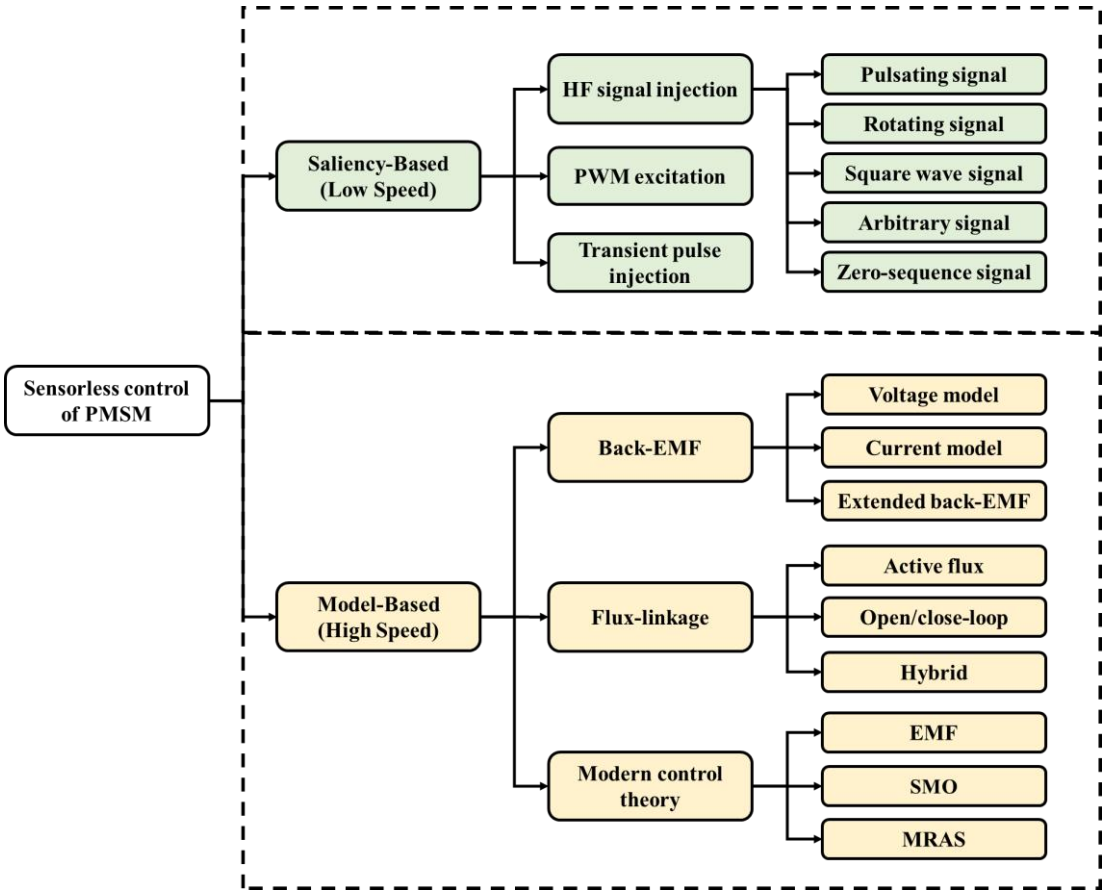

Fig. 1.12. Classification of sensorless control techniques for PMSMs [WAN20A] [WU20] [ZHU23].

A. Saliency-based sensorless control methods

Due to the anisotropic properties of PMSMs, there exists geometric or magnetic saliency that varies with rotor position. This machine saliency, being independent of rotor speed, can be utilized for sensorless position estimation at zero and low speeds. For a salient machine such as an IPMSM, the inductance variation with respect to rotor position is depicted in Fig. 1.13.

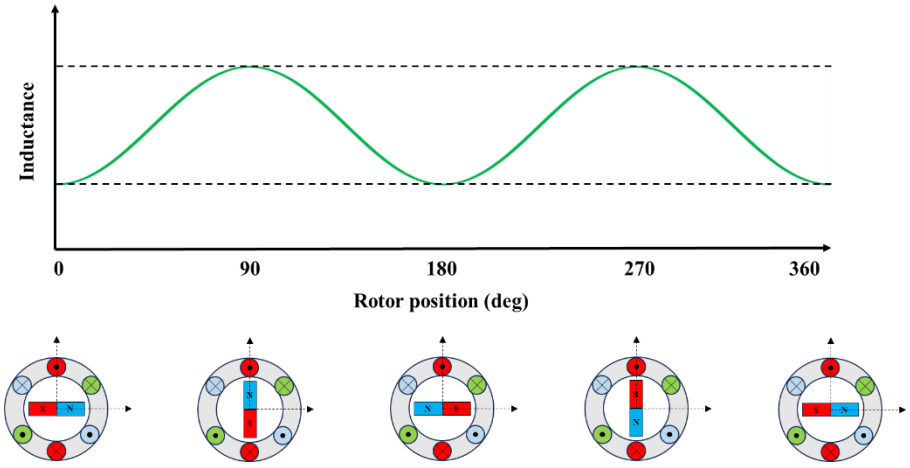

Fig. 1.13. Inductance variation against rotor position without considering armature reaction [KAN10] [WU20].

Saliency-based methods are commonly used to obtain rotor position information by monitoring the saliency at low-speed ranges for PMSM drives. According to the injected signals, the saliency-based methods can be categorized pulsating signal injection [LIU14] [XU16A] [SHU22], rotating signal injection [JAN95] [DEG98] [RAC10] , square wave injection [YOO11], and random injection [WAN16] [WAN17A] [ZHA19D].

- **HF machine model**

According to the voltage equation of IPMSM in the synchronous reference frame presented in (1.13) and (1.14). A HF signal, with the frequency much higher than the operating speed is injected into the system, the voltage drops across the stator resistance and the terms associated with ω_r can be neglected [RAC08]. Therefore, the HF voltage model of IPMSM can be expressed by

$$\begin{bmatrix} u_{dh} \\ u_{qh} \end{bmatrix} = \begin{bmatrix} L_{dh} & 0 \\ 0 & L_{qh} \end{bmatrix} p \begin{bmatrix} i_{dh} \\ i_{qh} \end{bmatrix} \tag{1.29}$$

where L_{dh} and L_{qh} represent the HF incremental dq-axis inductances. u_{dh}, u_{qh}, i_{dh} and i_{qh} are the HF dq-axis voltages and currents. When considering the cross-coupling effect, the above equation can be presented as

$$\begin{bmatrix} u_{dh} \\ u_{qh} \end{bmatrix} = \begin{bmatrix} L_{dh} & L_{dqh} \\ L_{qdh} & L_{qh} \end{bmatrix} p \begin{bmatrix} i_{dh} \\ i_{qh} \end{bmatrix} \tag{1.30}$$

where L_{dqh} and L_{qdh} are the HF mutual inductances due to the cross-coupling effect.

The HF signal injection (HFSI) methods are typically implemented within either a stationary reference frame or an estimated synchronous reference frame. The interrelation between these different reference frames is shown in Fig. 1.14.

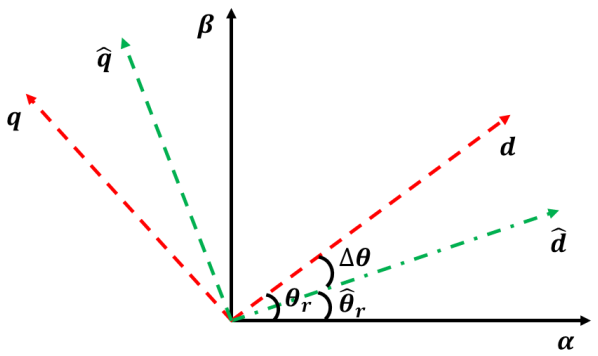

Fig. 1.14. Relationship between three reference frames.

Then, the HF voltage model of IPMSM in the stationary reference frame can be expressed by

$$\begin{bmatrix} u_{\alpha h} \\ u_{\beta h} \end{bmatrix} = T(\theta_r) \begin{bmatrix} L_{dh} & L_{dqh} \\ L_{qdh} & L_{qh} \end{bmatrix} T^{-1}(\theta_r) * p \begin{bmatrix} i_{\alpha h} \\ i_{\beta h} \end{bmatrix}$$

$$= \begin{bmatrix} L_{sa} - L_{sd}\cos(2\theta_r) - L_{dqh}\sin(2\theta_r) & -L_{sd}\sin(2\theta_r) + L_{dqh}\cos(2\theta_r) \\ -L_{sd}\sin(2\theta_r) + L_{dqh}\cos(2\theta_r) & L_{sa} + L_{sd}\cos(2\theta_r) + L_{dqh}\sin(2\theta_r) \end{bmatrix} * p \begin{bmatrix} i_{\alpha h} \\ i_{\beta h} \end{bmatrix} \quad (1.31)$$

$$L_{sa} = \frac{L_{dh} + L_{qh}}{2} \quad (1.32)$$

$$L_{sd} = -\frac{L_{dh} - L_{qh}}{2} \quad (1.33)$$

Then, the differential terms of HF current response in the $\alpha\beta$-axis can be derived as

$$p \begin{bmatrix} i_{\alpha h} \\ i_{\beta h} \end{bmatrix} = \begin{bmatrix} \frac{1}{L_p} + \frac{1}{L_n}\cos(2\theta_r + \theta_m) & \frac{1}{L_n}\sin(2\theta_r + \theta_m) \\ \frac{1}{L_n}\sin(2\theta_r + \theta_m) & \frac{1}{L_p} - \frac{1}{L_n}\cos(2\theta_r + \theta_m) \end{bmatrix} * \begin{bmatrix} u_{\alpha h} \\ u_{\beta h} \end{bmatrix} \quad (1.34)$$

$$\theta_m = \tan^{-1}\left(\frac{-L_{dqh}}{L_{sd}}\right) \quad (1.35)$$

$$L_p = \frac{L_{dh}L_{qh} - L_{dqh}^2}{L_{sa}} \quad (1.36)$$

$$L_n = \frac{L_{dh}L_{qh} - L_{dqh}^2}{\sqrt{L_{sd}^2 + L_{dqh}^2}} \quad (1.37)$$

where θ_m is referred to as the cross-coupling angle. It can be shown that the carrier current response includes information about the rotor position. L_p is the positive sequence inductance, L_n is the negative sequence inductance Normally, $L_p \ll L_n$.

In a sensorless control system, where the actual rotor position is unknown, the voltage model in (1.30) can be transformed into the estimated synchronous reference frame, as shown below.

$$\begin{bmatrix}\hat{u}_{dh}\\ \hat{u}_{qh}\end{bmatrix} = T(\Delta\theta_r)\begin{bmatrix}L_{dh} & L_{dqh}\\ L_{qdh} & L_{qh}\end{bmatrix}T^{-1}(\Delta\theta_r) * p\begin{bmatrix}\hat{i}_{dh}\\ \hat{i}_{qh}\end{bmatrix}$$
$$= \begin{bmatrix}L_{sa} - L_{sd}\cos(2\Delta\theta_r) - L_{dqh}\sin(2\Delta\theta_r) & -L_{sd}\sin(2\Delta\theta_r) + L_{dqh}\cos(2\Delta\theta_r)\\ -L_{sd}\sin(2\Delta\theta_r) + L_{dqh}\cos(2\Delta\theta_r) & L_{sa} + L_{sd}\cos(2\Delta\theta_r) + L_{dqh}\sin(2\Delta\theta_r)\end{bmatrix} * p\begin{bmatrix}\hat{i}_{dh}\\ \hat{i}_{qh}\end{bmatrix} \quad (1.38)$$

Similarly, the differential terms of HF current response can be given by

$$p\begin{bmatrix}\hat{i}_{dh}\\ \hat{i}_{qh}\end{bmatrix} = \begin{bmatrix}\frac{1}{L_p} + \frac{1}{L_n}\cos(2\Delta\theta_r + \theta_m) & \frac{1}{L_n}\sin(2\Delta\theta_r + \theta_m)\\ \frac{1}{L_n}\sin(2\Delta\theta_r + \theta_m) & \frac{1}{L_p} - \frac{1}{L_n}\cos(2\Delta\theta_r + \theta_m)\end{bmatrix} * \begin{bmatrix}\hat{u}_{dh}\\ \hat{u}_{qh}\end{bmatrix} \quad (1.39)$$

As shown above, the carrier current responses in the estimated synchronous reference frame also contain rotor position information and a position error θ_m is introduced by the cross-coupling effect.

- **HFSI methods**

Pulsating signal injection-based sensorless control method has been well-developed due to their inherent advantages, including reduced computational intensity, faster dynamic response, and intrinsic cancellation of filter lags during signal processing [RAC10]. The pulsating signal injection-based method can be mainly divided into *d*-axis injection and *q*-axis injection. With the *d*-axis voltage injection method, the introduced current ripple on the *q*-axis is limited, resulting in less torque ripple. Consequently, *d*-axis current injection is more commonly used.

For *d*-axis pulsating signal injection-based sensorless control method, an additional HF sinusoidal voltage signal is injected to the stator windings, and can be expressed as

$$\begin{bmatrix}v_{dh}\\ v_{qh}\end{bmatrix} = u_{hf}\begin{bmatrix}\cos(\omega_{hf}t)\\ 0\end{bmatrix} \quad (1.40)$$

where u_{hf} and ω_{hf} are the amplitude and frequency of the injected pulsating sinusoidal voltage signal. The *d*-axis pulsating signal injection-based sensorless control method is presented in Fig. 1.15.

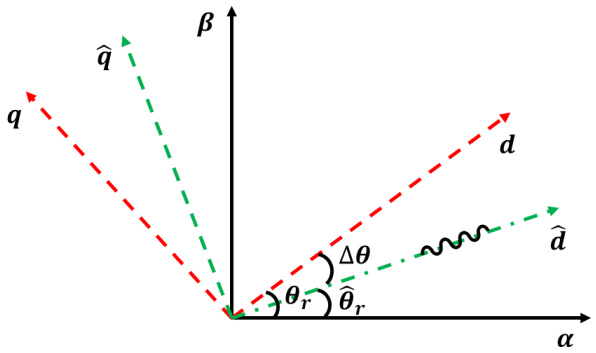

Fig. 1.15. *D*-axis pulsating signal injection-based sensorless control method.

Then, the carrier current responses can be expressed as follows.

$$p\begin{bmatrix}\hat{i}_{dh}\\ \hat{i}_{qh}\end{bmatrix}=\begin{bmatrix}\frac{1}{L_p}+\frac{1}{L_n}\cos\left(2\Delta\theta_r+\theta_m\right) & \frac{1}{L_n}\sin\left(2\Delta\theta_r+\theta_m\right)\\ \frac{1}{L_n}\sin\left(2\Delta\theta_r+\theta_m\right) & \frac{1}{L_p}-\frac{1}{L_n}\cos\left(2\Delta\theta_r+\theta_m\right)\end{bmatrix} * u_{hf}\begin{bmatrix}\cos\left(\omega_{hf}t\right)\\ 0\end{bmatrix} \tag{1.41}$$

$$\begin{bmatrix}\hat{i}_{dh}\\ \hat{i}_{qh}\end{bmatrix}=\begin{bmatrix}\frac{u_{hf}}{\omega_{hf}L_p}+\frac{u_{hf}}{\omega_{hf}L_n}\cos\left(2\Delta\theta_r+\theta_m\right)\\ \frac{u_{hf}}{\omega_{hf}L_n}\sin\left(2\Delta\theta_r+\theta_m\right)\end{bmatrix} * \sin\left(\omega_{hf}t\right) \tag{1.42}$$

$$\begin{bmatrix}\hat{i}_{dh}\\ \hat{i}_{qh}\end{bmatrix}=\begin{bmatrix}I_p+I_n\cos\left(2\Delta\theta_r+\theta_m\right)\\ I_n\sin\left(2\Delta\theta_r+\theta_m\right)\end{bmatrix} * \sin\left(\omega_{hf}t\right) \tag{1.43}$$

$$I_p=\frac{u_{hf}}{\omega_{hf}L_p} \tag{1.44}$$

$$I_n=\frac{u_{hf}}{\omega_{hf}L_n} \tag{1.45}$$

where I_p and I_n are the amplitude of positive and negative HF carrier current.

From (1.43), it is evident that the carrier current response is amplitude modulated by the rotor position information (assume that cross-coupling angle θ_m is constant for the given load conditions). When the estimated position error $\Delta\theta_r$ is sufficiently small, the amplitude of $\hat{i}_{qh}$ becomes very small. Therefore, the q-axis carrier current response ($\hat{i}_{qh}$) is usually used to extract the rotor position information. To extract the rotor position information, a demodulation process is required to filter the HF component and obtain the amplitude of the q-axis carrier current response $\hat{i}_{qh}$. The block diagram of the demodulation method is shown in Fig. 1.16.

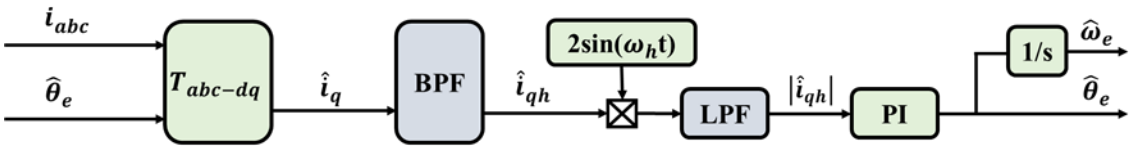

Fig. 1.16. Demodulation of pulsating signal injection-based method.

The demodulation process can be presented as

$$\begin{bmatrix} |\hat{i}_{dh}| \\ |\hat{i}_{qh}| \end{bmatrix} = LPF\left(\begin{bmatrix} \hat{i}_{dh} \\ \hat{i}_{qh} \end{bmatrix} * 2\sin(\omega_{hf}t)\right) = \begin{bmatrix} I_p + I_n\cos(2\Delta\theta_r + \theta_m) \\ I_n\sin(2\Delta\theta_r + \theta_m) \end{bmatrix} \tag{1.46}$$

After demodulation, the amplitude of the q-axis response current can be obtained and then the q-axis response current as the input of the position observer. When the estimated position error $\Delta\theta_r$ is approaching to zero, the rotor position is obtained.

Rotating signal injection-based sensorless control method is another commonly used technique in sensorless control. When a rotating carrier voltage signal is injected into an IPMSM, two types of signal response can be used to estimate the saliency position: negative sequence carrier current [RAC08] [RAC10] [BAS11] [GAB13] [MED15] [KIM16] [CHE16] [HOS16] [JIN18] [SHU22] and zero sequence carrier signal [BRI05] [GAR07] [ALM17] [XU16A] [XU16B]. Although the zero sequence component-based method can increase accuracy in the estimated position and a larger estimation bandwidth due to its insensitivity to distortion in the injected carrier voltage [BRI05] [GAR07] [ALM17] [XU16A] [XU16B], it is rarely used because it requires an additional sensor to measure the zero sequence voltage. Therefore, only the negative sequence carrier current-based method is discussed here.

In the rotating signal injection method, a balanced HF sinusoidal voltage signal is introduced into the stationary reference frame, as represented by

$$\begin{bmatrix} v_{dh} \\ v_{qh} \end{bmatrix} = u_{hf}\begin{bmatrix} \cos(\omega_{hf}t) \\ \sin(\omega_{hf}t) \end{bmatrix} \tag{1.47}$$

The conventional rotating signal injection is shown in Fig. 1.17.

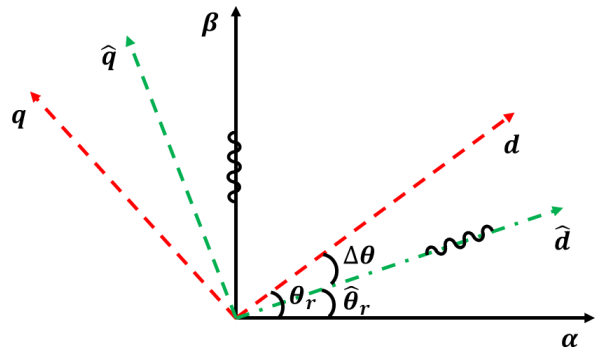

Fig. 1.17. Conventional rotating signal injection-based sensorless control method.

After injection, the differential terms of carrier current responses in the stationary reference frame can be expressed as

$$p\begin{bmatrix} i_{\alpha h} \\ i_{\beta h} \end{bmatrix} = \begin{bmatrix} \frac{1}{L_p} + \frac{1}{L_n}\cos(2\theta_r + \theta_m) & \frac{1}{L_n}\sin(2\theta_r + \theta_m) \\ \frac{1}{L_n}\sin(2\theta_r + \theta_m) & \frac{1}{L_p} - \frac{1}{L_n}\cos(2\theta_r + \theta_m) \end{bmatrix} * u_{hf}\begin{bmatrix} \cos(\omega_{hf}t) \\ \sin(\omega_{hf}t) \end{bmatrix} \quad (1.48)$$

After injection, the $\alpha\beta$-axis carrier current response can be expressed as

$$\begin{bmatrix} i_{\alpha h} \\ i_{\beta h} \end{bmatrix} = \begin{bmatrix} \frac{u_{hf}}{\omega_{hf}L_p}\sin(\omega_{hf}t) + \frac{u_{hf}}{\omega_{hf}L_n}\sin(\omega_{hf}t - 2\theta_r + \theta_m) \\ -\frac{u_{hf}}{\omega_{hf}L_p}\cos(\omega_{hf}t) + \frac{u_{hf}}{\omega_{hf}L_n}\cos(2\theta_r + \theta_m - \omega_{hf}t) \end{bmatrix} \quad (1.49)$$

$$\begin{bmatrix} i_{\alpha h} \\ i_{\beta h} \end{bmatrix} = \begin{bmatrix} I_p\cos\left(\omega_{hf}t - \frac{\pi}{2}\right) \\ I_p\sin\left(\omega_{hf}t - \frac{\pi}{2}\right) \end{bmatrix} + \begin{bmatrix} I_n\cos\left(-\omega_{hf}t + 2\theta_r + \theta_m + \frac{\pi}{2}\right) \\ I_n\sin\left(-\omega_{hf}t + 2\theta_r + \theta_m + \frac{\pi}{2}\right) \end{bmatrix} \quad (1.50)$$

$$I_{hf} = I_p e^{j(\omega_{hf}t - \frac{\pi}{2})} + I_n e^{j(-\omega_{hf}t + 2\theta_r + \theta_m + \frac{\pi}{2})} \quad (1.51)$$

where I_{hf} is HF carrier current vector. From (1.51), the carrier current response consists of two components. The first term is a positive sequence component, which has the same frequency as the injected carrier voltage signal, the second term is referred to as the negative sequence component, which contains the rotor position information. Consequently, the negative sequence component can be used to track the rotor position [RAC08].

Given the low amplitude of the negative sequence component, it is essential to filter out the fundamental and positive sequence components from the total current response. There are two typical demodulation methods employed for rotor position estimation. The first method is the "Heterodyning method," shown in Fig. 1.18(a). This method involves shifting the positive

sequence component of the carrier current to the HF domain. This frequency shift enables the LPF to filter out the positive sequence easily. The isolated negative sequence is then utilized for accurate rotor position estimation [JAN95]. The second method is "synchronous reference frame filter (SRFF)," as shown in Fig. 1.18(b) [DEG98] [GAR07] [RAC10]. In the SRFF method, the signal is transformed into a synchronous reference frame, where the negative sequence components are more readily distinguishable. By applying SRFF, the negative sequence components are effectively separated from the positive sequence components. These remaining negative sequence components are used to determine the rotor position information. The detailed block diagram of the signal demodulation processes are presented in Fig. 1.18.

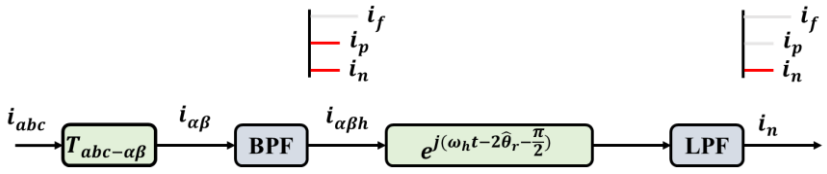

(a) Heterodyning method [JAN95]

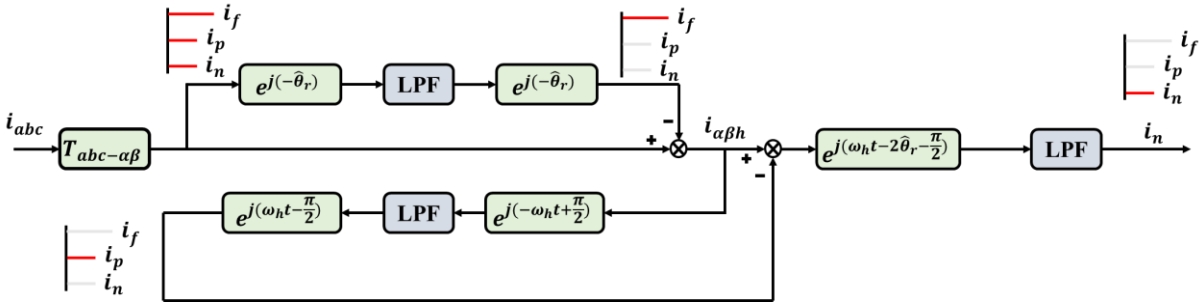

(b) SRFF method [GON12] [WU20]

Fig. 1.18. Signal demodulation process for rotating signal injection-based method. (a) Heterodyning method [JAN95]. (b) SRFF method [GON12] [WU20].

After demodulation, the negative sequence current i_n is obtained as

$$i_n = I_n e^{j(2\Delta\theta_r+\theta_m)} \tag{1.52}$$

$$i_n = \begin{bmatrix} i_{nd} \\ i_{nq} \end{bmatrix} = \begin{bmatrix} I_n \cos(2\Delta\theta_r + \theta_m) \\ I_n \sin(2\Delta\theta_r + \theta_m) \end{bmatrix} \tag{1.53}$$

Ignoring the influence of cross-coupling effect, the estimated position aligns with the actual position after the estimated q-axis current is minimized. However, it generally requires more complex signal demodulation processing and computational resources compared to the pulsating signal injection-based sensorless control method.

As discussed above, the conventional pulsating sinusoidal signal and rotating signal injection-based sensorless control methods typically require an LPF to eliminate HF signals during the demodulation process. However, the use of LPFs significantly limits the bandwidth of position estimation and the dynamic response of the system. The pulsating sinusoidal voltage signal and the rotating voltage signal are both modulated by the PWM signal, which is a square wave. When using this method, the frequency of the injected voltage signal is inherently limited by the characteristics of the sinusoidal modulation. However, when a pulsating square wave signal is used for injection, it can achieve much higher frequencies. This higher frequency injection capability is due to the nature of the square wave signal, which allows for rapid switching and does not suffer from the same frequency limitations as sinusoidal signals. As a result, the pulsating square wave signal injection-based method has gained popularity in recent years. This method is advantageous because it simplifies the demodulation process, eliminating the need for an additional LPF [WAN20A] [WU20] [ZHU23]. Square wave signals can be injected into both the estimated synchronous reference frame [KIM12] [WAN20A] and the stationary reference frame [YOO11]. Using the estimated synchronous injection as an example, Fig. 1.19 shows the pulsating square wave signal injected into the estimated *d*-axis.

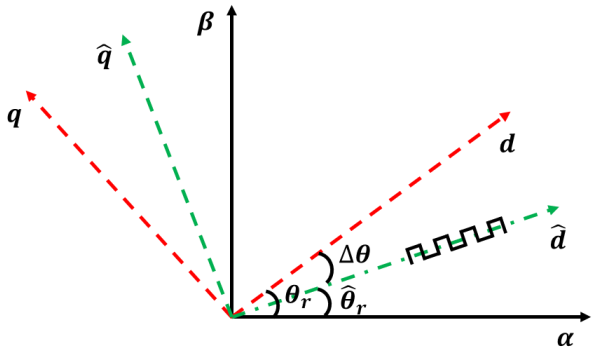

Fig. 1.19. Conventional pulsating square wave signal injection in estimated *d*-axis.

The injected square wave voltage signal can be presented by

$$\hat{v}_{dh} = \begin{cases} u_{hf} & \text{half duty} \\ -u_{hf} & \text{otherwise} \end{cases} \tag{1.54}$$

Then, the differential carrier current responses in the estimated reference frame can be described as follows.

$$\begin{bmatrix} \Delta\hat{i}_{dh} \\ \Delta\hat{i}_{qh} \end{bmatrix} = \begin{cases} u_{hf}\Delta T \begin{bmatrix} \frac{1}{L_p} + \frac{1}{L_n}\cos\left(2\Delta\theta_r + \theta_m\right) \\ \frac{1}{L_n}\sin\left(2\Delta\theta_r + \theta_m\right) \end{bmatrix} & \hat{v}_{dh} > 0 \\ -u_{hf}\Delta T \begin{bmatrix} \frac{1}{L_p} + \frac{1}{L_n}\cos\left(2\Delta\theta_r + \theta_m\right) \\ \frac{1}{L_n}\sin\left(2\Delta\theta_r + \theta_m\right) \end{bmatrix} & \hat{v}_{dh} < 0 \end{cases} \tag{1.55}$$

where ΔT is the half cycle of the injected square wave voltage signal.

From (1.55), it is evident that the differential carrier current responses in the *q*-axis carries the rotor position information. The demodulation process is similar to the pulsating sinusoidal voltage signal injection-based sensorless control method as shown in Fig. 1.16. By using a PI regulator to force the *q*-axis HF response current to zero, the rotor position can be determined.

Meanwhile, the HFSI-based sensorless control methods mentioned above use HF voltage signals with fixed frequency and amplitude. These fixed signals, however, are prone to generating acoustic noise [WAN16] and electromagnetic interference (EMI) issues [WAN17A]. To mitigate these problems, researchers have proposed methods that inject HF signals with non-fixed frequencies or amplitudes [TAN14] [WAN16] [WAN17A]. A popular method involves injecting random voltage signals, which broadens the spectra of the induced currents and thus reduces noise. For example, in [WAN16], a pseudo-random HF square wave voltage is injected into the estimated synchronous reference frame. The pseudo-random nature of the signal helps to further alleviate noise and interference issues. By using these advanced methods, the issues of acoustic noise and EMI in high-frequency signal injection can be significantly reduced, leading to more efficient and quieter sensorless control systems.

TABLE 1.2

COMPARISON OF VARIOUS SIGNAL INJECTION-BASED METHODS [WAN20A] [WU20] [ZHU23]

	Pulsating Sinsoudial		**Rotating**	**Pulsating Square Wave**	**Random**
Coordinate	Stationary	Estimated synchronous	Stationary	Estimated synchronous	Estimated synchronous
Injected signal	Pulsating	Pulsating	Rotating	Square wave	Square wave
Demoudulation process	Medium	Medium	Complex	Simple	Medium
Bandwidth	Medium	Medium	Low	High	High
Static performance	Medium	Medium	Low	High	High
Dynamic performance	Medium	Medium	Low	High	High
Torque ripple	Medium	Medium	Large	Small	Small
Audible noise	Medium	Medium	Large	Medium	Small
Parameter sensitivity	Yes	No	No	No	No

- **Magnetic polarity detection**

The inductance varies twice per electrical period, leading to a potential 180-degree angle ambiguity [JAN06]. It is necessary to identify the magnetic polarity to ensure accurate starting torque in saliency-based sensorless control methods. The fundamental principle for detecting magnetic polarity relies on the magnetic saturation effect [SCH97]. When a positive *d*-axis current is applied, it increases the saturation of the stator iron core, thereby reducing the *d*-axis inductance. Conversely, a negative *d*-axis current decreases saturation, increasing the *d*-axis inductance. Magnetic polarity can be determined through three main methods: short pulse injection [MIK00] [MUR12], secondary harmonics-based method [JEO05B] [RAC10] [XU16B], and *d*-axis current injection [GON13]. Fig. 1.20 shows the comparison of different magnetic polarity detection methods.

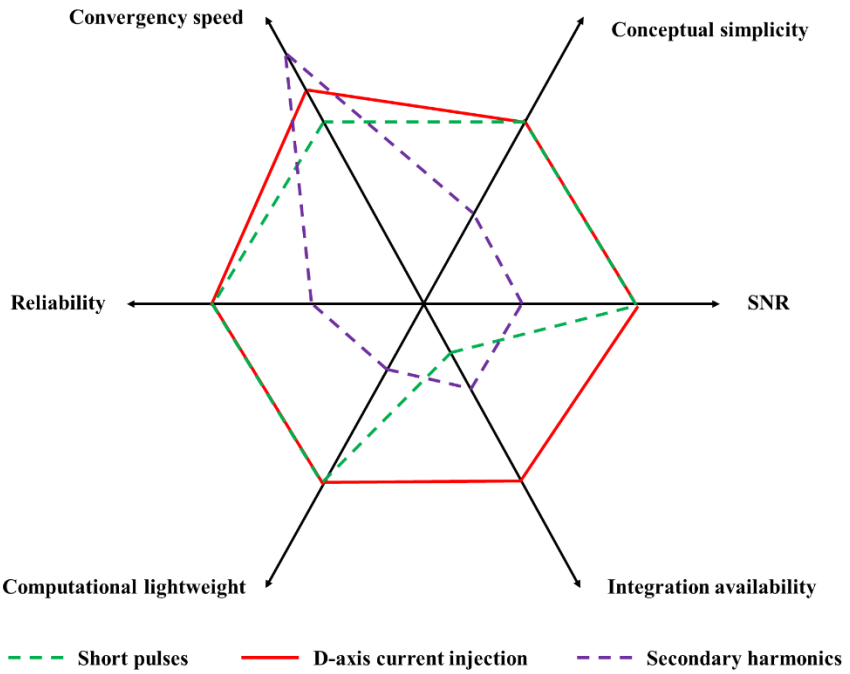

Fig. 1.20. Comparison of different magnetic polarity detection methods [GON12] [WU20].

- **Cross-coupling compensation**

Saliency-based sensorless control methods rely on the magnetic anisotropy of the motor. The cross-coupling effect, which refers to the mutual inductance between the *d*-axis and *q*-axis of the motor, complicates the estimation process by introducing errors in the inductances. Specifically, the mutual inductance caused by cross-coupling distorts the *d*-axis and *q*-axis inductances, leading to inaccuracies in rotor position estimation [BIA05] [GUG06] [LI09] [SHU22] [ZHU23].

As (1.30), when considering the cross-coupling effect, the HF voltage equation can be presented as

$$\begin{bmatrix} v_{dh} \\ v_{qh} \end{bmatrix} = \begin{bmatrix} L_{dh} & L_{dqh} \\ L_{qdh} & L_{qh} \end{bmatrix} p \begin{bmatrix} i_{dh} \\ i_{qh} \end{bmatrix} \tag{1.56}$$

where L_{dqh} and L_{qdh} are the HF incremental mutual inductances due to the cross-coupling effect, and they are equal.

As (1.35), the cross-coupling angle can be expressed as

$$\theta_m = \tan^{-1}\left(\frac{-L_{dqh}}{L_{sd}}\right) \tag{1.57}$$

According to [WU20] [SHU22], cross-coupling effect compensation can be divided into two types: offline-based compensation method [ZHU07] [LI09] [DE10] [XU14] [WAN19B] and online-based compensation method [REI08] [MOR21]. Offline-based compensation methods involve pre-calculating compensation values using offline measurements or simulations. These methods require the motor to be characterized in a controlled environment where cross-coupling effects are accurately measured. The resulting compensation values are stored and used during operation to correct rotor position estimation. While this approach ensures high accuracy due to the controlled environment, it lacks adaptability to changes in motor parameters or operating conditions over time and requires an initial setup that can be time-consuming.

On the other hand, online-based compensation methods dynamically adjust compensation values during motor operations. By using real-time data to estimate and correct cross-coupling effects, these methods allow the system to adapt to varying conditions, ensuring consistent performance. This adaptability eliminates the need for extensive pre-characterization of the motor, saving time and effort. However, the real-time nature of these methods introduces a higher computational load and potential for reduced accuracy due to noise or latency in measurement and processing systems.

In summary, offline-based compensation offers high accuracy with less computational demand but lacks flexibility, whereas online-based compensation provides adaptability at the expense of increased computational complexity and potential accuracy challenges.

B. Fundamental model-based sensorless control methods

As aforementioned, saliency-based sensorless control methods are effective at low and zero-speed ranges. However, the use of injected extra signals in these methods can lead to undesirable effects, including increased losses, torque ripples, and acoustic noise [WAN20A] [ZHU23]. Additionally, at higher operating speeds, the maximum output voltage of the inverter may limit the feasibility of adding the injected signal. Thus, it is recommended to employ saliency-based methods with signal injection only at low and zero-speed ranges [STA14] [LEE15] [ZHA17]. Meanwhile, the fundamental model-based sensorless control methods are more effective in high-speed regions where the back-EMF is large [ZHU23]. The basic idea of these methods is to estimate the EMF or flux using the fundamental model and employ a position/speed observer to accurately determine rotor position and speed. The typical rotor position estimation process is shown in Fig. 1.21.

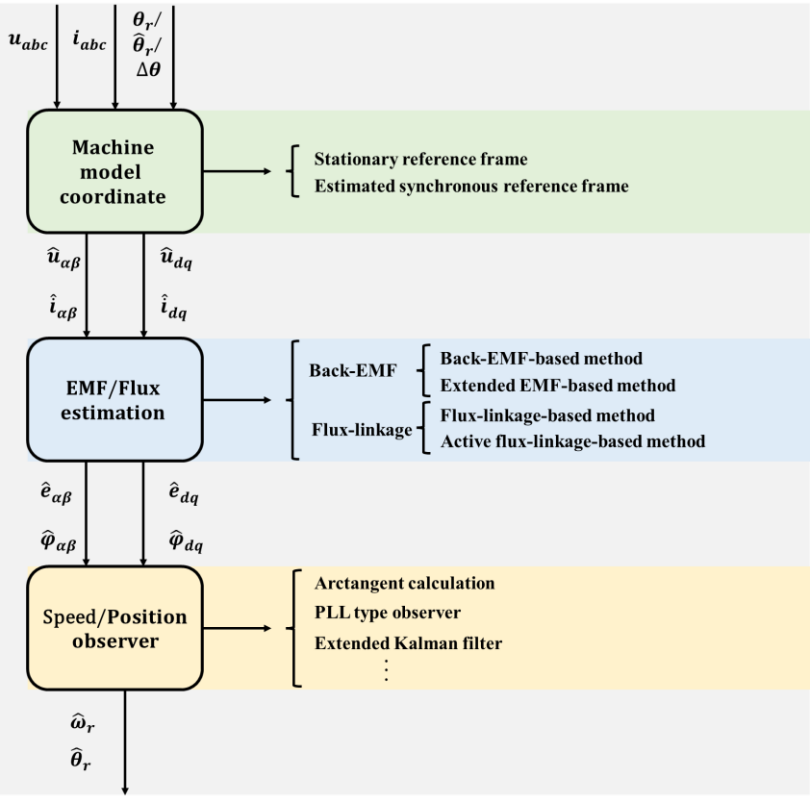

Fig. 1.21. Typical rotor position estimation process of fundamental model-based methods [WAN20A] [WU20] [ZHU23].

- **Back-EMF-based method**

The voltage equations of SPMSM in the synchronous reference frame can be expressed as

$$\begin{bmatrix} u_d \\ u_q \end{bmatrix} = \begin{bmatrix} R_s + pL_s & \omega_e L_s \\ \omega_e L_s & R_s + pL_s \end{bmatrix} \begin{bmatrix} i_d \\ i_q \end{bmatrix} + \begin{bmatrix} 0 \\ \omega_e \varphi_f \end{bmatrix} \tag{1.58}$$

where u_d, u_q, i_d, and $i_q$represent the dq-axis stator voltages and currents in the synchronous reference frame, resprectively. φ_f is the flux-linkages, ω_e is the electrical rotor speed, L_s is the stator inductance.

In a sensorless control system, the actual rotor position is unknown. Therefore, the voltage model in (1.58) can be transformed into the estimated synchronous reference frame as shown below.

$$\begin{bmatrix} \hat{u}_d \\ \hat{u}_q \end{bmatrix} = \begin{bmatrix} R_s + pL_s & -\omega_e L_s \\ \omega_e L_s & R_s + pL_s \end{bmatrix} \begin{bmatrix} \hat{i}_d \\ \hat{i}_q \end{bmatrix} + \begin{bmatrix} \hat{E}_d \\ \hat{E}_q \end{bmatrix} \tag{1.59}$$

$$\begin{bmatrix}\hat{E}_d\\ \hat{E}_q\end{bmatrix} = \omega_e\varphi_f\begin{bmatrix}-\sin\Delta\theta_r\\ \cos\Delta\theta_r\end{bmatrix} \tag{1.60}$$

where ∧ are the estimated variations in the estiamted reference frame.

Then, the estimated rotor position error can be obtained as

$$\Delta\theta_r = \tan^{-1}\left(-\frac{\hat{E}_d}{\hat{E}_q}\right) \approx -\frac{\hat{E}_d}{\hat{E}_q} \tag{1.61}$$

The estimated rotor position error can be directly calculated using the arctangent function, as shown in (1.61). This error can then be minimized to zero using a position observer, such as a phase-locked loop (PLL). When the estimated rotor position error $\Delta\theta_r$ approaches zero, it indicates that the estimated rotor position is very close to the actual rotor position. This close alignment ensures that the sensorless estimation is highly accurate, resulting in effective and stable motor control. However, for the salient machine, such as IPMSM, the *dq*-axis inductance is different. The voltage equation (1.58) can be expressed as

$$\begin{bmatrix}u_d\\ u_q\end{bmatrix} = \begin{bmatrix}R_s + pL_d & -\omega_e L_q\\ \omega_e L_d & R_s + pL_q\end{bmatrix}\begin{bmatrix}i_d\\ i_q\end{bmatrix} + \begin{bmatrix}0\\ \omega_e\varphi_f\end{bmatrix} \tag{1.62}$$

where L_d, and L_q are the *dq*-axis apparent inductances. The inductance matrix is asymmetry in the salient machines, making it difficult to directly extract the back-EMF from the estimated reference frame. To address this issue, [MOR02] and [CHE03] proposed the concept of "extended back-EMF" (EEMF) for salient machines. The EEMF model was developed to unify the back-EMF-based sensorless control methods for both non-salient machines and salient machines. This unified model provides a general solution that applies to all types of PMSMs, ensuring consistent performance across different motor designs. By applying the EEMF, the voltage equations can be expressed as

$$\begin{bmatrix}u_d\\ u_q\end{bmatrix} = \begin{bmatrix}R_s + pL_d & -\omega_e L_q\\ \omega_e L_q & R_s + pL_d\end{bmatrix}\begin{bmatrix}i_d\\ i_q\end{bmatrix} + \begin{bmatrix}0\\ E_{ex}\end{bmatrix} \tag{1.63}$$

$$E_{ex} = \omega_e\varphi_f + \left(L_d - L_q\right)\left(\omega_e i_d - p i_q\right) \tag{1.64}$$

In the EEMF-based sensorless control method, the estimated reference frame is used since the rotor position is unknown, and then the voltage equations are presented as

$$\begin{bmatrix}\hat{u}_d\\ \hat{u}_q\end{bmatrix}=\begin{bmatrix}R_s+pL_d & -\omega_e L_q\\ \omega_e L_q & R_s+pL_d\end{bmatrix}\begin{bmatrix}\hat{i}_d\\ \hat{i}_q\end{bmatrix}+\begin{bmatrix}\hat{E}_d\\ \hat{E}_q\end{bmatrix} \tag{1.65}$$

$$\begin{bmatrix}\hat{E}_d\\ \hat{E}_q\end{bmatrix}=E_{ex}\begin{bmatrix}-\sin\Delta\theta_r\\ \cos\Delta\theta_r\end{bmatrix}+\Delta\omega_e L_d\begin{bmatrix}\hat{i}_d\\ \hat{i}_q\end{bmatrix} \tag{1.66}$$

where $\Delta\omega_e$ is the estimated speed error.

Assuming that the estimation error between the estimated speed and the actual speed $\Delta\omega_e$ is sufficiently small, the position error can be expressed as

$$\Delta\theta_r=\tan^{-1}\left(-\frac{\hat{E}_d}{\hat{E}_q}\right)\approx-\hat{E}_d/\hat{E}_q \tag{1.67}$$

Similarly, $\Delta\theta_r$ can be controlled to 0 by PLL type observer. Thus, the estimated rotor position can be aligned with the actual rotor position. The block diagram of the EEMF-based position observer is shown in Fig. 1.22.

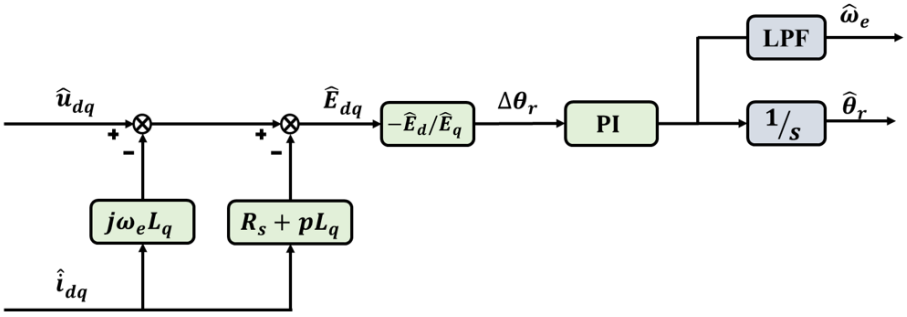

Fig. 1.22. EEMF-based position observer.

- **Flux-linkage-based method**

The voltage and flux-linkage of non-salient machine in the stationary reference frame can be presented as

$$\begin{bmatrix}u_\alpha\\ u_\beta\end{bmatrix}=\begin{bmatrix}R_s & 0\\ 0 & R_s\end{bmatrix}\begin{bmatrix}i_\alpha\\ i_\beta\end{bmatrix}+\rho\begin{bmatrix}\varphi_\alpha\\ \varphi_\beta\end{bmatrix} \tag{1.68}$$

$$\begin{bmatrix}\varphi_\alpha\\ \varphi_\beta\end{bmatrix}=\begin{bmatrix}L_s & 0\\ 0 & L_s\end{bmatrix}\begin{bmatrix}i_\alpha\\ i_\beta\end{bmatrix}+\begin{bmatrix}\varphi_{m\alpha}\\ \varphi_{m\beta}\end{bmatrix} \tag{1.69}$$

$$\begin{bmatrix}\varphi_{m\alpha}\\ \varphi_{m\beta}\end{bmatrix}=\varphi_f\begin{bmatrix}\cos\theta_r\\ \sin\theta_r\end{bmatrix} \tag{1.70}$$

where u_α, u_β, i_α, i_β, φ_α, φ_β, and L_s are the stator voltages, currents, flux-linkages, and phase

inductances in the stationary reference frame, respectively. $\varphi_{m\alpha}$ and $\varphi_{m\beta}$ are the PM excitation flux-linkage. The phasor diagram of flux-linkage is shown in Fig. 1.23.

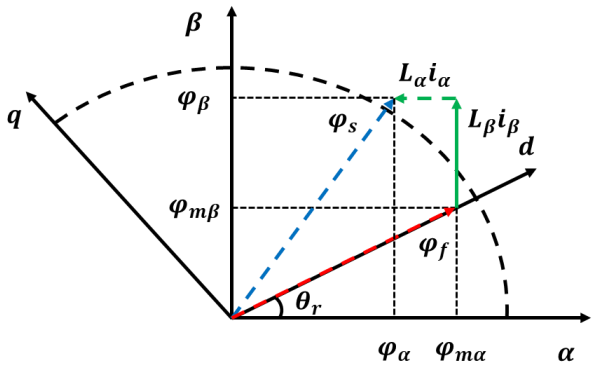

Fig. 1.23. Phasor diagram of flux-linkage [WU20].

According to (1.68) to (1.70), the rotor position can be obtained as

$$\theta_r = \tan^{-1}\left(\frac{\varphi_\beta - L_s i_\beta}{\varphi_\alpha - L_s i_\alpha}\right) = \tan^{-1}\left(\frac{\varphi_{m\beta}}{\varphi_{m\alpha}}\right) \tag{1.71}$$

$$\varphi_\alpha = \int (u_\alpha - R_s i_\alpha) dt \tag{1.72}$$

$$\varphi_\beta = \int (u_\beta - R_s i_\beta) dt \tag{1.73}$$

Similarly, for a salient-pole machine, the voltage equation in the stationary reference frame can be expressed as

$$\begin{bmatrix} u_\alpha \\ u_\beta \end{bmatrix} = \begin{bmatrix} R_s & 0 \\ 0 & R_s \end{bmatrix} \begin{bmatrix} i_\alpha \\ i_\beta \end{bmatrix} + \rho \begin{bmatrix} \varphi_\alpha \\ \varphi_\beta \end{bmatrix} \tag{1.74}$$

$$\begin{bmatrix} \varphi_\alpha \\ \varphi_\beta \end{bmatrix} = \begin{bmatrix} L_{\alpha\alpha} & M_{\alpha\beta} \\ M_{\beta\alpha} & L_{\beta\beta} \end{bmatrix} \begin{bmatrix} i_\alpha \\ i_\beta \end{bmatrix} + \varphi_f \begin{bmatrix} \cos\theta_r \\ \sin\theta_r \end{bmatrix} \tag{1.75}$$

$$L_{\alpha\beta} = \begin{bmatrix} L_{\alpha\alpha} & M_{\alpha\beta} \\ M_{\beta\alpha} & L_{\beta\beta} \end{bmatrix} = \begin{bmatrix} \Sigma L + \Delta L \cos(2\theta_r) & \Delta L \sin(2\theta_r) \\ \Delta L \sin(2\theta_r) & \Sigma L - \Delta L \cos(2\theta_r) \end{bmatrix} \tag{1.76}$$

$$\Sigma L = \frac{L_d + L_q}{2} \quad \Delta L = \frac{L_d - L_q}{2} \tag{1.77}$$

where $L_{\alpha\alpha}$, $L_{\beta\beta}$, $M_{\alpha\beta}$, and $M_{\beta\alpha}$ are the self- and mutual- inductances in the stationary reference frame, respectively. $L_{\alpha\beta}$ is the inductance matrix of $\alpha\beta$-axis, ΣL and ΔL are the average and differential values of dq-axis inductances. As shown in (1.76), the inductance matrix's

asymmetry makes it complex to determine the rotor position. To address this, the concept of "active flux-linkage" was proposed in [BOL08] and [BOL09]. This approach unifies the treatment of non-salient and salient machines, simplifying the flux-linkage estimation process. The active flux-linkage can be presented by

$$\varphi_a = \varphi_f + (L_q - L_d) i_d \tag{1.78}$$

Therefore, the flux-linkage equation in the stationary can be expressed as

$$\begin{bmatrix} \varphi_\alpha \\ \varphi_\beta \end{bmatrix} = \begin{bmatrix} L_q & 0 \\ 0 & L_q \end{bmatrix} \begin{bmatrix} i_\alpha \\ i_\beta \end{bmatrix} + \varphi_a \begin{bmatrix} \cos\theta_r \\ \sin\theta_r \end{bmatrix} \tag{1.79}$$

Thus, the rotor position can be obtained by

$$\theta_r = \tan^{-1}\left(\frac{\varphi_\beta - L_q i_\beta}{\varphi_\alpha - L_q i_\alpha}\right) \tag{1.80}$$

Back-EMF-based sensorless control methods and flux-linkage-based sensorless control methods are both based on the fundamental model of the machine. They can operate in both the stationary reference frame and the estimated synchronous reference frame. Table 1.3 shows the comparison of these two sensorless control methods [ZHU23].

TABLE 1.3

COMPARISON OF BACK-EMF AND FLUX-LINKAGE-BASED METHODS [ZHU23]

	Back-EMF	**Flux-linkage**
Implementation equation	$e_x = u_x - R_s i_s - L_y \frac{di_x}{dt}$	$\varphi_x = \int (u_x - R_s i_s) dt - L_y i_x$
Speed dependency	Dependent	Independent
Calculation	Differential	Integral
Robustness to noise	Low	High
Dynamic performance	High	Low
Parameter sensitivity	Yes	Yes

1.3 Small DC-Link Capacitor-Based PMSM Drive Systems

1.3.1 Characteristics of Small DC-Link Capacitor-Based PMSM Drive Systems

With the advancement of power electronics technology, variable-frequency drives (VFDs) have

become widely used in low-power domestic applications such as air conditioners, refrigerators, and vacuum cleaners, as well as in industrial applications like fans and pumps [TAK01] [LAM09] [JUN14]. Nowadays, most VFD systems employ large-volume electrolytic dc-link capacitors to maintain a constant dc-link voltage and ensure system stability. However, the use of large-volume electrolytic capacitors could introduce some issues such as increased size and high cost. Additionally, stabilizing the dc-link voltage with large capacitors leads to a significant presence of harmonics in the grid side current, which can degrade the power grid and threaten its normal operation [WAN20B]. To address this issue, PFC circuits are commonly implemented to improve grid side power quality, although this further adds to the cost and size of the drive systems [LIS05] [ZHA19A]. In response to these challenges, Japanese scholars first proposed a drive design that uses small dc-link capacitors instead of large-volume dc-link capacitors and cancels the PFC circuit [TAK01]. The circuit topology structure is shown in Fig. 1.24.

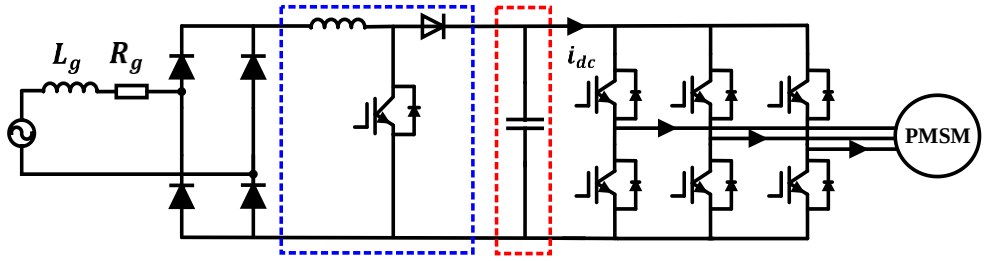

(a) Conventional PMSM drive systems

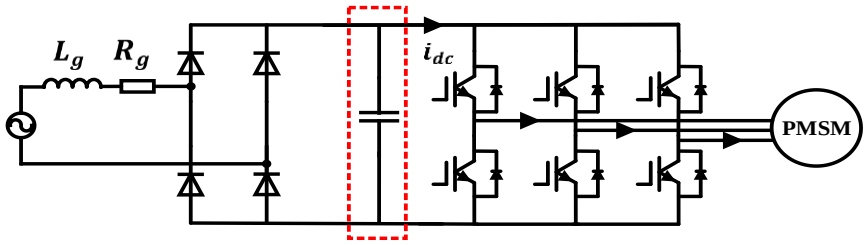

(b) Small dc-link capacitor-based PMSMs drive systems [TAK01]

Fig. 1.24. Topology of the PMSM drive systems. (a) Conventional PMSM drive systems. (b) Small dc-link capacitor-based PMSMs drive systems [TAK01].

Due to single-phase uncontrolled rectifier and small dc-link capacitor, the dc-link voltage can be expressed as

$$u_{dc} = u_{dc,0} + \sum_{k=1}^{n} u_{dc,k} \sin(2k\omega_g t + \varphi_{dc,k}) \tag{1.81}$$

where $u_{dc,0}$, $u_{dc,k}$, and $\varphi_{dc,k}$ are the average value, the kth order harmonic, and the phase angle of fluctuating dc-link voltage, ω_g is the grid frequency.

As shown in Fig. 1.25, the grid voltage is rectified by an uncontrolled single-phase rectifier in the small dc-link capacitor-based PMSM drive systems, resulting in a half-wave input voltage. Therefore, the 100 Hz harmonic component is inevitably generated in the dc-link voltage. Meanwhile, the dc-link capacitor discharges according to its discharge time constant, transferring energy to the motor. The voltage after rectifier and the voltage in the capacitor together affect the actual dc-link voltage. The larger value between the grid voltage and the capacitor voltage determines the dc-link voltage as shown in Fig. 1.25.

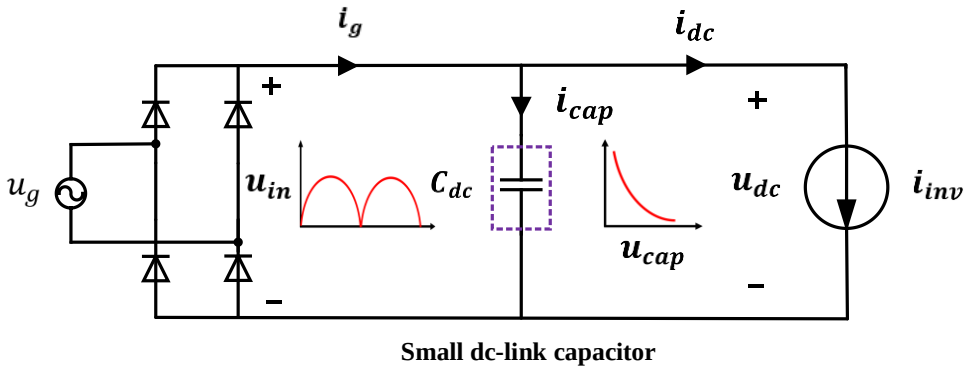

Fig. 1.25. Equivalent circuit of small dc-link capacitor-based PMSM drive systems.

The input voltage as shown in Fig. 1.25 can be expressed by

$$u_{in} = A\sin(2\pi\omega_g t) \tag{1.82}$$

where u_{in} is the input voltage, A is the amplitude of grid voltage, ω_g is the frequency of grid voltage.

The voltage across a capacitor during discharge can be described by

$$u_{cap} = U_0 \exp(-t/RC_{dc}) \tag{1.83}$$

where u_{cap} is the capacitor voltage, U_0 is the initial voltage across the dc-link capacitor, R is the equivalent resistance in the discharge path, C_{dc} is the capacitance of the dc-link capacitor.

The time constant of a dc-link capacitor discharge process is defined as the time it takes for the voltage across the capacitor to decrease to approximately 36.8% of its initial value. It is

calculated as

$$\tau = RC_{dc} \tag{1.84}$$

As shown in Fig. 1.25, the dc-link voltage depends on the higher value between the input voltage and the capacitor voltage.

$$u_{dc} = \max\left(u_{in}, u_{cap}\right) \tag{1.85}$$

One cycle of fluctuating dc-link voltage can be divided into three stages according to the relationship between the input voltage and the capacitor's terminal voltage. During Stage I, the input voltage begins to decline, concurrently with a reduction in the capacitor's terminal voltage. If the capacitor's discharge time constant is short as shown in Fig. 1.26(a), indicative of a smaller dc-link capacitance value, the input voltage may exceed the capacitor's terminal voltage. During this stage, the input voltage charges the capacitor, and the dc-link voltage is primarily determined by the input voltage. In Stage II, the input voltage descends below the capacitor's terminal voltage. The dc-link voltage is mainly dependent on the capacitor's terminal voltage. During Stage III, the input voltage rises above the capacitor's terminal voltage, and the dc-link voltage is primarily influenced by the input voltage. Therefore, a harmonic in the dc-link voltage forth the frequency of the input voltage, which is 200 Hz, is generated.

However, if the capacitance value increases, the discharge time constant is lengthened, and the capacity of store charge is increased. Consequently, within one cycle of the fluctuating dc-link voltage, the duration in which the input voltage exceeds the capacitor's terminal voltage fades as shown in Fig. 1.26.

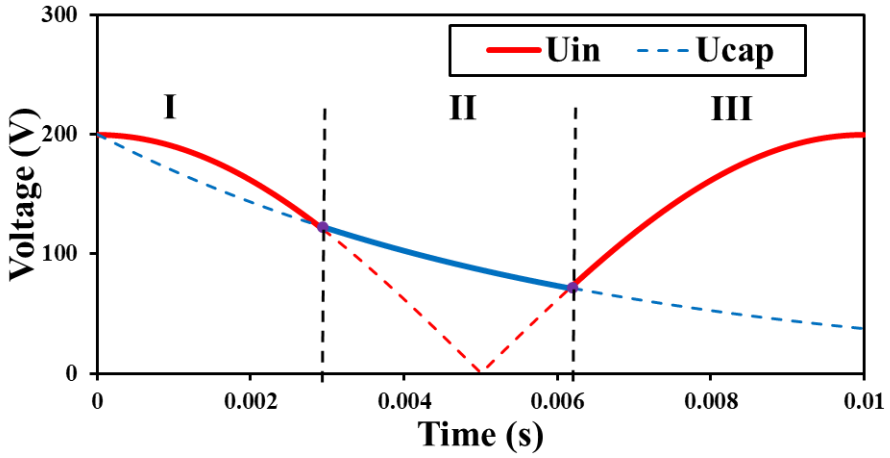

(a) 20 μF

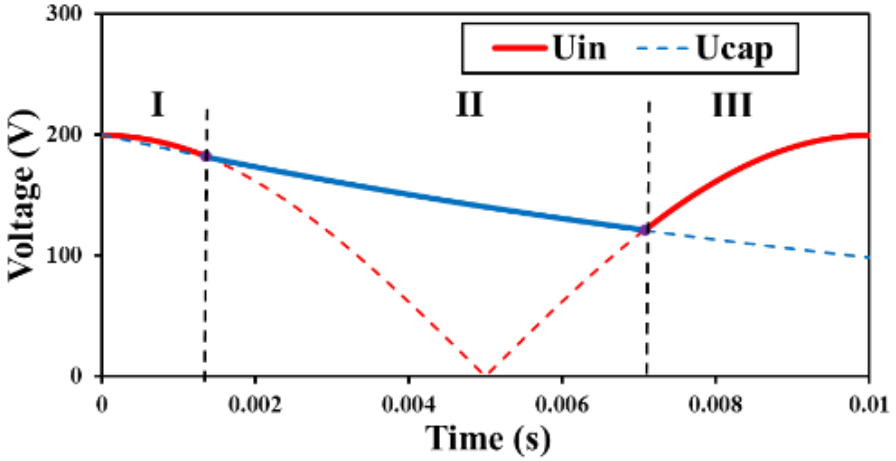

(b) 100 μF

Fig. 1.26. dc-link voltage with different capacitance. (a) 20 μF. (b) 100 μF.

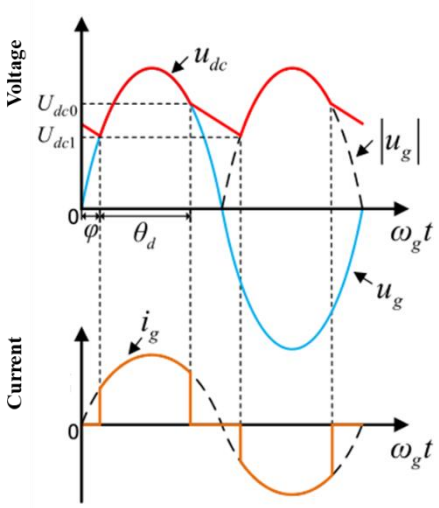

Fig. 1.27. Ideal waveforms of grid side voltage, current and dc-link voltage [CHE22].

As shown in Fig. 1.27, in one fluctuation cycle of $|u_g|$, the dc-link voltage can be divided into two cases. When the input voltage is lower than the capacitor's voltage, the diode in the uncontrolled rectifier bridge turns off, and the turn-off angle is denoted as φ. When the input voltage is higher than the capacitor's voltage, the diode in the uncontrolled rectifier bridge turns on, and the conduction angle is defined as θ_d. When the input voltage is lower than the capacitor's voltage, the diode is turn-off.

According to Fig. 1.27, the discharging time $t_{discharge}$ can be derived as

$$t_{discharge} = \frac{\pi - \theta_d}{\omega_g} \tag{1.84}$$

When the capacitor discharge ends, the voltage across the capacitor becomes equal to the input

voltage. At this point, the dc-link voltage can be expressed as follows.

$$u_{dc1} = U_g|\sin(\varphi)| \tag{1.85}$$

According to (1.82) to (1.85),

$$\sin(\varphi) = \sin(\varphi + \theta_d)\, e^{\frac{\pi-\theta_d}{\omega_g R_{inv} C_{dc}}} \tag{1.86}$$

where C_{dc} is the dc-link capacitance, R_{inv} is the inverter equivalent input resistance.

In the diode conduction stage, i.e., θ_d, the capacitor's voltage is less than the input voltage, and the diode is turned on. In this case, the dc-link voltage and grid side current follow the sinusoidal fluctuation of the grid side input voltage. Therefore, the current flowing through the capacitor can be expressed as

$$i_{cap} = C_{dc}\frac{du_{cap}}{dt} = C_{dc}\frac{d|u_g|}{dt}$$

$$= \begin{cases} C_{dc}\omega_g U_g \cos(\omega_g t) & t \in (\dfrac{2K\pi+\varphi}{\omega_g}, \dfrac{2K\pi+\varphi+\theta_d}{\omega_g}) \\ -C_{dc}\omega_g U_g \cos(\omega_g t) & t \in (\dfrac{(2K+1)\pi+\varphi}{\omega_g}, \dfrac{(2K+1)\pi+\varphi+\theta_d}{\omega_g}) \end{cases} \quad K \in N \tag{1.87}$$

where i_{cap} is the current flowing through the capacitor.

Therefore, the current flowing through the load resistor can be expressed as

$$i_{inv} = \frac{u_{dc}}{R_{inv}} = \begin{cases} \dfrac{U_g \sin(\omega_g t)}{R_{inv}} & t \in (\dfrac{2K\pi+\varphi}{\omega_g}, \dfrac{2K\pi+\varphi+\theta_d}{\omega_g}) \\ -\dfrac{U_g \sin(\omega_g t)}{R_{inv}} & t \in (\dfrac{(2K+1)\pi+\varphi}{\omega_g}, \dfrac{(2K+1)\pi+\varphi+\theta_d}{\omega_g}) \end{cases} \quad K \in N \tag{1.88}$$

When $t = \frac{(2K+1)\pi+\varphi+\theta_d}{\omega_g}$ $K \in N$, the rectifier diode does not conduct, and the grid side current is instantly clamped to zero as shown in Fig. 1.27. Then, the grid side current should satisfies

$$i_g = i_{cap} + i_{inv} = -C_{dc}\omega_g U_g \cos(\omega_g t) - \frac{U_g \sin(\omega_g t)}{R_{inv}} = 0 \tag{1.89}$$

$$-C_{dc}\omega_g U_g \cos(\varphi + \theta_d) - \frac{U_g \sin(\varphi + \theta_d)}{R_{inv}} = 0 \tag{1.90}$$

Therefore, the conduction angle φ can be derived as

$$\theta_d = \pi - \arctan\left(C_{dc}\omega_g R_{inv}\right) - \varphi \tag{1.91}$$

Combining (1.86) with (1.91),

$$\sin\varphi = \frac{C_{dc}\omega_g R_{inv}}{\sqrt{1+(C_{dc}\omega_g R_{inv})^2}} e^{-\frac{\arctan(C_{dc}\omega_g R_{inv})}{\omega_g R_{inv} C_{dc}}} e^{-\frac{\varphi}{\omega_g R_{inv} C_{dc}}} \tag{1.92}$$

From the above analysis, it can be observed that when $C_{dc}\omega_g R_{inv}$ is known, θ_d and φ can be determined. As shown in Fig. 1.28, assuming a load resistance of 6 Ω and a grid frequency of 50 Hz, the relationship between θ_d & φ and the small dc-link capacitance can be established. In the small dc-link capacitor-based PMSM drive systems, the conduction angle of the uncontrolled rectifier diode on the grid side is larger than in conventional large-volume dc-link capacitor-based PMSM drive systems due to the presence of small capacitance. As the capacitance decreases, the conduction angle θ_d of the uncontrolled rectifier diode increases and the dc-link voltage follows the envelope of the grid voltage, leading to significant coupling between the rectifier and inverter sides as shown in Fig. 1.29, which complicates the control. In contrast, the dc-link voltage remains relatively constant in large-volume dc-link capacitor-based PMSM drive systems, and the energy between the rectifier and inverter sides is essentially decoupled, making the control easier.

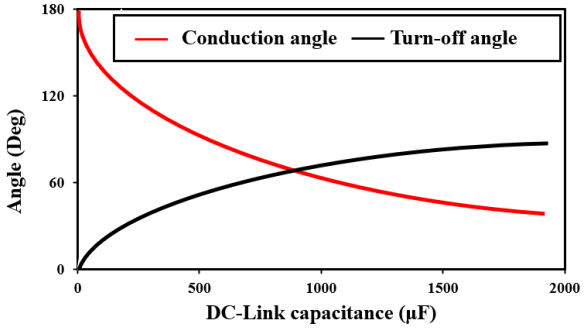

Fig. 1.28. Relationship between conduction angle and turn-off angle with capacitance value.

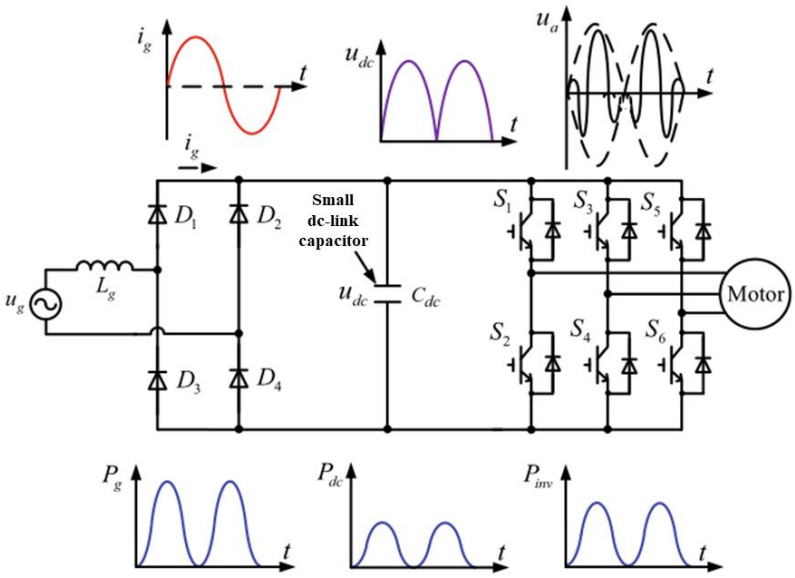

Fig. 1.29. Power characteristics of drive system [WAN20B].

1.3.2 Overview of Challenges and Literature Review

Given their low cost and compact size, PMSM drive systems utilizing small-volume dc-link capacitors are widely employed in applications where high control accuracy is not critical, such as domestic appliances. Moreover, the use of small dc-link capacitors leads to increased dc-link voltage fluctuation. This effect has the advantage of extending the duration within a single grid cycle during which the grid side voltage exceeds the dc-link voltage, thereby increasing the conduction angle of the rectifier diodes [TAK02][HAG03] [SON15]. By employing specific control strategies, it is possible to omit the PFC circuit and improve the system's PF.

However, the capacitance of small-volume dc-link capacitors is only about 1/50 to 1/20 that of conventional large-volume capacitors [TAK01] [LEE14]. This limited energy storage capability poses challenges in maintaining stable dc-link voltage, affecting the high-performance control of the motor. Therefore, investigating the characteristics of small-volume dc-link capacitor-based PMSM drive systems and developing optimization strategies and topologies to enhance their performance is of significant importance. Nowadays, universities and research institutions such as Seoul National University, Harbin Institute of Technology, Zhejiang University, Huazhong University of Science and Technology, Aalborg University, and Nagaoka University of Technology have all made significant achievements in this field. Companies like Siemens (inverters), Daikin (household inverter air conditioners), Toyota (Prius improvements), Samsung (air purifiers), and LG (elevator-specific inverters) have begun releasing related products. Additionally, companies such as Midea, Gree, and Haier are developing their related products [WAN20B] [LI22A]. Considering the current research focus

and challenges in application and commercialization, the primary research areas in this field, including high PF control strategies, grid side current harmonic suppression strategies due to inductor-capacitor (LC) resonance, grid side current control, stability conditions and control methods, beat phenomenon suppression techniques, overmodulation and six-step operation, FW control optimization, sensorless control optimization, and topology optimization techniques. An overview of current research in these areas is illustrated in Fig. 1.30.

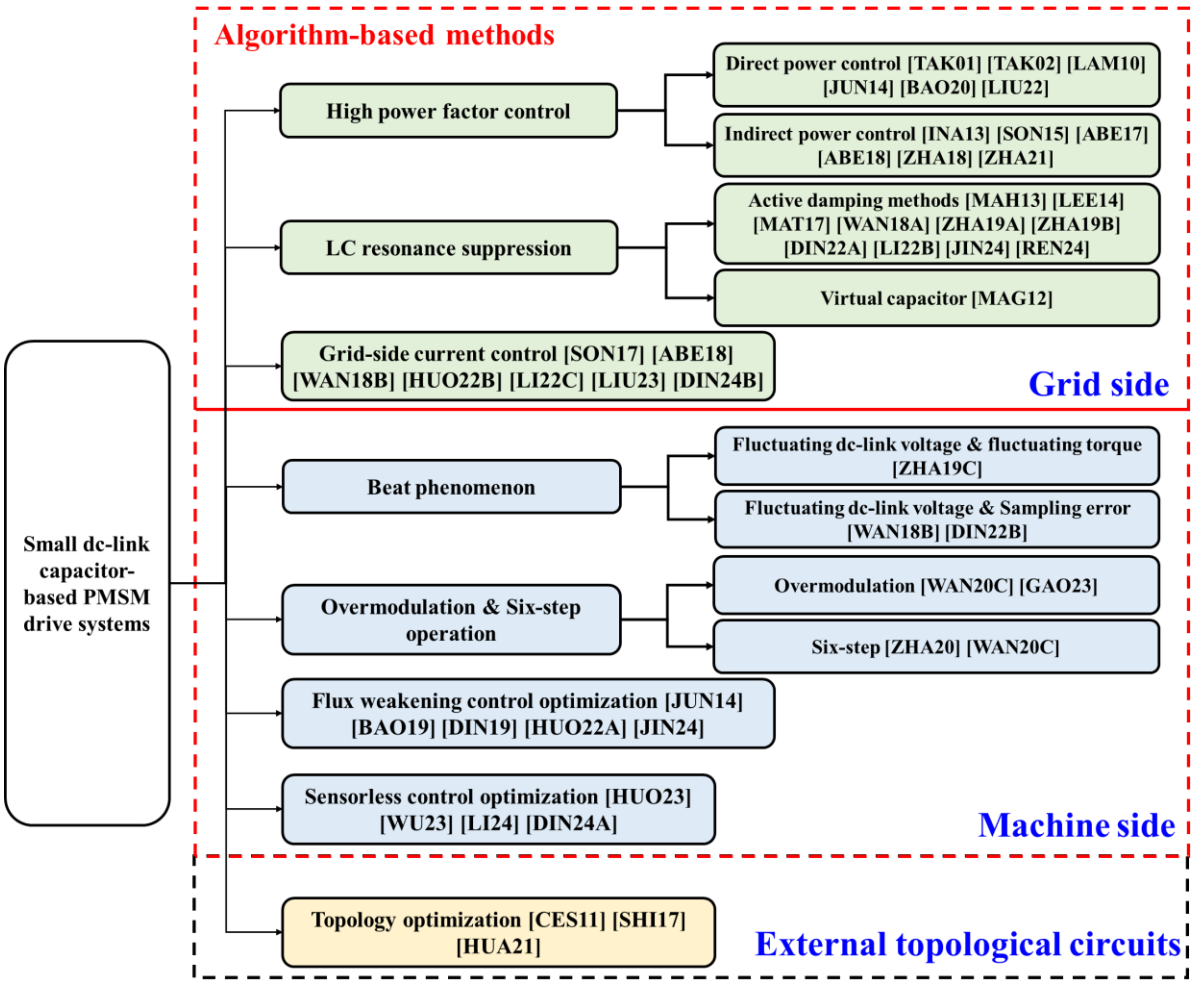

Fig. 1.30. Overview of current research.

1.3.3 Different Optimization Strategies

The research on small dc-link capacitor-based PMSM drive systems can be divided into algorithm-based and topology-based methods. Algorithm-based methods include grid side and machine-side optimization strategies, such as high PF control [TAK01] [TAK02] [LAM10] [INA11] [INA13] [JUN14] [SON15] [ABE17] [ABE18] [ZHA18A] [BAO20] [ZHA21] [LIU22], grid side current ripple suppression and stability improvements [MAH13] [LEE14] [MAT17] [SON17] [ABE18] [WAN18B] [WAN18A] [ZHA19A] [ZHA19C] [HUO22A]

[LI22B] [DIN22A] [LI22C] [LIU23] [DIN24B] [JIN24A] [REN24], and FOC control optimization [JUN14] [BAO19] [DIN19] [ZHA20] [WAN20C] [HUO22B] [HUO23] [GAO23] [WU23A] [WU23B] [LI24] [DIN24A] [JIN24B]. Topology-based optimization methods primarily focus on using additional circuits to control dc-link voltage fluctuations. These methods aim to enhance the structural and functional aspects of drive systems to improve overall performance and reliability [CES11] [SHI17] [HUA21].

A. High PF control

In conventional large dc-link capacitor-based PMSM drive systems, PFC circuits manage the dc-link voltage and grid side current, ensuring compliance with the industry requirement of a PF above 0.95 [TAK01] [HAG03] [ZHA19C] [YAN21]. However, in small dc-link capacitor-based PMSM drive systems, the limited energy storage capacity of small dc-link capacitors, coupled with the absence of a PFC circuit, leads to insufficient energy storage capability. This results in significant coupling between the grid side input power and the inverter power, causing the dc-link voltage fluctuation. Conversely, this characteristic also provides an opportunity to improve the grid side PF [WAN20B] [LI22A]. To achieve a high PF on the grid side, it is crucial to analyze the factors influencing the PF in small dc-link capacitor-based PMSM drive systems.

The grid side PF can be expressed as

$$PF = \cos\delta \frac{1}{\sqrt{1 + (THD)^2}} \tag{1.93}$$

where δ is the phase difference between the grid voltage and current, $\cos\delta$ represents the phase shift PF, total harmonic distortion (THD) is the total harmonic distortion.

The THD can be expressed as

$$THD = \frac{\sqrt{i_{2rms}^2 + i_{3rms}^2 + i_{4rms}^2 + i_{5rms}^2 + i_{6rms}^2 + \cdots}}{i_{1rms}} \times 100\% \tag{1.94}$$

where i_{nrms} is the RMS value of the nth harmonic of the grid side current.

From (1.93), it can be observed that to improve the grid side PF, the phase difference between the grid voltage and current should be minimized, and the harmonic content of the grid side input current should be reduced. The energy relationship from the grid side to the machine side is examined from a power perspective to facilitate analysis.

In a small dc-link capacitor-based PMSM drive system, the power contributions from the small line inductance and line resistance on the grid side are negligible. Assuming the diode bridge conduction voltage drop and inverter switching losses are also negligible, the grid input power P_g can be expressed as the sum of the energy supplied to the dc-link capacitor P_{dc} and the inverter P_{inv}.

$$P_g = P_{dc} + P_{inv} \tag{1.95}$$

The energy of dc-link capacitor can be calcultated by

$$P_{dc} = u_{dc} C_{dc} \frac{du_{dc}}{dt} = \frac{1}{2} U_g^2 C_{dc} \sin(2\theta_g) \tag{1.96}$$

For the grid input power, the grid voltage can be expressed as

$$u_g = U_g \sin \theta_g \tag{1.97}$$

where u_g is the grid voltage U_g is the amplitude of the grid voltage, and θ_g is the phase angle of the grid.

$$\theta_g = \omega_g t \tag{1.98}$$

To improve the grid side PF and reduce the harmonics in the grid side current, the grid current should ideally be sinusoidal and in phase with the grid voltage. Therefore, the ideal grid input current and grid power can be expressed as

$$i_g^* = I_g \sin \theta_g \tag{1.99}$$

$$P_g^* = U_g I_g \sin^2 \theta_g \tag{1.100}$$

where i_g^* and P_g^* are the ideal grid current and ideal grid side power. I_g is the amplitude of grid voltage and grid current.

Thus, the ideal inverter output power P_{inv}^* can be expressed as

$$P_{inv}^* = U_g I_g \sin^2 \theta_g - \frac{1}{2} U_g^2 C_{dc} \omega_g \sin(2\theta_g) \tag{1.101}$$

Based on (1.101), the power analysis diagram of small dc-link capacitor-based PMSM drive systems can be plotted as shown in Fig. 1.31. Due to the small dc-link capacitor, the power of the dc-link capacitor is low compared to the grid side power. The inverter output power is

approximately equal to the grid side power. Therefore, the grid side PF can be effectively improved by controlling the inverter output power to follow its ideal value.

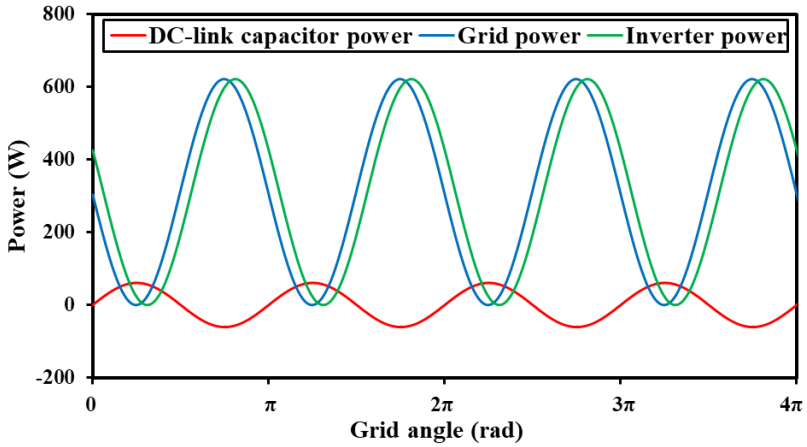

Fig. 1.31. Power analysis diagram of small dc-link capacitor-based PMSM drive systems.

[TAK01] [TAK02] first proposed the PF control method based on FW control to obtain the high PF in the small dc-link capacitor-based PMSM drive system. In [SON15], the reference *dq*-axis currents are redefined based on the current operating state of the motor and the information from dc-link voltage harmonics. This approach allows for direct control of the inverter output power, effectively managing motor torque and simultaneously suppressing grid input current harmonics. Meanwhile, the grid current harmonics are suppressed by lowering the *d*-axis current at a low dc-link voltage area in [SON17]. In [ZHA18A], the inverter power is directly controlled to achieve an HF factor. A power feedback loop is implemented, where the error between the actual power and the set power is processed through a PR controller and applied to the *q*-axis reference current regulation. In [ABE17], two PF correction methods for small dc-link capacitor-based PMSM drive systems are presented to achieve high PF and reduce input current harmonics. [ABE18] proposes a direct dc-link current control method to minimize source current harmonics without additional passive components. Both methods can be implemented to meet the IEC 61000-3-2 standards.

B. LC resonance suppression strategies

As mentioned above, the reduced capacitance of the dc-link capacitor leads to a strong coupling effect between the grid side and the inverter side. In practical systems, a large filter inductor can be used on the grid side to reduce the grid side current harmonic [BIE09] [BAI14]. However, it may also cause LC resonance issues, resulting in significant harmonic components in the grid side current at the resonance frequency [ZHA18A] [WAN20B]. Therefore, it is

necessary to study methods for suppressing LC resonance to improve the quality of the grid side current. Moreover, when the inverter-motor system operates under an ideal constant power load (CPL) condition, the input impedance of the inverter becomes negative [MAG12] [LEE14]. Consequently, when the dc-link voltage increases, the motor current must decrease to maintain the constant power output of the motor. This negative interaction between voltage and current exacerbates the grid side LC resonance, leading to system instability. If the amplitude of the LC resonance further increases, the drive system could experience overvoltage or overcurrent situations, potentially causing direct damage to the system. The equivalent circuit model of the small dc-link capacitor-based PMSM drive systems is shown in Fig. 1.32.

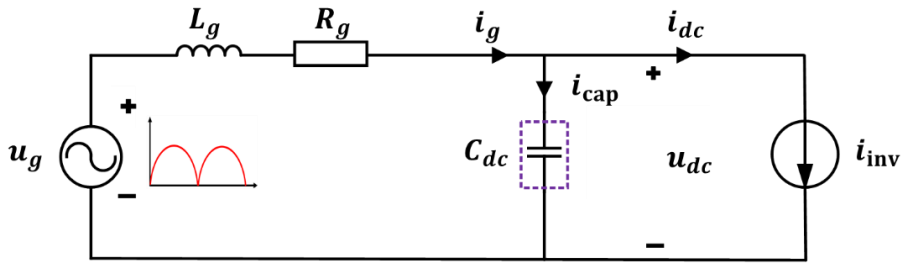

Fig. 1.32. Equivalent circuit of the small dc-link capacitance-based PMSM drive systems.

The grid side voltage and grid side current i_g can be expressed as

$$u_g = L_g \frac{di_g}{dt} + R_g i_g + u_{dc} \tag{1.102}$$

$$i_g = i_{\text{cap}} + i_{\text{inv}} \tag{1.103}$$

The inverter input current i_{inv} can be expressed as [LEE14] [MAT17] [WAN18A] [WAN20B]

$$i_{\text{inv}} = \frac{P_L}{u_{dc}} = \frac{P_L}{u_{dc,0} + \Delta u_{dc}} \tag{1.104}$$

where P_L is the load power, $u_{dc,0}$ is the average value of the dc-link voltage, and Δu_{dc} represents the small-signal variation of the dc-link voltage.

According to [LEE14] [MAT17] [WAN18A] [WAN20B], after linearizing (1.104), the inverter input current can be presented by

$$i_{\text{inv}} = \frac{P_L}{u_{dc,0}} - \frac{P_L}{u_{dc,0}^2} \Delta u_{dc} = \frac{P_L}{u_{dc,0}} + K \Delta u_{dc} \tag{1.105}$$

The current flow through the dc-link capacitor can be expressed as

$$i_{\text{cap}} = C_{dc}\frac{du_{dc}}{dt} \tag{1.106}$$

Combining (1.102) with (1.106), the grid side characteristic equation of the drive system can be expressed as

$$s^2 + \left(\frac{R_g}{L_g} - \frac{P_L}{C_{dc}u_{dc,0}^2}\right)s + \frac{1}{L_g C_{dc}}(1 - \frac{P_L P_g}{u_{dc,0}^2}) = 0 \tag{1.107}$$

According to the Routh-Hurwitz criterion, the stability condition for the grid side of the drive system requires that all the coefficients of the characteristic equation must be positive, and the first column of the Routh array must not change sign. Thus, the stability condition for the drive system can be obtained as

$$\begin{cases} 1 - \dfrac{P_L P_g}{u_{dc,0}^2} > 0 \\ \dfrac{R_g}{L_g} - \dfrac{P_L}{C_{dc}u_{dc,0}^2} > 0 \end{cases} \tag{1.108}$$

The first condition of (1.108) is usually easy to satisfy, because

$$u_{dc,0}^2 \gg P_L P_g \tag{1.109}$$

The second condition can be expressed as

$$\frac{C_{dc}}{P_L} > \frac{L_g}{R_g u_{dc,0}^2} \tag{1.110}$$

From (1.110), it can be seen that the stability of the drive system is related to the grid side filter inductance, equivalent resistance, motor power, and the dc-link capacitance. For small dc-link capacitor-based PMSM drive systems, the dc-link capacitance value can be reduced to 1/50 to 1/20 of that in the conventional PMSM drive system. As a result, the stability of the system is significantly affected. When the dc-link capacitance value changes, the pole distribution of the drive system's characteristic equation is shown in Fig. 1.33(a) [WAN18B] [ZHA19A] [ZHA19C]. It shows that as the capacitance value decreases, the poles of the characteristic equation shift from the left half-plane to the right half-plane, reducing the system's damping. This shift can potentially cause the drive system to transition from a stable state to an unstable one. From (1.110), it is evident that while increasing the grid side filter inductance theoretically reduces grid side current harmonics, it also affects the stability of the drive system. In practice,

the LC resonance induced by the filter inductance can lead to a notable increase in grid side current harmonics, thereby affecting the quality of the grid side current. The LC resonance frequency ω_{res} can be expressed as follows.

$$\omega_{\text{res}} = \frac{1}{\sqrt{L_g C_{dc}}} \tag{1.111}$$

where ω_{res} is the LC resonance frequency.

The Bode plot of the drive system, as shown in Fig. 1.33(b) [WAN18B] [ZHA19A] [ZHA19C], indicates a significant resonance peak near the resonance frequency. This peak causes the grid side current harmonics at the resonance frequency to exceed acceptable levels, failing to meet harmonic standards. Therefore, it is essential to investigate methods for suppressing LC resonance to mitigate its adverse effect.

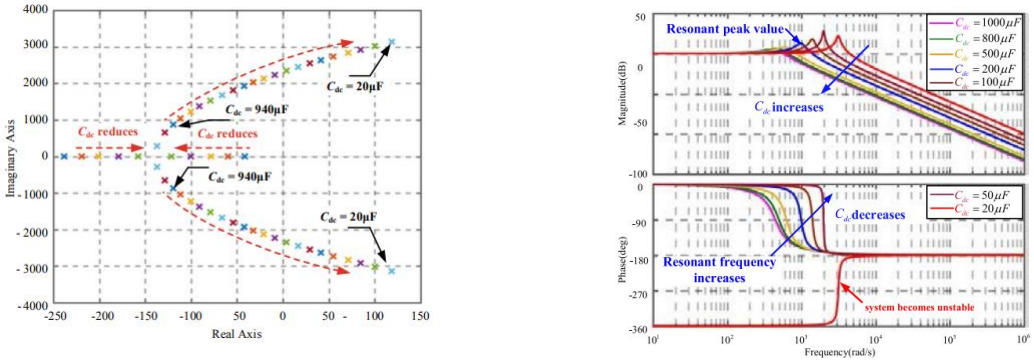

(a) Pole distribution (b) Bode diagram

Fig. 1.33. Stability analysis of the drive system. (a) Pole distribution. (b) Bode diagram [WAN18B] [ZHA19A] [ZHA19C].

LC resonance in small dc-link capacitor-based PMSM drive systems occurs due to insufficient system damping. To suppress LC resonance, system damping can be increased typically by introducing power resistors on the grid side. Currently, LC resonance suppression techniques are broadly categorized into two types: passive damping control methods [DRA18] and active damping control methods [BIE09] [CES11] [MAH13] [LEE14] [BAI14] [WAN18A] [ZHA19A] [ZHA19C] [DIN22A] [LI22B] [LI22C] [JIN24A]. Passive methods involve adding damping circuits, such as resistors and capacitors to meet the specific system requirements, which can increase size and cost and potentially reduce reliability by altering circuit topology. Active damping control methods, on the other hand, are achieved by introducing virtual resistors, which emulate the effect of actual power resistors, thereby suppressing grid side LC resonance through equivalent input impedance.

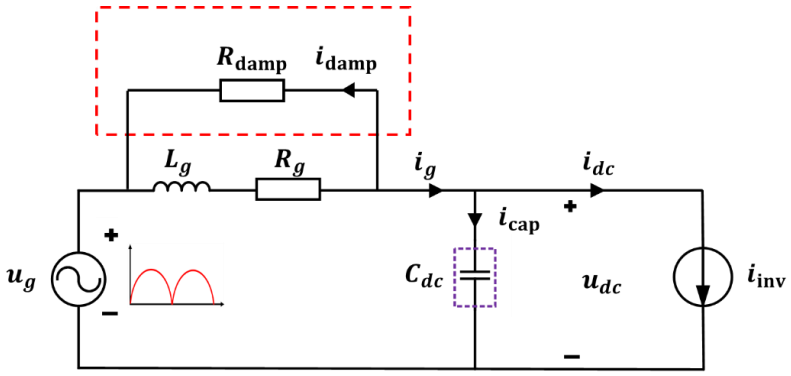

(a) Equivalent circuit diagram of the drive system with virtual resistors

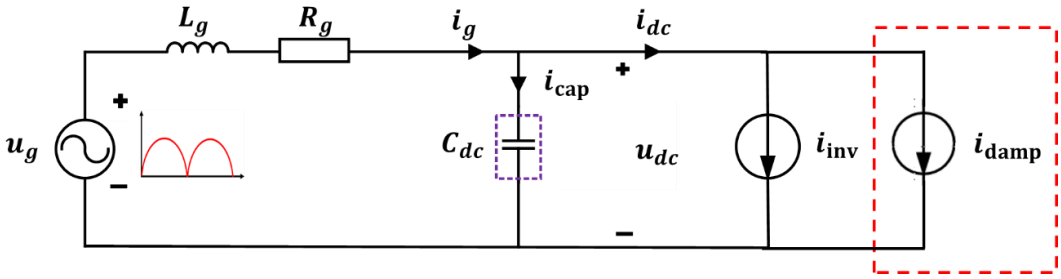

(b) Equivalent damping current with virtual resistors

Fig. 1.34. Circuit schematic of LC resonance suppression strategy based on active damping control method. (a) Diagram of equivalent circuit of drive system with virtual resistors. (b) Diagram of equivalent damping current with virtual resistors.

According to Fig. 1.34, the grid side voltage and current equations are derived as

$$u_g = L_g \frac{di_g}{dt} + R_g i_g + u_{dc} \tag{1.112}$$

$$i_g = i_{\text{cap}} + i_{\text{inv}} + i_{\text{damp}} \tag{1.113}$$

Combining (1.105) with (1.113), the inverter input current can be presented by

$$i_g = C_{dc} \frac{du_{dc}}{dt} + \frac{P_L}{u_{dc,0}} - \frac{P_L}{u_{dc,0}^2} \Delta u_{dc} + \frac{u_{dc} - u_g}{R_{\text{damp}}} \tag{1.114}$$

Combining (1.114) with (1.112), the transfer function of grid side voltage and current can be expressed as

$$\frac{u_{dc}}{u_g} = \frac{L_g s + (R_g + R_{\text{damp}})}{L_g C_{dc} R_{\text{damp}} s^2 + \left(C_{dc} R_g R_{\text{damp}} + L_g - \frac{L_g R_{\text{damp}} P_L}{u_{dc,0}^2} \right) s + (R_g + R_{\text{damp}} - \frac{R_g R_{\text{damp}} P_L}{u_{dc,0}^2})} \tag{1.115}$$

Then, the stability condition for the drive system can be obtained as [LEE14]

$$\begin{cases} \left(C_{dc}R_g - \dfrac{L_g P_L}{u_{dc,0}^2}\right) R_{\text{damp}} + L_g > 0 \\ R_g + (1 - \dfrac{R_g P_L}{u_{dc,0}^2}) R_{\text{damp}} > 0 \end{cases} \tag{1.116}$$

It can be seen that after introducing virtual resistors, both conditions in (1.116) are easily satisfied, indicating that this method effectively enhances the stability of the drive system.

According to [LEE14] [ZHA19A], it is complicated to directly modify the inverter input current to achieve an equivalent damping current. Therefore, the damping current i_{damp} is generally represented as damping power P_{damp}, which is then superimposed on the inverter's output power. The inverter's output voltage is adjusted to modify the output power accordingly. The expression for the damping power derived from the damping current can be obtained as

$$P_{\text{damp}} = u_{dc} i_{\text{damp}} = u_{dc} \frac{u_{dc} - u_g}{R_{\text{damp}}} \tag{1.117}$$

Since the inverter output power is primarily related to the q-axis, the equivalent damping power can be achieved by superimposing an output voltage component onto the q-axis. The required output voltage to be superimposed on the q-axis can be calculated as

$$\Delta u_q = \frac{2P_{\text{damp}}}{i_q} \tag{1.118}$$

In [LEE14], the effect of virtual resistors was achieved by modifying the inverter output voltage to effectively simulate a parallel connection with the grid side filter inductance and suppressed LC resonance. Further analysis in [ZHA19A], four configurations where virtual resistors were either series or parallel connected with the grid side inductance or the dc-link capacitor is investigated. The study provided Routh stability criteria tables and Bode plots for each configuration. After a comprehensive analysis of the drive system characteristics in each case, the configuration with virtual resistors in series with the grid side filter inductance was selected. This setup, combined with a feedforward compensation strategy, reduced the effect of grid side voltage harmonics. Furthermore, a virtual capacitor was added in parallel with the small dc-link capacitor within the drive system's topology in [MAG12],. The effect of this virtual capacitor was simulated by adjusting the reference q-axis current. However, the coupling characteristics of the d-axis power introduced some control challenges.

C. Beat phenomenon

Typically, the interaction between two signals with closely spaced frequencies can lead to a low-frequency oscillation known as the beat phenomenon. In the small dc-link capacitor-based PMSM drive systems, the reduction in dc-link capacitance results in periodic fluctuations in the dc-link voltage. The inverter output voltage frequency changes with the motor speed, and when it becomes close to the frequency of the dc-link voltage fluctuations, a beat phenomenon occurs. This issue is also observed in traction systems and has attracted significant attention [OUY11][JIA18]. Moreover, in small dc-link capacitor-based PMSM drive systems, there is significant coupling between the grid side input power and the inverter-side output power. At specific operating frequencies, both the grid side current and the motor current can experience beat frequencies, which increase system noise and additional losses and may even cause resonance with the mechanical system, potentially affecting the normal operation of the drive system. To address these issues, it is important to analyze and suppress the effect of the beat phenomenon on grid side currents and motor currents in small dc-link capacitor-based PMSM drive systems.

In small dc-link capacitor-based PMSM drive systems, the fluctuating dc-link voltage can be presented as

$$u_{dc} = u_{dc,0} + \sum_{k=1}^{n} u_{dc,k} \sin\left(2k\omega_g t + \varphi_{dc,k}\right) \tag{1.119}$$

According to the PWM theory, three-phase voltages u_a, u_b, and u_c can be simplified as

$$\begin{bmatrix} u_a(t) \\ u_b(t) \\ u_c(t) \end{bmatrix} = \frac{m u_{dc}}{2} \begin{bmatrix} \sin\left(\omega_e t + \varphi_e\right) \\ \sin\left(\omega_e t + \varphi_e - \frac{2\pi}{3}\right) \\ \sin\left(\omega_e t + \varphi_e + \frac{2\pi}{3}\right) \end{bmatrix} \tag{1.120}$$

Ignoring the higher-order harmonics of fluctuating dc-link voltage, the phase voltage $u_a(t)$ can be derived as

$$
\begin{aligned}
u_a(t) &= \frac{m}{2}\sin(\omega_e t + \varphi_e)\left[u_{dc,0} + u_{dc,1}\sin\left(2\omega_g t + \varphi_{dc,1}\right)\right] \\
&= \frac{m}{2}u_{dc,0}\sin(\omega_e t + \varphi_e) + \frac{m}{2}u_{dc,1}\sin(\omega_e t + \varphi_e)\sin\left(2\omega_g t + \varphi_{dc,1}\right) \\
&= \frac{m}{2}u_{dc,0}\sin(\omega_e t + \varphi_e) - \frac{m}{4}u_{dc,1}\cos\left[\left(\omega_e + 2\omega_g\right) + \varphi_e + \varphi_{dc,1}\right] \\
&\quad + \frac{m}{4}u_{dc,1}\cos\left[\left(\omega_e - 2\omega_g\right) + \varphi_e - \varphi_{dc,1}\right]
\end{aligned}
\tag{1.121}
$$

As shown above, when ω_e is close to $2\omega_g$, the phase voltage u_a contains a low-frequency component. This low-frequency component can cause noticeable low-frequency oscillations in the motor phase voltage, which is known as the beat phenomenon.

As explained above, the use of a small dc-link capacitor could lead to significant dc-link voltage fluctuations. As a result, these fluctuations can interact with other oscillating components in the PMSM drive system easily. This interaction, especially when the frequencies are close but not identical, can result in the beat phenomenon. The beat phenomenon produces a new, low-frequency oscillation that can affect system stability and performance, potentially causing issues such as increased noise and mechanical resonance. In [ZHA19B], the beat phenomenon caused by the interaction between the fluctuating dc-link voltage and the fluctuating load torque in air conditioning compressors is investigated. To address these issues, a power balancing control method and a fluctuated torque suppression technique are proposed to mitigate these effects. In [WAN18B] [DIN22B], it is identified that the sampling delays of fluctuating dc-link voltage can lead to PWM output voltage errors. These errors introduce harmonics into the stator current that are related to the frequency of the dc-link voltage fluctuations, thereby causing beat phenomenon. To address this, the studies propose a sampled dc-link voltage reconstruction method according to its periodicity to eliminate the harmonics in the stator current caused by sampling errors and the resulting beat phenomenon.

D. Overmodulation & six-step operation

In small dc-link capacitor-based PMSM drive systems, the use of a small dc-link capacitor leads to significant dc-link voltage fluctuation due to limited energy storage. These fluctuations can cause adverse effects such as insufficient dc-link voltage, increased harmonic distortion, reduced efficiency, and potential instability in the PMSM drive systems.

The overmodulation method is used to extend the inverter's output voltage beyond the linear

modulation region, thereby maximizing the utilization of the available dc-link voltage. The overmodulation method allows the motor to achieve higher speeds and torque by pushing the modulation index above 0.9069 [WAN20C] [BRO21] [GAO23] [ZHA24]. In the small dc-link capacitor-based PMSM drive systems, where the dc-link voltage fluctuates. Therefore, the overmodulation method can be a valuable strategy to compensate for the lower available dc-link voltage condition caused by fluctuating dc-link voltage, allowing for better performance in high-demand situations. However, the increased harmonic content due to overmodulation can exacerbate issues related to current ripple and acoustic noise [WAN20C] [BRO21].

Six-step operation, also known as block commutation, is another technique employed to maximize the utilization of the dc-link voltage. In this mode, the inverter output waveform transits to a six-step waveform, which is essentially a series of square waves. This operation is especially useful in high-speed applications, such as railway traction, where the need for high power output exceeds the capabilities of the linear modulation range. In PMSM drive systems with small dc-link capacitor, six-step operation helps achieve higher output voltages and thus higher speeds under constrained dc-link voltage conditions. However, similar to overmodulation, it introduces significant current and torque ripples due to the non-sinusoidal nature of the voltage waveform. These ripples can lead to increased losses, noise, and even mechanical vibrations [ZHA20] [WAN20C] [BRO21] [JIN24B]. Fig. 1.35 shows the modulation regions in space vector pulse width modulation (SVPWM) for a three-phase inverter. When the reference voltage u_{ref} falls within the incircle of the hexagon (Yellow), defined by $u_{ref} \leq \frac{\sqrt{3}}{3} u_{dc}$, the modulation index m is less than or equal to 0.9069. In this linear modulation region, the motor operates efficiently in both steady-state and dynamic conditions. However, the inverter's capacity is not fully utilized in this range. When the modulation index m exceeds 0.9069, the motor operates in the overmodulation region until it reaches the excircle of the hexagon, entering the nonlinear modulation area of SVPWM. While this allows for better utilization of the inverter's capacity, it also results in increased current harmonics and oscillations, particularly under speed control modes [ZHA20] [WAN20C] [BRO21]. If the reference voltage exceeds the excircle of the hexagon, the motor will enter six-step operation.

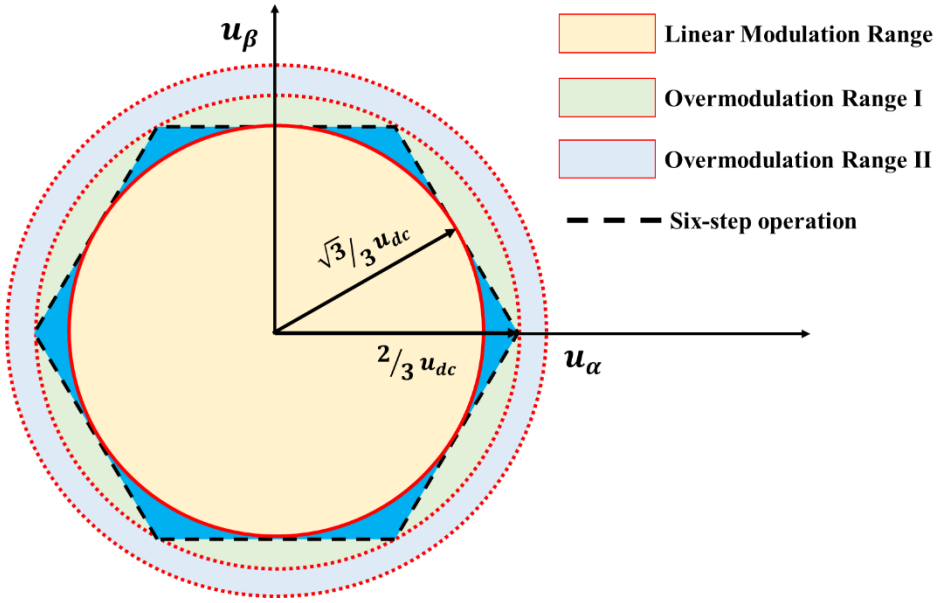

Fig. 1.35. Modulation regions in SVPWM.

Overall, both methods can improve the utilization of the available dc-link voltage to a certain extent. However, despite their benefits, both overmodulation and six-step operation do not fundamentally solve the problems associated with small dc-link capacitors. Therefore, while overmodulation and six-step operation provide temporary and partial solutions, the fundamental issues related to small dc-link capacitors, such as instability and increased harmonics, remain challenges that need further solutions, such as advanced filtering techniques or energy storage enhancements.

In [WAN20C], an optimized voltage boundary-based overmodulation strategy for small dc-link capacitor-based PMSM drive systems is proposed to mitigate the stator voltage distortion and uncontrollable six-step operation transition caused by typical overmodulation and dc-link voltage fluctuation. The proposed method enhances system performance by selectively switching between actual and fixed dc-link voltages for SVPWM. In [JIN24B], an overmodulation voltage boundary adaptation-based FW strategy for high-speed PMSM drives is proposed to reduce the motor current harmonics in overmodulation. The proposed strategy dynamically adjusts the voltage boundaries using continuous voltage vectors and optimizes the voltage boundary in the steady state to maximize the utilization of the dc-link voltage while maintaining THD limits.

E. FW control method with fluctuating dc-link voltage

As previously mentioned, while overmodulation and six-step operation can be employed to maximize inverter output, these methods can lead to increased current harmonics and torque

ripple, particularly under conditions of fluctuating dc-link voltage where the hexagonal boundary is also subject to fluctuations. The FW control method can extend the speed range and maintain the performance of PMSM drive systems under low dc-link voltage conditions by reducing the magnetic flux, allowing the motor to operate beyond its base speed. The FW control method can effectively mitigate the challenges posed by fluctuating dc-link voltage without introducing additional current and torque harmonics. Thus, the study of FW control in small dc-link capacitor-based PMSM drive systems is therefore of significant importance.

However, FW control poses certain challenges in the presence of fluctuating dc-link voltage. Specifically, these voltage fluctuations induce corresponding fluctuations in the *dq*-axis voltages, which can degrade the control performance in FB-FW control systems [JUN14]. Additionally, an analysis of the small-signal model of FB-FW control in [HUO22B] reveals that severe fluctuations in the *q*-axis voltage, particularly when it becomes negative, can cause the system to enter a positive feedback mode, leading to inherent instability.

Furthermore, the accurately induced *d*-axis current in FB-FW control necessitates precise data on the dc-link voltage and *dq*-axis voltages, both of which are prone to fluctuations. The phase difference between the fluctuating dc-link voltage and *dq*-axis voltages introduces deviations in the calculated *d*-axis current. Moreover, the PI controller commonly used in conventional FB-FW control methods is unable to adequately compensate for the AC component introduced by fluctuating dc-link voltage, further impairing system control performance. These challenges underscore the complexity and potential instability introduced by fluctuating voltages in the application of FW control in small dc-link capacitor-based PMSM drive systems. In [JUN14], a FW control method based on “average voltage constraints” is employed, which requires only controlling the average value of the motor voltage within half a cycle of the grid side input voltage to meet the voltage constraint conditions and ignoring the ac component of fluctuating dc-link voltage. In [BAO19], the motor voltage and dc-link voltage are normalized, and the voltage error is processed through proportional control to determine the *d*-axis current, effectively avoiding calculation errors caused by excessive dc-link voltage fluctuations. In [HUO22B], a *q*-axis voltage control method is proposed to ensure the FW control loop operates under negative feedback conditions, thereby improving the stability of the FW control.

F. Sensorless control method with fluctuating dc-link voltage

Sensorless control eliminates the need for position sensors such as optical encoders, magnetic encoders, and resolvers, which helps reduce the size and cost of PMSM drive systems. This

technique is particularly advantageous in harsh environments where high temperatures, humidity, and corrosive refrigerants can easily damage physical sensors, thus compromising the reliability of the drive system. However, in PMSM drive systems with small dc-link capacitors, the inherent fluctuations in the dc-link voltage complicate the implementation of sensorless control. These fluctuations oscillate at twice the grid frequency and introduce harmonics in the voltages, current, torque and speed. These issues pose challenges to the accuracy and stability of sensorless control algorithms.

In the zero and low-speed range, additional HF voltage signals are required injected into the system to extract rotor position information. However, in PMSM drive systems with small dc-link capacitors, conventional position sensorless control methods that rely on HF voltage signal injection may be constrained by insufficient dc-link voltage due to fluctuations. Furthermore, conventional HF voltage signal injection techniques can introduce increased losses, torque ripples, and acoustic noise, which can degrade the overall efficiency and performance of the drive system. However, up to date, there has been no research addressing the influence of these dc-link voltage fluctuations on HFSI-based sensorless control methods, nor have there been studies proposing mitigation strategies for these effects.

For the fundamental model-based sensorless control method in the middle and high-speed range, the rotor position and speed are typically estimated using motor electrical parameters and models, such as back-EMF or observer-based methods. The accuracy of these estimations is heavily dependent on stable voltage and current signals. Fluctuations in the dc-link voltage can disrupt these signals, leading to inaccuracies in the estimated rotor position and speed. This disruption can degrade the control precision of the motor, which can be problematic even in applications where precise torque and speed control are not critical, such as in variable-frequency air conditioning systems.

Therefore, the influence of dc-link voltage fluctuations on sensorless control strategies needs to be analyzed and mitigated. Innovative compensation techniques and advanced filtering algorithms are necessary to mitigate these effects and ensure system stability and performance under the challenging conditions presented by fluctuating dc-link voltage. In [HUA17] [HUO23] [DIN24A] [YAN24], different filters are developed to suppress the harmonics in estimated back-EMFs and estimated position errors to improve the accuracy of the sensorless control method. In [LI24], an adaptive synchronous rotating frame transformation is introduced to suppress the back-EMF harmonics caused by a small dc-link capacitor.

G. Topology optimization

Topological circuit optimization is also an essential method for enhancing the performance of small dc-link capacitor-based PMSM drive systems, as it enables effective decoupling between the grid side and the machine side. This decoupling can optimize the grid side power factor, and mitigate the dc-link voltage fluctuation. By addressing these issues, the improved topologies enhance the system's stability, efficiency, and overall performance, thereby expanding the practical applications and reliability of small dc-link capacitor-based PMSM drive systems in various demanding environments.

In [HUA21], a second harmonic current compensator was introduced in parallel with the dc link to regulate reactive power. Three different damping topology circuits were analyzed. A dc-link shunt compensator connected in parallel with the dc link is proposed in [SHI17] which operates without the need for any power factor correction circuits or large grid filter inductors, ensuring that the grid current meets IEC61000-3-12 standards. While these topology circuit schemes offer high reliability, they also tend to increase the size and cost of the drive systems. As a result, algorithm-based methods have emerged as an effective alternative in various applications.

1.4 Outline and Contributions of the Thesis

Existing research on the optimization of small dc-link capacitor-based PMSM drive systems has primarily focused on the grid side and sacrificed the control performance of the machine side. Only in recent years has attention been directed towards addressing the influence on control performance on the machine side. Therefore, this study investigates the optimization of motor control performance in small dc-link capacitor-based PMSM drive systems, specifically focusing on aspects such as dc-link voltage sensor faults, sensorless control methods, and FW control. The research outline is shown in Fig. 1.36.

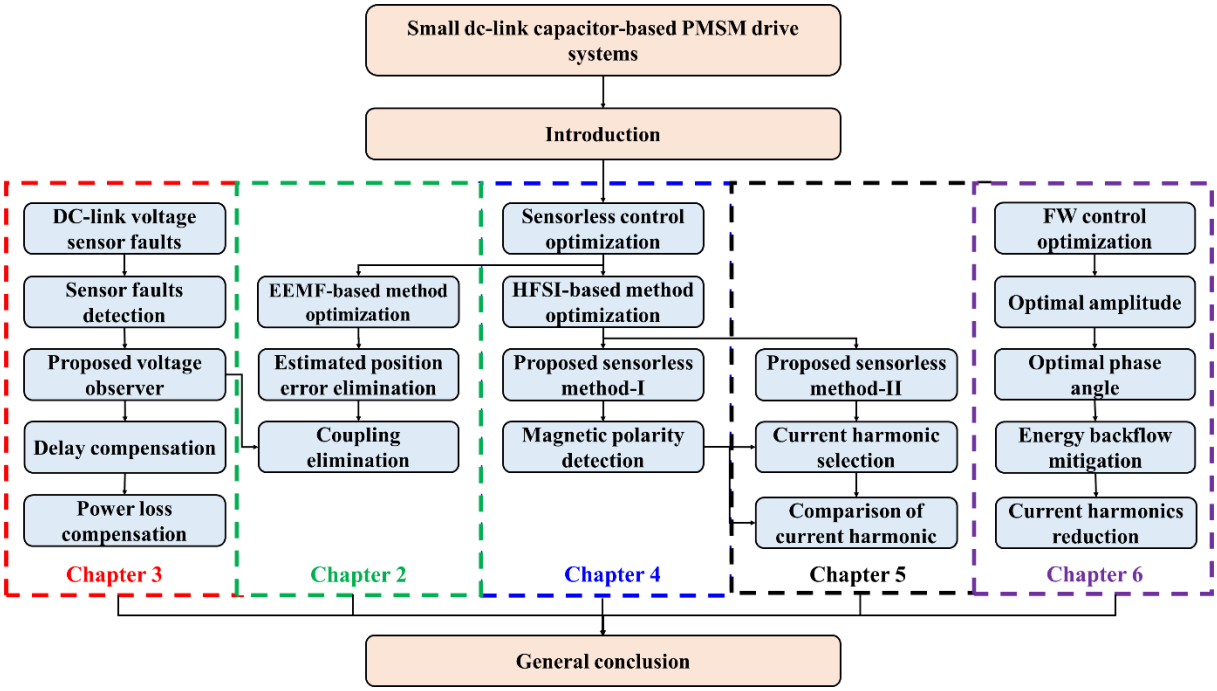

Fig. 1.36. Outline of thesis.

The chapters of the thesis are briefly described as follows.

Chapter 2: For fluctuating dc-link voltage and dc-link voltage sensor faults, an improved EEMF-based sensorless control method for small dc-link capacitor-based PMSM drive systems is proposed. Firstly, the influence of dc-link voltage fluctuation on the EEMF-based sensorless control method is investigated. It is found that the estimated rotor position error harmonics could be introduced. Then, the influence of dc-link voltage sensor faults on the EEMF-based sensorless control method is investigated. It is shown that the dc-link voltage measurement error can introduce a dc offset in the estimated position error under the EEMF-based sensorless control method. To mitigate these issues, the chapter proposes a dc-link voltage observer that is immune to dc-link voltage measurement errors and estimated position errors. The observer utilizes the estimated dc-link voltage to eliminate the position error offset caused by measurement inaccuracies. Furthermore, to enhance the practical applicability of the observer, the effects of magnetic saturation are analyzed using finite element analysis (FEA), revealing that parameter mismatches have a negligible effect on the observer. Additionally, the chapter addresses the coupling issue arising from using estimated dc-link voltage in EEMF-based sensorless control, proposing a back-EMF harmonic suppression method to mitigate harmonics in the estimated back-EMF, speed, position error, and dc-link voltage. This approach effectively eliminates the estimated position error caused by fluctuating dc-link voltage and coupling issues, achieving satisfactory system control performance.

Chapter 3: For estimated dc-link voltage error caused by time delay and power loss, the influence of these challenges on the proposed dc-link voltage observer and the EEMF-based sensorless control method are first investigated. To address these issues, a time delay compensation method based on dc-link voltage reconstruction is proposed to eliminate the adverse effects of sampling and estimation delays. Then, a power compensation method is introduced to mitigate the effect of power losses on the estimated dc-link voltage. These enhancements not only improve the accuracy of the proposed dc-link voltage observer but also expand its applicability to more complex and demanding operational environments.

Chapter 4: In the zero and low-speed regions, the effectiveness of conventional HF voltage signal injection-based sensorless control methods can be limited due to insufficient dc-link voltage, which is often worsened by significant dc-link voltage fluctuation. Moreover, these HF signal injection methods can increase losses, torque ripples, and acoustic noise. To address these issues, this chapter introduces a novel sensorless control method that leverages inherent current harmonics resulting from dc-link voltage fluctuation to determine the rotor position to eliminate the need for additional HF voltage injection. Furthermore, this method utilizes these unavoidable current harmonics to identify magnetic polarity, offering superior performance compared to conventional secondary harmonics-based polarity detection methods, especially under heavy load conditions. Additionally, a lookup table derived from FEA has been developed to mitigate the sensitivity of the proposed sensorless control method to motor parameter mismatches, ensuring more accurate rotor position estimation.

Chapter 5: In the previous Chapter, a lookup table was established to mitigate the effects of motor parameter mismatches on the proposed sensorless control strategy. However, the lookup table method has inherent limitations. It relies on precomputed data, requiring additional memory resources. Furthermore, if the input data does not exactly match the values stored in the lookup table, parameter mismatches can occur, which may compromise the accuracy of rotor position estimation. Moreover, the proposed sensorless control method in Chapter 4 requires both *dq*-axis current signals and the amplitude and phase of the *dq*-axis voltages, increasing dependency on multiple variables. This dependency can limit the precision of rotor position estimation and, consequently, the overall system performance. Thus, this chapter introduces an improved sensorless control method that is immune to motor parameter mismatches and requires only the *q*-axis current and the phase angle of the *dq*-axis voltages to reduce sensitivity to multiple variables. Furthermore, the chapter systematically compares the proposed sensorless control methods based on 100 Hz and 200 Hz harmonics. These findings

provide a robust solution for the HFSI-based sensorless control method under severe dc-link voltage fluctuations, ensuring consistent performance across different operating environments.

Chapter 6: The energy backflow phenomenon in small dc-link capacitor-based PMSM drive systems is identified and investigated in this chapter, particularly when operating at high speeds and/or under heavy load conditions. The large amplitude of back-EMF could exceed the minimum value of fluctuating dc-link voltage, leading to notable energy backflow. This unintended energy backflow not only poses risks to power devices but also introduces challenges to system stability and efficiency. The FW control strategy can effectively mitigate energy backflow by controlling the *d*-axis current to reduce the back-EMF. However, FW control also presents challenges in systems with fluctuating dc-link voltage, as these fluctuations can cause corresponding fluctuations in the *dq*-axis voltages, degrading the control performance of the FW control method. An analysis of the small-signal model of FB-FW control reveals that severe fluctuations in the *q*-axis voltage, especially when it becomes negative, can induce a positive feedback mode, leading to inherent instability. To address these issues, this chapter proposes a quasi-proportional integral resonant (quasi-PIR) based FW control method. Furthermore, an optimal phase angle selection method based on the least mean square (LMS) algorithm and gradient descent (GD) algorithm for *d*-axis reference current is introduced to suppress current ripple caused by the fluctuating dc-link voltage. This approach enhances the control performance and stability of the PMSM drive system under variable operating conditions.

Chapter 7: The general conclusion is drawn in this chapter, and the potential future works are discussed.

Overall: The major contributions of this thesis are briefly summarized as follows.

1. The influence of dc-link voltage sensor faults on EEMF-based sensorless control methods is investigated and a dc-link voltage observer is proposed. The challenges in practical operation, such as parameter mismatches, coupling between estimated dc-link voltage and rotor position, sampling delays, and power losses are comprehensively analyzed and mitigation.

2. For middle and high-speed sensorless control, the effects of fluctuating dc-link voltage on EEMF-based sensorless control are investigated and a back-EMF harmonics suppression method is proposed to eliminate the estimated rotor position error harmonics.

3. For zero and low-speed sensorless control, two different sensorless control methods are introduced, which do not require additional voltage signal injection to estimate rotor position. Furthermore, a magnetic polarity detection method based on inherent current harmonics is proposed to determine magnetic polarity.

4. The unavoidable energy backflow phenomenon is analyzed. Then, a novel FW control method that optimizes both the amplitude and phase of the reference *d*-axis current is proposed to enhance control performance.

CHAPTER 2

IMPROVED EXTENDED EMF-BASED SENSORLESS CONTROL FOR IPMSMS WITH SMALL DC-LINK CAPACITOR CONSIDERING DC-LINK VOLTAGE SENSOR FAULTS

This chapter proposes an improved EEMF-based sensorless control method for permanent magnet synchronous machine drive systems with a small dc-link capacitor, while considering the dc-link voltage sensor faults. Due to fluctuating dc-link voltage, precise and stable dc-link voltage information is extremely important. It is demonstrated that the dc-link voltage measurement error will introduce a dc offset in the estimated position error under EEMF-based sensorless control. To address this issue, a dc-link voltage observer is proposed in this chapter, which is immune to dc-link voltage measurement error and estimated position error. Specifically, the estimated position error caused by the dc-link voltage measurement error can be eliminated by using the estimated dc-link voltage. Meanwhile, to further improve the realism and practicality of the proposed observer, the magnetic saturation effect is analyzed using FEA. It is found that the parameter mismatch has only a minor effect on the proposed observer. In addition, this chapter identifies the coupling issue introduced by using the estimated dc-link voltage in the EEMF-based sensorless control method and a back-EMF harmonic suppression method is proposed to suppress the harmonics in the estimated back-EMF, speed, position error, and dc-link voltage, thereby eliminating the coupling issue. A satisfactory system control performance can be achieved, which is validated by experiments.

2.1 Introduction

Small dc-link capacitor-based PMSM drive systems have become a popular research topic due to low price and reduced size of small volume dc-link capacitor [HUA17] [ZHA18A] [ZHA19A] [YAN22A] [HUO23]. However, small dc-link capacitors will generate large dc-link voltage ripples which will cause fluctuations in *dq*-axis voltages and currents. In the model-based sensorless control method of PMSM drive systems, the estimated position error harmonics are introduced from the fluctuating *dq*-axis voltages and currents [MOR02] [CHE03] [HUA17] [ZHA18A] [ZHA19A] [YAN22B] [HUO23]. Two effective filters are proposed in

[HUO23] [HUA17] to suppress the estimated back-EMF harmonics and the estimated rotor position error harmonics caused by small dc-link capacitor.

In addition, a reliable dc-link voltage sensor is required to measure the dc-link voltage, especially in the voltage source inverter (VSI)-based PMSM drive system with a small dc-link capacitor, where the dc-link voltage is always fluctuating. The influence of dc-link voltage fluctuation on the EEMF-based sensorless control is considered in [HUA17] [HUO23], but these two papers are both based on the dc-link voltage sensor and assume that the measured voltage is accurate. However, the dc-link voltage sensor may be faulty due to high humidity, high temperature, electromagnetic interference, and mechanical vibration [JEO05A] [SAL10] [YU13] [FOO15] [TEN17] [XIA17] [KOM18] [TRI19] [WAN19C] [WAN20D] [KOW22] [SKO22] [PES23] [HEI23] [XIA23]. In this case, the information on dc-link voltage could be lost, which will compromise the stability of the system. Additionally, it may introduce a dc-link voltage measurement error, such as zero drift and gain variation, etc. The dc-link voltage measurement errors will inevitably produce biased *dq*-axis voltages, which further deteriorate the EEMF-based sensorless control strategy.

Therefore, recent research has increasingly focused on the fault detection of a dc-link voltage sensor and estimation of dc-link voltage to mitigate system vulnerabilities. To detect the speed, dc-link voltage, and phase current sensor faults, an observer-based method [FOO15]. These methods can effectively identify stuck, offset, and noise faults in constant-speed drives. However, these methods do not address post-fault remediation. Moreover, a neural network fault classification method for induction motor drives is proposed in [SKO22], where the fault-tolerant control (FTC) strategy is employed to ensure continuous operation despite current sensor failure. The effect of dc-link voltage measurement error on the model predictive control (MPC) of the PMSM control system is investigated in [WAN20D]. In [JEO05A], a method for detecting faults in dc-link voltage sensor is introduced, employing the concept of power balance. However, in [JEO05A] [WAN20D], when the dc-link voltage sensor fails, the nominal value of dc-link voltage is used to replace the measured value. This could lead to system malfunctions, especially when the dc-link voltage fluctuation is large.

Therefore, a high-performance dc-link voltage observer is critical when the dc-link voltage sensor fails. A simple dc-link voltage sensor fault detection method is proposed in [WAN19C] by combining the current model-based stator flux observer with the voltage model-based stator flux observer in the dual-three phase PMSM drive system, where the dc-link voltage

measurement error is compensated. In [YU13] [PES23], the optimal dc-link voltage is calculated and adaptively regulated in electric vehicles (EVs) to enhance the overall efficiency of traction motor drives. In [SAL10], a sliding-mode (SMO) model reference adaptive based observer is proposed to estimate dc-link voltage for the MPC control in the PMSM drive system. In [TEN17], the adaptive observer is used to estimate the dc-link voltage and suppress the resistance estimation error caused by the dc-link voltage measurement error. In [TRI19], a compensation method for current and dc-link voltage measurement error in PWM rectifiers is proposed. Two dc-link voltage estimation methods based on measured currents, motor speed and duty cycle are proposed in [HEI23], but the encoder failure situation is not considered. An innovative approach is proposed in [XIA23], by using an unknown input SMO together with an adaptive FTC technique to detect and remedy grid current and dc-link voltage sensor faults for single-phase grid-connected converters. In [KOM18], an advanced FTC method with a high-order SMO is developed to detect and mitigate the influence of sensor faults. A diagnostic and remedy approach for current and dc-link voltage sensor faults in a single-phase PWM rectifier control mechanism-based electric traction system is proposed in [XIA17]. However, the above-mentioned studies primarily address scenarios with constant dc-link voltage. When a small dc-link capacitor is employed, the dc-link voltage fluctuation inevitably occurs as mentioned before. To date, this issue requires further investigation.

This chapter proposes an observer-based dc-link voltage estimation method for EEMF-based sensorless control, where the influence of dc-link voltage sensor faults can be eliminated. Furthermore, this chapter investigates the influences of several practical factors, such as magnetic saturation, parameter mismatch, and harmonics of *dq*-axis back-EMFs, on the performance of the proposed method under EEMF-based sensorless control.

The contributions of this chapter are twofold.

Firstly, this chapter proposes a proportional integral resonance (PIR) controller-based dc-link voltage observer, along with a dc-link voltage sensor fault detection method. The proposed observer demonstrates robustness against the magnetic saturation and motor parameter mismatches, including stator resistance, *dq*-axis inductances, and PM flux linkage.

Secondly, this chapter identifies a common coupling issue existing in the simultaneous estimations of dc-link voltage and speed under EEMF-based sensorless control. This issue introduces additional specific harmonics in the system, such as in dc-link voltage, currents, and estimated position error, especially when employing a small dc-link capacitor. To address this

issue, a back-EMF harmonic suppression method is proposed by utilizing notch filters. As demonstrated, this method effectively suppresses harmonics in the estimated dc-link voltage, speed, and rotor position, thereby resolving the coupling issue and eliminating the harmonics introduced by dc-link voltage fluctuation. Finally, experiments validate the proposed method which can greatly improve the robustness and effectiveness of the EEMF-based sensorless control system.

The rest of this chapter is organized as follows. Sections 2 and 3 outline the challenges posed by dc-link voltage fluctuation and the dc-link voltage sensor faults on EEMF-based sensorless control, respectively. Section 4 proposes the dc-link voltage observer along with the back-EMF harmonic suppression method. Section 5 discusses the effects of magnetic saturation and parameter mismatch on the proposed observer. Section 6 presents the experiment results that demonstrate the robustness and effectiveness of the proposed method in the improvement of performance under EEMF-based sensorless control. Finally, section 7 draws the conclusion of this chapter.

This chapter is based on the papers published in:

[YAN22A] J. Yan, X. Wu, and Z. Q. Zhu, "Analysis of extended EMF based sensorless control with dc-link voltage fluctuation," *Proc. Int. Conf. on Power Electronics, Machines. and Drives (PEMD)*, Newcastle, UK, 2022, pp. 327-334.

[YAN22B] J. Yan, X. Wu, Z. Q. Zhu, and C. Liu, "Influence of dc-link voltage measurement error on extended EMF based sensorless control with reduced dc-link capacitor," *2022 25th Int. Conf. Electr. Mach. and Syst. (ICEMS)*, Thailand, pp. 1-6. 2022.

[YAN24] J. Yan, X. M. Wu, Z. Q. Zhu, and C. Liu, "Improved extended EMF-based sensorless control for IPMSMs with small dc-link capacitor considering dc-link voltage measurement error," *IEEE Trans. Ind. Appl.*, early access, 2024, doi: 10.1109/TIA.2024.3397960.

2.2 System Model and DC-Link Voltage Fluctuation Issues

The block diagram of the IPMSM drive system fed by VSI with a small dc-link capacitor usually applied to domestic appliances is shown in Fig. 2.1.

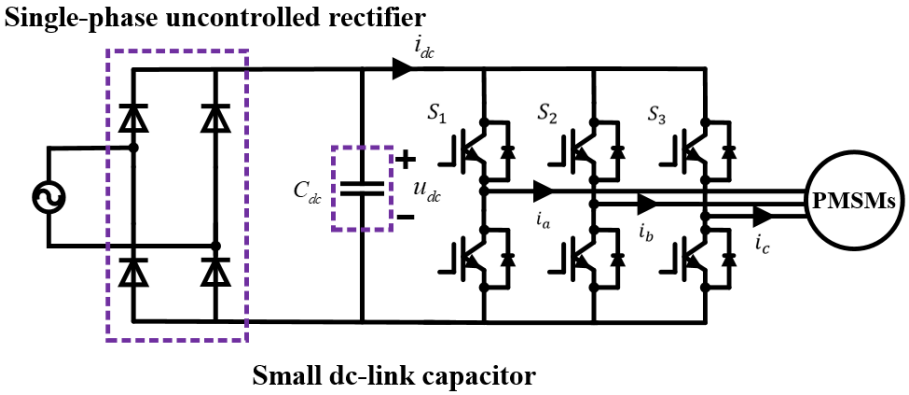

Fig. 2.1. IPMSM drive system fed by VSI with small dc-link capacitor.

For the single-phase diode-based rectifier, the fluctuating dc-link voltage can be expressed as

$$u_{dc} = u_{dc,0} + \sum_{k=1}^{n} u_{dc,k} \sin(2k\omega_g t + \varphi_g) \tag{2.1}$$

where $u_{dc,0}$ is the amplitude of the dc component of fluctuating dc-link voltage, $u_{dc,k}$ and φ_g are the amplitude and phase of the kth order harmonic of fluctuating dc-link voltage.

According to [HUA17] [YAN22A], [HUO23], the estimated dq-axis voltages and currents in the estimated reference frame can be expressed by

$$\begin{cases} \hat{u}_d = \hat{u}_{d,0} + \sum_{k=1}^{n} \hat{u}_{d,k} \sin(2k\omega_g t + \varphi_{d,k}^{u}) \\ \hat{u}_q = \hat{u}_{q,0} + \sum_{k=1}^{n} \hat{u}_{q,k} \sin(2k\omega_g t + \varphi_{q,k}^{u}) \end{cases} \tag{2.2}$$

$$\begin{cases} \hat{i}_d = \hat{i}_{d,0} + \sum_{k=1}^{n} \hat{i}_{d,k} \sin(2k\omega_g t + \varphi_{d,k}^{i}) \\ \hat{i}_q = \hat{i}_{q,0} + \sum_{k=1}^{n} \hat{i}_{q,k} \sin(2k\omega_g t + \varphi_{q,k}^{i}) \end{cases} \tag{2.3}$$

where $\hat{u}_{d,0}$, $\hat{u}_{q,0}$, $\hat{i}_{d,0}$ and $\hat{i}_{q,0}$ are the amplitudes of dc components of estimated dq-axis voltages and currents, $\hat{u}_{d,k}$ $\hat{u}_{q,k}$ $\hat{i}_{d,k}$, and $\hat{i}_{q,k}$ are the amplitudes of kth order harmonic, $\varphi_{d,k}^{u}$, $\varphi_{q,k}^{u}$, $\varphi_{d,k}^{i}$ and $\varphi_{q,k}^{i}$ are the phases of the kth order harmonic of dq-axis voltages and currents.

Assuming that the derivative of the dq-axis currents is 0, the estimated dq-axis back-EMFs can be obtained as

$$\begin{aligned}\hat{E}_d &= \hat{u}_{d,0} - R_s\hat{i}_{d,0} + \hat{\omega}_{e,0}L_q\hat{i}_{q,0} \\ &+ \sum_{k=1}^{n} A_{d,k}(\hat{u}_{d,k} - R_s\hat{i}_{d,k} + L_q\hat{i}_{q,k}\hat{\omega}_{e,0} + L_d\hat{i}_{q,0}\hat{\omega}_{e,k})\, sin(\,2k\omega_g t\, + \varphi_{d,k,A}) \\ &+ \sum_{k=1}^{n} L_q\hat{\omega}_{e,k}\, sin(\,2k\omega_g t + \varphi_{k,\omega}) \sum_{k=1}^{n} i_{q,k}\, sin(\,2k\omega_g t + \varphi_{q,k}^{i})\end{aligned} \tag{2.4}$$

$$\begin{aligned}\hat{E}_q &= \left[\hat{u}_{q,0} - R_s\hat{i}_{q,0} - \hat{\omega}_{e,0}L_q\hat{i}_{d,0}\right] \\ &+ \sum_{k=1}^{n} A_{q,k}(\hat{u}_{q,k} - R_s\hat{i}_{q,k} - L_q\hat{i}_{d,k}\hat{\omega}_{e,0} - L_q\hat{i}_{d,0}\hat{\omega}_{e,k})\, sin(\,2k\omega_g t + \varphi_{q,k,A}) \\ &- \sum_{k=1}^{n} L_q\hat{\omega}_{e,k}\, sin(\,2k\omega_g t + \varphi_{k,\omega}) \sum_{k=1}^{n} \hat{i}_{d,k}\, sin(\,2k\omega_g t + \varphi_{d,k}^{i})\end{aligned} \tag{2.5}$$

where $A_{d,k}$, $A_{q,k}$, $\varphi_{d,k,A}$ and $\varphi_{q,k,A}$ are the equivalent amplitude and phase of the estimated *dq*-axis back-EMFs.

The rotor position error can be expressed by

$$\Delta\theta_r \approx -\frac{\hat{E}_d}{\hat{E}_q} \approx \sum_{k=1}^{n} \Delta\theta_{r,k}\, sin(\,2k\omega_g t + \varphi_{k,\theta}) \tag{2.6}$$

where $\Delta\theta_{r,0}$ is the amplitude of the dc component of estimated position error. $\Delta\theta_{r,k}$ is amplitude of the *k*th order harmonic, and $\varphi_{k,\theta}$ is the phase of the *k*th order harmonic of estimated position error, respectively.

Through the phase-locked loop, the estimated speed is obtained by the estimated rotor position error. Therefore, the estimated speed can be expressed by [HUA17] [YAN22A], [HUO23]

$$\hat{\omega}_e = \hat{\omega}_{e,0} + \sum_{k=1}^{n} \hat{\omega}_{e,k}\, sin(\,2k\omega_g t + \varphi_{k,\omega}) \tag{2.7}$$

where $\hat{\omega}_e$ is the estimated speed, $\hat{\omega}_{e,0}$, $\hat{\omega}_{e,k}$, and $\varphi_{k,\omega}$ are the amplitude of the dc component, amplitude, and phase of the *k*th order harmonic of estimated speed error, respectively.

Overall, it can be observed that when the dc-link voltage has a significant fluctuation, it is important to consider the harmonics in the estimated position error and speed to improve the

control performance of the EEMF-based sensorless control. Besides, further deterioration also occurs when there is a dc-link voltage sensor faults, which is described in the next section.

2.3 Influence of DC-Link Voltage Sensor Measurement Error on EEMF Sensorless Control

In some applications, the dc-link voltage sensor may have some detection failures due to electrostatic corrosion, high temperature, high humidity, and mechanical vibration, such as zero offset, gain change, and signal loss. Therefore, the dc-link voltage sensor faults are likely to appear [JEO05A] [WAN20D]. The measured dc-link voltage can be expressed as

$$u_{dc}^{m} = k_{dc} u_{dc}^{a} + u_{\mathrm{dc,offset}} \tag{2.8}$$

where u_{dc}^{m} and u_{dc}^{a} are the measured and actual dc-link voltage, $u_{\mathrm{dc,offset}}$ is the dc offset (normally is 0), k_{dc} is the gain value (normally is 1).

The dc-link voltage sensor faults can lead to the disappearance of the detection signal, which will directly compromise the stability of system. Additionally, it may introduce a dc-link voltage measurement error.

In case of the existing dc-link voltage measurement error due to voltage sensor faults, the measured dc-link voltage can be expressed as

$$u_{dc}^{m} = (K_{dc}\hat{u}_{dc,0} + \Delta u_{dc,offset}) + K_{dc}\sum_{k=1}^{n} \hat{u}_{dc,k} \sin(2k\omega_g t + \varphi_g) \tag{2.9}$$

Therefore, the *dq*-axis voltages and currents considering the dc-link voltage measurement error can be represented as

$$\begin{cases} \hat{u}_{d}^{m} = (K_{dc}\hat{u}_{d,0} + \Delta u_{d,offset}) + K_{dc}\sum_{k=1}^{n} \hat{u}_{d,k} \sin(2k\omega_g t + \varphi_{d,k}^{u}) \\ \hat{u}_{q}^{m} = (K_{dc}\hat{u}_{q,0} + \Delta u_{q,offset}) + K_{dc}\sum_{k=1}^{n} \hat{u}_{q,k} \sin(2k\omega_g t + \varphi_{q,k}^{u}) \end{cases} \tag{2.10}$$

$$\begin{cases} \hat{i}_d^m = (K_{dc,id}\hat{i}_{d,0} + \Delta i_{d,offset}) + K_{dc,id}\sum_{k=1}^{n} \hat{i}_{d,k}\, sin(\,2k\omega_g t + \varphi_{d,k}^{i}) \\ \hat{i}_q^m = (K_{dc,iq}\hat{i}_{q,0} + \Delta i_{q,offset}) + K_{dc,iq}\sum_{k=1}^{n} \hat{i}_{q,k}\, sin(\,2k\omega_g t + \varphi_{q,k}^{i}) \end{cases} \tag{2.11}$$

where $\hat{u}_d^m$, $\hat{u}_q^m$, $\hat{i}_d^m$, and $\hat{i}_q^m$ are the *dq*-axis voltages and currents with dc-link voltage measurement error, $\Delta u_{d,offset}$, $\Delta u_{q,offset}$, $\Delta i_{d,offset}$, and $\Delta i_{q,offset}$ are the dc offsets of *dq*-axis voltages and currents caused by dc-link voltage measurement error, $K_{dc,id}$ and $K_{dc,iq}$ are the gain variations of *dq*-axis currents with dc-link voltage measurement error.

Since the scaling errors of *dq*-axis voltages are proportional to the dc-link voltage, the gain change of the *dq*-axis voltages is the same as the gain change of the dc-link voltage. However, the values of *dq*-axis currents will not change since the phase currents are directly measured by sensors and are mainly related to the operating conditions. Thus, $K_{dc,id}$ and $K_{dc,iq}$ are 1, and $\Delta i_{d,offset}$ and $\Delta i_{q,offset}$ are 0.

The estimated *dq*-axis back-EMFs can be derived by

$$\begin{aligned} \hat{E}_d^e = {} & \left(K_{dc}\hat{u}_{d,0} + \Delta u_{d,offset}\right) - R_s\hat{i}_{d,0} + \hat{\omega}_{e,0}^e L_q \hat{i}_{q,0} \\ & + \sum_{k=1}^{n} A_{d,k}^e [K_{dc}\hat{u}_{d,k} - R_s\hat{i}_{d,k} + L_q\hat{i}_{q,k}\hat{\omega}_{e,0}^e + L_d\hat{i}_{q,0}\hat{\omega}_{e,k}^a] \sin(\,2k\omega_g t + \varphi_{d,k,A}^e) \\ & + \sum_{k=1}^{n} L_q\hat{\omega}_{e,k}^a \sin(\,2k\omega_g t + \varphi_{d,k,A}^e) \sum_{k=1}^{n} \hat{i}_{q,k} \sin(\,2k\omega_g t + \varphi_{d,k,A}^e) \end{aligned} \tag{2.12}$$

$$\begin{aligned} \hat{E}_q^e = {} & (K_{dc}\hat{u}_{q,0} + \Delta u_{q,offset}) - R_s\hat{i}_{q,0} - \hat{\omega}_{e,0}^e L_q \hat{i}_{d,0} \\ & + \sum_{k=1}^{n} A_{q,k}^e [K_{dc}\hat{u}_{q,k} - R_s\hat{i}_{q,k} - L_q\hat{i}_{d,k}\hat{\omega}_{e,0}^e - L_q\hat{i}_{d,0}\hat{\omega}_{e,k}^e]\, sin(\,2k\omega_g t + \varphi_{q,k,A}^e) \\ & - \sum_{k=1}^{n} L_d\hat{\omega}_{e,k}^e\, sin(\,2k\omega_g t + \varphi_{q,k,A}^e) \sum_{k=1}^{n} \hat{i}_{d,k}\, sin(\,2k\omega_g t + \varphi_{q,k,A}^e) \end{aligned} \tag{2.13}$$

where $\hat{E}_d^e$ and $\hat{E}_q^e$ are the *dq*-axis back-EMFs with the dc-link voltage measurement error, $A_{d,k}^e$, $A_{q,k}^e$, $\varphi_{d,k,A}^e$, and $\varphi_{q,k,A}^e$ represent the equivalent amplitude and phase of the *k*th harmonic of the estimated *dq*-axis back-EMFs with dc-link voltage measurement errors, respectively.

Due to the existence of the dc-link voltage measurement error, the estimation position error is shown as:

$$\Delta\theta_r^e \approx -\frac{\hat{E}_d^e}{\hat{E}_q^e} \approx \Delta\theta_{r,offset}^e + \sum_{k=1}^{n} \Delta\theta_{r,k}^e \, sin(\, 2k\omega_g t + \varphi_{k,\theta}^e) \tag{2.14}$$

where $\Delta\theta_r^e$ is the estimated position error with dc-link voltage measurement error, $\Delta\theta_{r,offset}^e$, is the amplitude of the dc component, $\Delta\theta_{r,k}^e$ is the amplitude of the kth order harmonic of estimated position error with dc-link voltage measurement error, $\varphi_{k,\theta}^e$ is the phase of the kth harmonic of estimated position error.

Therefore, the estimated rotor speed can be expressed by

$$\hat{\omega}_e^e = \hat{\omega}_{e,0}^e + \sum_{k=1}^{n} \hat{\omega}_{e,k}^e \, sin(\, 2k\omega_g t + \varphi_{k,\omega}^e) \tag{2.15}$$

where $\hat{\omega}_e^e$ is the estimated speed, $\hat{\omega}_{e,0}^e$ is the amplitude of the dc component of estimated speed, $\hat{\omega}_{e,k}^e$ and $\varphi_{k,\omega}^e$ are the amplitude and phase of the kth order harmonic of estimated speed with dc-link voltage measurement error.

It is obvious that the dc-link voltage measurement error can result in biased dq-axis voltages, back-EMFs, and estimated position error, which deteriorates the performance of EEMF-based sensorless control. Furthermore, in the steady-state of EEMF-based sensorless control with $i_d = 0$ control strategy, the estimated position error can be expressed as

$$\Delta\theta_r \approx -\frac{\hat{E}_d}{\hat{E}_q} = \frac{\hat{u}_d - R_s\hat{i}_d - pL_d\hat{i}_d + \omega_e L_q\hat{i}_q}{\hat{u}_q - R_s\hat{i}_q - pL_d\hat{i}_q - \omega_e L_q\hat{i}_d} \approx \frac{\hat{u}_d + \omega_e L_q\hat{i}_q}{\hat{u}_q - R_s\hat{i}_q} \tag{2.16}$$

Without dc-link voltage measurement errors, the estimated d-axis back-EMF is always zero under different operating conditions. Therefore, the estimated rotor position error is maintained at zero. When dc-link voltage measurement errors are present in the system, the dq-axis voltages can be expressed as follows.

$$\begin{cases} \hat{u}_d^m = K_{dc}\hat{u}_d \\ \hat{u}_q^m = K_{dc}\hat{u}_q \end{cases} \tag{2.17}$$

Therefore, the error in the estimated position can be approximated as follows.

$$\Delta\theta_r \approx \frac{K_{dc}\hat{u}_d + \omega_e L_q \hat{i}_q}{K_{dc}\hat{u}_d - R_s \hat{i}_q} \tag{2.18}$$

The values of *dq*-axis currents will not change with dc-link voltage measurement errors since the phase currents are directly measured by sensors and are determined by the operating conditions. Therefore, it can be concluded that the estimated rotor position error can be influenced by different operating conditions when dc-link voltage measurement errors are present.

To eliminate the estimated position error due to dc-link voltage measurement error, a dc-link voltage sensor fault detection method [JEO05A] is initially employed to identify sensor faults. Subsequently, a PIR controller-based dc-link voltage observer is proposed, which will be introduced in the following section.

2.4 Proposed DC-Link Voltage Observer

2.4.1 Proposed DC-link Voltage Observer

Assuming an ideal inverter with no power loss, the power balance equation for the inverter can be expressed as

$$P_{\text{inv}}^{\text{ref}} = \frac{3}{2}\left(u_d i_d + u_q i_q\right) = u_{dc} i_{dc} \tag{2.19}$$

where $P_{\text{inv}}^{\text{ref}}$ represents the actual inverter power.

Assuming that the current sensors are error-free, the dc-link current can be calculated by

$$i_{dc} = i_{\text{a}}\text{S}_{\text{a}} + i_{\text{b}}\text{S}_{\text{b}} + i_{\text{c}}\text{S}_{\text{c}} \tag{2.20}$$

where S_{a}, S_{b}, S_{c} are the switching status of the three upper IGBTs.

Fig. 2.2. shows the measured results of three-phase currents, duty cycle, and the reconstructed dc-link current. The IPMSM is operated at 300 r/min under 2 Nm, and the reconstructed dc-link current exhibits an average value of ~0.45 A, closely aligning with the simulation results.

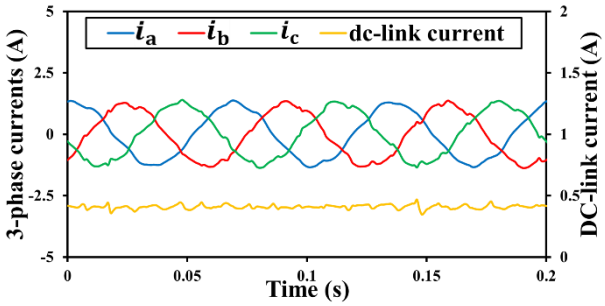

(a)

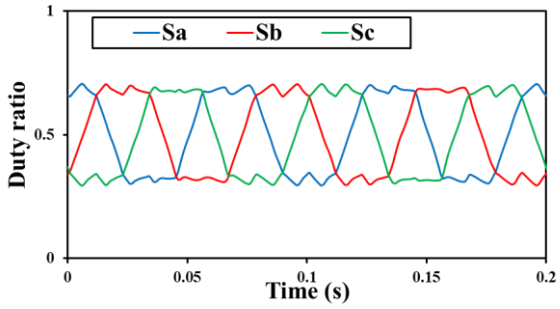

(b)

Fig. 2.2. Measured results of dc-link current reconstruction at 300 r/min and 2 Nm load condition. (a) Three-phase currents and dc-link current. (b) Switching status.

Since the *dq*-axis voltages are proportional to the dc-link voltage value, the dc-link voltage measurement error will inevitably produce the wrong *dq*-axis voltages. Thus, the *dq*-axis voltages cannot be used to calculate the actual inverter output power.

Therefore, the actual inverter power can be expressed by

$$P_{\text{inv}}^{\text{ref}} = \frac{3}{2}\left\{R_s\left(i_d^2 + i_q^2\right) + \left(L_d i_d \frac{di_d}{dt} + L_q i_q \frac{di_q}{dt}\right) + \omega_e\left[\varphi_f i_q + \left(L_d - L_q\right) i_d i_q\right]\right\} \tag{2.21}$$

Fig. 2.3 presents the block diagram of the proposed dc-link voltage observer. Initially, the reference inverter power $P_{\text{inv}}^{\text{ref}}$ is computed using (2.21) and serves as the input to the voltage estimation loop. Subsequently, the estimated inverter power $P_{\text{inv}}^{\text{est}}$ is calculated by multiplying the estimated dc-link voltage with the calculated dc-link current by three-phase currents and duty cycle, providing a feedback signal for comparison with $P_{\text{inv}}^{\text{ref}}$. The deviation between $P_{\text{inv}}^{\text{ref}}$ and $P_{\text{inv}}^{\text{est}}$, denoted as the power error $P_{\text{inv}}^{\text{err}}$, which is processed by the PIR controller. The PIR controller fine-tunes the estimated dc-link voltage to minimize the power error, thus closely aligning the estimated voltage with the actual voltage. When the inverter power error approaches zero, the estimated dc-link voltage approaches the actual dc-link voltage value. The PIR controller is implemented to ensure convergence between the dc component of the

estimated and actual dc-link voltages and their respective 100 Hz voltage harmonics. Furthermore, the differential process outlined in (2.21) can introduce notable harmonics, especially in the case of dc-link voltage fluctuation situations. Therefore, A low pass filter (LPF) is utilized to further improve the accuracy of the estimated dc-link voltage by removing high-frequency harmonics that arise from the differential process.

Given that the proposed voltage observer is immune to *dq*-axis voltages, it remains unaffected by dc-link voltage sensor faults. Furthermore, the estimated dc-link voltage is not influenced by the estimated position error. Consequently, this observer is well-suited for integration into the EEMF-based method.

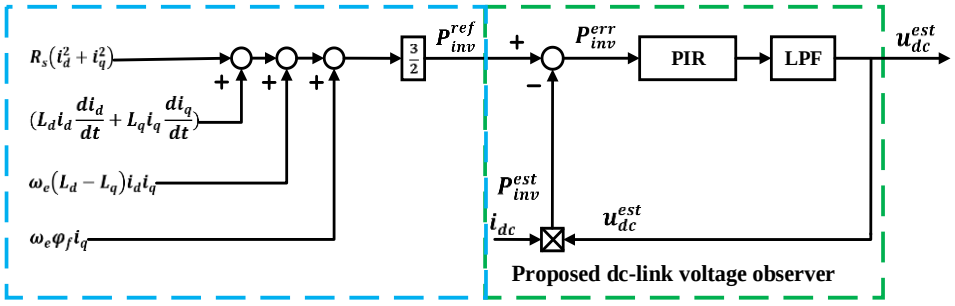

Fig. 2.3. Block diagram of proposed voltage observer.

A dc-link voltage sensor fault detection method [JEO05A] based on the inverter power balance is used and can be expressed as

$$\frac{3}{2}(u_d i_d + u_q i_q) - T_e \omega_m = a \tag{2.22}$$

When the difference a exceeds a certain threshold, it indicates that the dc-link voltage sensor fault exists. When the dc-link voltage sensor fails, the estimated dc-link voltage is used, thereby eliminating the estimated position error caused by the dc-link voltage sensor fault.

2.4.2 Influence of Estimated Back-EMF Harmonics

As previously analyzed, the fluctuating dc-link voltage, primarily at 100 Hz frequency, can induce the estimated *dq*-axis back-EMFs fluctuation, which in turn leads to the estimated rotor position and estimated speed fluctuation.

Furthermore, the additional estimated speed harmonics can introduce additional harmonics in the estimated dc-link voltage. When this estimated dc-link voltage is utilized within the system, the dc-link voltage harmonics can introduce additional estimated back-EMF harmonics, which can further amplify the harmonics in the estimated speed. Therefore, a coupling issue between

the estimated dc-link voltage harmonics and the estimated speed harmonics may occur in the system. This interaction deteriorates the system's control performance.

Considering the estimated speed harmonics, the power can be determined by combining (2.7) and (2.21)

$$P_{inv}^{\omega_{eac}} = \frac{3}{2} R_s\left(i_d^2 + i_q^2\right) + \frac{3}{2}\left(L_d i_d \frac{di_d}{dt} + L_q i_q \frac{di_q}{dt}\right) + \frac{3}{2}\left[\omega_{e,0} + \sum_{k=1}^{n} \widehat{\omega}_{e,k}\, sin(2k\omega_g t + \varphi_{k,\omega})\right]\left[\varphi_f i_q + \left(L_d - L_q\right) i_d i_q\right] \tag{2.23}$$

where $P_{\text{inv}}^{\omega_{e\_ac}}$ is the inverter power considering the estimated speed harmonics.

The estimated dc-link voltage error considering the estimated speed harmonics can be expressed by

$$\Delta u_{dc}^{\Delta\omega_e} = \frac{P_{inv}^{ref} - P_{inv}^{\omega_{eac}}}{i_{dc}} = \frac{\frac{3}{2}\sum_{k=1}^{n} \widehat{\omega}_{e,k}\, sin(2k\omega_g t + \varphi_{k,\omega})\left[\left(L_d - L_q\right) i_d i_q + \varphi_f i_q\right]}{i_{dc}} \tag{2.24}$$

where $\Delta u_{dc}^{\Delta\omega_e}$ is the estimated dc-link voltage error due to estimated speed harmonics.

To solve this, an improved EEMF-based sensorless control is proposed in the next section.

2.4.3 Improved EEMF-Based Sensorless Control with Back-EMF Harmonic Suppression Method

The harmonics in the estimated speed could be mitigated by limiting the bandwidth of the PI controller within the PLL. However, setting the bandwidth of the PI controller too narrowly may limit the tracking ability of PLL, leading to slower dynamics in the EEMF-based sensorless control system. Similarly, while reducing the cut-off frequency of the LPF can suppress the estimated speed harmonics, it may also slow down the dynamics performance and fail to adequately address the harmonics in the estimated position. The notch filter is an attractive method for harmonic suppression due to its ability to precisely target and eliminate specific unwanted frequency components [WAN14] [ALZ17] [QU23]. In [HUA19] [TAG19] [SOM23], the notch filter is employed to regulate the dc-link voltage by filtering out undesirable harmonics in single-phase grid-connected inverters or converters. In [WAN14] [WU23A] [DIN24B], the notch filter is utilized to remove unwanted harmonics to improve the effectiveness of sensorless control techniques.

In this chapter, two notch filters are employed to attenuate the 100 Hz harmonic present in the estimated *dq*-axis back-EMFs. This approach can not only reduce the harmonics in the estimated position and speed caused by dc-link voltage fluctuation but also mitigate the coupling issue between the estimated dc-link voltage harmonics and the estimated speed harmonics.

The transfer function for the notch filter is given as follow.

$$G_{(s)} = \frac{\widehat{\omega}_{e,dc}}{\widehat{\omega}_e} = \frac{s^2 + \omega_c^2}{s^2 + \mu s + \omega_c^2} \tag{2.25}$$

where μ and ω_c represent the gain coefficient and the center frequency of the notch filter.

The block diagram and bode plot of the notch filter are shown in Fig. 2.4. As analyzed previously, the 100 Hz harmonic, which is twice the grid frequency, significantly influences the estimated back-EMFs. Consequently, the center frequency (ω_c) is set to 2π×100 Hz to effectively eliminate the 100 Hz harmonic. The gain coefficient (μ) is crucial for determining the convergence rate of the notch filter. According to [WAN14] [ALZ17] [QU23], the notch filter should be configured to be under-damped to enhance the convergence rate. Thus, the gain coefficient μ is often set to less than twice the center frequency ω_c. While increasing μ can improve the dynamic response of the system, it may also introduce larger steady-state errors. Therefore, the value of μ should be selected by compromising the fast convergence rate with lower steady-state error. To achieve the most satisfactory convergence rate and dynamic response, the gain coefficient was set to 8 based on the experimental results.

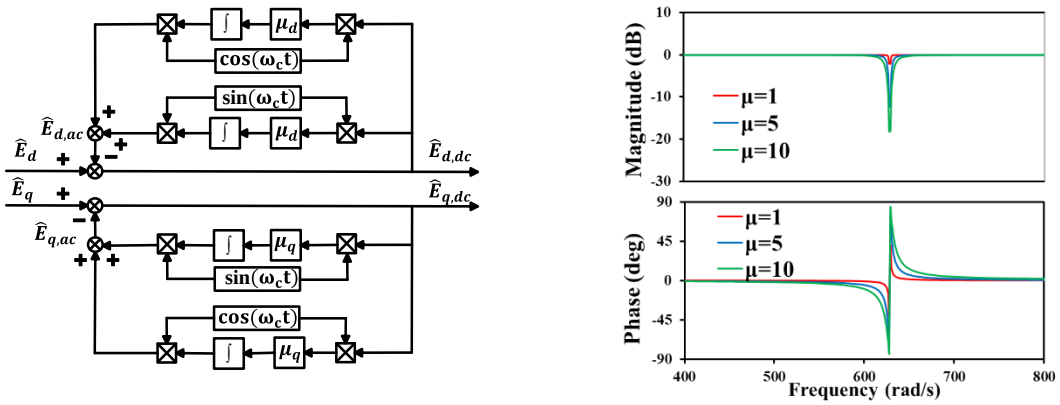

(a) Block diagram (b) Bode plot

Fig. 2.4. Back-EMF harmonic suppression method-based notch filters. (a) Block diagram. (b) Bode plot.

The overall block diagram of EEMF-based sensorless control with proposed dc-link voltage observer and back-EMF harmonic suppression method is shown in Fig. 2.5.

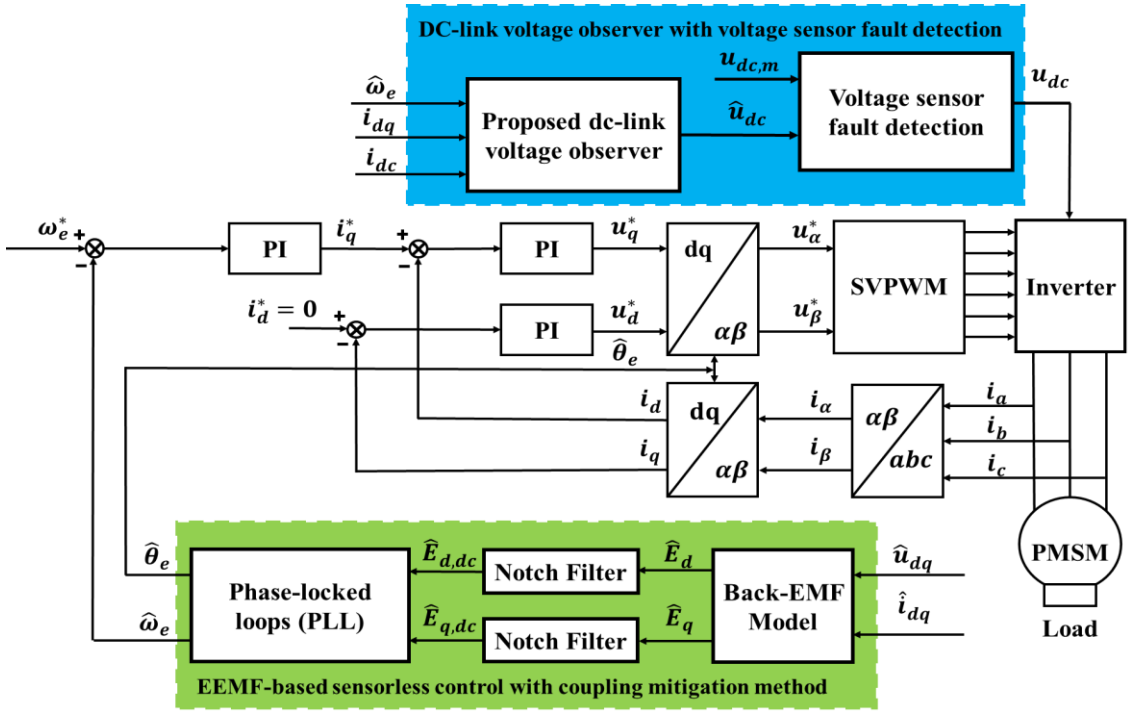

Fig. 2.5. Overall block diagram of EEMF-based sensorless control with proposed dc-link voltage observer.

2.5 Effect of Parameters Mismatch

The parameter mismatches are unavoidable when considering the design and implementation of the proposed dc-link voltage observer. Such mismatches could potentially affect the performance of the proposed observer. Therefore, the effect of parameters mismatch on the proposed voltage observer and the EEMF-based sensorless control are thoroughly investigated as shown below.

2.5.1 Stator Resistance

The stator resistance causes copper losses which can affect the overall power calculation. Therefore, power calculation errors due to stator resistance mismatch need to be considered. The inverter power with the nominal value of the stator resistance can be expressed as

$$P_{inv}^{R_s^{nom}} = \frac{3}{2} R_s^{nom}\left(i_d^2 + i_q^2\right) + \left(L_d i_d \frac{di_d}{dt} + L_q i_q \frac{di_q}{dt}\right) + \omega_e\left[\varphi_f i_q + \left(L_d - L_q\right) i_d i_q\right] \quad (2.26)$$

where R_s^{nom} is the nominal value of the stator resistance. $P_{\text{inv}}^{R_s^{\text{nom}}}$ is the inverter power with the nominal value of the stator resistance.

The difference in power calculation due to resistance changes can be expressed as

$$\Delta P_{inv}^{\Delta R_s} = P_{inv} - P_{inv}^{R_{s\_nom}} = \frac{3}{2}\Delta R_s\left(i_d^2 + i_q^2\right) \tag{2.27}$$

where $\Delta R_s = R_s - R_s^{\text{nom}}$ is the difference between the actual and nominal values of the stator resistance.

The power calculation error caused by resistance mismatch is proportional to the sum of the square of *dq*-axis currents and the change in resistance. Since the system is under $i_d = 0$ control, the power change is mainly related to the load condition.

2.5.2 *Dq*-axis Inductances

The inductances are easily affected by magnetic saturation. The potential inductance mismatch can affect power calculation and the accuracy of estimated dc-link voltage. To address this, the effect of magnetic saturation on *dq*-axis inductances with various operation conditions is thoroughly calculated by FEA first. Then, the effect of inductance mismatch on the proposed dc-link voltage observer is discussed. Fig. 2.6 shows the FEA results of *dq*-axis inductances under different *dq*-axis currents. By way of example, the *d*-axis inductance varies from 39 mH to 37 mH at $i_d = 0$ with different *q*-axis currents. Similarly, the *q*-axis inductance varies from 55 mH to 44.5 mH when $i_d = 0$, with different *q*-axis currents.

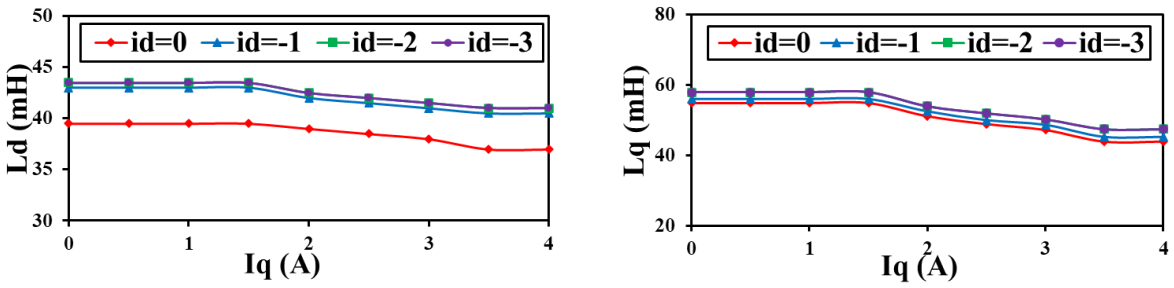

(a) *D*-axis inductance (b) *Q*-axis inductance

Fig. 2.6. Dq-axis inductances under different dq-axis currents. (a) *D*-axis inductance. (b) *Q*-axis inductance.

The inverter power calculation with nominal value of d-axis inductance can be expressed as

$$\begin{aligned} P_{inv}^{L_d^{nom}} &= \frac{3}{2}R_s\left(i_d^2 + i_q^2\right) + \left(L_d^{nom} i_d \frac{di_d}{dt} + L_q i_q \frac{di_q}{dt}\right) \\ &+ \omega_e\left[\varphi_f i_q + \left(L_d^{nom} - L_q\right) i_d i_q\right] \end{aligned} \tag{2.28}$$

where L_d^{nom} is the nominal value of the *d*-axis inductance. $P_{\text{inv}}^{L_d^{\text{nom}}}$ is the inverter power with nominal value of the *d*-axis inductance.

The difference in power calculation due to *d*-axis inductance mismatch can be expressed as

$$\Delta P_{inv}^{\Delta L_d} = P_{inv} - P_{inv}^{L_{d\_nom}} = \frac{3}{2}\Delta L_d \left(i_d \frac{di_d}{dt} + \omega_e i_d i_q \right) \tag{2.29}$$

where $\Delta L_d = L_d - L_d^{\text{nom}}$ is the difference between the actual and nominal values.

The inverter power calculation with nominal value of *q*-axis inductance can be expressed as

$$P_{inv}^{L_q^{nom}} = \frac{3}{2} R_s \left(i_d^2 + i_q^2 \right) + \left(L_d i_d \frac{di_d}{dt} + L_q^{nom} i_q \frac{di_q}{dt} \right) + \omega_e \left[\varphi_f i_q + \left(L_d - L_q^{nom} \right) i_d i_q \right] \tag{2.30}$$

where L_q^{nom} is the nominal value of *q*-axis inductance. $P_{\text{inv}}^{L_q^{\text{nom}}}$ is the inverter power with the nominal value of *q*-axis inductance.

The difference in power calculation due to *q*-axis inductance mismatch can be expressed as

$$\Delta P_{inv}^{\Delta L_q} = P_{inv} - P_{inv}^{L_{q\_nom}} = \frac{3}{2}\Delta L_q \left(i_q \frac{di_q}{dt} - \omega_e i_d i_q \right) \tag{2.31}$$

where $\Delta L_q = L_q - L_q^{\text{nom}}$ is the difference between the actual value and the nominal value.

In this chapter, due to $i_d = 0$ control strategy and the small value of the *dq*-axis inductance ($L_d^{\text{nom}} = 0.04$ H, $L_q^{\text{nom}} = 0.06$ H), the influence of the *dq*-axis inductance mismatch on the calculated inverter power is almost negligible.

2.5.3 Flux-Linkage

The flux-linkage mismatch can affect the inverter power calculation and the estimation performance of the proposed voltage observer. The inverter power with the nominal value of the flux-linkage can be expressed as

$$P_{inv}^{\varphi_f^{nom}} = \frac{3}{2} R_s \left(i_d^2 + i_q^2 \right) + \left(L_d i_d \frac{di_d}{dt} + L_q i_q \frac{di_q}{dt} \right) + \omega_e \left[\varphi_f^{nom} i_q + \left(L_d - L_q \right) i_d i_q \right] \tag{2.32}$$

where φ_f^{nom} is the nominal value of the flux linkage. $P_{\text{inv}}^{\varphi_f^{\text{nom}}}$ is the inverter power with nominal value of the flux-linkage.

The difference in power calculation due to flux-linkage mismatch can be given by

$$\Delta P_{inv}^{\Delta\varphi_f} = P_{inv} - P_{inv}^{\varphi_{f\_nom}} = \frac{3}{2}\Delta\varphi_f \omega_e i_q \tag{2.33}$$

where $\Delta\varphi_f = \varphi_f - \varphi_f^{\text{nom}}$ is the difference in rotor flux linkage between the actual and nominal values. As shown above, the change in inverter power calculation caused by flux-linkage mismatch is proportional to the motor speed and the q-axis current. The EEMF-based sensorless control mainly works in the high-speed range. Therefore, flux-linkage mismatch has the greatest influence on power calculation error and the performance of the proposed dc-link voltage observer.

2.6 Experimental Results

In this section, the estimation and control performance of the EEMF-based sensorless control method accounting for dc-link voltage measurement error is verified. The effectiveness of the proposed back-EMF harmonic suppression method on dc-link voltage observer and EEMF-based sensorless control is demonstrated. The parameters of the prototype IPMSM are shown in Table 2.1. For specific details regarding the experimental platform, please refer to Appendix 1. The prototype IPMSM is controlled by FOC based on dS1006 dSPACE, and the load machine is a dc machine. The AC power supply with a 200 V peak value is employed.

TABLE 2.1

PARAMETERS OF THE PROTOTYPE IPMSM [CHE99]

Rated voltage (peak)	158V
Rated current (peak)	4.0A
Rated power	0.6 kW
Rated torque	4.0 Nm
Pole pairs	3
Winding resistance per phase	6.0 Ω (20°C)
D-axis inductance	40 mH
Q-axis inductance	60 mH
D-axis inductance	40 mH
Swithcing frequency	10 kHz

Notably, despite that the rated speed of the machine is 1000 r/min and the rated load is 4 Nm, the presence of a small dc-link capacitor has significantly reduced the operational speed and load capacity, even with the dc-link voltage approaching the machine rated voltage. Also, it is worth mentioning that the turnaround time of the traditional control algorithm is around 12 μs in the experiments with a dSPACE. The utilisation of the proposed observer has minor computational burden, and turnaround time is only increased by 0.65 μs to 12.65 μs.

2.6.1 Effect of DC-link Voltage Fluctuation on EEMF

The measured result of the estimated position error caused by the dc-link voltage fluctuation is shown in Fig. 2.7. The dc-link voltage exhibits a peak-to-peak ripple of about 95 V. Considerable harmonics exist in estimated back-EMFs, causing the estimated position error to fluctuate from -5 degs to 5 degs and the performance of EEMF-based sensorless control becomes worse.

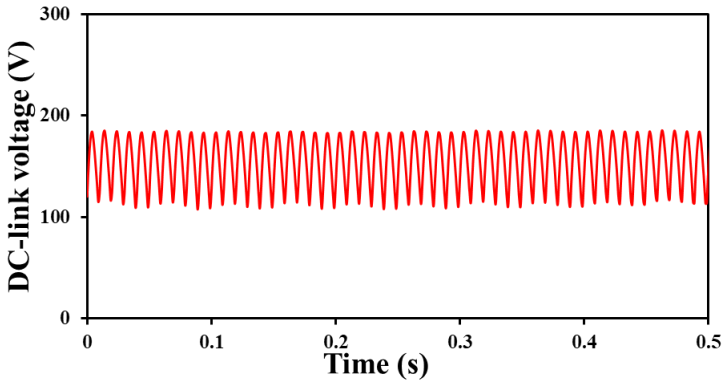

(a) dc-link voltage

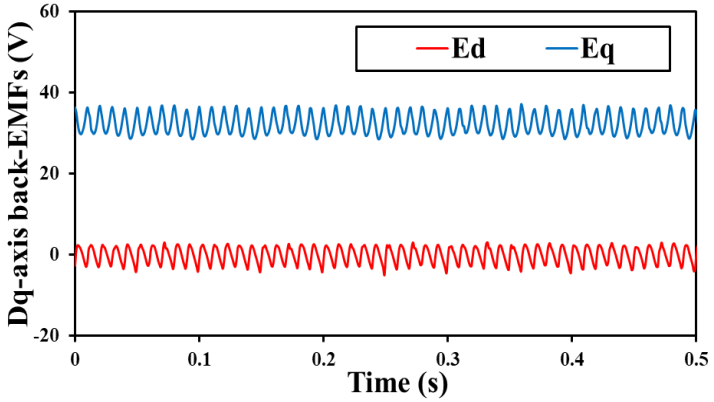

(b) Back-EMFs

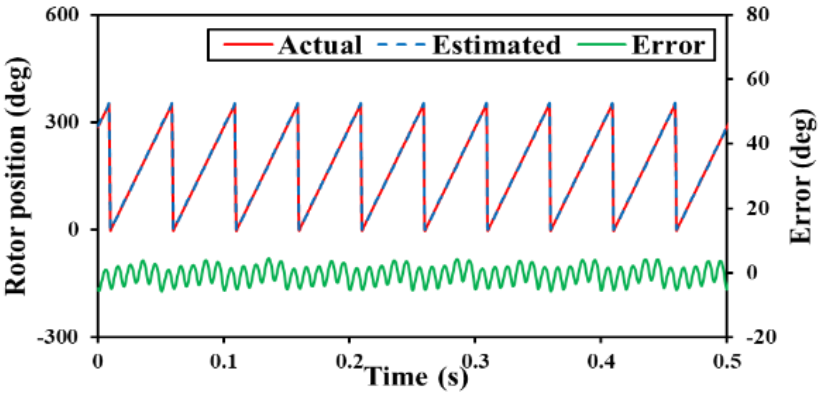

(c) Position and estimated error

Fig. 2.7. Measured results of EEMF-based with fluctuating dc-link voltage. (a) dc-link voltage. (b) Back-EMFs. (c) Position and estimated error.

2.6.2 Influence of DC-link Voltage Measurement Error

The measured results for the estimated position error, induced by dc-link voltage measurement errors, are shown in Fig. 2.8 and Fig. 2.9. The original peak value of dc-link voltage is set at 200 V, with the motor operating at a speed of 500 r/min under a load of 2 Nm. Initially, it is noted that harmonic distortions exist in the estimated position error, attributable to fluctuations in the dc-link voltage. In Fig. 2.8, the measured dc-link voltage includes a dc offset ranging from -20 V to 20 V. Consequently, the estimated position error varies between 12.5 degs and -10.5 degs. Fig. 2.9 illustrates the scenario where the measured dc-link voltage is subject to a gain error from -10% to 10%, resulting in a dc offset between -20 V and 20 and the average value of the estimated position error shifting from 11 degs to -10.5 degs. The dc offset in the estimated position error is directly proportional to the dc-link voltage measurement error, which further compromises the control performance of the EEMF-based sensorless control.

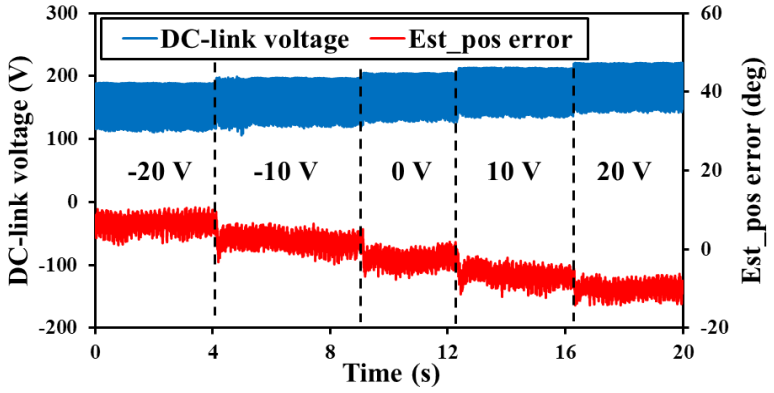

(a) dc-link voltage and estimated rotor position error

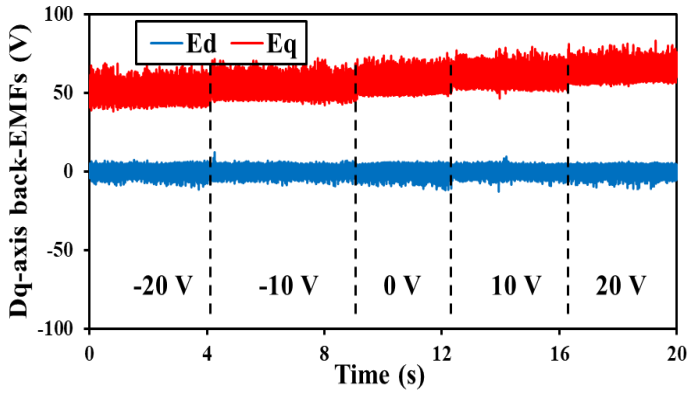

(b) Estimated back-EMFs

Fig. 2.8. Measured results of EEMF with dc-link voltage measurement dc offset. (a) dc-link voltage and estimated rotor position error. (b) Estimated back-EMFs.

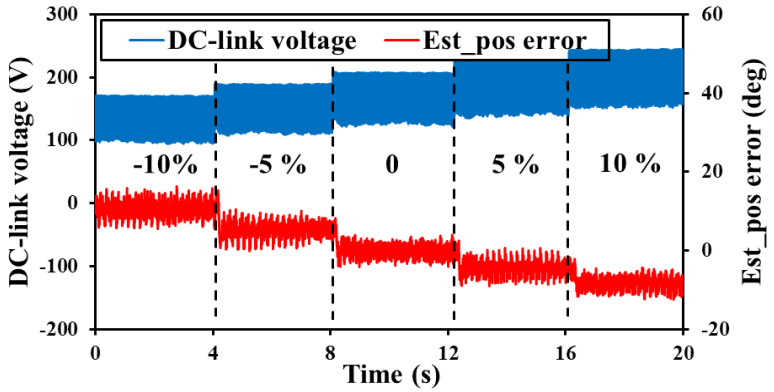

(a) dc-link voltage and estimated rotor position error

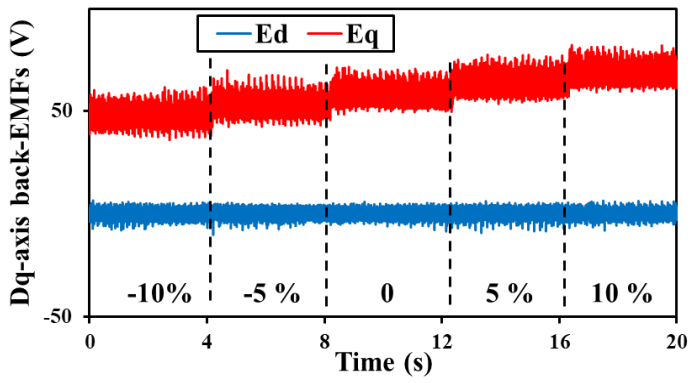

(b) Estimated back-EMFs

Fig. 2.9. Measured results of EEMF with dc-link voltage measurement gain error. (a) dc-link voltage and estimated rotor position error. (b) Estimated back-EMFs.

2.6.3 Proposed DC-link Voltage Observer

Fig. 2.10 to Fig. 2.12 show the measured results of EEMF-based sensorless control under

varying speeds (300, 400, and 500 r/min) with a constant load of 2 Nm, highlighting the transitioning between normal dc-link voltage sensor operation, sensor failure, and subsequent reliance on estimated dc-link voltage. Initially, the inverter power error, calculated using (2.22), serves as an indicator of the dc-link voltage sensor's status. A power error average below -10 signifies sensor faults. Up to 9.4 s, the dc-link voltage sensor functioned correctly. The presence of the small dc-link capacitor introduces system ripples as speed increases, yet the estimated position error sustains a minimal dc offset. After 9.4 s, a -20 V dc offset in the measured dc-link voltage results in an average power error larger than -10, a fault in the dc-link voltage sensor and the introduction of an approximate -10 deg dc offset in the estimated rotor position. The measured results suggest that the variation of speed has a negligible influence on the dc offset in the estimated position error under dc-link voltage measurement error. After 10 s, with the estimated dc-link voltage in use, a severe increase in system harmonics occurs due to coupling issues. However, this change markedly reduces the dc offset in the estimated position error, leading to its average close to zero.

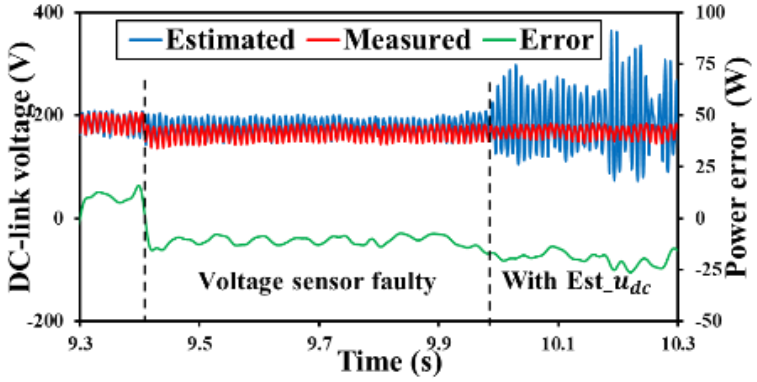

(a) Measured and estimated dc-link voltages and power errors

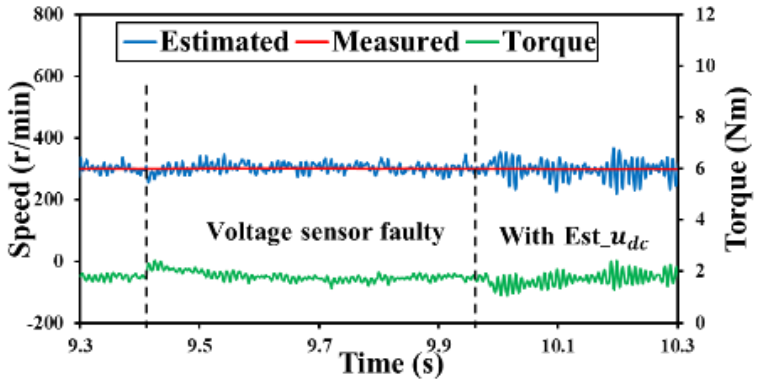

(b) Measured and estimated speeds and torques

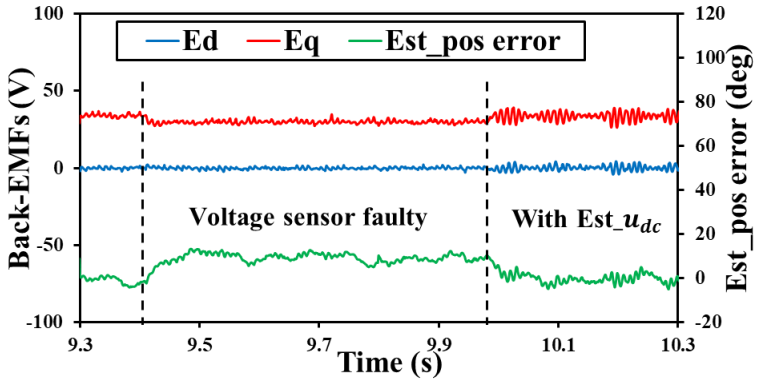

(c) Back-EMFs and estimated rotor position error

Fig. 2.10. Measured results of EEMF-based sensorless control at 300 r/min and under 2 Nm load condition. (a) Measured and estimated dc-link voltages and power errors. (b) Measured and estimated speeds and torques. (c) Back-EMFs and estimated rotor position error.

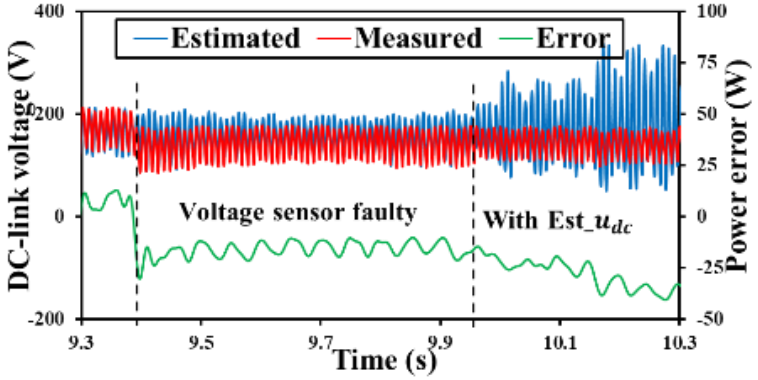

(a) Measured and estimated dc-link voltages and power errors

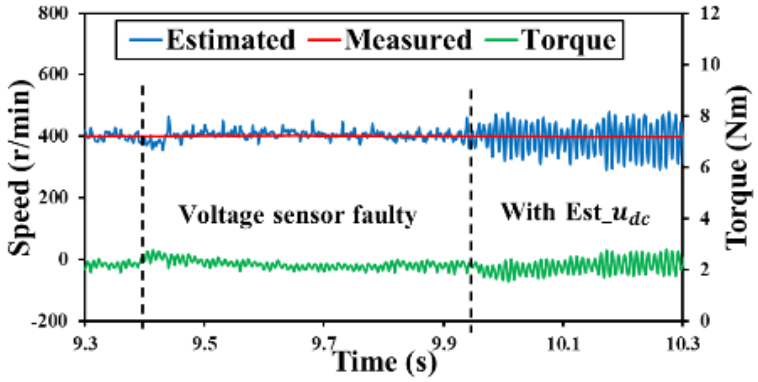

(b) Measured and estimated speeds and torques

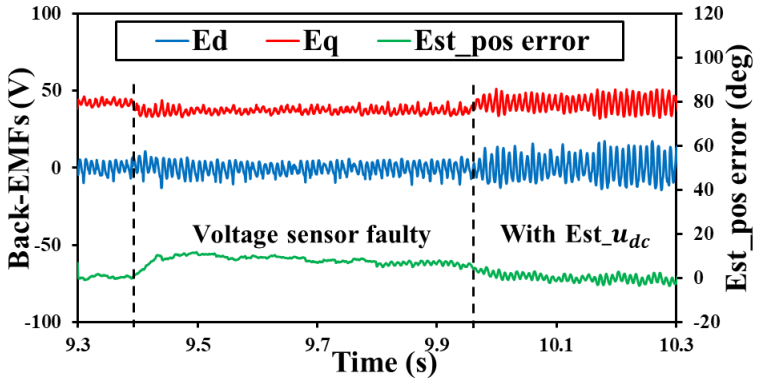

(c) Back-EMFs and estimated rotor position error

Fig. 2.11. Measured results of EEMF-based sensorless control at 400 r/min and under 2 Nm load condition. (a) Measured and estimated dc-link voltages and power errors. (b) Measured and estimated speeds and torques. (c) Back-EMFs and estimated rotor position error.

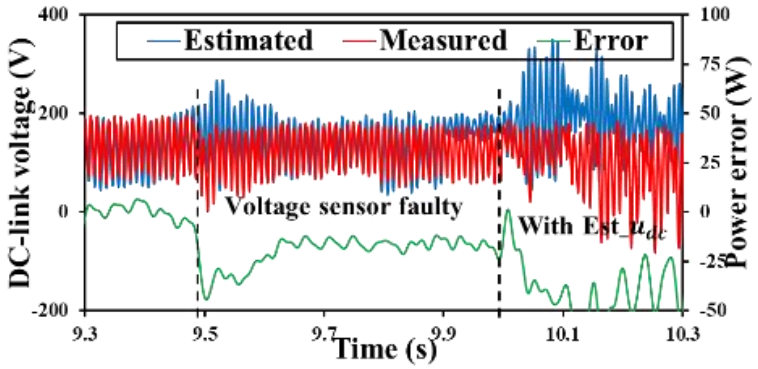

(a) Measured and estimated dc-link voltages and power errors

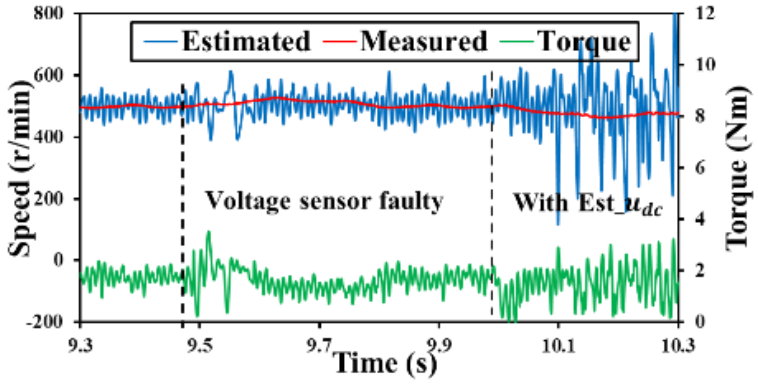

(b) Measured and estimated speeds and torques

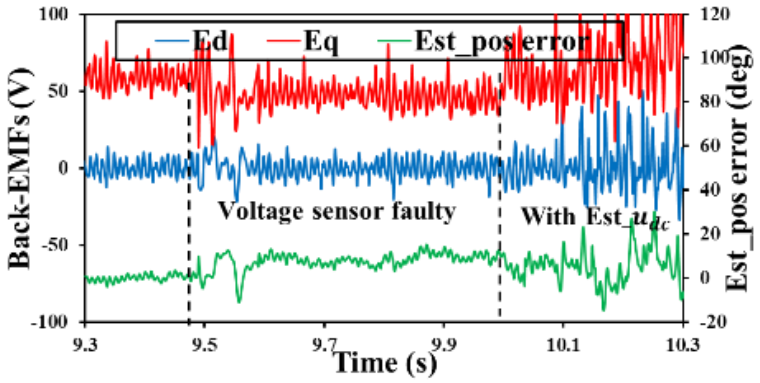

(c) Back-EMFs and estimated rotor position error

Fig. 2.12. Measured results of EEMF-based sensorless control at 500 r/min and under 2 Nm load condition. (a) Measured and estimated dc-link voltages and power errors. (b) Measured and estimated speeds and torques. (c) Back-EMFs and estimated rotor position error.

Fig. 2.13 to Fig. 2.15 illustrate the measured results of EEMF-based sensorless control at 500 r/min and under varying loads (0, 1, and 2 Nm), following the sequence from normal dc-link voltage sensor performance, sensor faults, using estimated dc-link voltage. Before 9.5s, the dc-link voltage observer operates without fault, and the system harmonics are negligible on no-load condition. However, as the load increases, the harmonics in the system increase. After 9.5 s, the measured dc-link voltage exhibits a -20V dc offset, leading to an increase in the estimated rotor position error. After 10 s, with the estimated dc-link voltage in use, the harmonics in the system increase rapidly, but the dc offset of the estimated position error is significantly reduced.

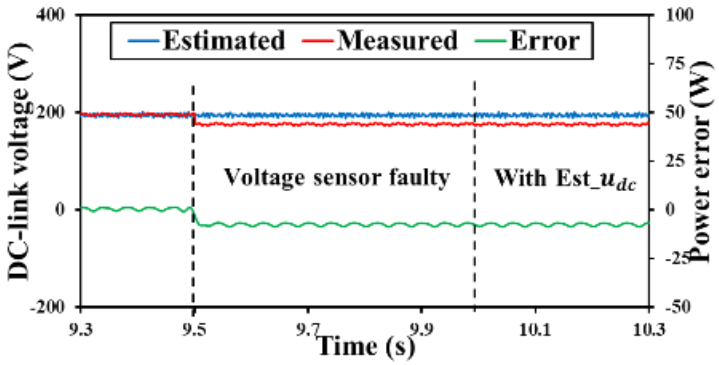

(a) Measured and estimated dc-link voltages and power errors

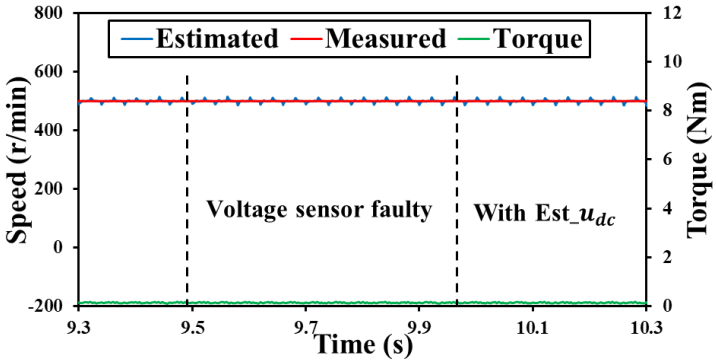

(b) Measured and estimated speeds and torques

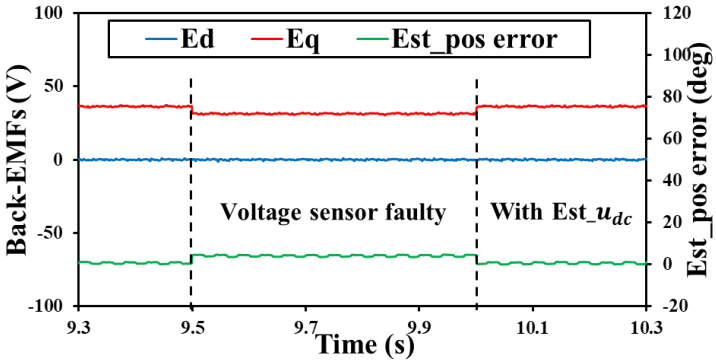

(c) Back-EMFs and estimated rotor position error

Fig. 2.13. Measured results of EEMF-based sensorless control at 500 r/min and under 0 Nm condition. (a) Measured and estimated dc-link voltages and power errors. (b) Measured and estimated speeds and torques. (c) Back-EMFs and estimated rotor position error.

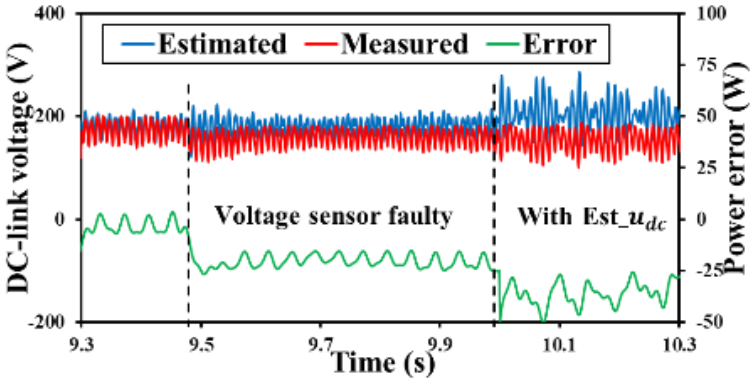

(a) Measured and estimated dc-link voltages and power errors

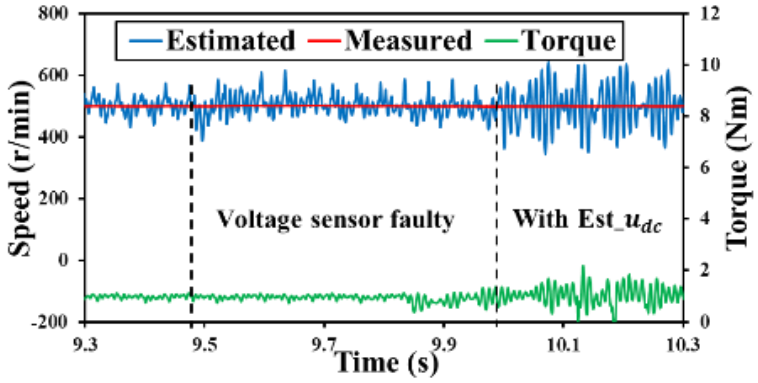

(b) Measured and estimated speeds and torques

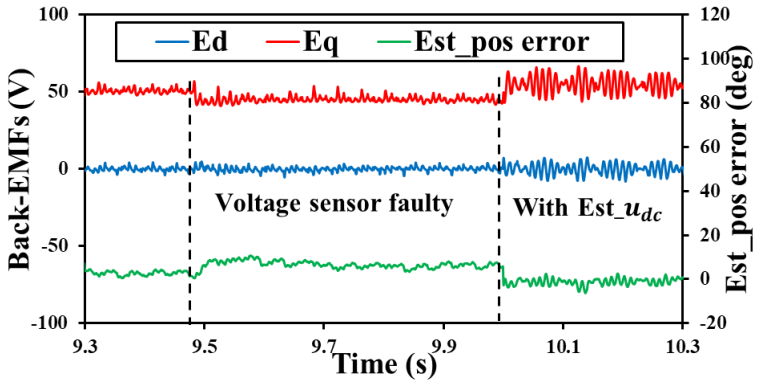

(c) Back-EMFs and estimated rotor position error

Fig. 2.14. Measured results of EEMF-based sensorless control at 500 r/min and under 1 Nm condition. (a) Measured and estimated dc-link voltages and power errors. (b) Measured and estimated speeds and torques. (c) Back-EMFs and estimated rotor position error.

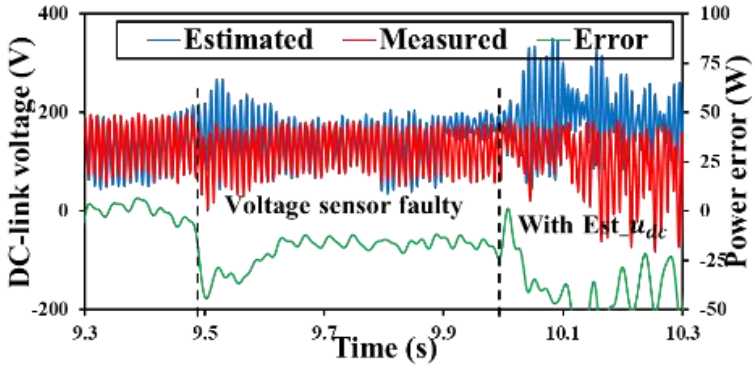

(a) Measured and estimated dc-link voltages and power errors

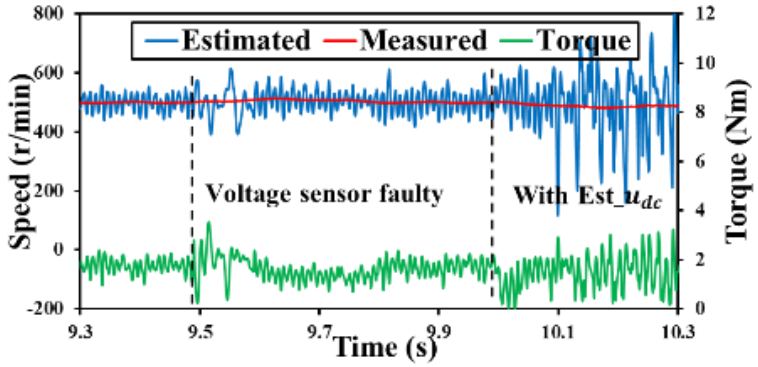

(b) Measured and estimated speeds and torques

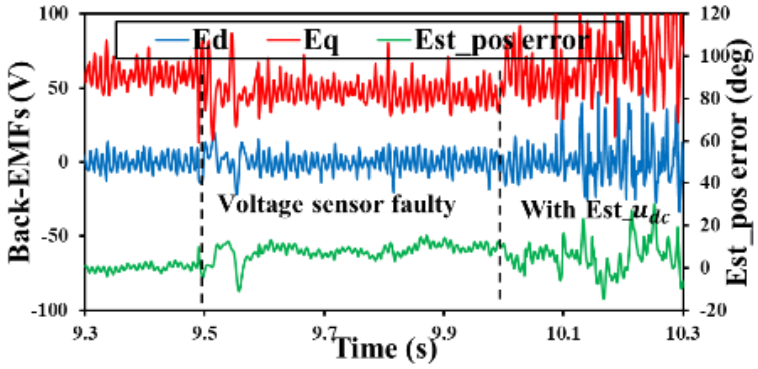

(c) Back-EMFs and estimated rotor position error

Fig. 2.15. Measured results of EEMF-based sensorless control at 500 r/min and under 2 Nm condition. (a) Measured and estimated dc-link voltages and power errors. (b) Measured and estimated speeds and torques. (c) Back-EMFs and estimated rotor position error.

2.6.4 Effect of Proposed Back-EMF Harmonic Suppression Method on DC-link Voltage Observer and EEMF-based Sensorless Control

Fig. 2.16 to Fig. 2.18 show the measured results of EEMF-based sensorless control with estimated dc-link voltage, without and with back-EMF harmonic suppression method under different speeds (300, 400, and 500 r/min) and with a constant load of 2 Nm. Before 15.1 s, significant harmonics exist in the system, and the system becomes unstable at 500 r/min. This instability is attributed to the harmonics induced by the small dc-link capacitor and the coupling issues between the estimated dc-link voltage and speed. After 15.1 s, the back-EMF harmonic suppression strategy is implemented. Substantial decreases in the harmonics of the estimated dc-link voltage, currents, rotor position error and speed can be observed. Particularly when the motor operates at 500 r/min, the harmonics in the estimated dc-link voltage are greatly reduced, with the peak-to-peak value reduced from 220 V to 125 V. The peak-to-peak value of the estimated speed decreased from 600 r/min to 150 r/min, the peak-to-peak value of the estimated

position error decreased from 40 degs to 8 degs, and the torque harmonics peak-to-peak value reduced from 2.2 Nm to 0.25 Nm. It can be concluded that the proposed back-EMF harmonic suppression method greatly improves the effectiveness of EEMF-based sensorless control when the estimated dc-link voltage is utilized.

Fig. 2.19 to Fig. 2.21 show the measured results of EEMF-based sensorless control with estimated dc-link voltage, without and with back-EMF harmonic suppression method at a constant speed of 500 r/min and under varying loads (0, 1, and 2 Nm). Before 15.1 s, notable harmonics existed in the system without the harmonic suppression method. Under no-load conditions, the system exhibits minimal harmonics, validating the effectiveness of the proposed dc-link voltage observer in the system with dc sources or large dc-link capacitor. After 15.1 s, the back-EMF harmonic suppression method is utilized, and the harmonics are considerably reduced across all load conditions. The measured results validate the feasibility of the proposed voltage observer and the effectiveness of the back-EMF harmonic suppression method.

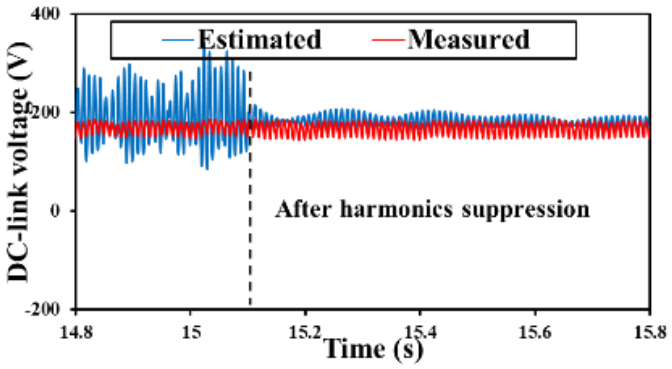

(a) Measured and estimated dc-link voltages

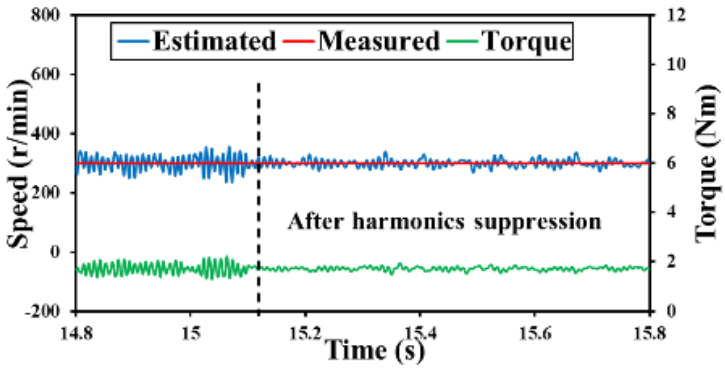

(b) Measured and estimated speeds and torques

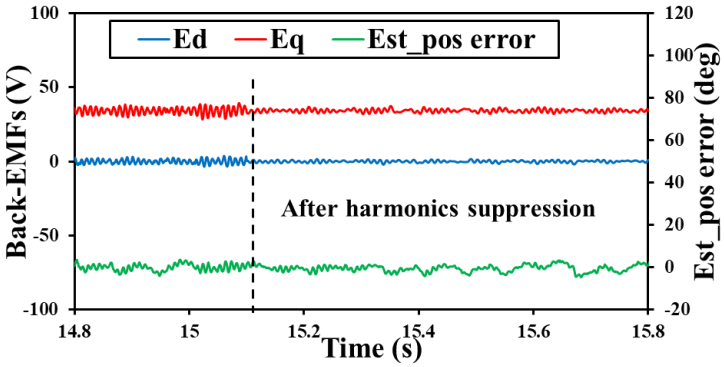

(c) Back-EMFs and estimated rotor position error

Fig. 2.16. Measured results of EEMF-based sensorless control with estimated dc-link voltage, without and with back-EMFs harmonic suppression method at 300 r/min and under 2 Nm condition. (a) Measured and estimated dc-link voltages. (b) Measured and estimated speeds and torques. (c) Back-EMFs and estimated rotor position error.

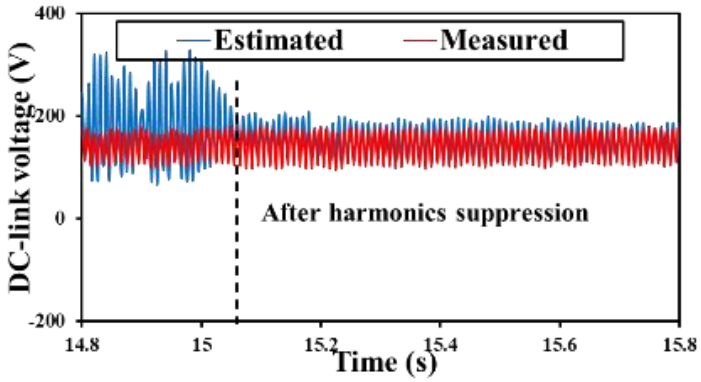

(a) Measured and estimated dc-link voltages

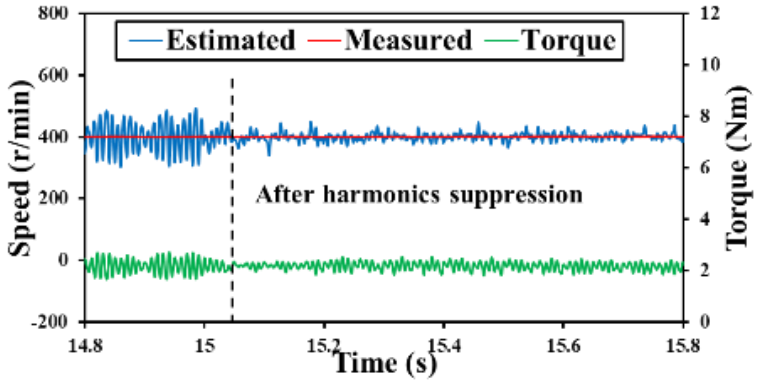

(b) Measured and estimated speeds and torques

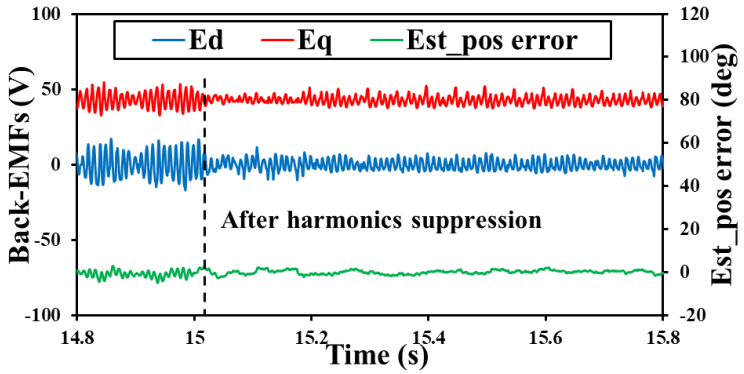

(c) Back-EMFs and estimated rotor position error

Fig. 2.17. Measured results of EEMF-based sensorless control with estimated dc-link voltage without and with back-EMFs harmonic suppression method at 400 r/min and under 2 Nm condition. (a) Measured and estimated dc-link voltages. (b) Measured and estimated speeds and torques. (c) Back-EMFs and estimated rotor position error.

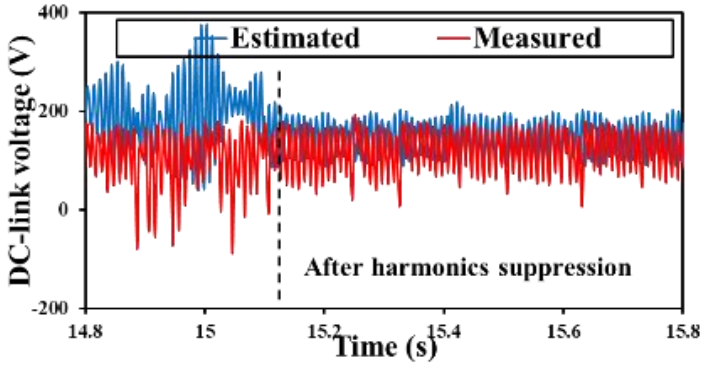

(a) Measured and estimated dc-link voltages

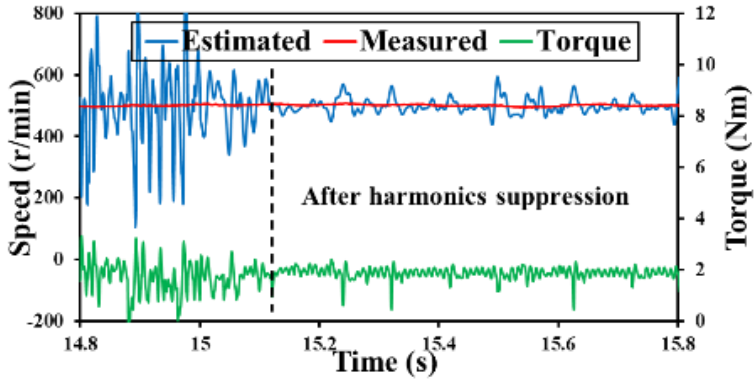

(b) Measured and estimated speeds and torques

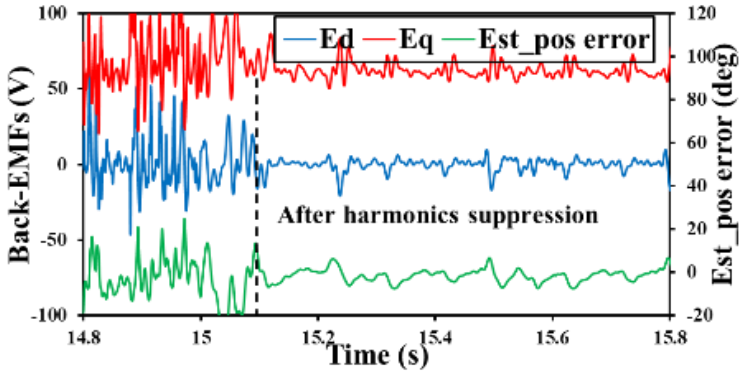

(c) Back-EMFs and estimated rotor position error

Fig. 2.18. Measured results of EEMF-based sensorless control with estimated dc-link voltage without and with back-EMFs harmonic suppression method at 500 r/min and under 2 Nm condition. (a) Measured and estimated dc-link voltages. (b) Measured and estimated speeds and torques. (c) Back-EMFs and estimated rotor position error.

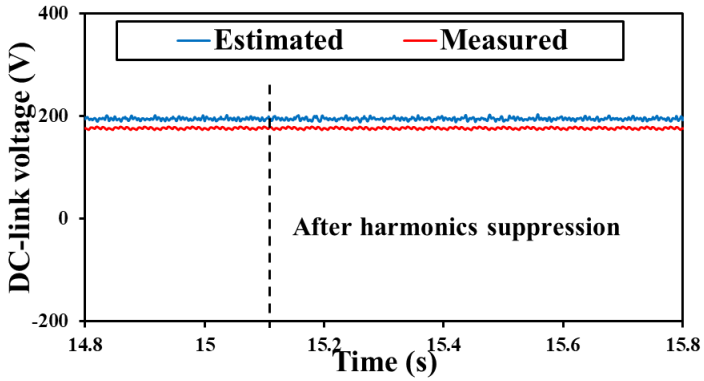

(a) Measured and estimated dc-link voltages

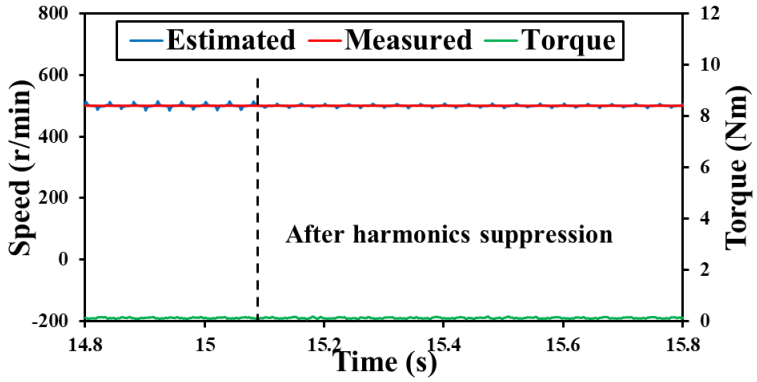

(b) Measured and estimated speeds and torques

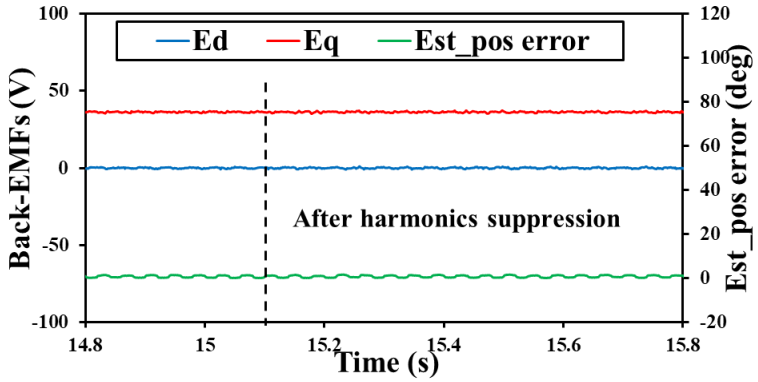

(c) Back-EMFs and estimated rotor position error

Fig. 2.19. Measured results of EEMF-based sensorless control with estimated dc-link voltage, without and with back-EMF harmonic suppression method at 500 r/min and under 0 Nm condition. (a) Measured and estimated dc-link voltages. (b) Measured and estimated speeds and torques. (c) Back-EMFs and estimated rotor position error.

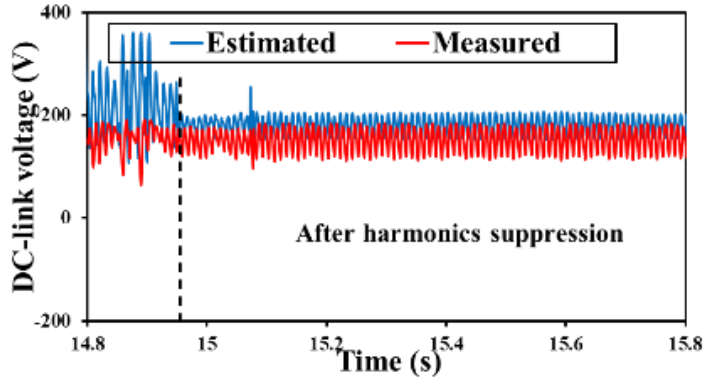

(a) Measured and estimated dc-link voltages

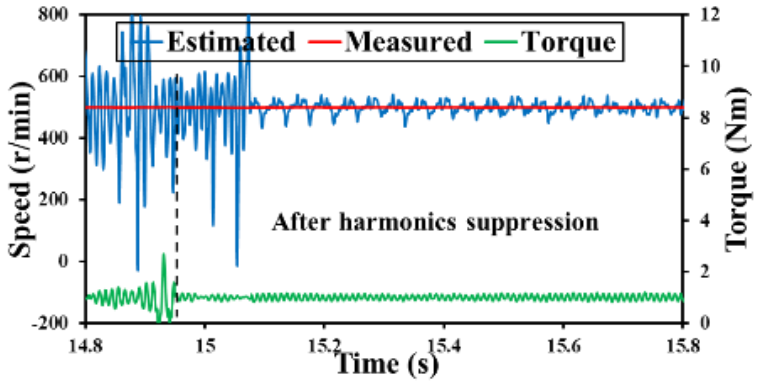

(b) Measured and estimated speeds and torques

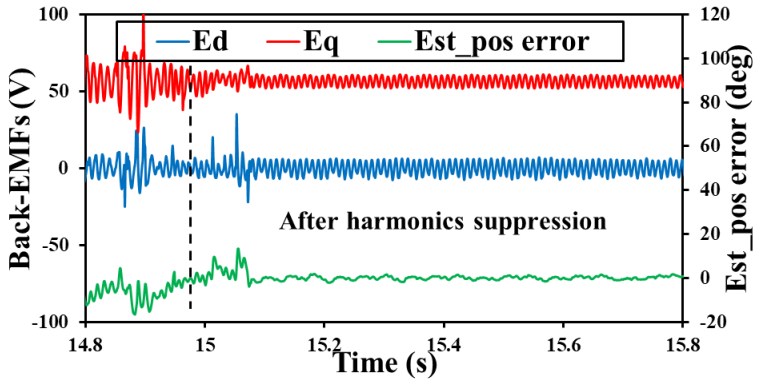

(c) Back-EMFs and estimated rotor position error

Fig. 2.20. Measured results of EEMF-based sensorless control with estimated dc-link voltage without and with back-EMF harmonic suppression method at 500 r/min and under 1 Nm condition. (a) Measured and estimated dc-link voltages. (b) Measured and estimated speeds and torques. (c) Back-EMFs and estimated rotor position error.

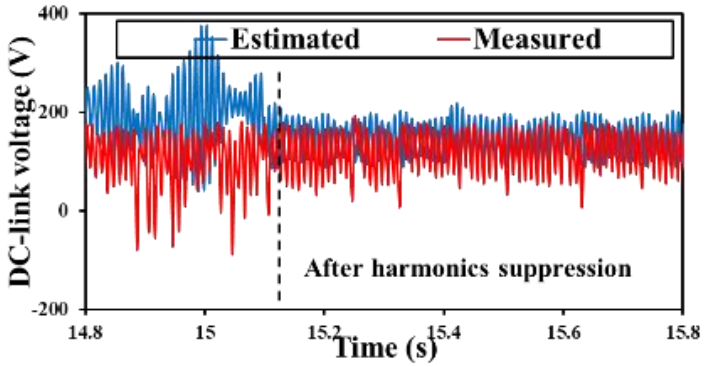

(a) Measured and estimated dc-link voltages

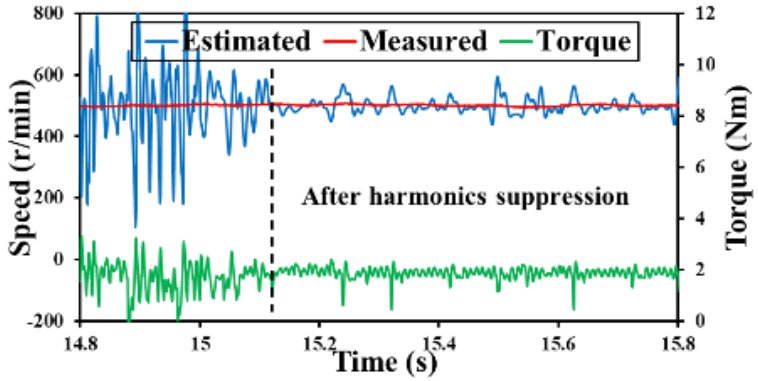

(b) Measured and estimated speeds and torques

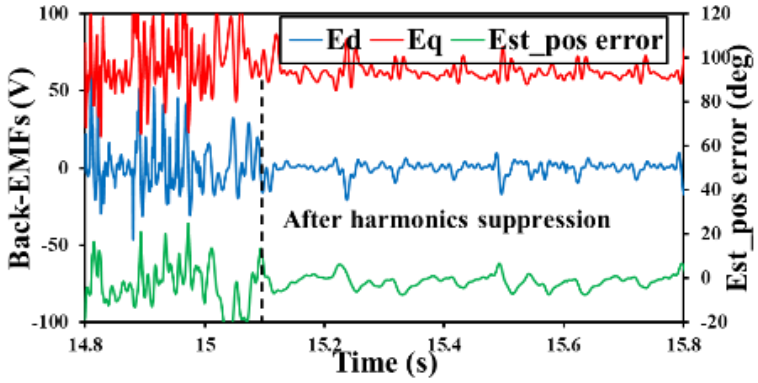

(c) Back-EMFs and estimated rotor position error

Fig. 2.21. Measured results of EEMF-based sensorless control with estimated dc-link voltage without and with back-EMF harmonic suppression method at 500 r/min and under 2 Nm condition. (a) Measured and estimated dc-link voltages. (b) Measured and estimated speeds and torques. (c) Back-EMFs and estimated rotor position error.

2.6.5 Effect of Parameter Mismatches

Fig. 2.22 shows the effect of resistance mismatch on the performance of the proposed voltage observer and EEMF-based sensorless control method under different operating conditions. The degree of resistance mismatch ranges from -20% to +20%. The estimated dc-link voltage error and the estimated rotor position error are so small that they can be considered negligible.

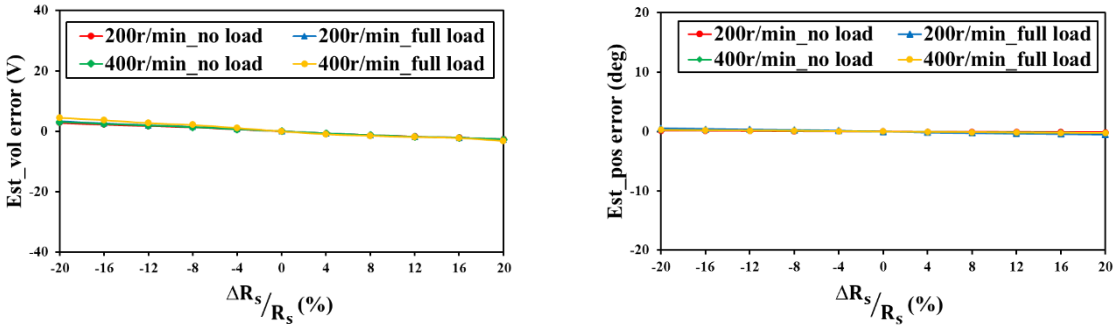

(a)) Estimated dc-link voltage error (b) Estimated rotor position error

Fig. 2.22. Measured results of estimated voltage and position error versus R_s mismatch with different operation conditions. (a) Estimated dc-link voltage error. (b) Estimated position error.

Figs. 2.23 and 2.24 show the influence of *dq*-axis inductances mismatch on the estimated dc-link voltage and position error under different operating conditions. The degree of *dq*-axis inductances mismatch is between ±20%. In Fig. 2.23, the estimated dc-link voltage error is between ± 2.5 V and the estimated position error is between ± 0.25 degs considering the *d*-axis inductance mismatch. In Fig. 2.24, the estimated voltage error is between ± 3 V and the

estimated position error is between ± 4 degs. which are negligible when considering the q-axis inductance mismatch.

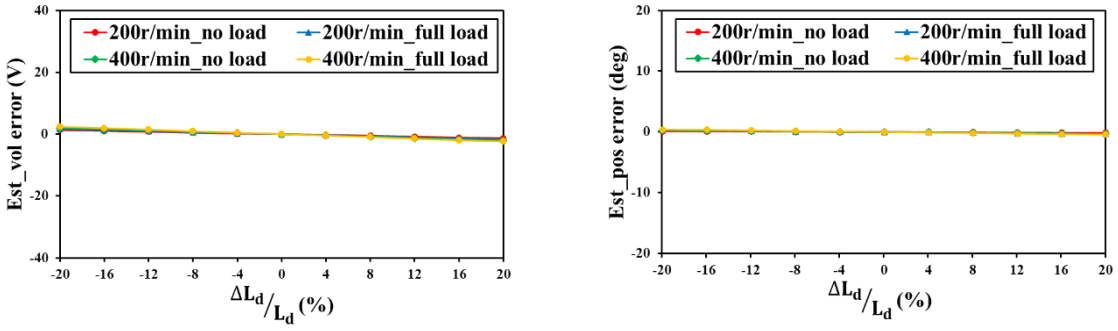

(a)) Estimated dc-link voltage error (b) Estimated rotor position error

Fig. 2.23. Measured estimated voltage and position error versus L_d mismatch with different speed and load conditions. (a) Estimated dc-link voltage error. (b) Estimated position error.

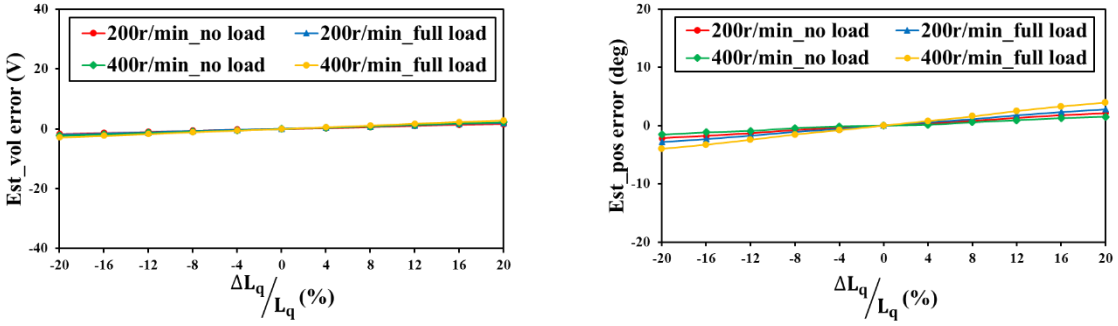

(a)) Estimated dc-link voltage error (b) Estimated rotor position error

Fig. 2.24. Measured estimated voltage and position error versus L_q mismatch with different speed and load conditions. (a) Estimated dc-link voltage error. (b) Estimated position error.

Fig. 2.25 illustrates the influence of flux-linkage mismatch on the estimated dc-link voltage and position errors across various speed and load conditions. The flux-linkage mismatch level is typically less than the resistance and inductance, the flux-linkage mismatch is confined within a ±10% range. According to the measured results, both the estimated dc-link voltage error and the position error exhibit a direct correlation with the extent of flux-linkage mismatch. Within the selected ±10% flux-linkage mismatch range, considering different operation conditions, the estimated voltage error is between ± 13V, and the estimated position error is between ± 6.5 degs, which is acceptable in the sensorless control method.

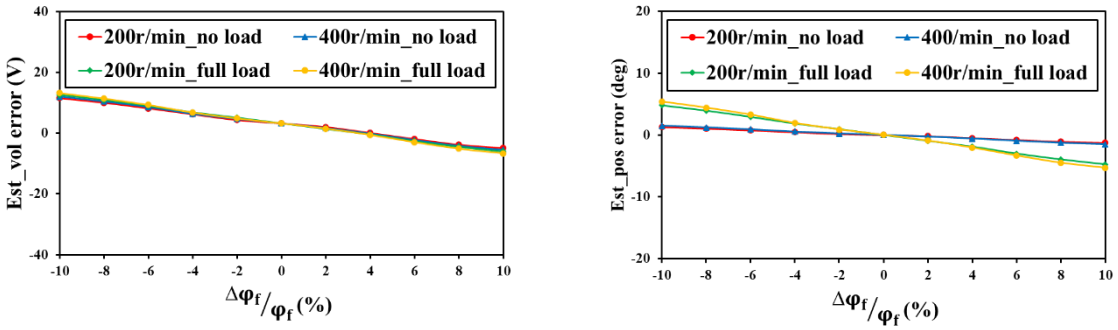

(a)) Estimated dc-link voltage error

(b) Estimated rotor position error

Fig. 2.25. Measured results of estimated dc-link voltage and position error versus φ_f mismatch with different speed and load conditions. (a) Estimated dc-link voltage error. (b) Estimated rotor position error.

2.6.6 Dynamic Performance of Improved EEMF-Based Sensorless Control with Proposed DC-Link Voltage Observer

Figs. 2.26 and Fig. 2.27 show the dynamic control performance of the improved EEMF-based sensorless control with estimated dc-link voltage and back-EMF harmonic suppression method. In Fig. 2.26, the motor speed is increased from 200 r/min to 250 r/min with a load of 1.5 Nm, and the peak-to-peak value of the measured dc-link voltage ripple is increased from 35 V to 60 V. In Fig. 2.27, the load is increased from 0.5 Nm to 1.5 Nm at 300 r/min speed. The peak-to-peak value of dc-link voltage is increased from 35 V to 80 V. From Fig. 2.26 and Fig. 2.27, the proposed dc-link voltage observer shows a good performance in both steady and dynamic states. The EEMF-based sensorless control can also track the actual rotor position well.

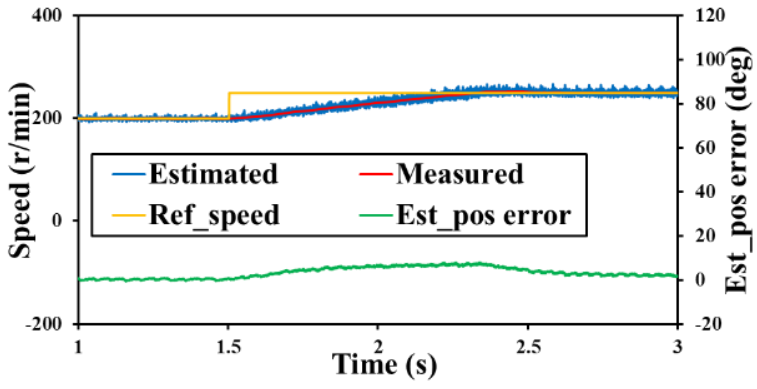

(a) Speed and estimated rotor position error

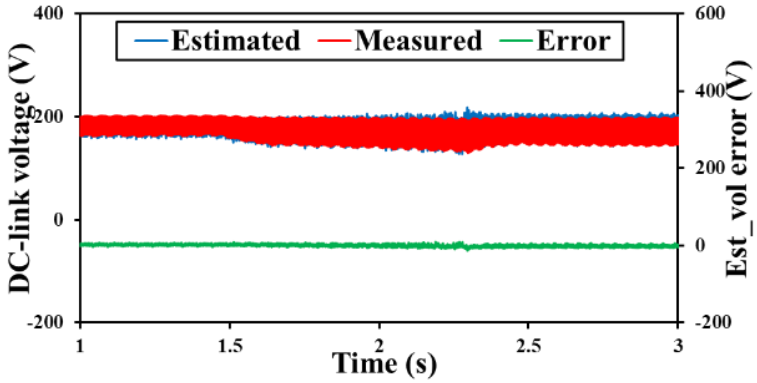

(b) dc-link voltage

Fig. 2.26. Measured results with speed increased from 200 r/min to 250 r/min. (a) Speed and estimated rotor position error. (b) dc-link voltage.

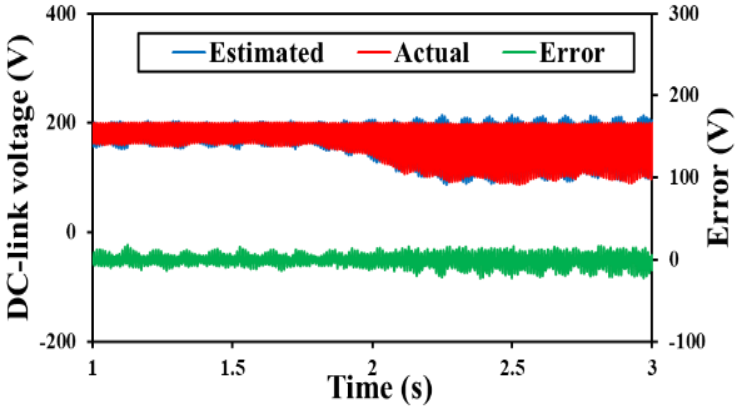

(a) dc-link voltage

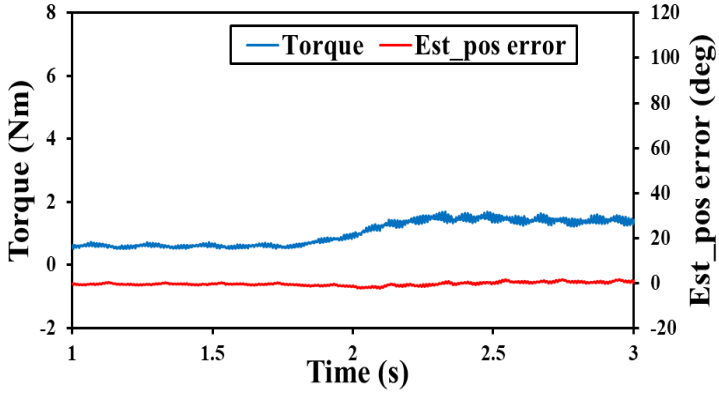

(b) Estimated rotor position error and Torque

Fig. 2.27. Measured results with load increased from 0.5 Nm to 1.5 Nm. (a) dc-link voltage. (c) Estimated rotor position error and Torque.

2.7 Conclusion

This chapter has improved EEMF-based sensorless control for small dc-link capacitor-based

IPMSM drive system. The effect of dc-link voltage fluctuation, together with dc-link voltage sensor faults, especially the dc-link voltage measurement error, on the EEMF-based sensorless control are studied. Theoretical and experimental analyses show that the dc-link voltage fluctuation can introduce the harmonics in the estimated rotor position error, and the dc-link voltage measurement error can cause the dc offset in the estimated rotor position error.

Firstly, this chapter proposed a dc-link voltage observer to estimate the dc-link voltage when the voltage sensor fails. Experimental results demonstrate that the observer can accurately track the dc-link voltage even under dc-link voltage fluctuation. The dc offset in the estimated position error due to the dc-link voltage measurement error was eliminated effectively. It was also demonstrated that the magnetic saturation and parameter mismatch have a minor effect on the proposed observer.

Secondly, a coupling issue was identified in the simultaneous estimation of dc-link voltage and speed, a back-EMF harmonic suppression method has been developed to effectively eliminate the harmonics in the estimated back-EMFs. Experimental results have validated that the back-EMF harmonic suppression method can improve the performance of the proposed dc-link voltage observer and EEMF-based sensorless control.

It is worth mentioning that the proposed dc-link voltage observer can also be used in any variable dc-link voltage drive system, such as EVs. Future work will focus on assessing the effect of current sensor failures and other issues on the performance of the proposed dc-link voltage observer.

CHAPTER 3

OPTIMIZATION OF DC-LINK VOLTAGE OBSERVER FOR SMALL DC-LINK CAPACITOR-BASED IPMSM

In Chapter 2, the proposed dc-link voltage observer and the back-EMF harmonic suppression method effectively mitigate the influence of dc-link voltage sensor faults and the dc-link voltage fluctuation issues. These proposed methods ensure the stability and accuracy of EEMF-based sensorless control in the presence of dc-link voltage sensor faults and dc-link voltage fluctuation. However, practical applications often face additional challenges, such as time delays and power losses, which can degrade the performance of the proposed dc-link voltage observer and the EEMF-based sensorless control method.

To address these issues, this chapter first investigates the influence of these challenges on the proposed dc-link voltage observer. Secondly, a time delay compensation method based on dc-link voltage construction for the estimated dc-link voltage is proposed to eliminate the influence of the time delays. Furthermore, a power compensation method is proposed to mitigate the influence of power losses on the estimated dc-link voltage. These optimizations not only enhance the precision of the proposed dc-link voltage observer but also extend its applicability to more complex and demanding environments. Finally, the accuracy and robustness of the proposed observer, along with the compensation methods, are validated by experiments.

The major part of this chapter is based on the papers published in:

[YAN22C] J. Yan, X. Wu, Z. Q. Zhu, and C. Liu, “A novel dc-link voltage observer with time delay compensation for small dc-link capacitor-based IPMSM with EEMF-based sensorless control,” *in Proc. IEEE 2nd Int. Conf. Sustain. Mobility Appl., Renewables Technol (SMART).*, pp. 1-6, Nov. 2022.

3.1 Introduction

In small dc-link capacitor-based PMSM drive systems, the dc-link voltage fluctuation is inevitable, particularly during high-speed and heavy-load operations. The continuous variation in dc-link voltage requires real-time and accurate acquisition of dc-link voltage information. Therefore, in Chapter 2, a dc-link voltage observer is proposed to eliminate the effect of dc-link voltage sensor faults. However, certain challenges may arise that could affect the performance of the proposed dc-link voltage observer in practical applications. For instance, in scenarios of fluctuating dc-link voltage, system sampling delay and observer delay due to LPF may introduce significant dc-link voltage estimation errors. The power calculation errors due to the extra motor losses and inverter losses may also introduce the dc-link voltage estimation error, which further affects the performance of the EEMF-based sensorless control method. These challenges should be further investigated and mitigated.

A. Time Delay Issues

Time delay issues can seriously affect the dynamic current response and stability of the PMSM drive systems [YAN22C]. In practical applications, these delays mainly origin from sampling, calculation and LPF. These time delays can cause phase lags, which can reduce the accuracy of the sampled signals [BAE03] [COR12] [CHO12] [FIS14] [SEP16] [LU18] [DIN22B] [YAN22D] [GON23] [CHA23] [NIC23] and estimated signals [XU17] [WU17] [ZHA19B] [GON20A] [MAI21] [WU22] [PAI23] [LUO24]. This can lead to poor system dynamic response and potential instability issues, especially during rapid load changes or high-speed operation [YAN22D]. Therefore, these time delay issues must be resolved to ensure the accuracy and stability of the PMSM drive systems.

The instability issues of full-digital regulators in PMSM drive systems caused by sampling and calculation delays are theoretically studied and compensated in [BAE03] [CHO12] [SEP16] [LU18]. In [WU17], the square-wave voltage injection method is used to detect magnetic polarity, canceling the effect of time delay caused by LPF. In [COR12] [FIS14] [JIN19] [GON23], the effects of sampling and calculation delays on the finite control set model predictive control method are analyzed and addressed. In [GON20A], a hyperbolic function-based switching function is implemented to reduce the chattering phenomenon of the sliding-mode observer (SMO) caused by LPFs and a current pre-compensation scheme based on a dual-sampling strategy in one switching period is proposed to solve the problem of calculation

delay caused by digital computation. In [XU17] [ZHA19B] [MAI21] [WU22], the influence of time delay issues caused by LPF and sampling process on HFSI-based sensorless control method is investigated, and corresponding methods are proposed to mitigate those effects. In [DIN22B], a beat phenomenon between the stator current harmonics caused by the voltage sampling delay and the fundamental current is identified and a dc-link voltage reconstruction method is proposed to mitigate this phenomenon. In [LUO24], a nonlinear saturation function is proposed to mitigate the amplitude attenuation and phase delay problems caused by LPF in SMO-based PMSM inter-turn short-circuit fault detection strategy.

B. Power Calculation Error Caused by Extra Motor Losses and Inverter Losses

In practical applications, PMSM drive systems could inevitably exhibit losses [BER01] [ZHU02] [LEE09] [ZHU11A] [HAS12] [NI15] [DIN16] [LAI20], especially motor losses and inverter losses, which can seriously affect the accuracy of power calculations in the proposed dc-link voltage observer. However, an ideal inverter without power losses and neglected motor losses is assumed in Chapter 2, leading to an underestimation of the actual power losses. Accurate power calculation, which considers all forms of system losses, is essential for the proposed dc-link voltage observer to function properly and provide accurate and reliable voltage estimations. Therefore, this Chapter considers the realistic losses and implements a power compensation strategy to improve the accuracy of the proposed dc-link voltage observer and enhance the control performance of the EEMF-based sensorless control method.

This chapter extends the analysis of the influencing factors on the proposed dc-link voltage observer described in Chapter 2 by considering practical factors such as time delays and system losses, and further optimizes the proposed dc-link voltage observer. In Section 3, the influence of time delays on the estimated dc-link voltage and estimated position error is examined, and a delay compensation method is proposed to mitigate these effects. In Section 4, the power calculation errors caused by system losses and their effect on the estimated dc-link voltage and estimated position error are investigated, with a compensation strategy introduced to correct these estimation errors. Section 5 presents experimental results demonstrating the accuracy and robustness of the optimized dc-link voltage observer, while Section 6 concludes this chapter by summarizing the findings and improvements.

3.2 Proposed DC-Link Voltage Observer

As described in Chapter 2, assuming an ideal inverter with no power losses, the power balance equation for the inverter can be expressed as

$$P_{inv}^{cal} = \frac{3}{2}\left(u_d i_d + u_q i_q\right) = u_{dc} i_{dc} \tag{3.1}$$

The dc-link current can be calculated by

$$i_{dc} = i_a s_1 + i_b s_2 + i_c s_3 \tag{3.2}$$

Then, the actual inverter power can be expressed by

$$P_{inv}^{cal} = \frac{3}{2}\left\{R_s\left(i_d^2 + i_q^2\right) + \left(L_d i_d \frac{di_d}{dt} + L_q i_q \frac{di_q}{dt}\right) + \omega_e\left[\varphi_f i_q + \left(L_d - L_q\right) i_d i_q\right]\right\} \tag{3.3}$$

In the proposed dc-link voltage observer outlined in Chapter 2, and as shown in Fig. 3.1, an LPF is used to remove the high-frequency harmonics generated by the differential process described in (3.3). However, the LPF introduces delays in the estimated dc-link voltage that can adversely affect the accuracy, dynamic response, and stability of the proposed dc-link voltage observer.

Moreover, the proposed observer does not fully account for system losses. According to (3.3), the observer only considers the copper losses due to the fundamental current components. It neglects the additional losses introduced by current harmonics, which result from inverter nonlinearity and dc-link voltage fluctuations. These harmonics introduce torque ripples and additional power losses that are not considered in Chapter 2. Furthermore, the observer does not account for iron losses (including hysteresis and eddy current losses) and stray losses. Thus, the observer underestimates the actual power dissipation in the system, leading to less accurate dc-link voltage and position estimations. To improve the accuracy and robustness of the dc-link voltage observer, it is essential to consider these practical factors and implement a comprehensive loss model that includes copper losses, iron losses, and stray losses. The corresponding compensation strategies for the system delays and losses is needed to further enhance the performance of the proposed observer.

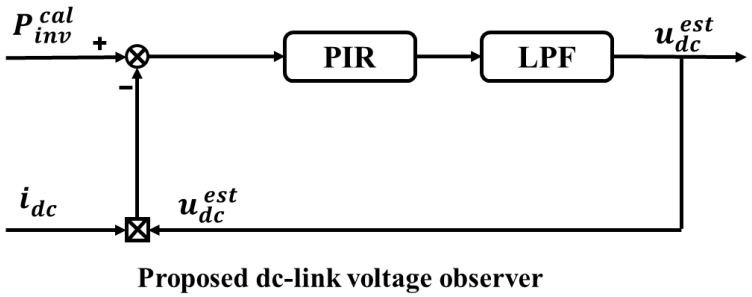

Fig. 3.1. Block diagram of the proposed dc-link voltage observer in Chapter 2.

3.3 Effect of Time Delays on Estimated DC-Link Voltage and Compensation Method

3.3.1 Effect of Observation Delay

As mentioned above, the LPF delay introduces the phase difference between the actual and estimated dc-link voltage, which produces a large periodic estimation error. When the estimated dc-link voltage is used as the input of SVPWM, the periodic estimation error could introduce *dq*-axis voltages and currents harmonics which can eventually degrade the control performance of EEMF-based sensorless control method.

Assuming that the delayed time caused by LPF is t_{LPF}, the estimated dc-link voltage is presented by:

$$u_{dc}^{est} = u_{dc,0}^{est} + \sum_{k=1}^{n} u_{dc,k}^{est} \, sin[\, 2k\omega_g(t - t_{LPF}) + \varphi_k] \tag{3.4}$$

3.3.2 Effect of Sampling Delay

The conventional SVPWM which is utilized in this research has an approximate sampling delay of 1.5 sampling cycles [BAE03] [DIN22B]. As shown in Fig. 3.2, the typical time sequence involves dc-link voltage sampling, control algorithm computation, and PWM output. At the nth sampling time nT_s, dc-link voltage is sampled. The calculation of the control algorithm is executed between nT_s and (n+1)T_s. After a delay of one sampling period, the PWM is updated and output between (n+1)T_s and (n+2)T_s. When following this time sequence, there is an inherent 0.5T_s delay in the PWM output. Consequently, the cumulative delay in the dc-link voltage, which includes both the calculation delay and PWM output delay, will be 1.5T_s. Therefore, the sampling delay will cause a 1.5T_s delay in the measured and actual dc-link

voltage, which may lead to harmonic error. This error can affect the control performance of EEMF.

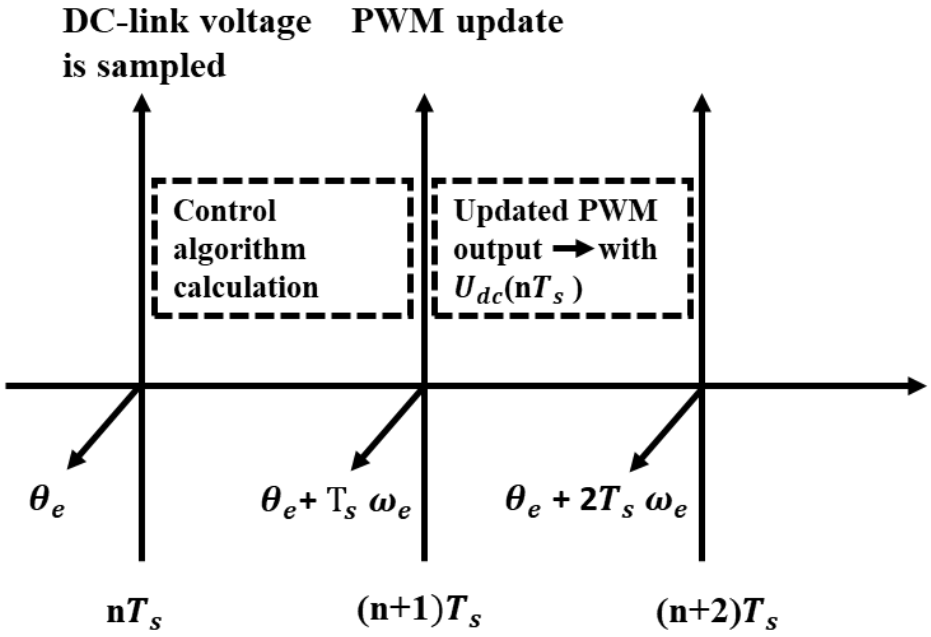

Fig. 3.2. Time sequence of sampling, calculation, and PWM output.

Considering the sampling delay and LPF delay, the estimated voltage can be expressed as:

$$u_{dc}^{est} = u_{dc,0}^{est} + \sum_{k=1}^{n} u_{dc,k}^{est}\, sin[\,2k\omega_g(t - t_d - t_{\frac{3}{2}T_s}) + \varphi_k] \tag{3.5}$$

Fig. 3.3 compares the proposed dc-link voltage observer using LPFs with different cutoff frequencies. In the left side, the LPF cutoff frequency is set to 300 Hz, while on the right side with a cutoff frequency of 600 Hz. When the cutoff frequency is 300 Hz, the estimated dc-link voltage waveform closely matches the measured fluctuating dc-link voltage. However, this introduces a significant estimation voltage error harmonic due to the LPF delay, causing notable harmonic errors in the estimated rotor position. Conversely, with a 600 Hz cutoff frequency, the 100 Hz harmonic in the estimated voltage error is reduced greatly, but higher-order harmonic components increase, leading to a decrease in the observer's overall performance.

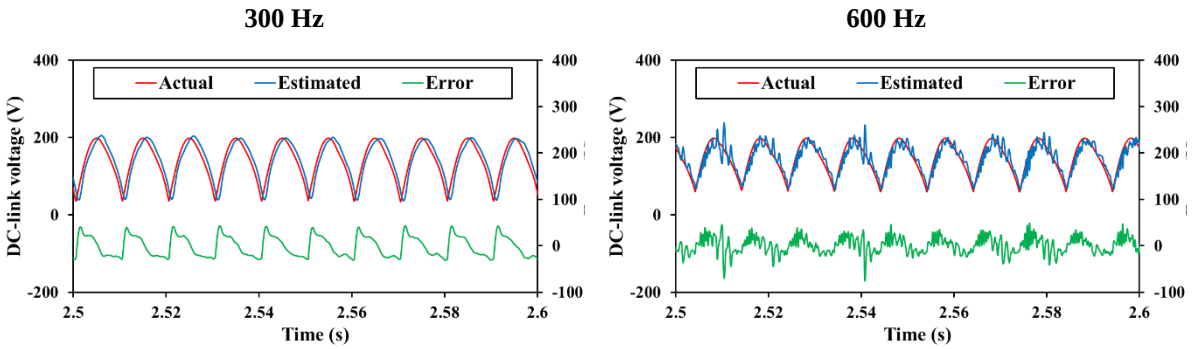

(a) DC-link voltage and estimation error

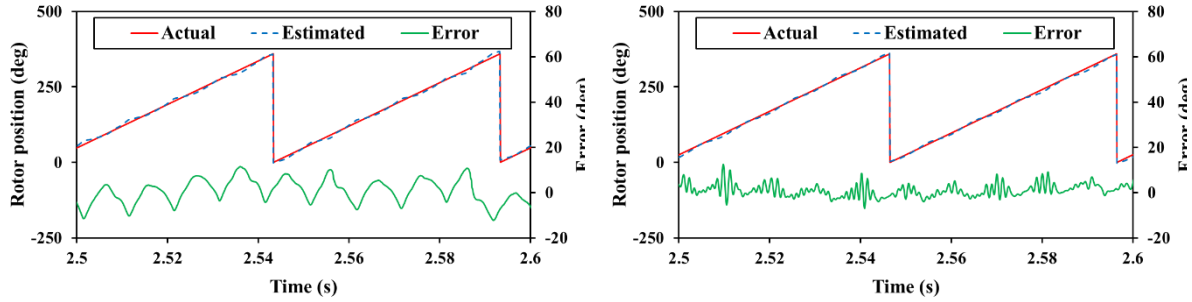

(b) Rotor position and estimation error

Fig. 3.3. Estimation performance of the proposed dc-link voltage observer with different cutoff frequencies of LPF (left column 300 Hz, right column 600 Hz). (a) DC-link voltage and estimation error. (b) Rotor position and estimation error.

3.3.3 Delay Compensation Method

To reduce the influence of time delays, the delay time due to the LPF is calculated first and the estimated dc-link voltage is reconstructed according to its periodicity. The delay time caused by the LPF can be expressed as

$$t_d = \frac{1}{2\pi f_c} \tag{3.6}$$

where f_c is cutoff frequency of the LPF, t_d is the delay time caused by LPF.

If the cutoff frequency of the LPF is 300 Hz, the delay time can be calculated as

$$t_d = \frac{1}{2\pi \cdot 300} = 0.00053\ s \tag{3.7}$$

Therefore, for LPF with a cutoff frequency of 300 Hz, the delay time is approximately 0.00053 s, which corresponds to a delay of 5.3 T_s for the system with a sampling frequency of 10 kHz.

According to the calculated delay time and the periodicity of dc-link voltage, the previous period of fluctuating dc-link voltage can be easily obtained. Fig. 3.4 shows the block diagram of delay compensation method. Firstly, the band pass filter (BPF) is used to obtain 100Hz ac component which is the dominant harmonic of fluctuating dc-link voltage. Then, the 100Hz ac component will be delayed at certain times. The estimated voltage is reconstructed by

$$K_{delay} = \frac{t_d}{T_s} + 1.5 \tag{3.8}$$

$$K_{dc} = \frac{T_{dc}}{T_s} = 100 \tag{3.9}$$

$$u_{dc}^{delay\_comp} = \left(u_{dc}^{est} - u_{dc}^{2\omega_g}\right) + u_{dc}^{2\omega_g} Z^{-(K_{dc}-K_{delay})} \tag{3.10}$$

where K_{delay} is the delayed sampling times, T_s is the sampling time, which is 0.0001 s, $u_{dc}^{delay\_comp}$ is the reconstructed dc-link voltage, K_{dc} is the sampling times in one voltage harmonic period. T_{dc} is the time of one dc-link voltage fluctuation cycle which is 0.01 s, Z represents delay.

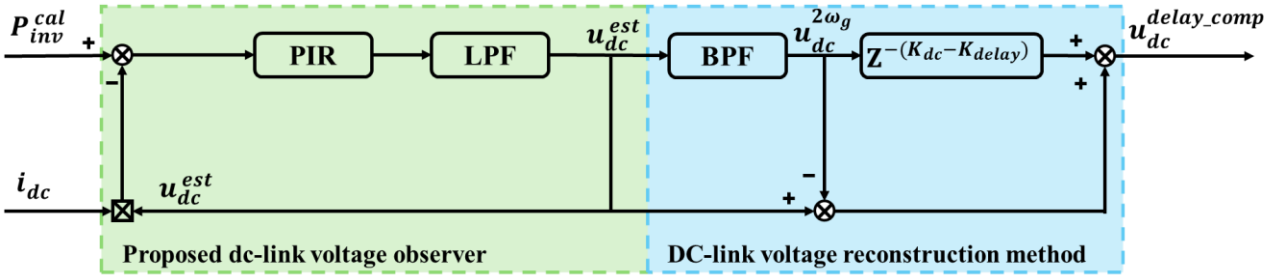

Fig. 3.4. Proposed dc-link voltage observer with delay compensation.

3.4 Effects of System Losses on Estimated DC-Link Voltage and Compensation Method

3.4.1 System Losses

A. Motor Losses

In PMSM drive systems, power losses include both motor losses and inverter losses. Motor losses mainly consist of copper losses, iron losses, and stray losses. Inverter losses primarily include switching losses and conduction losses [BER01] [ZHU02] [LEE09] [ZHU11A] [HAS12] [NI15] [DIN16] [LAI20]. The overall power loss can be expressed by

$$P_{loss} = P_{cu} + P_{ir} + P_{st} + P_{sw} + P_{co} \tag{3.11}$$

Copper losses occur due to the stator windings and are directly proportional to the square of the current flowing through the windings and can be expressed by [LEE09]

$$P_{cu} = 1.5R_s(i_d^2 + i_q^2) \tag{3.12}$$

Iron losses, including hysteresis losses and eddy current losses. The iron losses are frequency-dependent, with higher motor speeds resulting in increased losses. The iron losses can be approximated as [BER01] [ZHU02]

$$P_{ir} = K_h\omega_e\varphi_f^2 + K_e\omega_e^2\varphi_f^2 \tag{3.13}$$

where K_h and K_e are the coefficients of hysteresis loss and eddy current loss, respectively. The hysteresis loss coefficient $K_h = 1.71 \times 10^{-2}$, the eddy current coefficient $K_e = 4.39 \times 10^{-5}$ [CHE99] [ZHU02].

Stray losses are caused by space harmonics and slot harmonics in the winding, as well as additional losses from manufacturing imperfections and leakage flux which can be expressed by [[LEE09]]

$$P_{str} = 1.5C_{str}\omega_e^2(i_d^2 + i_q^2) \tag{3.14}$$

where C_{str} is the stray loss coefficient. Stray loss can be considered as the equivalent copper loss, which has a speed-dependent resistance. The stray loss coefficient $C_{str} = 4.6 * 10^{-7}$ [CHE99].

B. Inverter Losses

The losses in an inverter consist of switching losses and conduction losses. The expression of the switching loss P_{sw} of the IGBTs and the diodes is given by [HAS12]

$$P_{sw} = \frac{f_s}{\pi} \cdot (E_{ON,I} + E_{OFF,I} + E_{OFF,D}) \cdot \frac{u_{dc}}{v_{ref}} \cdot \frac{\sqrt{2}I_n}{I_{ref}} \tag{3.15}$$

where $\sqrt{2}I_n$ is the peak value of fundamental component of the ac line current, v_{ref} and I_{ref} are the reference voltage and current, respectively. $E_{ON,I}$ and $E_{OFF,I}$ are the turn-ON and turn-OFF energy losses of the IGBT, respectively. $E_{OFF,D}$ are the turn-OFF energy losses of the diode due to reverse recovery current.

The conduction losses can be given by [HAS12]

$$P_{co,I} = \sqrt{2}\left(\frac{1}{2\pi} + \frac{1}{8}\alpha cos\varphi\right) v_{ce0} I_n + 2(\frac{1}{8} + \frac{1}{3\pi}\alpha cos\varphi) r_{ce} I_n^2 \tag{3.16}$$

$$P_{co,D} = \sqrt{2}\left(\frac{1}{2\pi} - \frac{1}{8}\alpha cos\varphi\right) v_F I_n + 2(\frac{1}{8} - \frac{1}{3\pi}\alpha cos\varphi) r_F I_n^2 \tag{3.17}$$

where $P_{co,I}$ and $P_{co,D}$ are the conduction loss of inverter and diode, α and φ are the modulation index and the power factor angle, respectively. v_{ce} and r_{ce} are the fixed ON-state voltage drops and the ON-state resistances for IGBT, v_F and r_F are the fixed ON-state voltage drops and the ON-state resistances for diode, respectively. Because there are six IGBTs and diodes in an inverter, the total losses are given by

$$P_{in} = 6(P_{sw} + P_{co,I} + P_{co,D}) \tag{3.18}$$

As discussed above, the inherent power losses in the practical operation could cause the calculated power to be lower than the actual power. This difference leads to a dc offset in the estimated dc-link voltage. Therefore, a power loss compensation method is important for ensuring the accuracy and stability of the proposed dc-link voltage observer which is presented in the next.

3.4.2 Current Harmonics Losses

In addition to DC power losses, the AC power losses caused by dc-link voltage fluctuations and inverter nonlinearity should also be considered, especially in small dc-link capacitor-based PMSM drive system. These losses result in increased copper losses and stray losses. The skin depth δ_{skin} can be obtained by [HE22] [LIA24B]

$$\delta_{skin} = \sqrt{\frac{\rho}{\pi f \mu}} \tag{3.19}$$

where ρ is the resistivity of the conductor, μ is the permeability of the conductor, and f represents the fundamental frequency. In this chapter, the wire diameter is specified as 0.51 mm, which is significantly smaller than the skin depth of 6.52 mm at a rated speed of 1000 r/min. Consequently, the skin effect can be considered negligible.

A. Effects of Inverter Nonlinearity

In the practical application, it is necessary to introduce dead-time intervals to prevent simultaneous triggering of the inverter's switching devices on the same bridge arm. These switching devices exhibit nonlinear characteristics. These nonlinear factors result in distortion of the motor stator voltage, and the presence of high-order harmonics in the currents. Considering the inverter nonlinearity, the three-phase currents in the stationary abc coordinate system can be expressed as [ZHA04] [HWA10]

$$\begin{cases} i_a = i_1 \sin(\omega_e t + \theta_1) + i_5 \sin(-5\omega_e t + \theta_5) + i_7 \sin(7\omega_e t + \theta_7) \\ i_b = i_1 \sin\left(\omega_e t + \theta_1 - \frac{2}{3}\pi\right) + i_5 \sin\left(-5\omega_e t + \theta_5 - \frac{2}{3}\pi\right) + i_7 \sin\left(7\omega_e t + \theta_7 - \frac{2}{3}\pi\right) \\ i_c = i_1 \sin\left(\omega_e t + \theta_1 + \frac{2}{3}\pi\right) + i_5 \sin\left(-5\omega_e t + \theta_5 + \frac{2}{3}\pi\right) + i_7 \sin\left(7\omega_e t + \theta_7 + \frac{2}{3}\pi\right) \end{cases} \quad (3.20)$$

where i_1, i_5, and i_7 are the fundamental, 5th and 7th harmonics.

Then, the *dq*-axis currents can be presented as:

$$\begin{cases} i_d = i_{d,0} + i_5 \cos(-6\omega_e t + \theta_5) + i_7 \cos(6\omega_e t + \theta_7) \\ i_q = i_{q,0} + i_5 \sin(-6\omega_e t + \theta_5) + i_7 \sin(6\omega_e t + \theta_7) \end{cases} \quad (3.21)$$

After simplification:

$$\begin{cases} i_d = i_{d,0} + i_{d,6} \sin(6\omega_e t + \theta_{d,6}) \\ i_q = i_{q,0} + i_{q,6} \sin(6\omega_e t + \theta_{q,6}) \end{cases} \quad (3.22)$$

where $i_{d,0}$, $i_{q,0}$, $i_{d,6}$ and $i_{q,6}$ are the fundamental and 6th harmonics of *dq*-axis currents.

B. Effects of DC-Link Voltage Fluctuation

Due to the use of the small dc-link capacitor, the dc-link voltage has a harmonic which is twice the grid frequency. The voltage margin of the *dq*-axis current controllers can easily be insufficient. In this case, the *dq*-axis currents produce twice the grid frequency harmonic, especially when the motor speed is high or the load is large, the dc-link voltage fluctuation could be very significant. Therefore, it is necessary to consider the large amount of power consumed by dc-link voltage fluctuation. Hence, the *dq*-axis currents i_d and i_q under dc-link voltage fluctuation are presented as

$$\begin{cases} i_d = i_{d,0} + i_{d,1} \sin(2\omega_g t + \theta_{d,1}) \\ i_q = i_{q,0} + i_{q,1} \sin(2\omega_g t + \theta_{q,1}) \end{cases} \quad (3.23)$$

Considering the harmonics introduced by inverter nonlinearity and dc-link voltage fluctuation, the *dq*-axis currents can be expressed as

$$\begin{cases} i_d = i_{d,0} + i_{d,1}\, sin(\,2\omega_g t + \theta_{d,1}) + i_{d,6}\, sin\big(6\omega_e t + \theta_{d,6}\big) \\ i_q = i_{q,0} + i_{q,1}\, sin(\,2\omega_g t + \theta_{q,1}) + i_{q,6}\, sin\big(6\omega_e t + \theta_{q,6}\big) \end{cases} \tag{3.24}$$

Fig. 3.5 shows the measured results when the speed is 100 r/min (corresponding to the base frequency of 5 Hz), the load is 2 Nm, the inverter deadtime is 0.5 μs, and the dc-link voltage amplitude is 100 V. Significant harmonics are generated in the *dq*-axis currents and inverter power due to the inverter nonlinearity and dc-link voltage fluctuation. As shown in Fig. 3.6, the harmonics components include the 6th harmonic (30 Hz) caused by the inverter nonlinearity and twice the grid frequency component (100 Hz). Since these harmonics consume a certain amount of power, the mains power calculated in the observer is smaller than the actual value, resulting in an underestimation of the dc-link voltage, which ultimately leads to a dc offset in the estimated dc-link voltage.

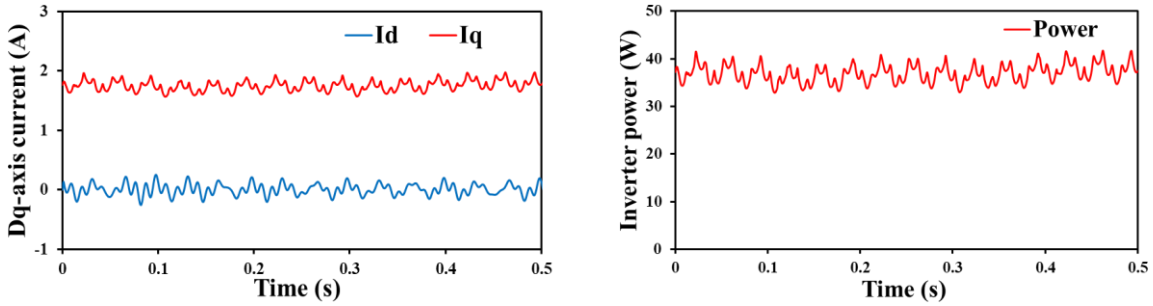

(a) *Dq*-axis currents (b) Inverter power

Fig. 3.5. Measured results when the system with current harmonics. (a) *Dq*-axis currents. (b) Inverter power.

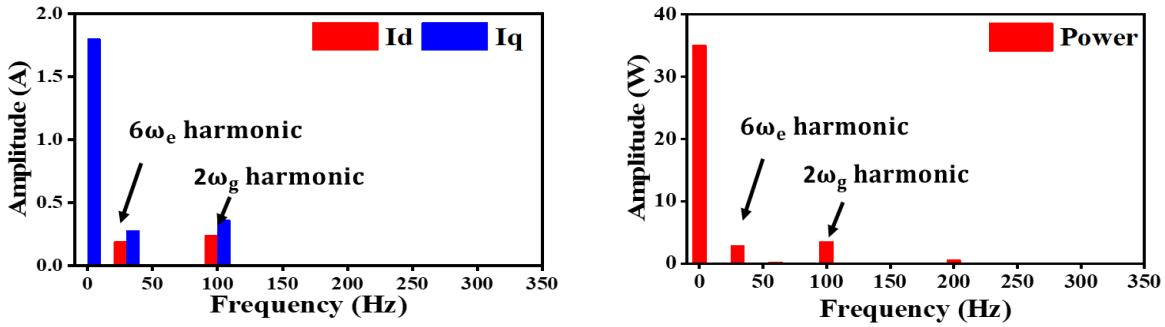

(a) *Dq*-axis currents (b) Inverter power

Fig. 3.6. Spectra of *dq*-axis currents and power with inverter nonlinearity and dc-link voltage fluctuation. (a) *Dq*-axis currents. (b) Inverter power.

3.4.3 Power Losses Compensation Method

As analyzed earlier, the 6th harmonic introduced by the inverter nonlinearity and twice the grid frequency harmonic introduced by dc-link voltage fluctuation will consume additional power. This additional power consumption will cause a dc offset in the calculated inverter power which is the input of the dc-link voltage observer. Then, the dc offset will occur in the estimated dc-link voltage and estimated position error. To solve this problem, this chapter proposes a power losses compensation method. The basic principle of the proposed compensation method is to calculate the power losses and compensate. The block diagram of the overall optimization method is shown in Fig. 3.8.

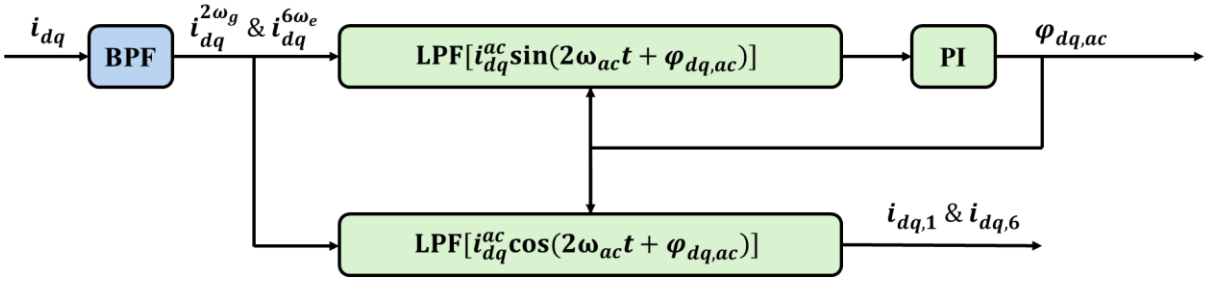

Fig. 3.7. Block diagram of signal processing.

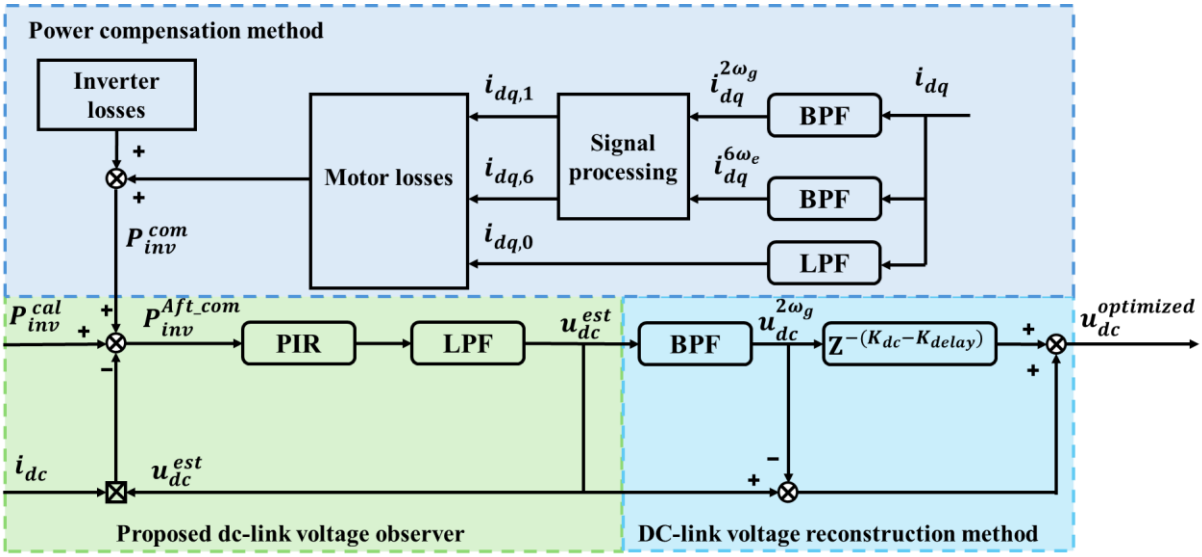

Fig. 3.8. Block diagram of the dc-link voltage observer optimization method.

3.5 Experimental Results

In this section, the estimation and control performance of proposed dc-link voltage observer and the influence of time delays and power losses on the estimated dc-link voltage error and estimated position error is first verified. Then, the effectiveness of delay compensation method and power compensation method are validated.

3.5.1 Effect of Time Delay and Power Loss Issues

Fig. 3.9 shows the influence of time delay and power loss issues on the proposed dc-link voltage observer. The speed is 200 r/min with a load of 1 Nm. In Fig. 3.9(a), the dc-link voltage observer can estimate the fluctuating dc-link voltage. However, the estimated dc-link voltage error contains a large dc offset and considerable harmonic errors. When the estimated dc-link voltage is applied to the system, it introduces the *q*-axis current harmonic as shown in Fig. 3.9(b). The estimated position error also produces significant dc offset and harmonic errors as shown in Fig. 3.9(c). From Fig. 3.10, the estimated dc-link voltage error harmonic (100Hz) generated by the delays is approximately 6.75% of the peak value, and the estimated position error harmonic component is around 3.15 deg; the dc offset in estimated dc-link voltage error caused by the power losses is about 11.5% of the peak value and the dc offset in estimated position error is 5.8 deg. Therefore, it is crucial to propose effective suppression strategies to reduce the estimated dc-link voltage errors and resulting estimated rotor position errors.

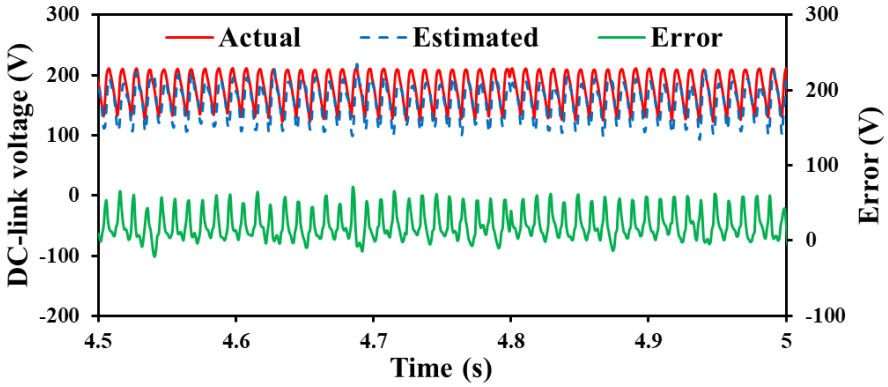

(a) dc-link voltage estimation

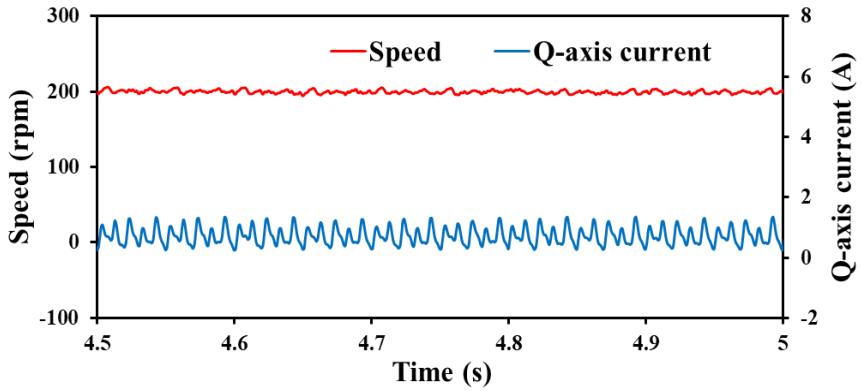

(b) *Q*-axis current and speed

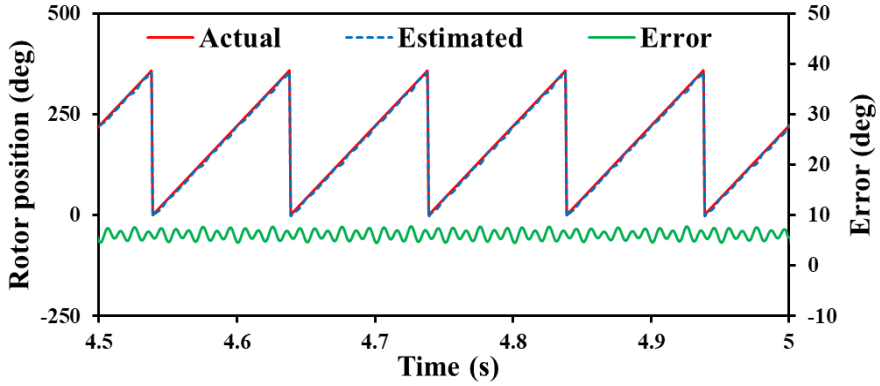

(c) Rotor position estimation

Fig. 3.9. Measured results with dc-link voltage and position sensorless control. (a) dc-link voltage estimation. (b) *Q*-axis current and speed. (c) Rotor position estimation.

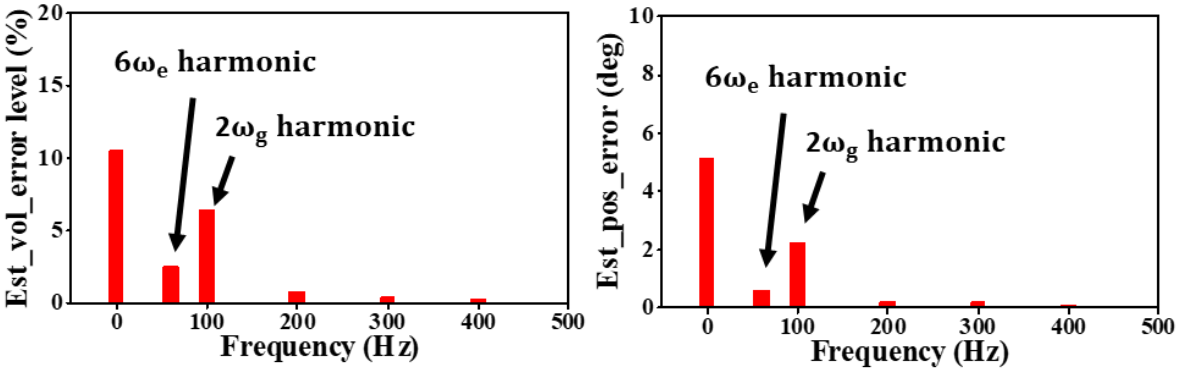

(a) dc-link voltage

(b) Rotor position estimation

Fig. 3.10. Spectra of estimated dc-link voltage error and estimated position error. (a) dc-link voltage estimation. (b) Rotor position estimation.

3.5.2 Time Delay Compensation

Fig. 3.11 shows the effectiveness of delay compensation method in reducing the harmonics in the estimated dc-link voltage error and estimated position error. Before 5s, the estimated dc-link voltage is used in the system, the harmonics in the estimated dc-link voltage error, the *q*-axis current, and the estimated position error are large because of the delay issues. After 5s, the delay compensation method is applied. The ripple of estimated dc-link voltage error peak-to-peak value is reduced from 75 V to 5 V, and the control performance of EEMF-based sensorless control method is also improved. Fig. 3.12 shows the spectra of the estimated dc-link voltage error and the estimated position error before and after applying the delay compensation method. When the delay compensation method is used, the 100Hz harmonic component in estimated dc-link voltage error is reduced from 6.75% to 1.25%, and position error is reduced from 3.15

deg to 0.3 deg. However, the dc offset in estimated dc-link voltage error and the estimated position error are considerable and need to be suppressed in the next section.

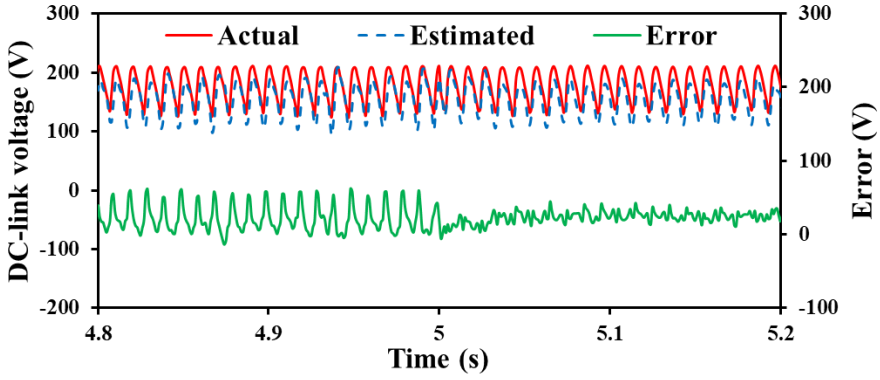

(a) dc-link voltage estimation

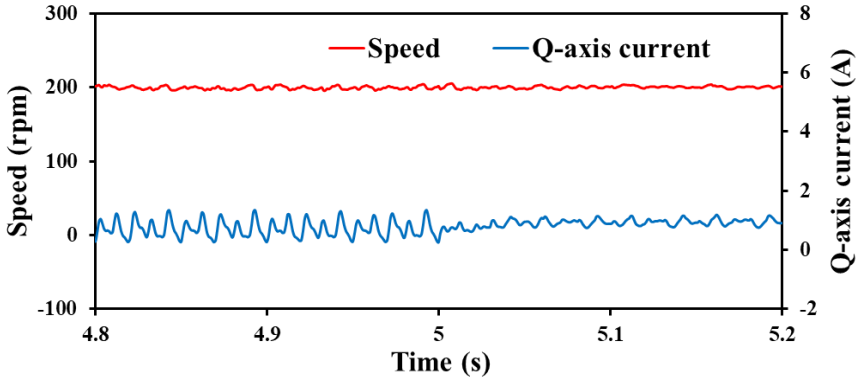

(b) *Q*-axis current and speed

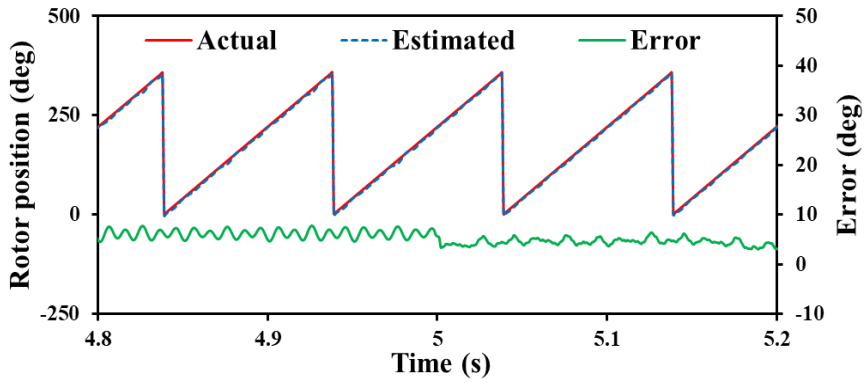

(c) Rotor position estimation

Fig. 3.11. Measured results before and after delay compensation. (a) dc-link voltage estimation. (b) *Q*-axis current and speed. (c) Rotor position estimation.

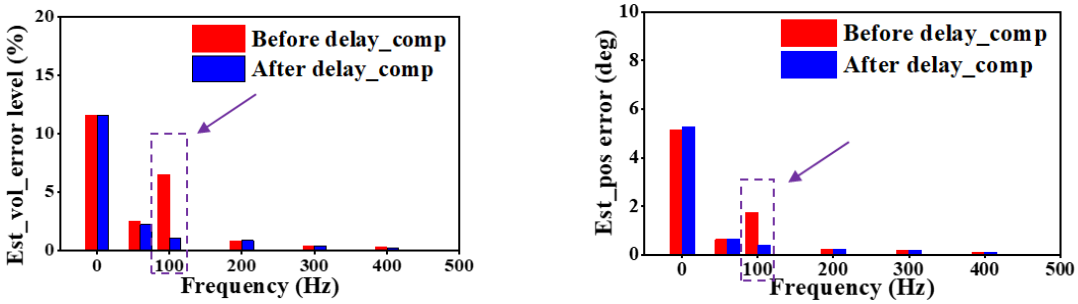

(a) dc-link voltage estimation (b) Rotor position estimation

Fig. 3.12. Spectra of estimated dc-link voltage error and position error before and after delay compensation. (a) dc-link voltage. (b) Rotor position estimation.

3.5.3 Power Losses Compensation

Fig. 3.13 shows the effectiveness of the proposed power compensation strategy in suppressing the dc offset in the estimated dc-link voltage error and the estimated position error. The motor speed is 200 r/min, and the load is 1 Nm. Before 5.05s, the inverter power average value is about 37.5 W, and the power loss is caused by the current harmonics. In this case, the estimated dc-link voltage error has a dc offset of approximately 22 V. The estimated position error also has a dc offset of approximately 5.7 degrees. After 5.05s, the proposed compensation strategy is applied. The average power has increased to 40 W. The dc offset of estimated dc-link voltage error and estimated position error is eliminated. Fig. 3.14 shows the spectra of estimated dc-link voltage error and estimated position error before and after the use of power compensation method. From Fig. 3.14, after applied the power compensation, the dc offset in the estimated dc-link voltage error and the estimated position error are significantly reduced.

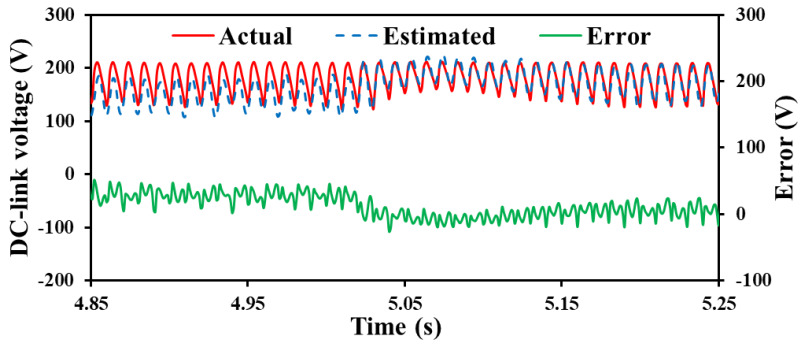

(a) dc-link voltage estimation

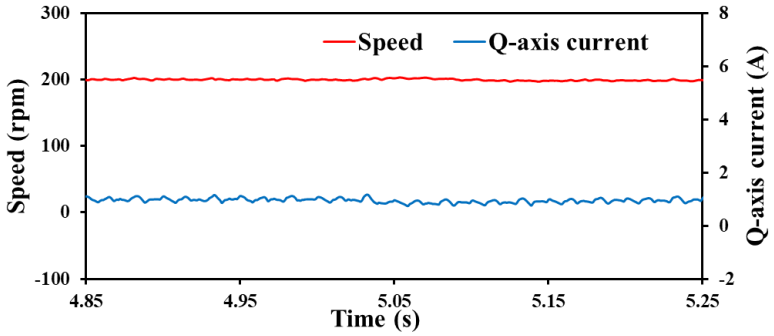

(b) *Q*-axis current and speed

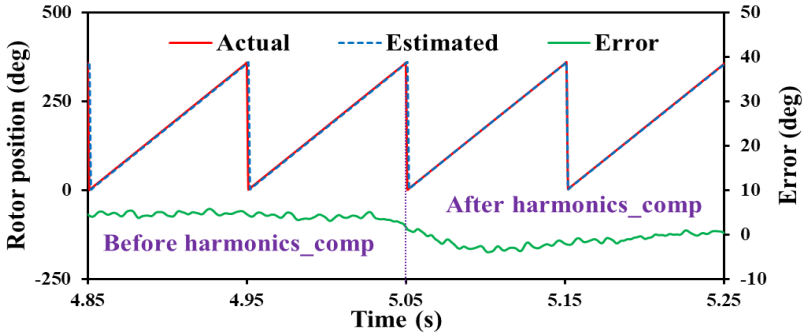

(c) Rotor position estimation

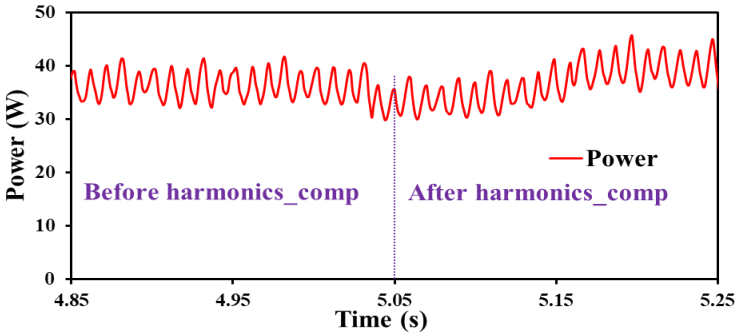

(d) Inverter power

Fig. 3.13. Measured results before and after current harmonic compensation. (a) dc-link voltage estimation. (b) *Q*-axis current and speed. (c) Rotor position estimation. (d) Inverter power.

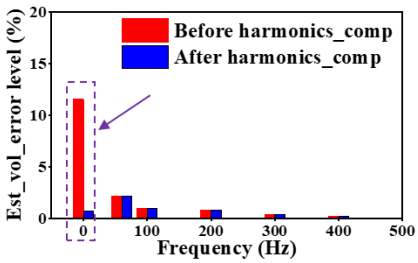

(a) dc-link voltage estimation

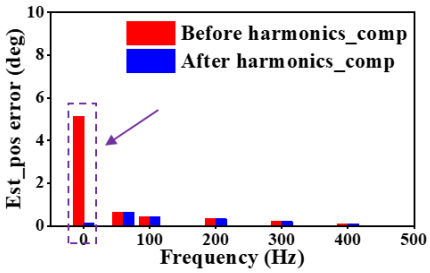

(b) Rotor position estimation

Fig. 3.14. Spectra of estimated dc-link voltage error and position error before and after current harmonic compensation. (a) dc-link voltage. (b) Rotor position estimation.

3.5.4 Dynamic Performance

Fig. 3.15 and Fig. 3.16 show the dynamic performance of the proposed dc-link voltage observer after using the delay compensation and power compensation method. The dc-link voltage amplitude is 200 V. In Fig. 3.15, the load is 0.5 Nm. As the motor speed is increased from 200 r/min to 250 r/min, the peak-to-peak value of the dc-link voltage has risen from 40 V to nearly 65 V. The dc-link voltage observer can not only accurately estimate the static dc-link voltage but also tracks dynamic variation of dc-link voltage. Simultaneously, the precise rotor position can be estimated. In Fig. 3.16, the load increases from 0.5 Nm to 2 Nm, and the peak-to-peak value of dc-link voltage increases from 40 V to 130 V. The dc-link voltage observer can still track the changing dc-link voltage. The estimated rotor position is also accurate. These results have clearly illustrated the accuracy of the proposed dc-link voltage observer.

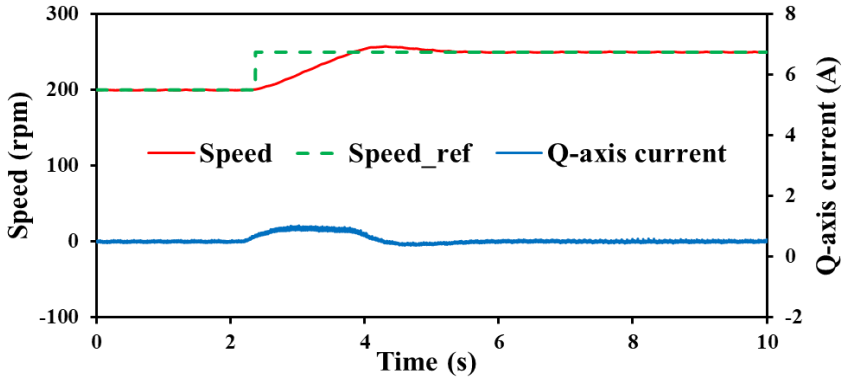

(a) *Q*-axis current and speed

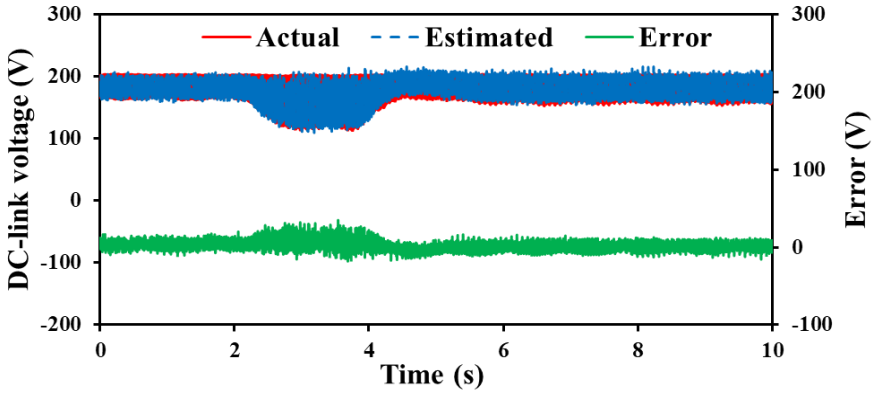

(b) dc-link voltage estimation

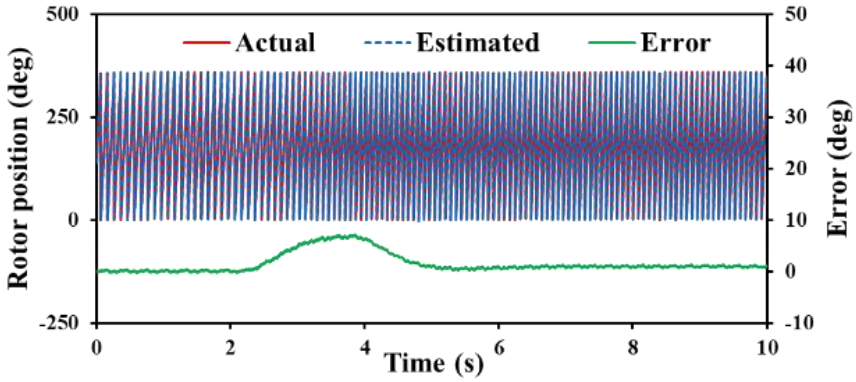

(c) Rotor position estimation

Fig. 3.15. Measured results with speed increased from 200 r/min to 250 r/min. (a) *Q*-axis current and speed. (b) dc-link voltage estimation. (c) Rotor position estimation.

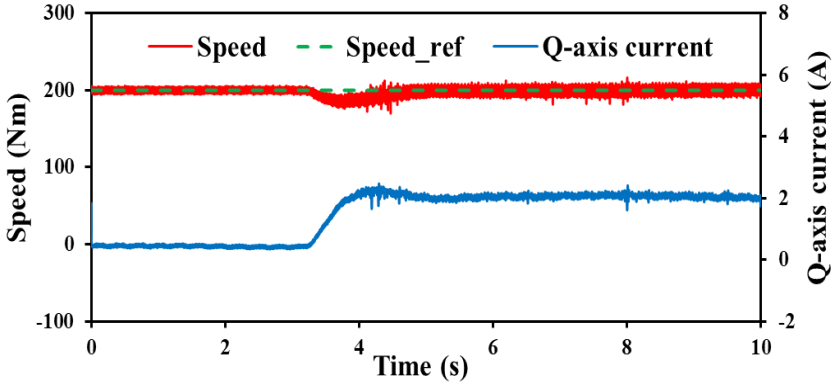

(a) *Q*-axis current and speed

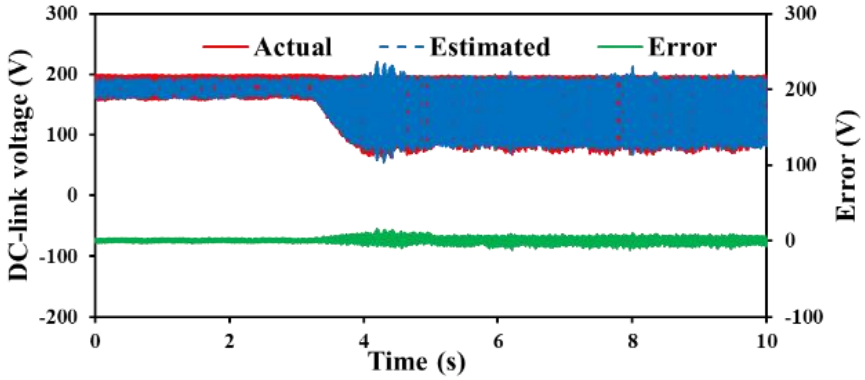

(b) dc-link voltage estimation

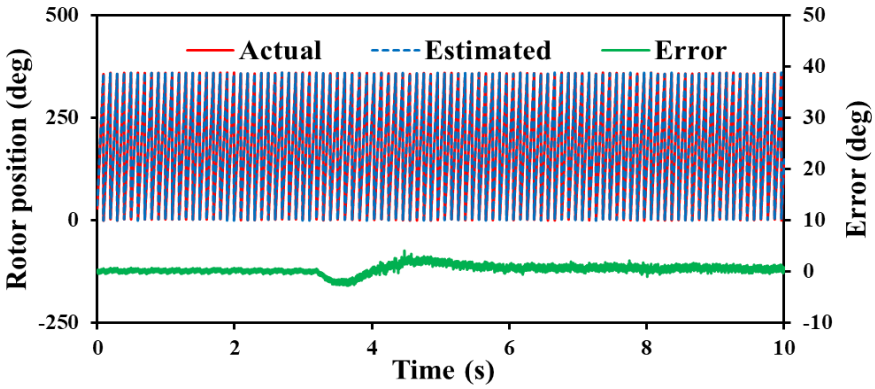

(c) Rotor position estimation

Fig. 3.16. Measured results with load increased from 0.5 Nm to 2 Nm. (a) *Q*-axis current and speed. (b) dc-link voltage estimation. (c) Rotor position estimation.

3.6 Conclusion

To reduce the cost and increase the reliability of EEMF-based sensorless control method in small dc-link capacitor-based PMSM drive systems. An improved dc-link voltage observer is proposed by utilizing a PIR-type observer to estimate the fluctuating dc-link voltage. In addition, for the main harmonic error (100 Hz) in dc-link voltage and position estimation caused by time delays, a periodicity-based dc-link voltage reconstruction method is implemented to eliminate the effect. Furthermore, a power compensation strategy is proposed to mitigate the dc offset in the estimated dc-link voltage and the estimated position caused by extra power losses. Finally, the effectiveness and robustness of the proposed dc-link voltage observer together with delay compensation and power compensation method are verified by experiments.

CHAPTER 4

NOVEL POSITION SENSORLESS CONTROL STRATEGY FOR IPMSM DRIVES WITH SMALL DC-LINK CAPACITOR

In small dc-link capacitor-based PMSM drive systems, the conventional position sensorless control method based on HF voltage signal injection may be limited by insufficient dc-link voltage caused by dc-link voltage fluctuation. Moreover, conventional HF voltage signal injection methods can increase losses, torque ripples, and acoustic noise. To tackle these challenges, this chapter proposes a novel sensorless control method utilizing the unavoidable current harmonics induced by inherent dc-link voltage fluctuation to obtain the rotor position, without extra HF voltage signal injection. Furthermore, the unavoidable current harmonics are also used to determine the magnetic polarity and demonstrate better performance than the conventional secondary harmonics-based polarity detection method, especially under heavy load conditions. Regarding the sensitivity of the proposed method to motor parameter mismatch, a lookup table is designed based on the FEA to mitigate the influence of the parameter mismatch on the estimated position error. Experimental results demonstrate the effectiveness and robustness of the proposed sensorless control and magnetic polarity detection methods, particularly under heavy load conditions.

This chapter is based on the paper submitted in:

J. Yan, Z. Q. Zhu, X. M. Wu, Y. Chen, H. Yang, L. H. Yang, C. H. Liu, "A novel position sensorless control strategy for IPMSM drives with small dc-link capacitor," *IEEE Trans. Power Electron.*, Under review.

4.1 Introduction

In recent years, the small volume dc-link capacitor-based PMSM drive systems have become a hot research topic, especially in household appliances, where precise control is less critical [JUN14]. This approach significantly reduces the volume, weight, and cost of the system, etc. [SAR05] [WAN18A] [ZHA19A]. Despite these benefits, small dc-link capacitor can inevitably cause dc-link voltage fluctuation under high-speed and/or heavy load conditions, which may deteriorate the control performance of the system. For example, the adoption of small dc-link

capacitor introduces increased torque ripple [LIU22], lower dc-link voltage utilization [WAN20C], and LC resonance-induced grid current degradation persistent [LEE14] [SON15] [SON17]. Dynamic load changes such as compressors can also cause beat phenomenon with fluctuating dc-link voltage [ZHA19B].

Furthermore, the fluctuating dc-link voltage could worsen the control performance of various control strategies such as FW control [DIN19] [HUO22B] and position sensorless control [HUA17] [HUO23] [DIN24A] [LI24] [YAN24]. For the fundamental model-based position sensorless control method used in the medium and high-speed ranges, the dc-link voltage fluctuation can lead to fluctuating back-EMFs [HUA17] [HUO23] [DIN24A] [LI24] [YAN24]. The estimated position error obtained by back-EMFs could consequently fluctuate and the control performance of the system deteriorates inevitably. In [HUA17] [HUO23] [DIN24A] [YAN24], different filters are developed to suppress the harmonics in estimated back-EMFs and estimated position errors to improve the accuracy of the sensorless control method. In [LI24], an adaptive synchronous rotating frame transformation is introduced to suppress the back-EMF harmonics caused by a small dc-link capacitor.

For the conventional position sensorless control method at zero or low-speed range, an extra HF voltage signal is injected into the system, and the rotor position and magnetic polarity information is deduced from the induced HF current signal [JEO05B] [JAN06] [LI09] [RAC10] [YOO11] [CUP12] [GON13] [XU16A] [XU16B] [WAN16] [YAN17] [WAN17A] [WAN17B] [ZHA18B] [NAD24]. In the small dc-link capacitor-based PMSM drive system, the inherent dc-link voltage fluctuation caused by small dc-link capacitors could reduce the effective voltage for signal injection. The insufficient injected voltage restricts the induced current signal for accurate position estimation and magnetic polarity detection, which leads to poor starting torque and unstable low-speed operation, ultimately compromising the control performance and efficiency of the PMSM drive systems.

However, the previous research has not yet discussed the influence of insufficient dc-link voltage caused by small dc-link capacitors on the conventional HFSI-based sensorless control method and magnetic polarity detection method. Furthermore, no research has proposed corresponding mitigation methods for this issue.

Therefore, this chapter first identifies the instability issues of conventional HFSI-based sensorless control method caused by small dc-link capacitor. To address these instability issues, a novel position sensorless control method and magnetic polarity detection method for small

dc-link capacitor-based IPMSM drive systems is proposed. The proposed methods utilize the inherent current harmonics introduced by the fluctuating dc-link voltage to estimate the rotor position and detect the magnetic polarity without the need for extra HF voltage signal injection. By utilizing these inherent harmonics, this chapter addresses the limitations of conventional sensorless methods with insufficient dc-link voltage, providing a robust solution to the challenges caused by small dc-link capacitor. In addition, in case of sensitivity of the proposed sensorless control method to inductance parameter mismatch due to magnetic saturation effect, a lookup table is designed based on the FEA to mitigate these effects.

The rest of this chapter is organized as follows. Section 4.2 describes the conventional HF pulsating signal injection-based sensorless control method and the dc-link voltage fluctuation issues in small dc-link capacitor-based IPMSM drive systems. Section 4.3 introduces the proposed sensorless control method and the magnetic polarity detection method for the small dc-link capacitor-based IPMSM drive systems. A lookup table is designed according to FEA to eliminate the effects of parameter mismatch on the proposed sensorless control method. Experimental validation of the proposed methods is presented in Section 4.4, demonstrating their accuracy and effectiveness under various operation conditions. Finally, Section 4.5 summarizes this chapter.

4.2 DC-Link Voltage Fluctuation Issues

As discussed in Chapter 1, Section 1.3.1, the harmonics at frequencies of 100 Hz and 200 Hz arise in small dc-link capacitor-based PMSM drive system. The measured results are presented in Fig. 4.1. The dc-link capacitance is set at 20 μF, the motor speed is maintained at 100 r/min, and the q-axis current is 2 A.

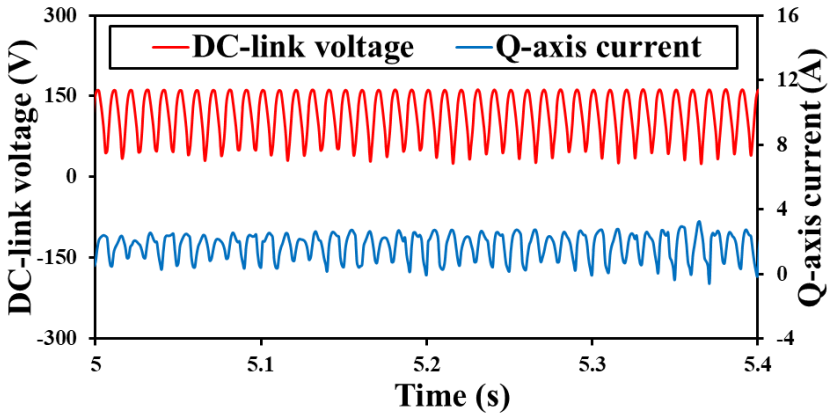

(a) dc-link voltage and q-axis current

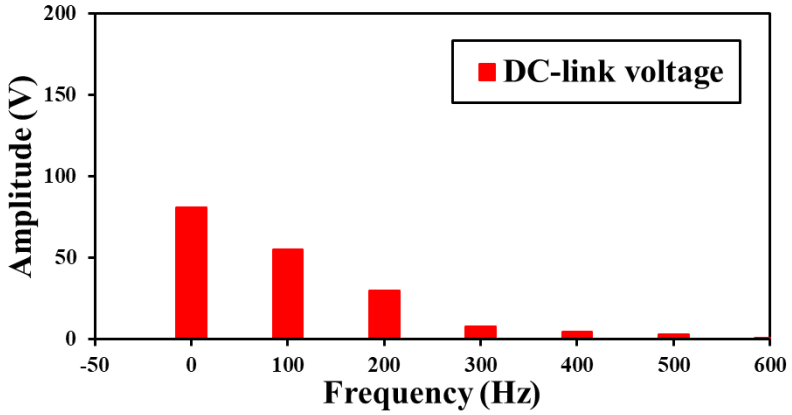

(b) Spectrum of dc-link voltage

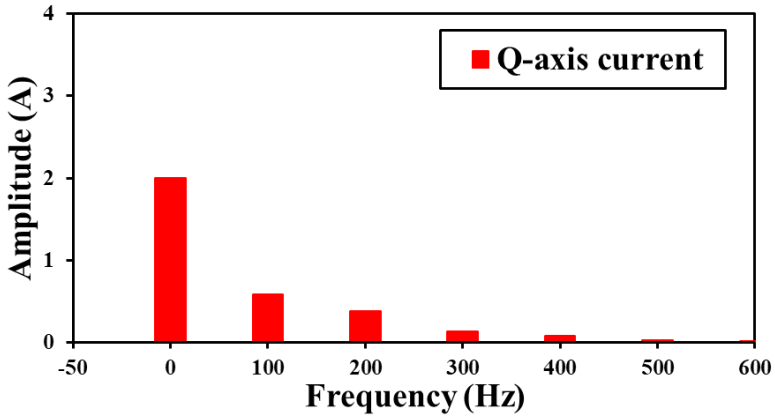

(c) Spectrum of *q*-axis current

Fig. 4.1. Measured results of small dc-link capacitor-based IPMSM drive system. (a) dc-link voltage and *q*-axis current. (b) Spectrum of dc-link voltage. (c) Spectrum of *q*-axis current.

It can be observed that the dc-link voltage fluctuates severely, with the peak-to-peak value of dc-link voltage ripple reaching 120V, the mean value of dc-link voltage dropping to 110V, and the minimum value of dc-link voltage dropping to 30V. The considerable dc-link voltage fluctuation could restrict the feasibility of the conventional HFSI-based sensorless control strategies that rely on the extra voltage signal injection, especially pronounced under heavy loads or dynamic changes process.

Therefore, the novel position sensorless control strategy that remains unaffected by severe dc-link voltage fluctuation is essential to be developed, especially zero or low-speed scenarios to ensure accurate rotor position estimation.

4.3 Proposed Sensorless Control Method in Small DC-Link Capacitor-Based PMSM Drive Systems

In response to the challenge mentioned above, a novel sensorless control strategy is proposed in this section. The proposed strategy eliminates the need for injecting extra voltage signals, instead utilizing the inherent current harmonics induced by the small dc-link capacitor to estimate the rotor position and magnetic polarity. Fig. 4.2 shows the block diagram of the proposed sensorless control method and magnetic polarity detection method utilizing inherent dc-link voltage fluctuation.

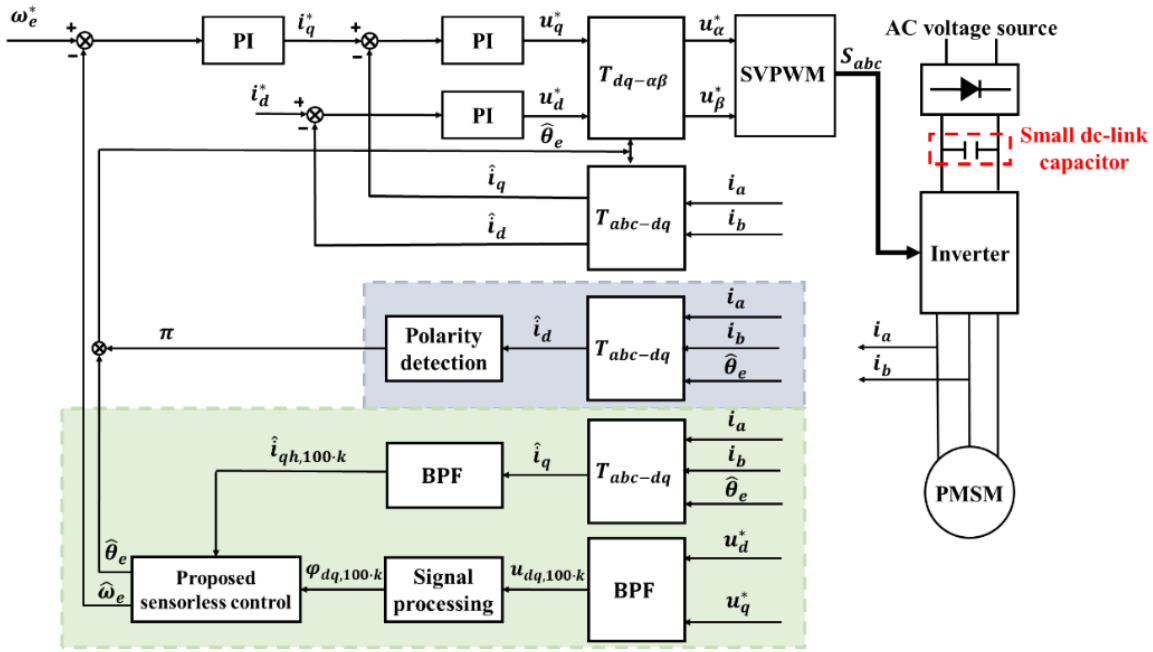

Fig. 4.2. Block diagram of proposed sensorless control method with magnetic polarity detection method utilizing inherent dc-link voltage fluctuation.

4.3.1 Proposed Sensorless Control Method Utilizing Inherent DC-Link Voltage Fluctuation

Due to the dc-link voltage fluctuation, the corresponding fluctuating *dq*-axis voltages can be expressed as [WAN20B]

$$\begin{bmatrix} u_d \\ u_q \end{bmatrix} = \begin{bmatrix} u_{d,0} + \sum_{k=1}^{n} u_{d,k} \sin(2k\omega_g t + \varphi_{d,k}) \\ u_{q,0} + \sum_{k=1}^{n} u_{q,k} \sin(2k\omega_g t + \varphi_{q,k}) \end{bmatrix} \tag{4.1}$$

where $u_{dq,0}$ and $u_{dq,k}$ are the dc components and the kth order harmonics of dq-axis voltages,

$\varphi_{dq,k}$ are the phase angles of the kth order harmonics of dq-axis voltages.

Due to dc-link voltage fluctuate on, the current response in the estimated synchronous reference frame can be expressed as

$$p\begin{bmatrix}\hat{i}_{dh,100\cdot k}\\ \hat{i}_{qh,100\cdot k}\end{bmatrix}=\begin{bmatrix}\frac{1}{L_p}+\frac{1}{L_n}\cos(2\Delta\theta_r) & \frac{1}{L_n}\sin(2\Delta\theta_r)\\ \frac{1}{L_n}\sin(2\Delta\theta_r) & \frac{1}{L_p}-\frac{1}{L_n}\cos(2\Delta\theta_r)\end{bmatrix}\cdot\begin{bmatrix}u_{dh,100\cdot k}\cos(\omega_{100\cdot k}t+\varphi_{d_{100\cdot k}})\\ u_{qh,100\cdot k}\cos(\omega_{100\cdot k}t+\varphi_{q_{100\cdot k}})\end{bmatrix} \quad (4.2)$$

where $u_{dqh,100\cdot k}$, $\hat{i}_{dqh,100\cdot k}$, and $\varphi_{dq_{100\cdot k}}$ are the voltages, currents, and phase angle of $100\cdot k$ Hz dq-axis harmonics, k is an integer greater than or equal to 1, $\omega_{100\cdot k}$ is $2\pi\times 100\cdot k$.

After simplification,

$$\begin{bmatrix}\hat{i}_{dh,100\cdot k}\\ \hat{i}_{qh,100\cdot k}\end{bmatrix}=\begin{bmatrix}D_p+D_n\cos(2\Delta\theta_r) & Q_n\sin(2\Delta\theta_r)\\ D_n\sin(2\Delta\theta_r) & Q_p-Q_n\cos(2\Delta\theta_r)\end{bmatrix}\cdot\begin{bmatrix}\sin(\omega_{100\cdot k}t+\varphi_{d_{100\cdot k}})\\ \sin(\omega_{100\cdot k}t+\varphi_{q_{100\cdot k}})\end{bmatrix} \quad (4.3)$$

$$D_p=\frac{u_{d,100\cdot k}}{\omega_{100\cdot k}L_p},\ D_n=\frac{u_{d,100\cdot k}}{\omega_{100\cdot k}L_n},\ Q_p=\frac{u_{q,100\cdot k}}{\omega_{100\cdot k}L_p},\ Q_n=\frac{u_{q,100\cdot k}}{\omega_{100\cdot k}L_n} \quad (4.4)$$

From (4.1) and (4.3), it is evident that both d-axis and q-axis currents exhibit HF harmonics whose frequencies are integer multiples of 100. However, the amplitudes and phases of these harmonics are not identical. As a result, conventional HFSI-based sensorless control methods are inadequate for decoupling and estimating the rotor position under these conditions. Consequently, this chapter proposes a novel demodulation method as described below.

$$\begin{bmatrix}|\hat{i}_{dh,100\cdot k}|\\ |\hat{i}_{qh,100\cdot k}|\end{bmatrix}=\mathrm{LPF}\left(\begin{bmatrix}\hat{i}_{dh,100\cdot k}2\sin(\omega_{100\cdot k}t+\varphi_{q_{100\cdot k}})\\ \hat{i}_{qh,100\cdot k}2\sin(\omega_{100\cdot k}t+\varphi_{d_{100\cdot k}})\end{bmatrix}\right)$$

$$=\mathrm{LPF}\left(\begin{bmatrix}D_p+D_n\cos(2\Delta\theta_r) & Q_n\sin(2\Delta\theta_r)\\ D_n\sin(2\Delta\theta_r) & Q_p-Q_n\cos(2\Delta\theta_r)\end{bmatrix}\cdot\begin{bmatrix}\sin(\omega_{100\cdot k}t+\varphi_{d_{100\cdot k}})\\ \sin(\omega_{100\cdot k}t+\varphi_{q_{100\cdot k}})\end{bmatrix}\cdot\begin{bmatrix}2\sin(\omega_{100\cdot k}t+\varphi_{q_{100\cdot k}})\\ 2\sin(\omega_{100\cdot k}t+\varphi_{d_{100\cdot k}})\end{bmatrix}\right) \quad (4.5)$$

$$= \mathrm{LPF}\left(\begin{bmatrix} D_p + D_n\cos(2\Delta\theta_r) & Q_n\sin(2\Delta\theta_r) \\ D_n\sin(2\Delta\theta_r) & Q_p - Q_n\cos(2\Delta\theta_r) \end{bmatrix} \cdot \begin{bmatrix} \sin(\omega_{100\cdot k}t + \varphi_{d_{100\cdot k}}) \\ \sin(\omega_{100\cdot k}t + \varphi_{q_{100\cdot k}}) \end{bmatrix} \cdot \begin{bmatrix} 2\sin(\omega_{100\cdot k}t + \varphi_{q_{100\cdot k}}) \\ 2\sin(\omega_{100\cdot k}t + \varphi_{d_{100\cdot k}}) \end{bmatrix}\right)$$

$$= 2\mathrm{LPF}\left(\begin{bmatrix} \left\{\begin{matrix}[D_p + D_n\cos(2\Delta\theta_r)]\sin(\omega_{100\cdot k}t + \varphi_{d_{100\cdot k}}) + \\ Q_n\sin(2\Delta\theta_r)\sin(\omega_{100\cdot k}t + \varphi_{q_{100\cdot k}})\end{matrix}\right\}\sin(\omega_{100\cdot k}t + \varphi_{q_{100\cdot k}}) \\ \left\{\begin{matrix}[D_p + D_n\cos(2\Delta\theta_r)]\sin(\omega_{100\cdot k}t + \varphi_{d_{100\cdot k}}) + \\ Q_n\sin(2\Delta\theta_r)\sin(\omega_{100\cdot k}t + \varphi_{q_{100\cdot k}})\end{matrix}\right\}\sin(\omega_{100\cdot k}t + \varphi_{q_{100\cdot k}}) \end{bmatrix}\right)$$

$$= \begin{bmatrix} Q_n\sin(2\Delta\theta_r) + D_p\delta_{dq} + D_n\cos(2\Delta\theta_r)\delta_{dq} \\ D_n\sin(2\Delta\theta_r) + Q_p\delta_{dq} - Q_n\cos(2\Delta\theta_r)\,\delta_{dq} \end{bmatrix}$$

$$\delta_{dq} = \cos(\varphi_{u_q} - \varphi_{u_d}) \tag{4.6}$$

Therefore, the estimated position error could be derived by the *dq*-axis carrier currents.

$$\left|\hat{i}_{dh,100\cdot k}\right| + \frac{D_n}{Q_n}\left|\hat{i}_{qh,100\cdot k}\right| - 2D_p\delta_{dq} = \left(Q_n + \frac{D_n^2}{Q_n}\right)\sin(2\Delta\theta_r) \tag{4.7}$$

$$\left|\hat{i}_{dh,100\cdot k}\right| - \frac{D_p}{Q_p}\left|\hat{i}_{qh,100\cdot k}\right| + 2D_n\cos(2\Delta\theta_r)\delta_{dq} = \left(Q_n - \frac{D_pD_n}{Q_p}\right)\sin(2\Delta\theta_r) \tag{4.8}$$

where $\hat{i}^d_{dh,100\cdot k}$, $\hat{i}^q_{dh,100\cdot k}$, $\hat{i}^d_{qh,100\cdot k}$, and $\hat{i}^q_{qh,100\cdot k}$ are the demodulated *dq*-axis currents by phase angle of *dq*-axis voltages, δ_{dq} is the cosine of the phase difference between *dq*-axis voltages.

From above equations, both (4.7) and (4.8) can be used to obtain signals containing rotor position information. When the right side of (4.7) and (4.8) approaches zero, the actual rotor position is accurately obtained. However, (4.7) is preferable to (4.8) for estimating the rotor position because $\left(Q_n - \frac{D_pD_n}{Q_p}\right)$ in (4.8) could potentially equal zero. This scenario would adversely affect the accuracy of the rotor position estimation. In contrast, (4.7) does not have this inherent issue, making it more reliable for precise rotor position estimation.

Fig. 4.3 presents the block diagram of the signal processing to extract the phase information of *dq*-axis voltage harmonics. Through the signal processing, the phase and amplitude of the *dq*-axis voltage harmonics can be obtained. Fig. 4.4 shows the block diagram of the proposed sensorless control method. The $100 \cdot k$ Hz *dq*-axis current harmonics are obtained using a BPF. Then, processed by (4.5) and (4.7). The signal with the rotor position information is obtained. When the signal approaches 0 by the position observer, the actual rotor position is obtained.

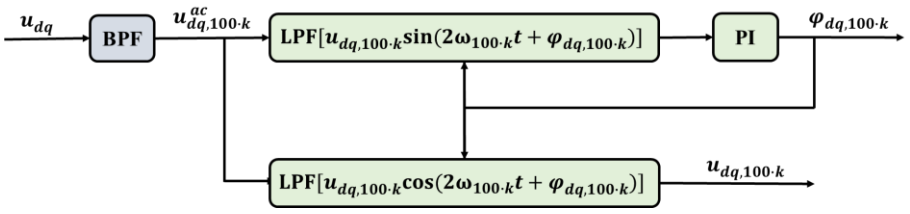

Fig. 4.3. Block diagram of signal processing.

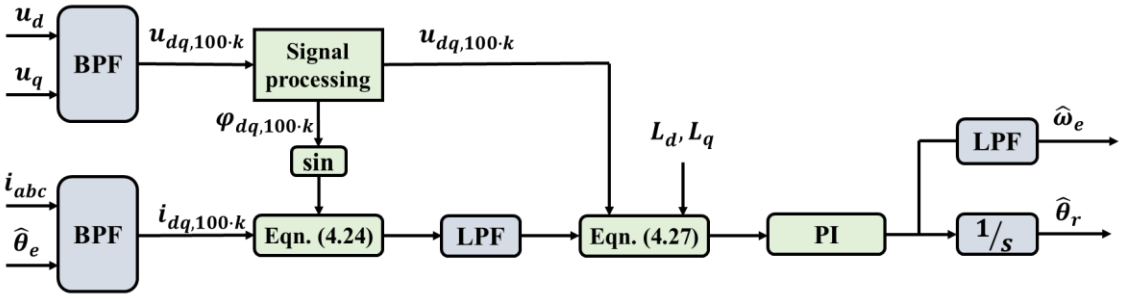

Fig. 4.4. Block diagram of proposed sensorless control method.

4.3.2 Magnetic Polarity Detection Utilizing Inherent DC-Link Voltage Fluctuation

Magnetic polarity detection is crucial to the effectiveness of the HFSI-based sensorless control method, particularly due to the inherent variations in inductance caused by the magnetic polarity that occur twice within one electrical period, leading to a 180-degree angle offset [WAN20A] [ZHU23]. For the conventional secondary harmonic-based magnetic polarity detection method, the *d*-axis induced current considering magnetic saturation can be simplified as [JEO05B]:

$$\begin{bmatrix}\hat{i}_{dh,sat}\\ \hat{i}_{qh,sat}\end{bmatrix}=\begin{bmatrix}I_p+I_n\cos(2\Delta\theta_r)\\ I_n\sin(2\Delta\theta_r)\end{bmatrix}\cdot\sin(\omega_{hf}t)+\begin{bmatrix}I_{sat}\cos^2(\Delta\theta_r)\cos(\Delta\theta_r)\\ I_{sat}\cos^2(\Delta\theta_r)\sin(\Delta\theta_r)\end{bmatrix}\cdot\sin^2(\omega_{hf}t) \tag{4.9}$$

where $I_{sat}>0$.

The magnetic polarity information can be obtained by

$$\hat{i}_{dh,\cos(2\omega_{hf}t)}=LPF\left(\hat{i}_{dh,sat}\cos(2\omega_h t)\right)=-\frac{1}{4}I_{sat}\cos^2(\Delta\theta_r)\cos(\Delta\theta_r) \tag{4.10}$$

As can be seen from (4.10), with correct polarity alignment, $\hat{i}_{dh,\cos(2\omega_{hf}t)}$ should be negative. If $\hat{i}_{dh,\cos(2\omega_{hf}t)}$ is positive, the estimated rotor direction should be adjusted by π to obtain the accurate rotor position information.

In this chapter, the second harmonic-based magnetic polarity detection method utilizing

inherent dc-link voltage fluctuation caused by the small dc-link capacitor is proposed. The proposed method employs lower frequency with potentially larger amplitude signals than conventional methods. Consequently, the detection results are more reliable than those achieved with conventional methods. The lower frequency of the detection signal allows for a higher signal-to-noise ratio (SNR), while the larger amplitude enhances the visibility of the secondary harmonic components related to magnetic saturation effects, compared to the conventional methods.

4.3.3 Effect of Parameters Mismatch

From (4.8), (4.23) and (4.26), to obtain the rotor position information, it is necessary to have not only the amplitude of the *dq*-axis voltages but also accurate D_p which is related to the motor inductance parameters. Thus, the inductance mismatches are unavoidable to considered when design and implementation of the proposed sensorless control method. Any inevitable mismatch in inductance parameters will affect the accuracy of D_p, and consequently, the proposed sensorless control method. Such mismatches can lead to inaccuracies in rotor position estimation and overall control performance. Therefore, the effect of parameter mismatches on the proposed sensorless control method should be mitigated effectively.

D_p can be presented as

$$D_p = \frac{u_{d,100\cdot k}}{\omega_{100\cdot k} L_p} = \frac{u_{d,100\cdot k}(L_{dh} + L_{qh})/2}{\omega_{100\cdot k}(L_{dh} L_{qh})} \tag{4.11}$$

Given the reliance of the proposed sensorless control method on *dq*-axis inductances, it is essential to investigate the *dq*-axis inductances mismatch caused by magnetic saturation. *Dq*-axis inductances are sensitive to magnetic saturation, which can significantly affect the estimated rotor position and the performance of the proposed sensorless control method.

To address these concerns, a detailed FEA is conducted to examine the effects of magnetic saturation on *dq*-axis inductances mismatch under various operating conditions. Fig. 4.5 shows the FEA results, indicating that *d*-axis inductance decreases from 39 mH to 37 mH with varying *q*-axis currents at $i_d = 0$. Similarly, *q*-axis inductance decreases from 55 mH to 44.5 mH by changes in *q*-axis current at $i_d = 0$.

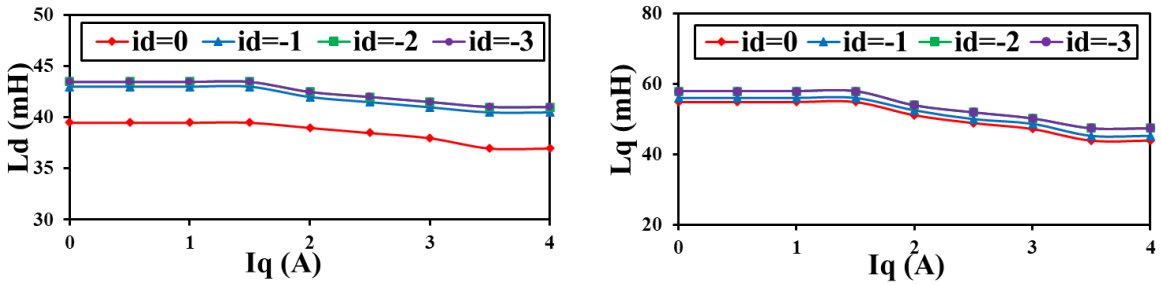

(a) *d*-axis inductance (b) *q*-axis inductance

Fig. 4.5. *Dq*-axis inductances under different *dq*-axis currents. (a) *d*-axis inductance. (b) *q*-axis inductance.

Based on the FEA results, the *dq*-axis inductance mismatch under different operating conditions is determined. Then, a lookup table is used to adjust the *dq*-axis inductance parameters in real-time dynamically to address the issue of parameter mismatch. This lookup table is designed to correct any discrepancies between the actual and expected parameters. By using this method, the influence of parameter mismatch on the accuracy of position estimation is effectively eliminated, ensuring more reliable and precise rotor position information.

4.4 Experiment Validation

In this section, the instability issues of the conventional pulsating signal injection-based sensorless control method due to significant dc-link voltage fluctuation are firstly illustrated. To solve these challenges, a novel position sensorless control method and magnetic polarity detection method are proposed under severe dc-link voltage fluctuation scenarios. Then, a lookup table is designed according to FEA, Finally, the performance of the proposed sensorless control method with the designed lookup table and magnetic polarity detection method are validated. The small dc-link capacitance used in this chapter is 20 μF, and it is worth mentioning that the conventional large dc-link capacitance is 1600 μF. During the experiments, magnetic cross-coupling issues are eliminated using the lookup table-based methods described in [LI09] [RAC10] [CUP12].

4.4.1 Conventional HF Pulsating Signal Injection Method in Small DC-Link Capacitor-Based PMSM Drive System

Fig. 4.6 shows the measured results of open-loop estimation of the conventional pulsating signal injection-based sensorless control method described in section 4.2.1 in the small dc-link capacitor-based IPMSM drive systems. In the case of open loop estimation, the system uses

the actual rotor position obtained by the encoder and the rotor position is estimated by the conventional sensorless method, where the amplitude of the injected *d*-axis voltage is 20 V with a frequency of 500 Hz. It is observable that the conventional sensorless method can track the rotor position effectively before 7s. However, as the *q*-axis current increased to 3 A after 7s, significant fluctuations appeared in the dc-link voltage, with peak-to-peak ripple reaching approximately 130 V and minimum values around 35 V. These substantial dc-link voltage drops lead to instability in the open-loop estimation, ultimately causing the conventional sensorless control method to fail. The right colume show the measured results of the closed-loop control performance of the conventional sensorless control method. In this scenario, the system utilizes the estimated position obtained by the conventional sensorless method. Initially, the system operates stably. However, as the load increases slowly, the severely dc-link voltage fluctuation causes the conventional sensorless control method destabilized due to insufficient dc-link voltage.

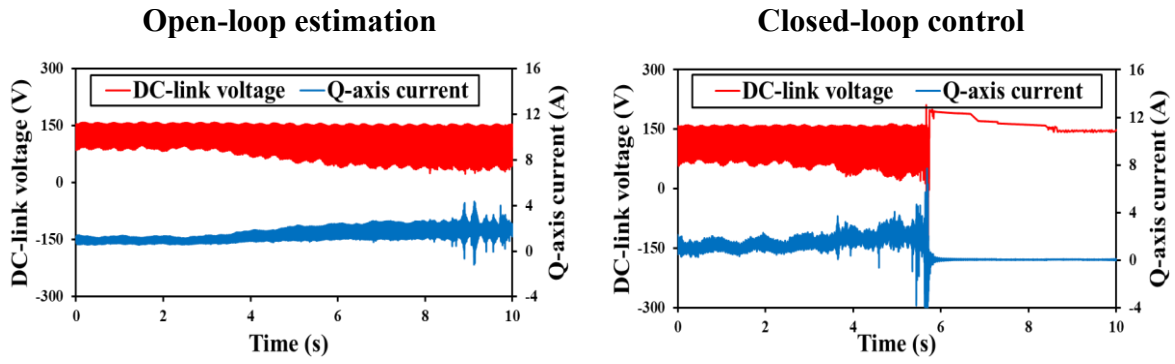

(a) dc-link voltage

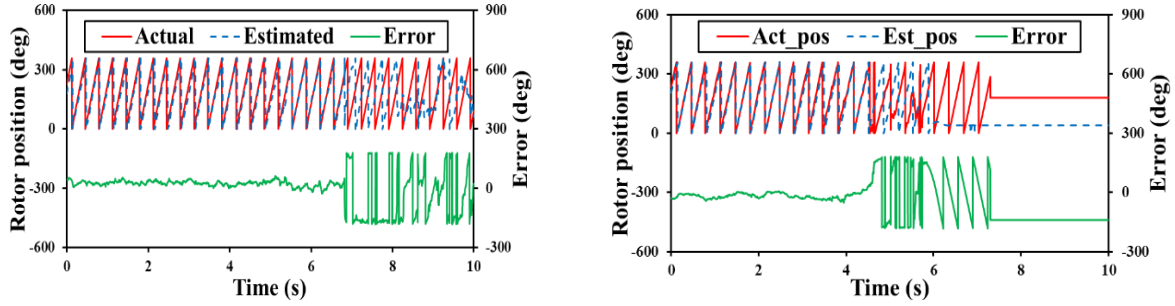

(a)) Rotor position and estimation error

Fig. 4.6. Measured results of conventional pulsating signal injection-based sensorless method in small dc-link capacitor-based IPMSM drive system with increasing load. (a) dc-link voltage. (b) Rotor position and estimation error.

Fig. 4.7 shows the summary of conventional sensorless control under varies operation conditions. The conventional sensorless control operates stably under light load conditions.

However, when the *q*-axis current exceeds 2.5 A, the system becomes unstable. The red marked points indicate the conditions under which the system tends to become a non-safe sensorless operation area (non-SSOA). The green marked points indicate the conditions under SSOA. Fig. 4.6 and Fig. 4.7 demonstrate the limitations of conventional HFSI-based sensorless control in the small dc-link capacitor-based PMSM drive systems.

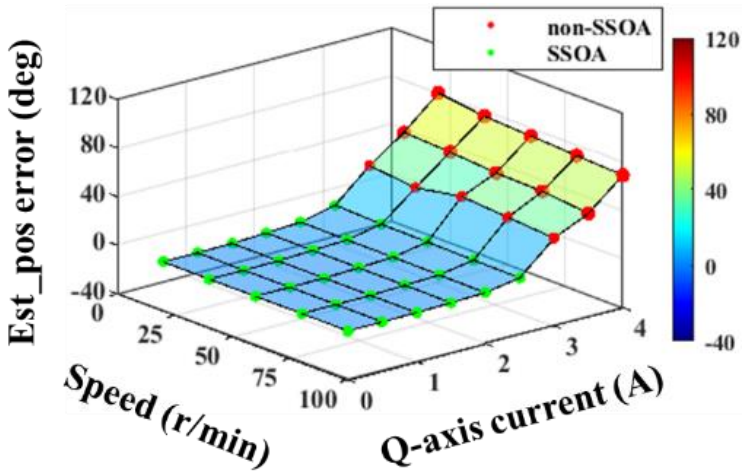

Fig. 4.7. Closed-loop control performance map of conventional pulsating signal injection-based sensorless method in small dc-link capacitor-based IPMSM drive system.

4.4.2 Proposed Sensorless Control Method Utilizing Inherent DC-link Voltage Fluctuation

Fig. 4.8 to Fig. 4.10 present the experimental results of the proposed sensorless control method based on 200 Hz harmonics under various operating conditions (from Fig. 4.8 to Fig. 4.10: 50 r/min and *q*-axis current is 1 A, 50 r/min and *q*-axis current is 2 A, 100 r/min and *q*-axis current is 2 A). It is revealed that at 50 r/min and *q*-axis current is 1 A, the dc-link voltage exhibits minimal fluctuations and the system's harmonic content is low. This scenario poses challenges for the proposed sensorless control method to accurately determine the rotor position. As the *q*-axis current increased to 2 A, the system experienced a larger harmonic component. Under these conditions, the system can accurately estimates the rotor position. When the motor speed is increased to 100 r/min, the dc-link voltage peak-to-peak value and the *dq*-axis voltage peak-to-peak values are increased slightly. Despite the presence of some harmonic components in the system, the rotor position estimation remains accurate.

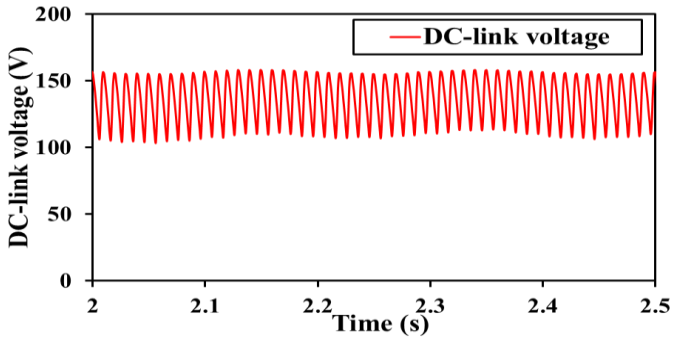

(a) dc-link voltage

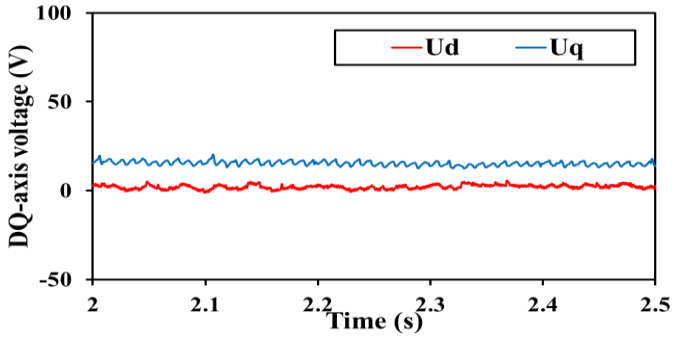

(b) *dq*-axis voltage

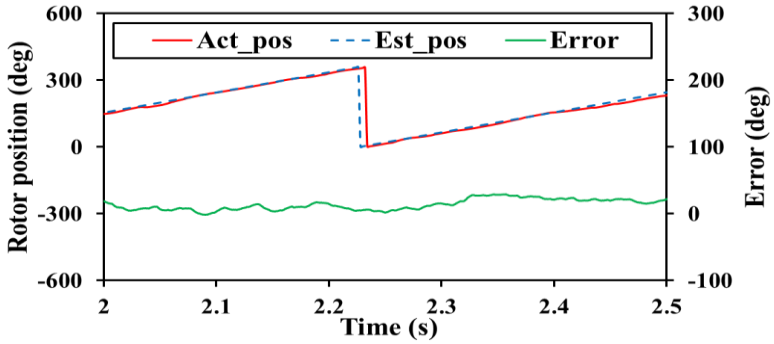

(c) Rotor position

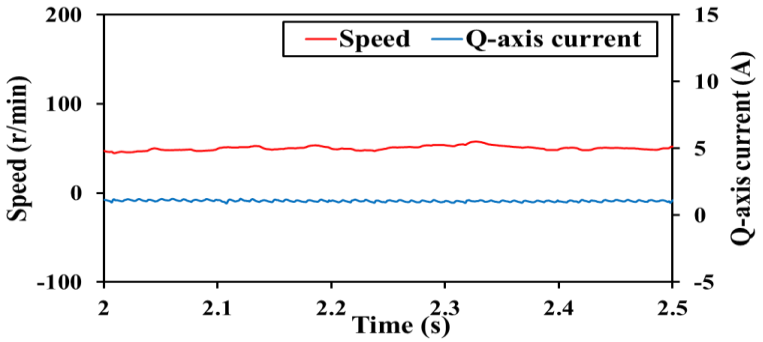

(d)) Speed and *q*-axis current

Fig. 4.8. Measured results of proposed sensorless control method under 50 r/min with 1 Nm load. (a) dc-link voltage. (b) *dq*-axis voltage. (c) Rotor position. (d) Speed and *q*-axis current.

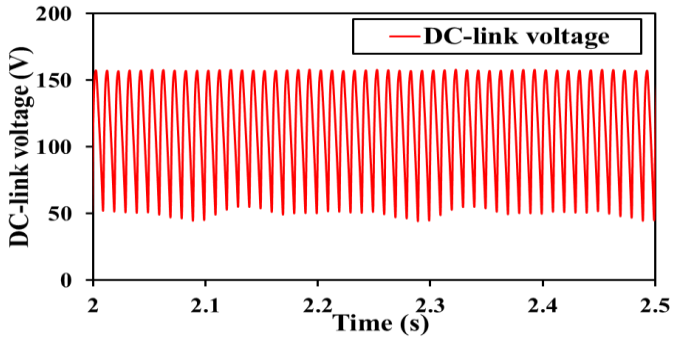

(a) dc-link voltage

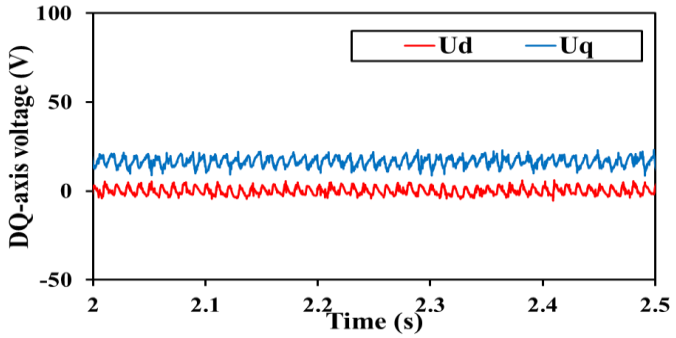

(b) *dq*-axis voltage

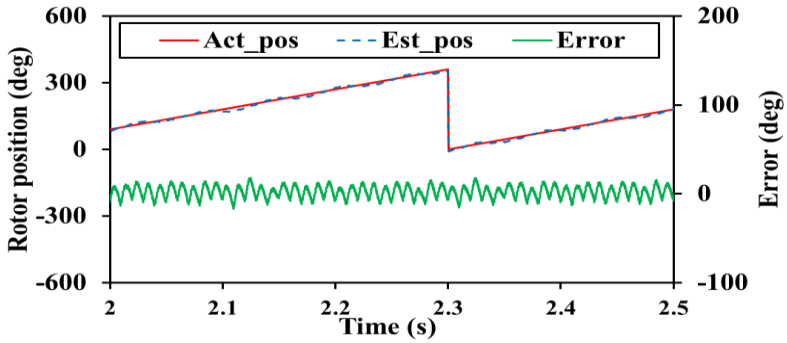

(c) Rotor position

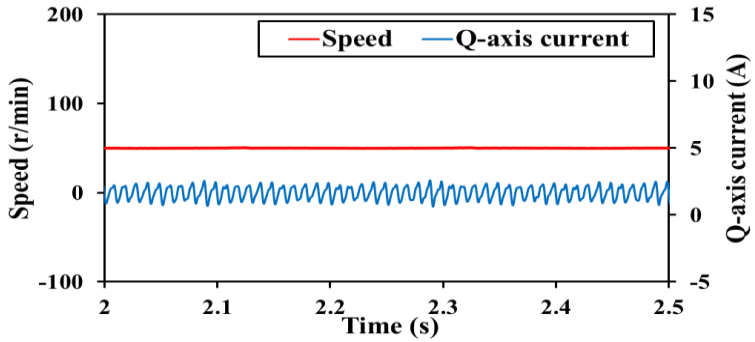

(d)) Speed and *q*-axis current

Fig. 4.9. Measured results of proposed sensorless control method under 50 r/min with 2 Nm load. (a) dc-link voltage. (b) *dq*-axis voltage. (c) Rotor position. (d) Speed and *q*-axis current.

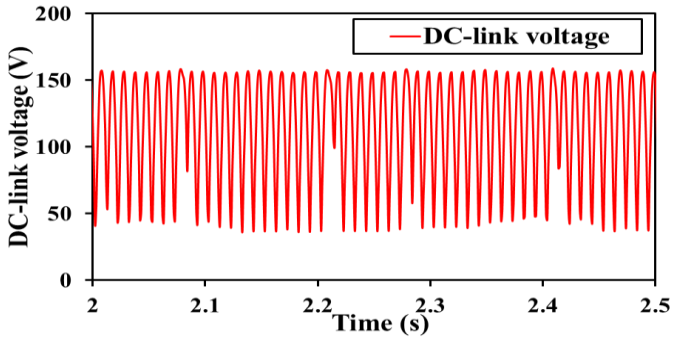

(a) dc-link voltage

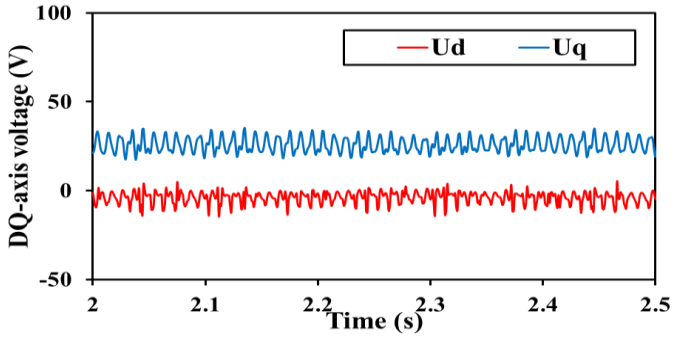

(b) *dq*-axis voltage

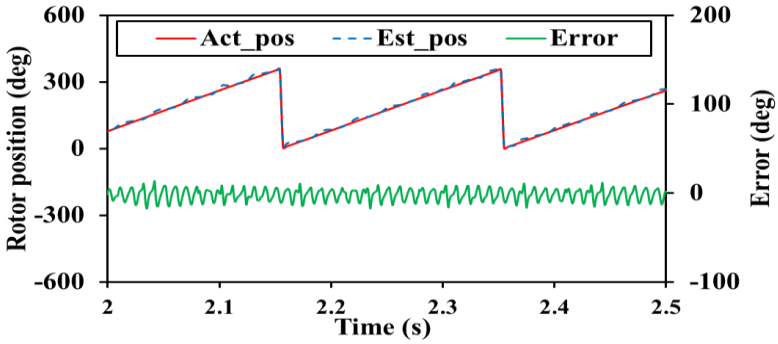

(c) Rotor position

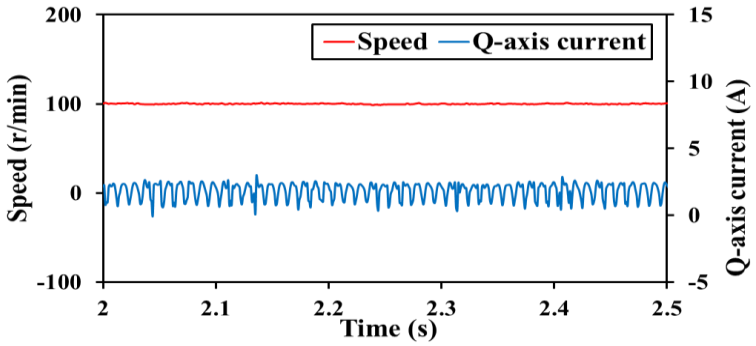

(d)) Speed and *q*-axis current

Fig. 4.10. Measured results of proposed sensorless control method under 100 r/min with 2 Nm load. (a) dc-link voltage. (b) *dq*-axis voltage. (c) Rotor position. (d) Speed and *q*-axis current.

Fig. 4.11 to Fig. 4.13 show the measured results of the proposed sensorless control method, which are based on 100 Hz harmonics, under varying operating conditions (from Fig. 4.11 to Fig. 4.13: 50 r/min and *q*-axis current is 1 A, 50 r/min and *q*-axis current is 2 A, 100 r/min and *q*-axis current is 2 A). In Fig. 4.11, the dc-link voltage fluctuation is small, and harmonic components are minimal. However, unlike the proposed sensorless control method with 200 Hz harmonics above, the proposed sensorless control method with 100 Hz harmonics can still accurately estimate the rotor position and maintain good control performance under these conditions. When the *q*-axis current increases to 2 A, the harmonic components in the system become more pronounced, with the dc-link voltage peak-to-peak value reaching 110 V and the *dq*-axis voltages peak-to-peak value are increased. The rotor position estimation remains accurate, demonstrating excellent control performance. At 100 r/min and *q*-axis current is 2 A, there is a slight increase in the dc-link voltage peak-to-peak value and a further increase in peak-to-peak value of *dq*-axis voltages. The rotor position continues to be estimated accurately, although some harmonic components are present in the system. The use of 100 Hz harmonics results in more noticeable estimation performance, especially at lower speeds and loads, such as 50 r/min and *q*-axis current of 1 A.

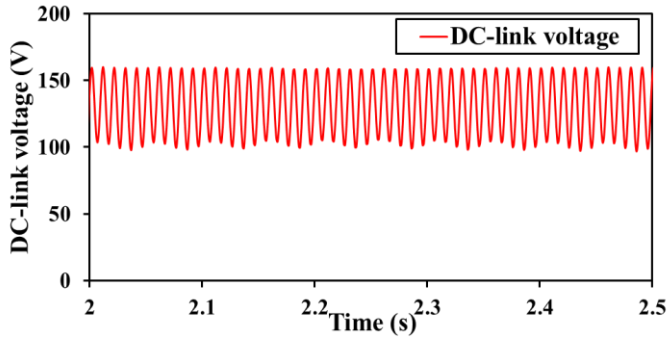

(a) dc-link voltage

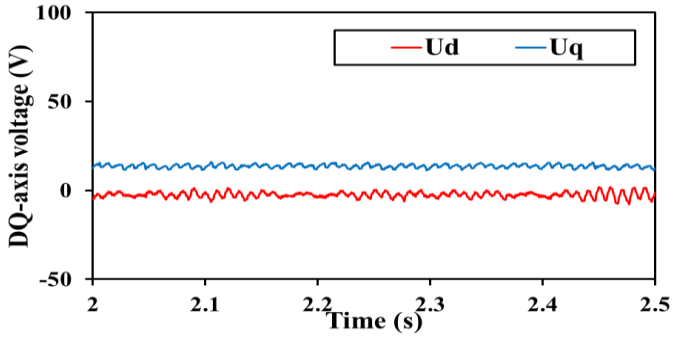

(b) *dq*-axis voltage

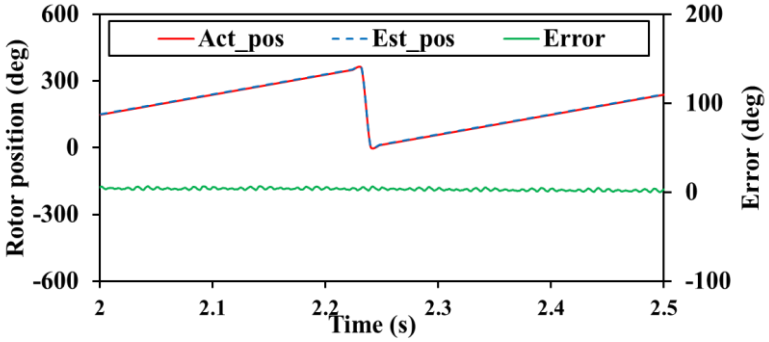

(c) Rotor position

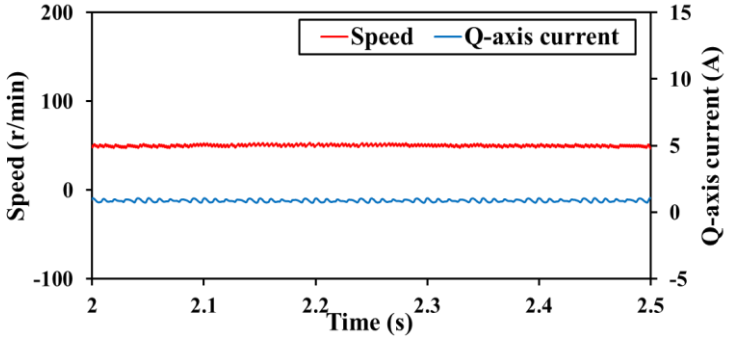

(d)) Speed and *q*-axis current

Fig. 4.11. Measured results of proposed sensorless method with 100 Hz harmonics under 50 r/min with 1 Nm load. (a) dc-link voltage. (b) *dq*-axis voltage. (c) Rotor position. (d) Speed and *q*-axis current.

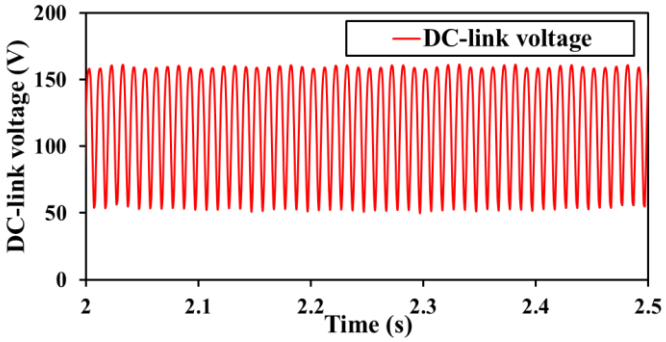

(a) dc-link voltage

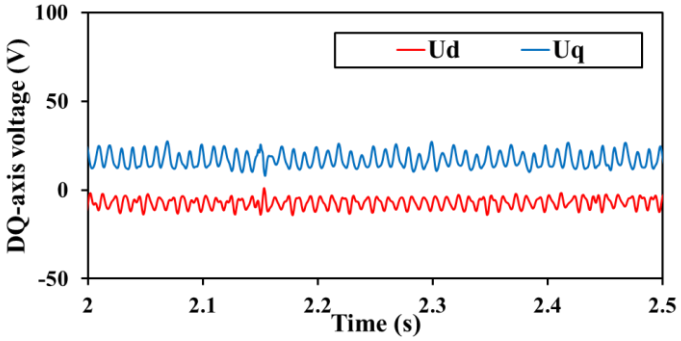

(b) *dq*-axis voltage

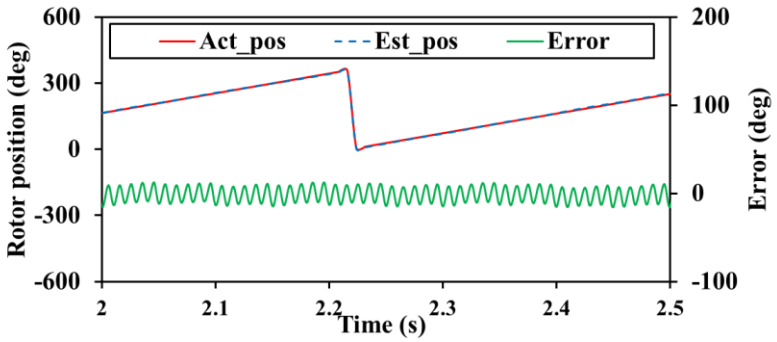

(c) Rotor position

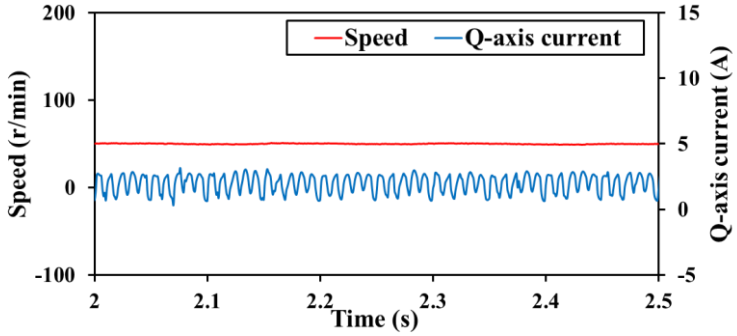

(d)) Speed and *q*-axis current

Fig. 4.12. Measured results of proposed sensorless control method with 100 Hz harmonics under 50 r/min with 2 Nm load. (a) dc-link voltage. (b) *dq*-axis voltage. (c) Rotor position. (d) Speed and *q*-axis current.

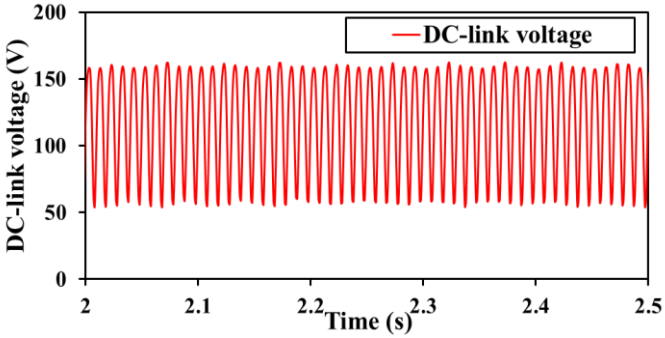

(a) dc-link voltage

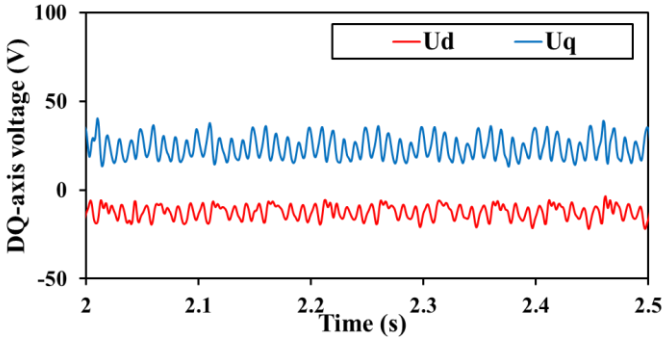

(b) *dq*-axis voltage

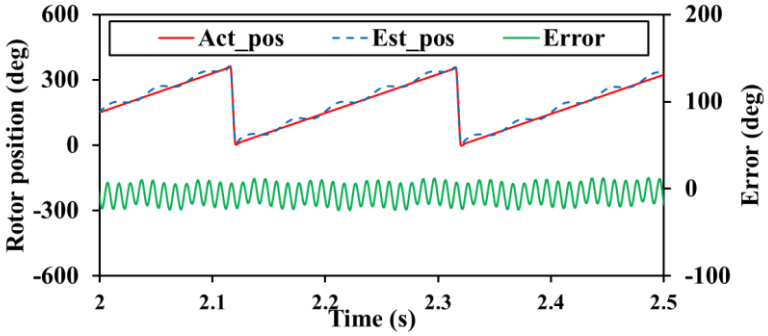

(c) Rotor position

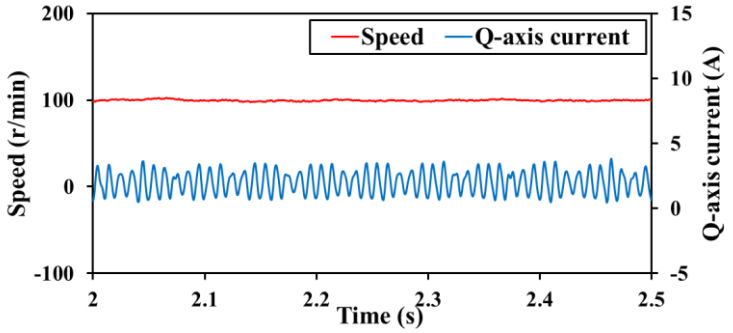

(d) Speed and *q*-axis current

Fig. 4.13. Measured results of proposed sensorless control method with 100 Hz harmonics under 100 r/min with 2 Nm load. (a) dc-link voltage. (b) *dq*-axis voltage. (c) Rotor position. (d) Speed and *q*-axis current.

Fig. 4.14 shows the control performance of the conventional and proposed sensorless method as the motor speed varies from 0 r/min to 100 r/min and the *q*-axis current is 0 A to 4 A. It can be observed that when the *q*-axis current is below 1.5 A, the proposed control method does not function effectively due to the relatively small current harmonics. However, the conventional method performs well under these light load conditions. On the other hand, the proposed control method can ensure a stable operation when the *q*-axis current exceeds 1.5 A up to the rated load, effectively addressing the limitations of conventional HFSI-based sensorless control methods under heavy load conditions. Fig. 4.14(b) combines results from Fig. 4.7 and Fig. 4.14(a), illustrating that the integration of the proposed with conventional sensorless method can provide an optimal performance. Specifically, at light loads, the conventional method is effective, while at heavy loads, the proposed method takes over. This combination ensures nearly seamless sensorless control under all load conditions in the low-speed range.

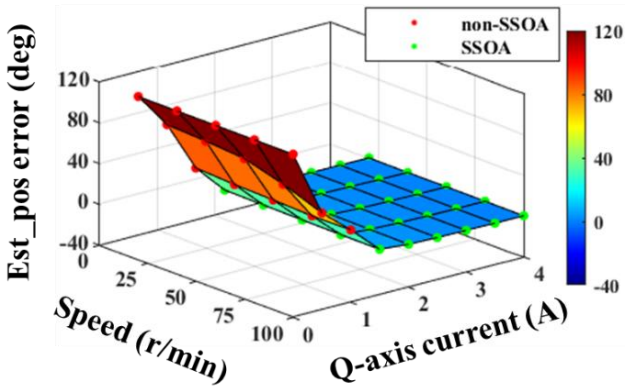

(a) Proposed sensorless control method

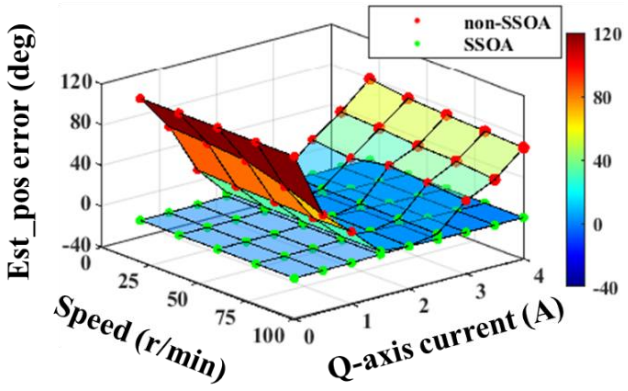

(b) Comparison of convention sensorless control method with proposed sensorless control method using 200 Hz harmonics

Fig. 4.14. Control performance map of the sensorless control method under different speed and load conditions. (a) Proposed sensorless control method. (b) Combination of convention sensorless control method with proposed sensorless control method using 200 Hz harmonics.

4.4.3. Proposed Magnetic Polarity Detection Utilizing Inherent DC-Link Voltage Fluctuation

Fig. 4.15 compares the conventional secondary harmonics-based magnetic polarity detection method based on extra HF signal injection and the proposed polarity detection method based on dc-link voltage fluctuation when the estimated rotor position error is 0 and π rad. In the experiment, the motor operates at 100 r/min and q-axis current is 2 A. Taken the estimation time and voltage utilization into consideration, an HF voltage signal with an amplitude of 20 V and a frequency of 500 Hz is injected [SHU21] [ZHU11B]. Regardless of the motor polarity, the proposed magnetic polarity detection method based on inherent dc-link voltage fluctuation shows more distinguishable results because the value of $\hat{i}_{dh,\cos(2\omega_{hf}t)}$ is larger compared to the conventional method.

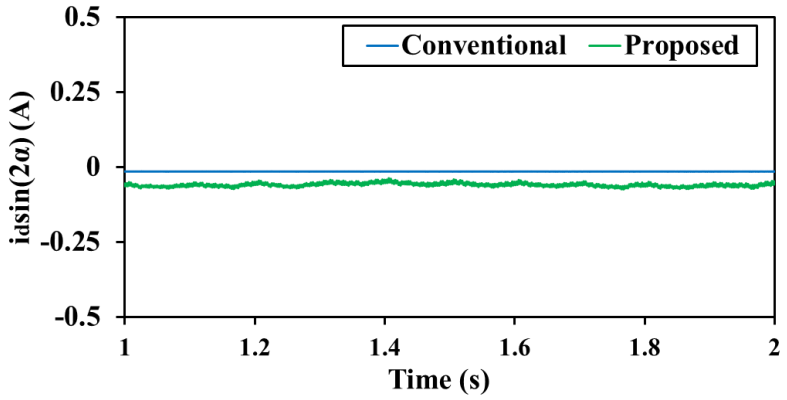

(a) $\Delta\theta_r = 0$

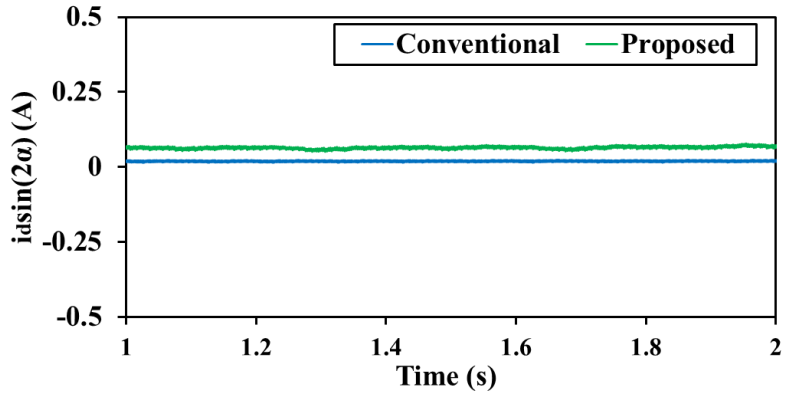

(b) $\Delta\theta_r = \pi$

Fig. 4.15. Comparison of secondary harmonics-based magnetic polarity detection method based on conventional signal injection and the proposed novel method based on fluctuating dc-link voltage. (a) $\Delta\theta_r = 0$. (b) $\Delta\theta_r = \pi$

4.4.4 Dynamic Performance

Fig. 4.16 and Fig. 4.17 show the dynamic control performance of the proposed sensorless control method based on 200 Hz. In Fig. 4.16, the motor speed is increased from 50 r/min to 100 r/min and q-axis current is 2 A. During this period, the peak-to-peak value of the dc-link voltage ripple is increased from 100 V to 120 V. The proposed sensorless control method can accurately track the actual position, despite the presence of some harmonics in the estimated position error. In Fig. 4.17, the motor speed is maintained at 100 r/min while the q-axis current increased from 1.5 A to 2.5 A. It can be observed that the estimated rotor position consistently aligns with the actual rotor position. The results demonstrate that the proposed sensorless control method performs well under dynamic conditions.

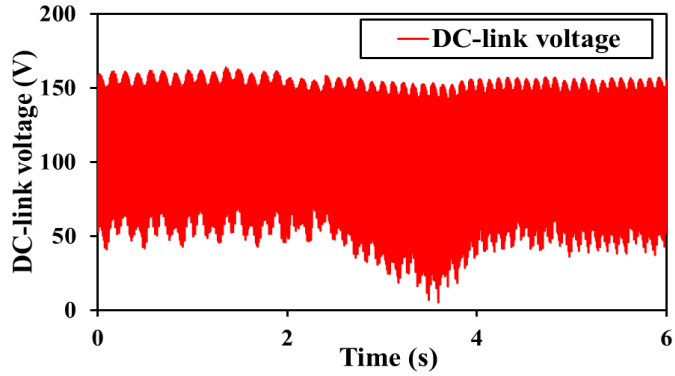

(a) dc-link voltage

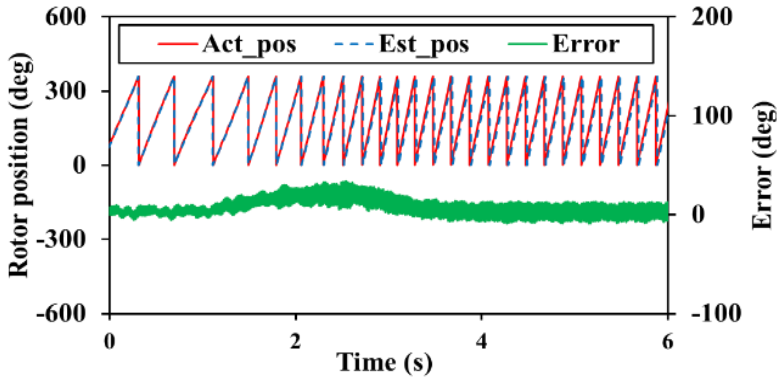

(b) Rotor position

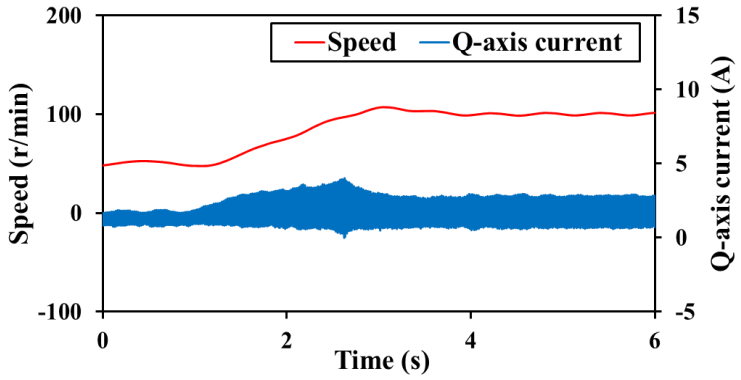

(c) Speed and *q*-axis current

Fig. 4.16. Measured results with speed increased from 50 r/min to 100 r/min when the proposed sensorless control method using 200 Hz harmonics. (a) dc-link voltage. (b) Rotor position. (c) Speed and *q*-axis current.

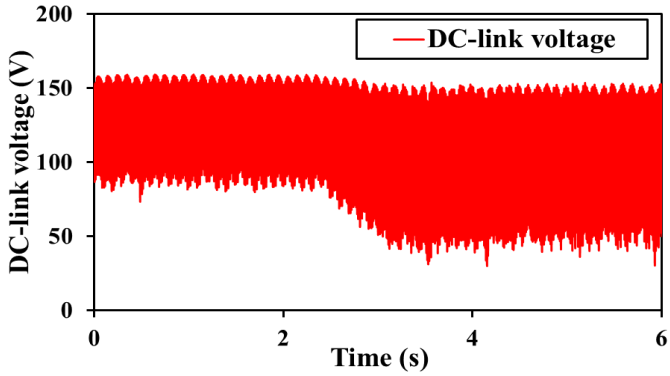

(a) dc-link voltage

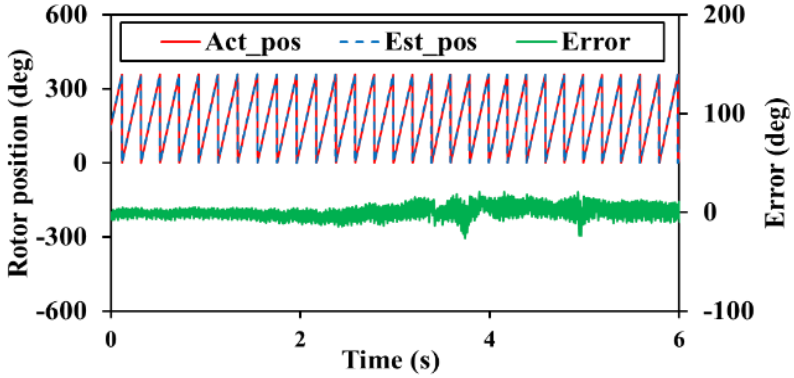

(b)) Rotor position

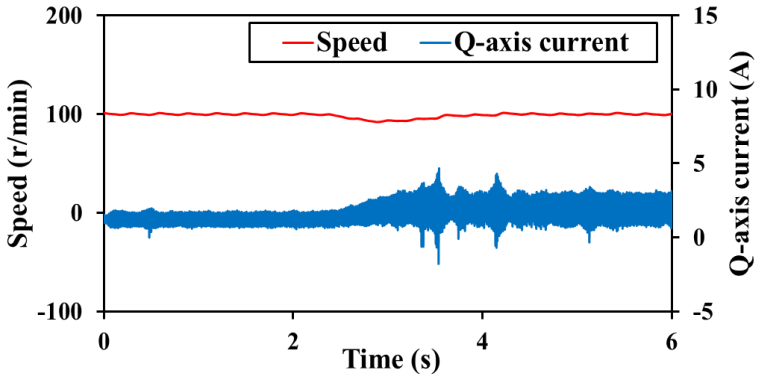

(c) Speed and *q*-axis current

Fig. 4.17. Measured results with and *q*-axis current increased from 1.5 A to 2.5 A when the proposed sensorless control method using 200 Hz harmonics. (a) dc-link voltage. (b) Rotor position. (c) Speed and *q*-axis current.

4.5 Conclusion

This chapter first identifies and investigates the instability issues of the conventional pulsating signal injection-based sensorless control method in small dc-link capacitor-based IPMSM drive systems under severe dc-link voltage fluctuation. Secondly, a novel position sensorless control

method utilizing the inherent current harmonics caused by small dc-link capacitor is proposed.

Furthermore, a magnetic polarity detection method that utilizes the inherent current harmonics is proposed. The proposed magnetic polarity detection method achieves more evident detection results by using lower-frequency current harmonics and larger amplitude current harmonics under heavy load conditions.

Finally, the experiment results illustrate the effectiveness of the proposed methods, especially under heavy load conditions.

CHAPTER 5

A NOVEL ROBUST POSITION SENSORLESS CONTROL STRATEGY FOR IPMSM DRIVES WITH SMALL DC-LINK CAPACITOR

Based on the proposed sensorless control method discussed in Chapter 4, the lookup table, despite its usefulness, has certain limitations. One significant issue is the dependency on precomputed data, which requires extra memory resources. Also, if the input data does not precisely match the values stored in the lookup table, a parameter mismatch can be introduced that compromises the accuracy of the rotor position estimation. In addition, the proposed sensorless control method requires not only the *dq*-axis current signals but also the amplitudes and phases of the *dq*-axis voltages. This dependency on multiple variables can limit the precision of rotor position estimation and, consequently, the overall system performance.

To address these challenges, this chapter introduces an improved sensorless control method that is immune to motor parameter mismatch. The proposed robust sensorless control method requires only the *q*-axis current and the phase angle of the *dq*-axis voltages, particularly reducing the sensitivity to multiple variables. This approach enhances the precision and reliability of the sensorless control strategies, ensuring better performance and robustness under various operating conditions. Finally, the proposed sensorless control method based on 100 Hz and 200 Hz harmonics is compared systemically. Experimental results demonstrate the effectiveness and robustness of the proposed sensorless control, particularly under heavy load conditions. The proposed methods provide robust solutions for sensorless control under severe dc-link voltage fluctuation, ensuring reliable performance in varying operation conditions.

This chapter is based on the chapter submitted in:

J. Yan, Z. Q. Zhu, X. M. Wu, Y. Chen, H. Yang, L. H. Yang, and C. H. Liu, “A novel position sensorless control strategy for IPMSM drives with small dc-link capacitor,” *IEEE Trans. Power Electron.*, Under review.

5.1 Introduction

In recent years, the development of small dc-link capacitor-based PMSM drive systems has

garnered substantial attention due to their high efficiency, compact size, and lower cost [ZHU07] [JUN14] [SAR05] [WAN18A] [ZHA19A] [WAN20B] [ZHU23]. A crucial aspect of PMSM drive systems is the accurate estimation of the rotor position, which is essential for achieving precise control and optimal performance. Traditionally, position sensors such as encoders or resolvers are used. However, these sensors add to the cost, size, and complexity of the system, prompting the need for sensorless control methods [ZHU23] [WAN20A]. Sensorless control methods typically rely on the estimation of the rotor position using electrical signals such as voltages and currents [LIU14] [ZHU23] [WAN20A]. One common approach in the zero and low-speed range involves the use of HF voltage signal injection to extract the rotor position information [JEO05B] [JAN06] [LI09] [RAC10] [YOO11] [CUP12] [GON13] [XU16A] [XU16B] [WAN16] [YAN17] [WAN17A] [ZHA18B] [NAD24]. However, this method has its limitations, particularly in systems with small dc-link capacitors where the dc-link voltage is fluctuating. The insufficient dc-link voltage caused by voltage fluctuations can restrain the effectiveness of HF signal injection. Moreover, the conventional HF voltage signal injection methods tend to increase losses, torque ripples, and acoustic noise, which are undesirable in high-performance drive systems [ZHU23] [WAN20A].

In Chapter 4, a sensorless control method utilizes the unavoidable current harmonics induced by dc-link voltage fluctuation to obtain the rotor position, without the need for extra HF voltage signal injection. While this method offers several advantages, it also depends heavily on accurate motor parameters, particularly the *dq*-axis inductances. This dependency necessitates the use of a lookup table, which, despite its utility, presents several drawbacks. The lookup table approach requires extra memory resources to store precomputed data. Additionally, when input data do not exactly match the stored values which potentially introduce errors that compromise the accuracy of rotor position estimation.

To overcome these challenges, this chapter proposes an improved sensorless control strategy that cancels the sensitivity to motor parameter mismatch. The proposed method only requires the *q*-axis current and the phase angle of the *dq*-axis voltages, thereby reducing the reliance on precise variations. This robust approach enhances the precision and reliability of the proposed sensorless control method, ensuring better performance across various operating conditions. Finally, the comparison study of the proposed methods using different harmonics (100 Hz harmonic and 200 Hz harmonics) is investigated in this Chapter.

5.2 Proposed Sensorless Control Method Utilizing Inherent DC-Link Voltage Fluctuation

5.2.1 Proposed Sensorless Control Method Utilizing Inherent DC-Link Voltage Fluctuation

Due to the demodulation method described in Chapter 4 requires accurate motor parameters. Therefore, a novel demodulation method which is immune to the motor parameters is described in this chapter. The estimated position error could be derived by the *dq*-axis current harmonics

$$\begin{aligned}\begin{bmatrix}\left|\hat{i}^{d}_{dh,100\cdot k}\right|\\ \left|\hat{i}^{q}_{dh,100\cdot k}\right|\end{bmatrix} &= \mathrm{LPF}\left(\begin{bmatrix}\hat{i}_{dh,100\cdot k}2\sin\left(\omega_{100\cdot k}t+\varphi_{d_{100\cdot k}}\right)\\ \hat{i}_{dh,100\cdot k}2\sin\left(\omega_{100\cdot k}t+\varphi_{q_{100\cdot k}}\right)\end{bmatrix}\right)\\ &= \begin{bmatrix} Q_n\sin(2\Delta\theta_r)\,\delta_{dq}+D_p+D_n\cos(2\Delta\theta_r)\\ Q_n\sin(2\Delta\theta_r)+D_p\delta_{dq}+D_n\cos(2\Delta\theta_r)\,\delta_{dq}\end{bmatrix}\end{aligned} \tag{5.1}$$

$$\delta_{dq}=\cos\left(\varphi_{u_q}-\varphi_{u_d}\right) \tag{5.2}$$

$$\begin{aligned}\begin{bmatrix}\left|\hat{i}^{d}_{qh,100\cdot k}\right|\\ \left|\hat{i}^{q}_{qh,100\cdot k}\right|\end{bmatrix} &= \mathrm{LPF}\left(\begin{bmatrix}\hat{i}_{qh,100\cdot k}2\sin\left(\omega_{100\cdot k}t+\varphi_{d_{100\cdot k}}\right)\\ \hat{i}_{qh,100\cdot k}2\sin\left(\omega_{100\cdot k}t+\varphi_{q_{100\cdot k}}\right)\end{bmatrix}\right)\\ &= \begin{bmatrix} D_n\sin(2\Delta\theta_r)+Q_p\delta_{dq}-Q_n\cos(2\Delta\theta_r)\delta_{dq}\\ D_n\sin(2\Delta\theta_r)\,\delta_{dq}+Q_p-Q_n\cos(2\Delta\theta_r)\end{bmatrix}\end{aligned} \tag{5.3}$$

$$\left|\hat{i}^{q}_{dh,100\cdot k}\right|-\left|\hat{i}^{d}_{dh,100\cdot k}\right|\delta_{dq}=Q_n\sin(2\Delta\theta_r)\,(1-\delta_{dq}^2) \tag{5.4}$$

$$\left|\hat{i}^{d}_{qh,100\cdot k}\right|-\left|\hat{i}^{q}_{qh,100\cdot k}\right|\delta_{dq}=D_n\sin(2\Delta\theta_r)\,(1-\delta_{dq}^2) \tag{5.5}$$

where $\hat{i}^{d}_{dh,100\cdot k}$, $\hat{i}^{q}_{dh,100\cdot k}$, $\hat{i}^{d}_{qh,100\cdot k}$, and $\hat{i}^{q}_{qh,100\cdot k}$ are the demodulated *dq*-axis currents by phase angle of *dq*-axis voltages, δ_{dq} is the cosine of the phase difference between *dq*-axis voltages.

Both fluctuating *dq*-axis current can be demodulated to obtain signals containing rotor position information. However, in the FOC with i_d=0 method, the *q*-axis current harmonic components are typically larger than those in the *d*-axis. Therefore, only the *q*-axis current is used to estimate the rotor position. It is worth mentioning that the term δ_{dq} represents the cosine of the phase angle difference between the *d*-axis and the *q*-axis voltages. Normally, the phase angle difference of *dq*-axis voltages is not 0 or 180 degrees. Therefore, $(1-\delta_{dq}^2)$ cannot be zero. From (5.5), the proposed sensorless control method only requires the *q*-axis current and the

phase angle of the dq-axis voltages. Fig. 5.1 shows the block diagram of the proposed sensorless control method. The $100 \cdot k$ Hz q-axis current harmonic is obtained using a BPF. Then, processed by (5.3) and (5.5). The signal with the rotor position information is obtained. When the signal approaches 0 by the position observer, the actual rotor position is obtained.

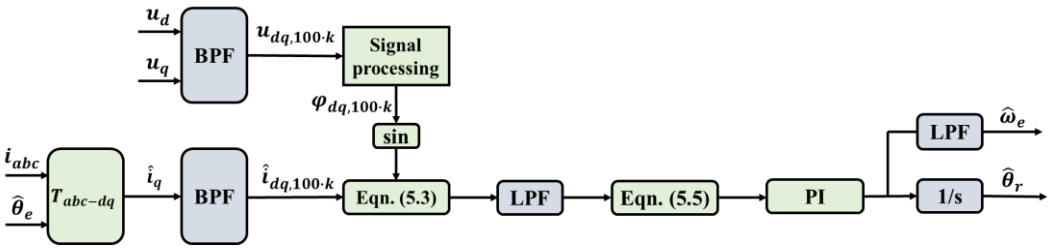

Fig. 5.1. Block diagram of proposed sensorless control method.

5.2.2 Current Harmonic Selection for Position Estimation

As shown in the Chapter 4, the measured results for the small dc-link capacitor-based IPMSM drive systems are shown in Fig. 5.2. The dc-link capacitance is set at 20 μF, the motor speed is maintained at 100 r/min, and the q-axis current is 2 A. As described before, in the small dc-link capacitor-based IPMSM drive systems, the AC source voltage is rectified by an uncontrolled single-phase rectifier, resulting in the notable 100 Hz harmonic components into the dc-link voltage. Additionally, due to the discharge characteristics of the dc-link capacitor, 200 Hz harmonics can also be observed. As shown in Fig. 5.2, the small dc-link capacitor mainly introduces notable 100 Hz and 200 Hz harmonics into the IPMSM drive systems. Both harmonics can be effectively utilized for rotor position estimation and magnetic polarity detection. However, utilizing 100 Hz and 200 Hz harmonics for rotor position estimation and magnetic polarity detection presents distinct advantages and disadvantages. The 100 Hz harmonic always has a larger amplitude and shows a potential versatility across a wider range of operating conditions. Additionally, the 100 Hz harmonic is particularly well-suited for magnetic polarity detection due to its higher amplitude and lower frequency [JEO05B] [LI09]. However, the implementation of the proposed sensorless control method based on the 100 Hz harmonic results in a reduction of the LPF bandwidth in the demodulation process, consequently affecting the dynamic performance of the system [WAN17B] [NIM14]. Conversely, using 200 Hz harmonic may be more suitable. Nonetheless, the 200 Hz harmonic exhibits a smaller amplitude, thereby restricting its applicability.

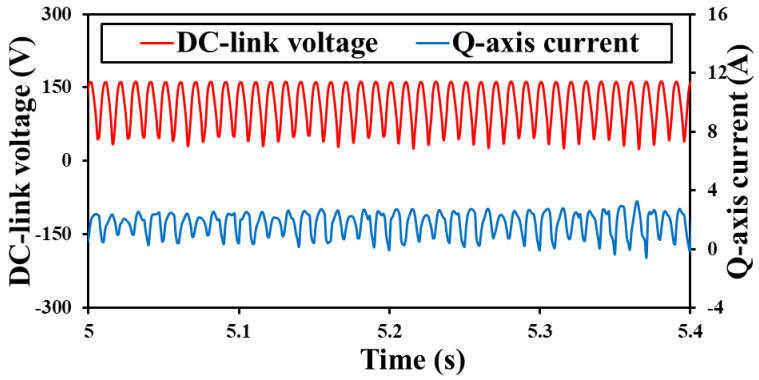

(a) dc-link voltage and *q*-axis current

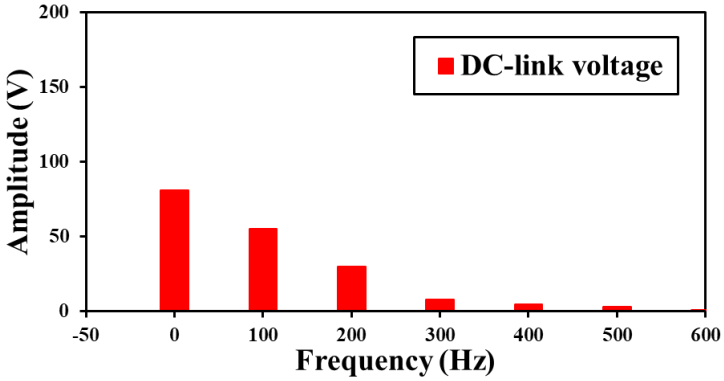

(b) Spectrum of dc-link voltage

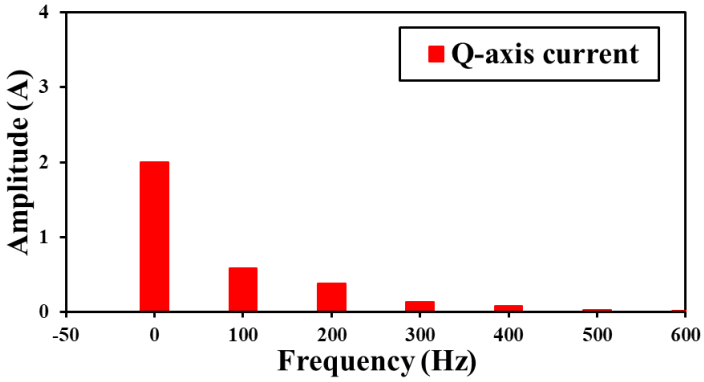

(c) Spectrum of *q*-axis current

Fig. 5.2. Measured results of small dc-link capacitor-based IPMSM drive system. (a) dc-link voltage and *q*-axis current. (b) Spectrum of dc-link voltage. (c) Spectrum of *q*-axis current.

5.3 Experiment Validation

In this section, the performance of the proposed robust sensorless control methods based on 100 Hz and 200 Hz are validated. Then, the proposed methods based on 100 Hz and 200 Hz current harmonics are systematically compared.

5.3.1 Proposed Sensorless Control Method Utilizing Inherent DC-link Voltage Fluctuation

Fig. 5.3 to Fig. 5.5 present the waveform of the proposed sensorless control method based on 200 Hz harmonics under various operating conditions (from Fig. 5.3 to Fig. 5.5: 50 r/min and *q*-axis current is 1 A, 50 r/min and *q*-axis current is 2 A, 100 r/min and *q*-axis current is 2 A). It can be observed that when the system operates at 50 r/min and *q*-axis current is 1 A, the dc-link voltage fluctuations are small, and the harmonic components in the system are minimal. In this scenario, it is difficult to accurately estimate the rotor position with the proposed sensorless control method, resulting in poor control performance. When the *q*-axis current increased to 2 A, the harmonic components in the system become more significant, with the dc-link voltage peak-to-peak value reaching 110 V, and the *dq*-axis voltage peak-to-peak values also increasing. Under these conditions, the rotor position can be accurately estimated, resulting in good control performance. When the motor speed is increased to 100 r/min, the dc-link voltage peak-to-peak value is slightly increased, and the *dq*-axis voltage peak-to-peak values are further increased. The rotor position can still be accurately estimated, although the system will have a certain number of harmonic components.

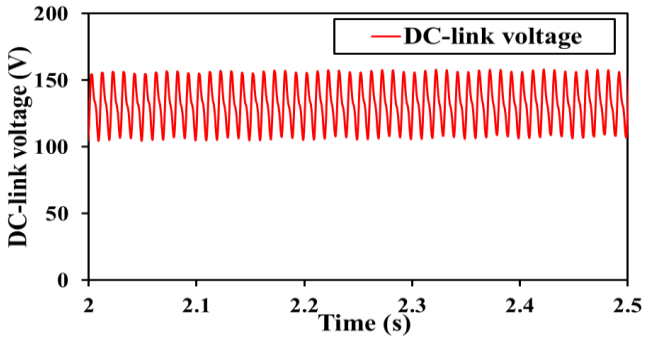

(a) dc-link voltage

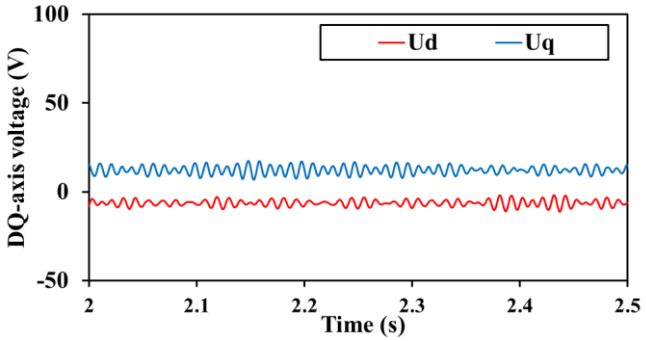

(b) *dq*-axis voltage

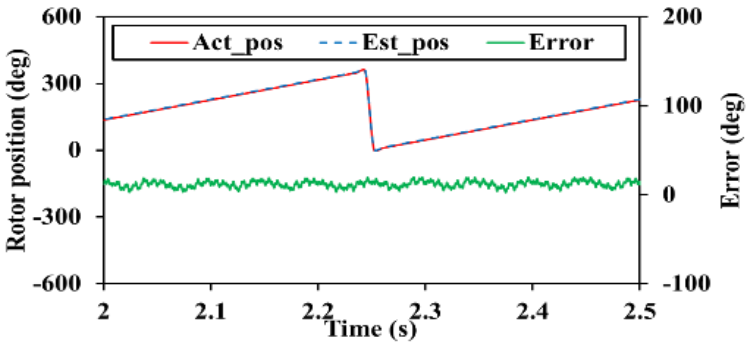

(c) Rotor position

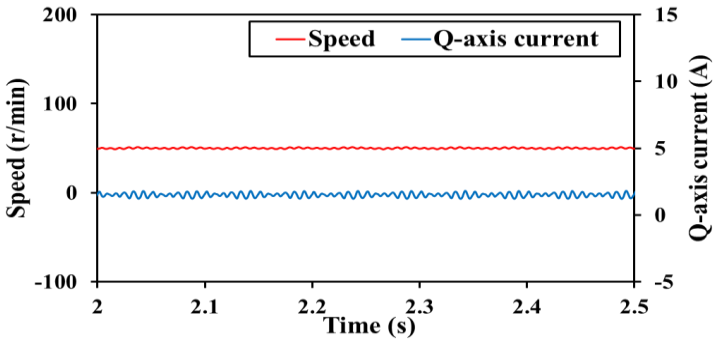

(d) Speed and *q*-axis current

Fig. 5.3. Measured results of proposed sensorless control method with 200 Hz harmonics under 50 r/min with 1 Nm load. (a) dc-link voltage. (b) *dq*-axis voltage. (c) Rotor position. (d) Speed and *q*-axis current.

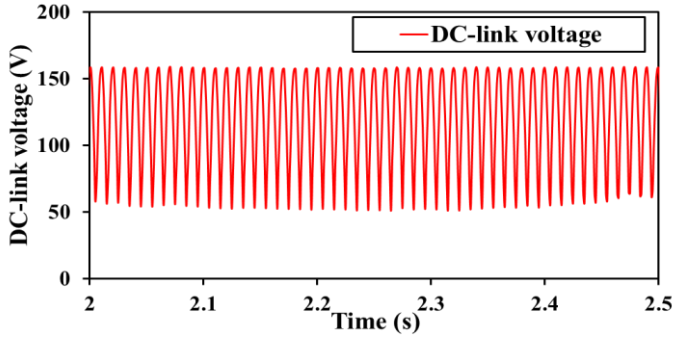

(a) dc-link voltage

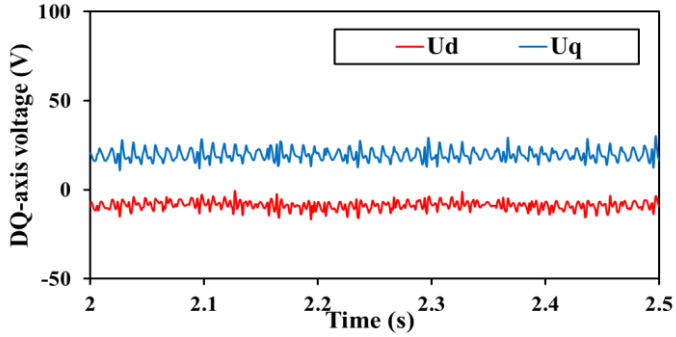

(b) *dq*-axis voltage

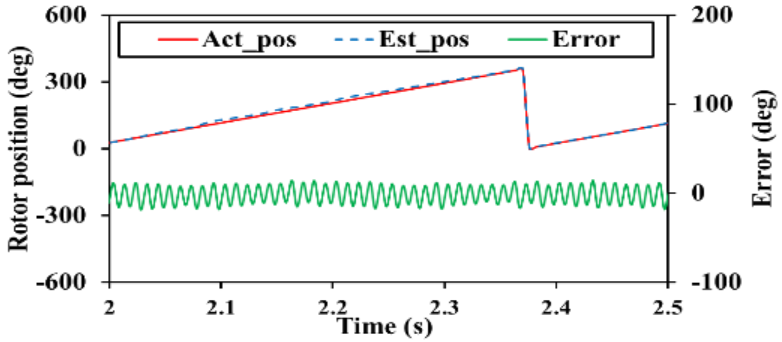

(c) Rotor position

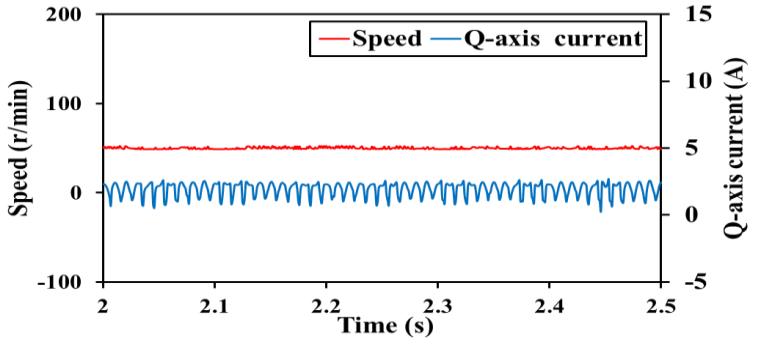

(d) Speed and *q*-axis current

Fig. 5.4. Measured results of proposed sensorless control method with 200 Hz harmonics under 50 r/min with 2 Nm load. (a) dc-link voltage. (b) *dq*-axis voltage. (c) Rotor position. (d) Speed and *q*-axis current.

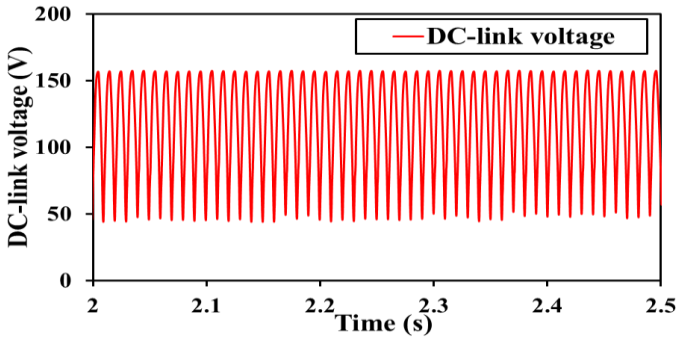

(a) dc-link voltage

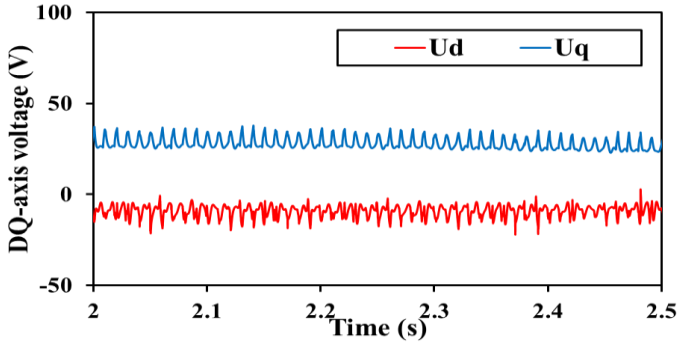

(b) *dq*-axis voltage

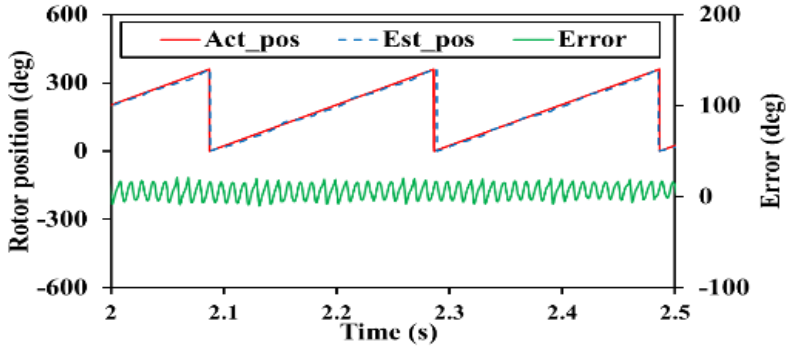

(c) Rotor position

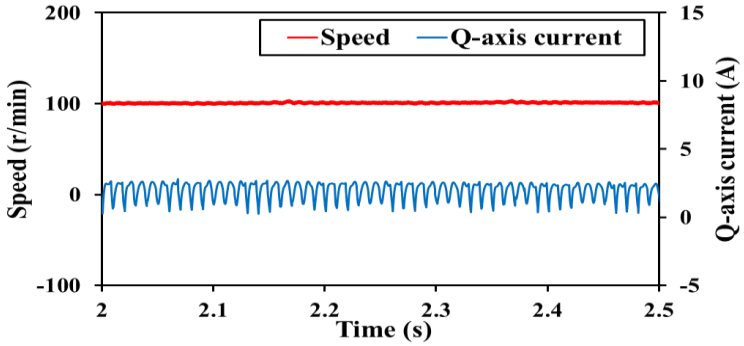

(d) Speed and *q*-axis current

Fig. 5.5. Measured results of proposed sensorless control method with 200 Hz harmonics under 100 r/min with 2 Nm load. (a) dc-link voltage. (b) *dq*-axis voltage. (c) Rotor position. (d) Speed and *q*-axis current.

Fig. 5.6 to Fig. 5.8 present the experimental results of the proposed sensorless control method based on 100 Hz harmonics under various operating conditions (from Fig. 5.6 to Fig. 5.8: 50 r/min and q-axis current is 1 A, 50 r/min and q-axis current is 2 A, 100 r/min and q-axis current is 2 A). At 50 r/min and q-axis current is 1 A, the dc-link voltage exhibits minimal fluctuations, and the system harmonics are low. However, the proposed sensorless control method can still operate stably. As the q-axis current is increased to 2 A, the harmonic components in the system become more notable. Under these conditions, the rotor position is accurately estimated. When the motor speed is increased to 100 r/min and q-axis current is 2 A, the dc-link voltage peak-to-peak value and the dq-axis voltage peak-to-peak values increase slightly. Despite the presence of some harmonic components, rotor position estimation remains accurate. Fig. 5.9 shows that the motor speed is changed from 0 r/min to 100 r/min and the q-axis current changes from 0 A to 4 A. The proposed method ensures stable operation when the q-axis current exceeds 1 A. While the proposed method struggles with q-axis current below 1 A due to small current harmonics, conventional methods perform well under these light loads. The proposed method based on 100 Hz harmonics, together with the conventional HFSI-based sensorless control methods ensures stable operation under any load conditions.

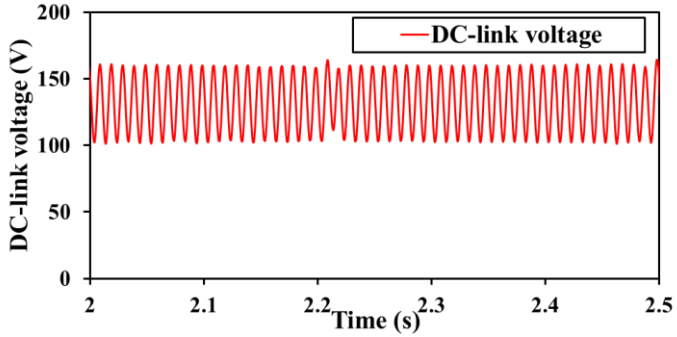

(a) dc-link voltage

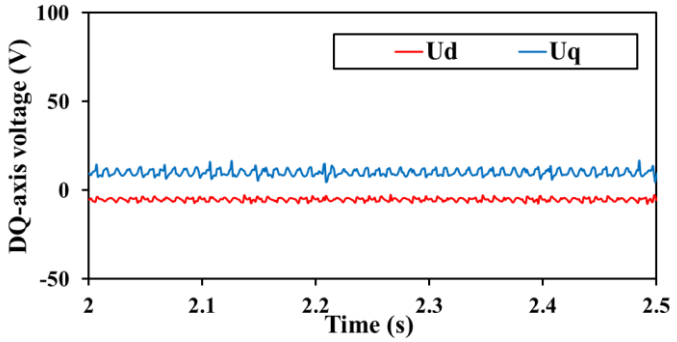

(b)) dq-axis voltage

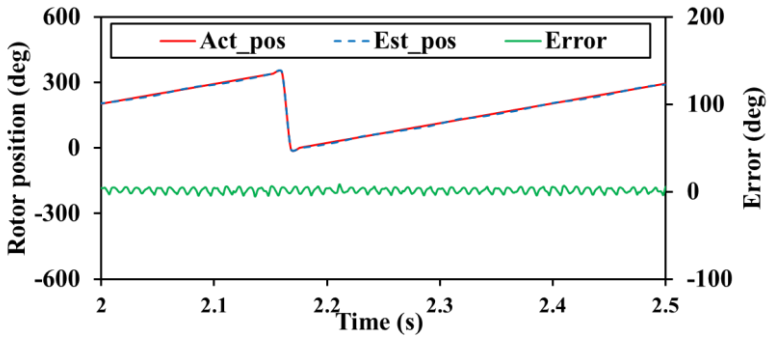

(c) Rotor position

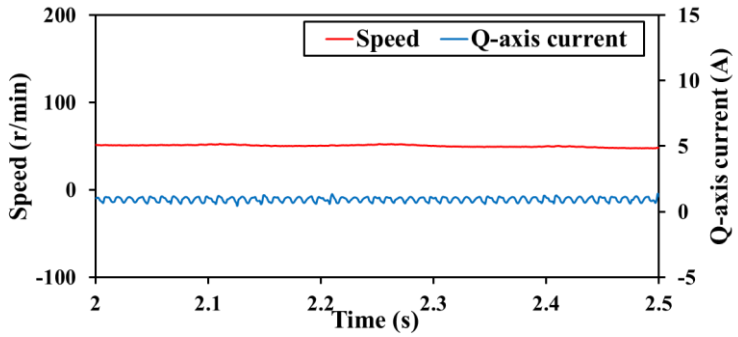

(d) Speed and *q*-axis current

Fig. 5.6. Measured results of proposed sensorless control method with 100 Hz harmonics under 50 r/min with 1 Nm load. (a) dc-link voltage. (b) *dq*-axis voltage. (c) Rotor position. (d) Speed and *q*-axis current.

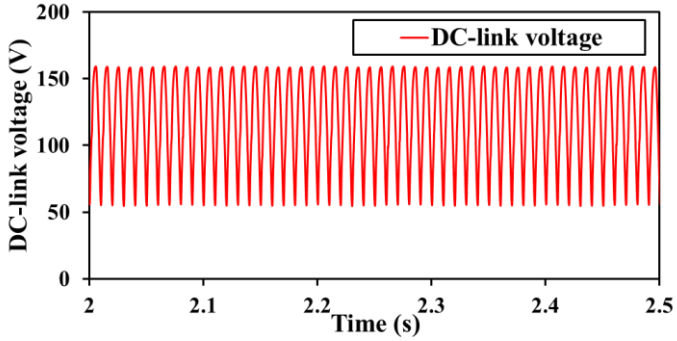

(a) dc-link voltage

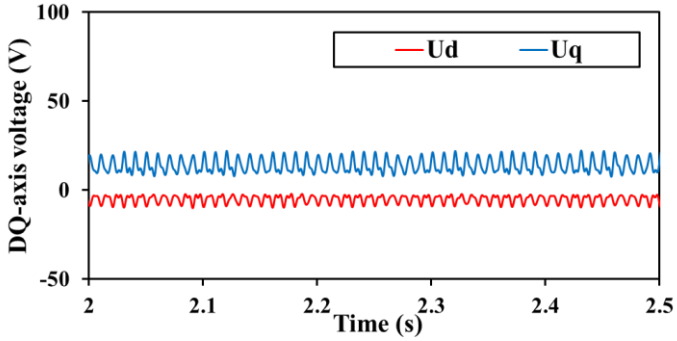

(b)) *dq*-axis voltage

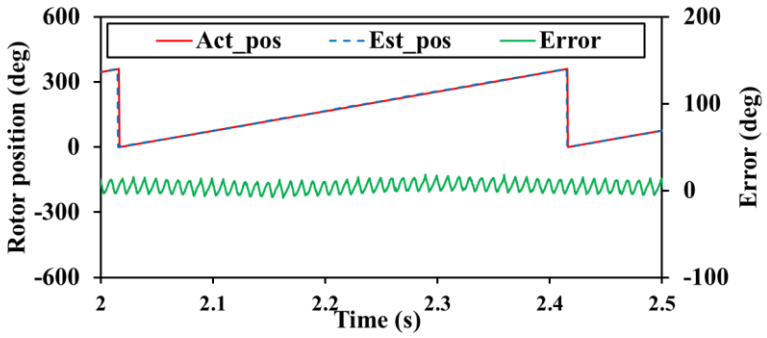

(c) Rotor position

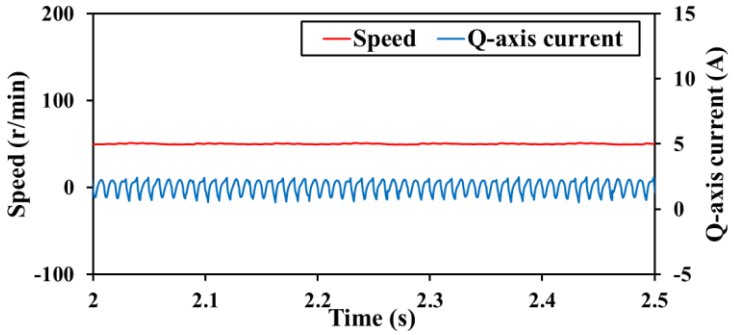

(d) Speed and *q*-axis current

Fig. 5.7. Measured results of proposed sensorless control method with 100 Hz harmonics under 50 r/min with 2 Nm load. (a) dc-link voltage. (b) *dq*-axis voltage. (c) Rotor position. (d) Speed and *q*-axis current.

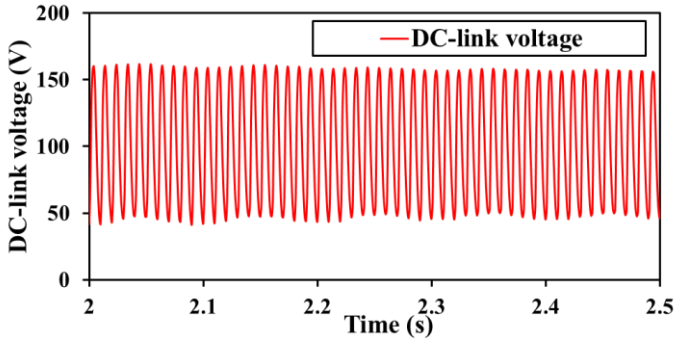

(a) dc-link voltage

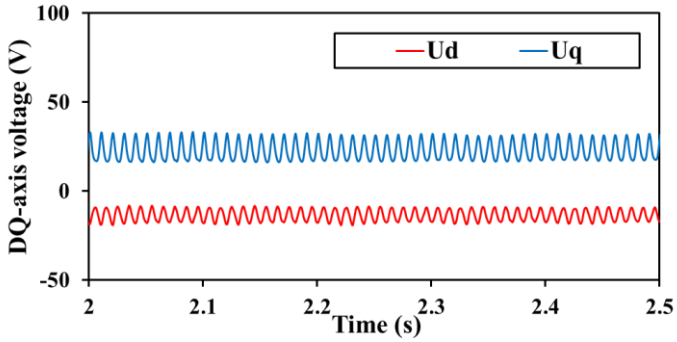

(b)) *dq*-axis voltag、

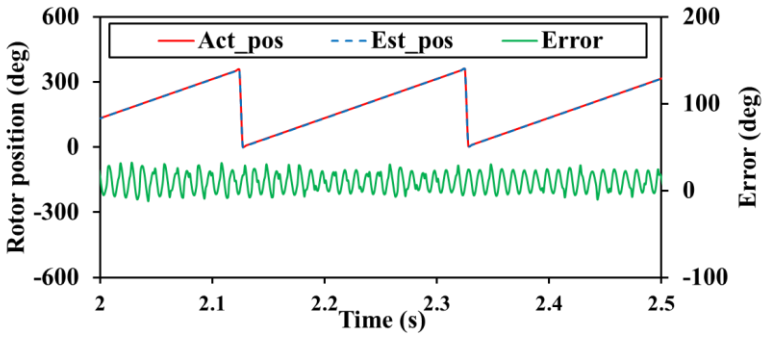

(c) Rotor position

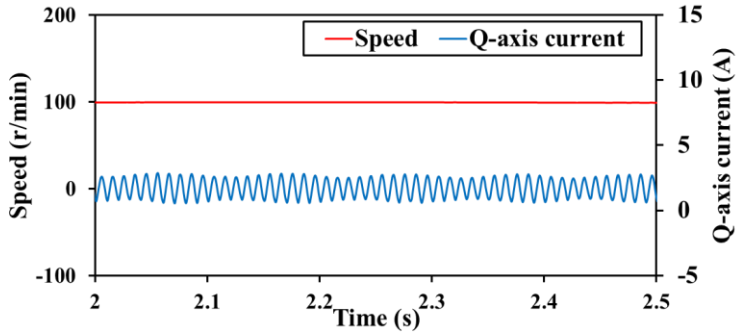

(d) Speed and *q*-axis current

Fig. 5.8. Measured results of proposed sensorless control method with 100 Hz harmonics under 100 r/min with 2 Nm load. (a) dc-link voltage. (b) *dq*-axis voltage. (c) Rotor position. (d) Speed and *q*-axis current.

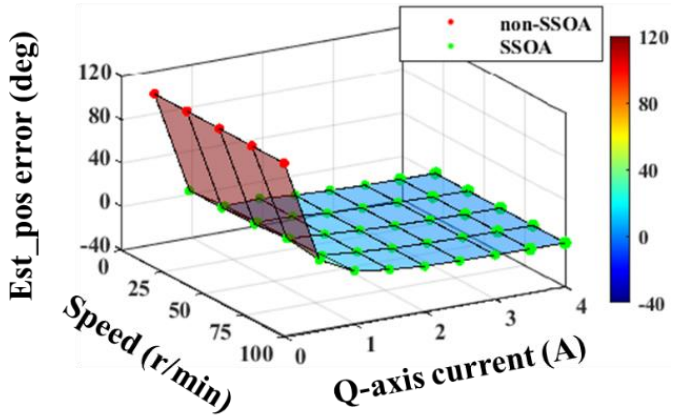

Fig. 5.9. Close-loop control performance of proposed sensorless control method with 100 Hz harmonics in small dc-link capacitor-based IPMSM drive system under different speed and load conditions.

Fig. 5.10 and Fig. 5.11 illustrate the dynamic control performance of the proposed sensorless control method based on 100 Hz harmonic. In Fig. 5.10, the motor speed is increased from 50 r/min to 100 r/min with a *q*-axis current of 1.5 A. During this period, the peak-to-peak value of the dc-link voltage rises from 80 V to 100 V. Despite the presence of some harmonics in the

estimated position error, the proposed sensorless control method accurately tracks the actual rotor position. In Fig. 5.11, the motor speed is kept constant at 100 r/min while the *q*-axis current increases from 1 A to 2.5 A. The estimated rotor position consistently aligns with the actual rotor position. These results demonstrate that the proposed sensorless control method maintains high performance under dynamic conditions.

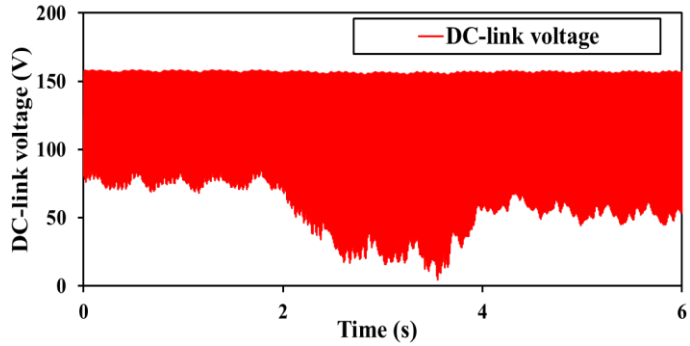

(a) dc-link voltage

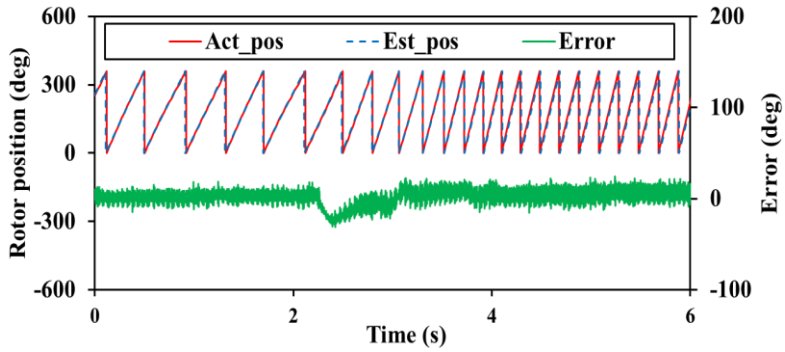

(b) Rotor position

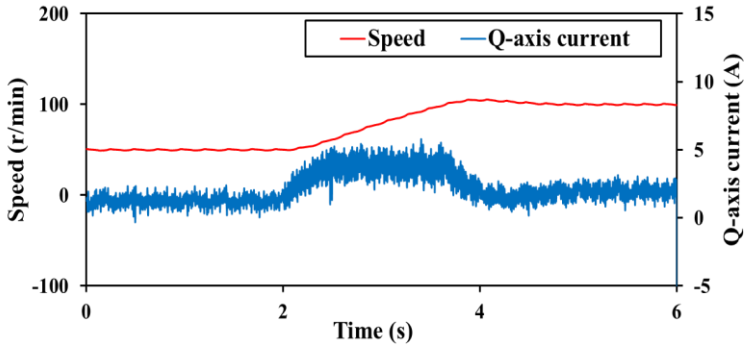

(c) Speed and *q*-axis current

Fig. 5.10. Measured results with speed increased from 50 r/min to 100 r/min when the proposed sensorless control method using 100 Hz harmonics. (a) dc-link voltage. (b) Rotor position. (c) Speed and *q*-axis current.

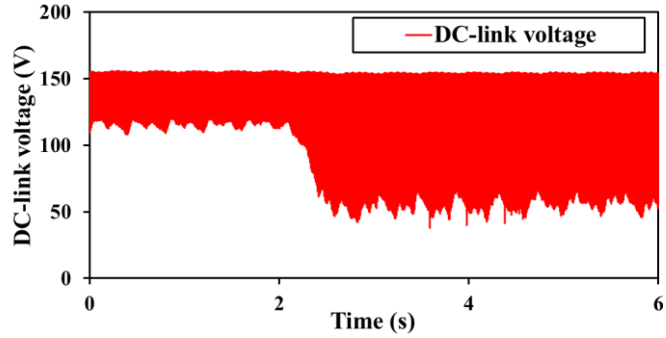

(a) dc-link voltage

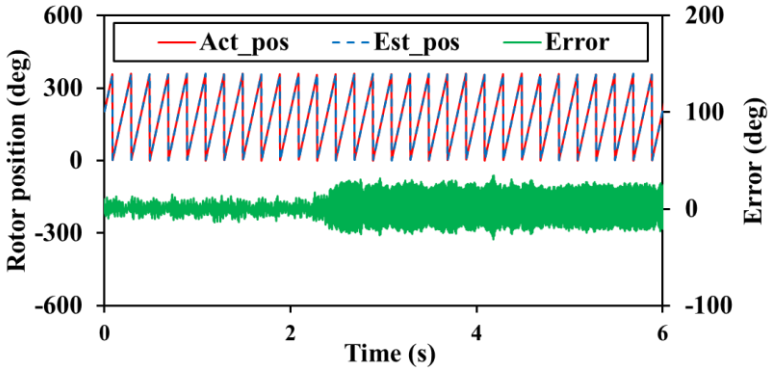

(b) Rotor position

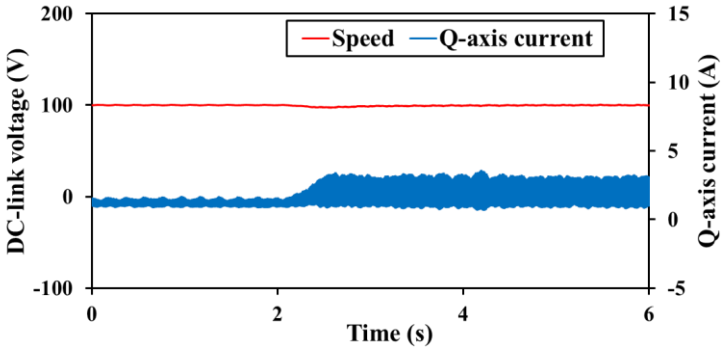

(c) Speed and *q*-axis current

Fig. 5.11. Measured results with and *q*-axis current increased from 1 A to 2.5 A when the proposed sensorless control method using 100 Hz harmonics. (a) dc-link voltage. (b) Rotor position (c) Speed and *q*-axis current.

5.3.2 Comparison of Proposed Sensorless Control Method with 100 Hz and 200 Hz Harmonic

Fig. 5.12 shows the measured results of the proposed sensorless control method with different harmonics under different operation conditions. In Fig. 5.12(a), the proposed sensorless control method based on 100 Hz harmonic ensures stable operation when the *q*-axis current exceeds 1

A, which can eliminate the limitations of conventional HFSI-based sensorless control methods under heavy load conditions. While the proposed sensorless method based on 200 Hz harmonics can only operate normally when the *q*-axis current exceeds 1.5 A. Fig. 5.12(b) combines the measured results of the proposed sensorless control method with different harmonics. It can be demonstrated that the proposed sensorless control method based on 100 Hz harmonic has a larger SSOA compared to the proposed method based on 200 Hz harmonic, making it more effective for a broader range of operating conditions.

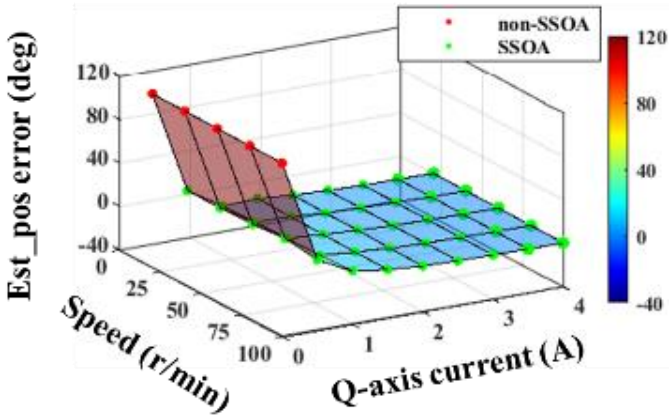

(a)) With 100 Hz harmonics

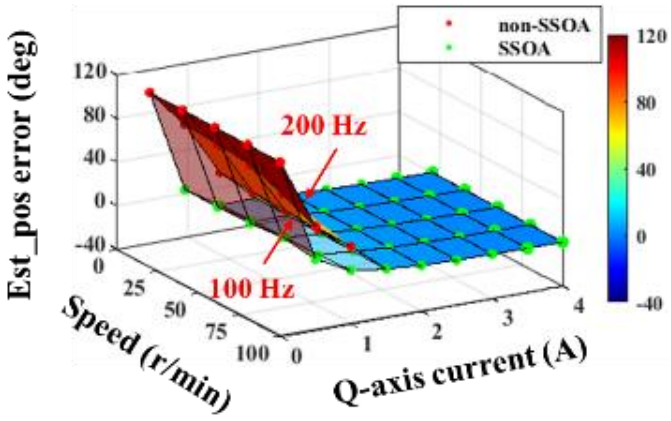

(b) Comparison of proposed sensorless control method based on 100 Hz and 200 Hz harmonics

Fig. 5.12. Control performance of the proposed sensorless control method with different harmonics under different speed and load conditions. (a) With 100 Hz harmonics. (b) Combination of proposed sensorless control method based on 100 Hz and 200 Hz harmonics.

Fig. 5.13 shows the comparison of the magnetic polarity detection of the proposed detection method based on 100 Hz harmonics and 200 Hz harmonics when the estimated rotor position error is 0 rad and π. It is revealed that the proposed sensorless control method based on 100 Hz harmonics shows more distinguishable polarity detection results compared to the method based

on 200 Hz harmonics, due to the lower 100 Hz harmonic frequency having a larger amplitude.

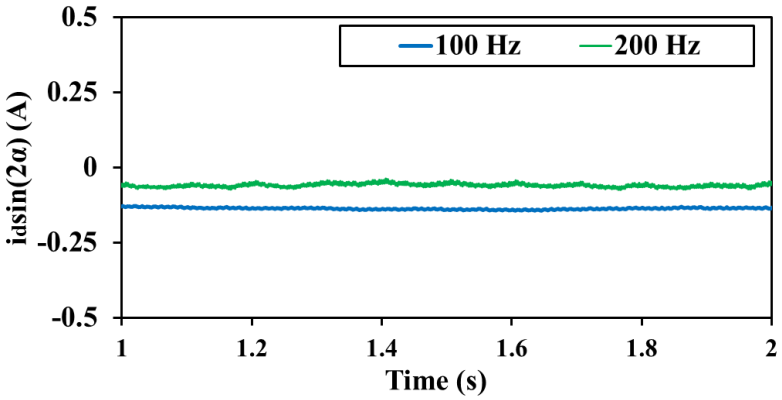

(a)) $\Delta\theta_r = 0$

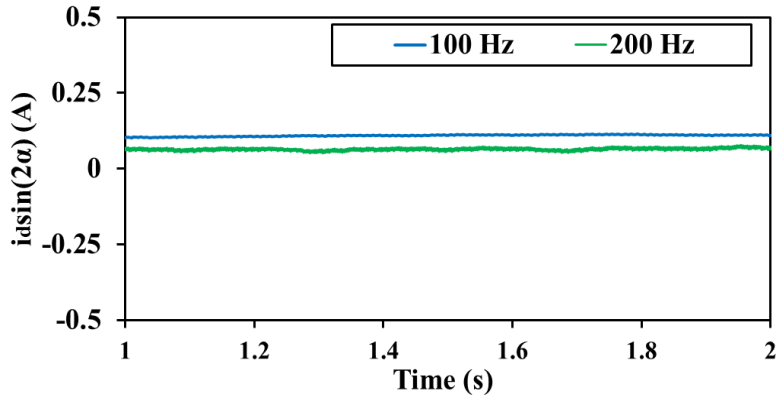

(b) $\Delta\theta_r = \pi$

Fig. 5.13. Comparison of the proposed polarity detection method based on 100 Hz and 200 Hz harmonics. (a) $\Delta\theta_r = 0$. (b) $\Delta\theta_r = \pi$.

According to [WAN17B] [NIM14], lower frequency signal injection strategies exhibit poorer dynamic characteristics due to the low bandwidth of LPF in the demodulation process. The experimental results confirm that the proposed sensorless control method based on 100 Hz harmonics has a slower dynamic response compared to the method based on 200 Hz harmonics.

Fig. 5.14 shows the comparison of the dynamic control performance of the proposed sensorless control method based on 100 Hz harmonics and based on 200 Hz harmonics. In this experiment, the motor speed increased from 100 r/min to 150 r/min. The proposed sensorless control method based on 100 Hz harmonics requires 3.2 seconds to achieve this speed change, while the method based on 200 Hz harmonics takes 2.4 seconds.

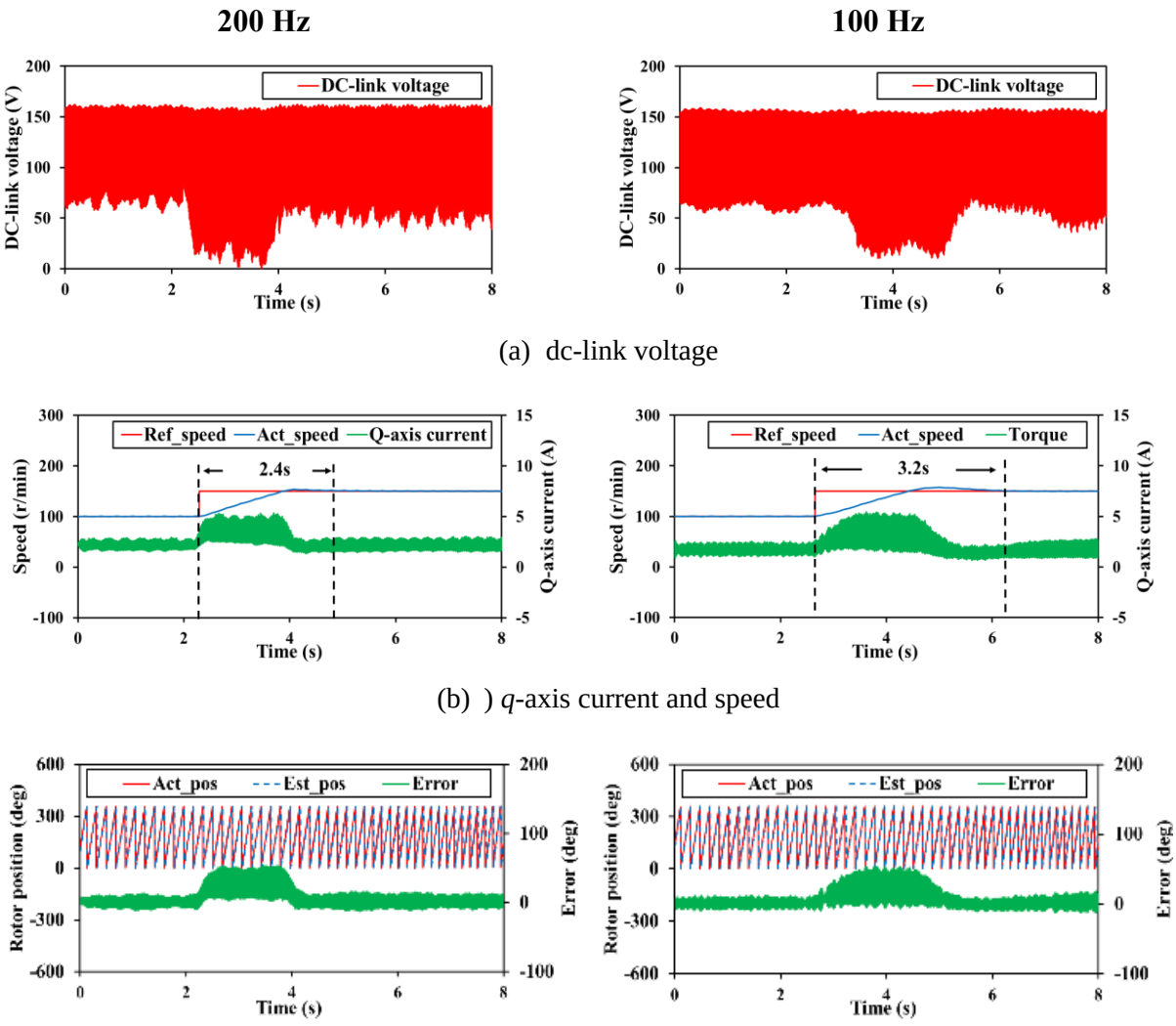

Fig. 5.14. Comparison of dynamic control performance of proposed sensorless control method based on 100 Hz and 200 Hz harmonics. (a) dc-link voltage. (b) *q*-axis current and speed. (a) Rotor position.

Table I compares the proposed methods based on 100 Hz and 200 Hz harmonics, respectively. The 100 Hz harmonic has a higher amplitude and wider applicability compared to the 200 Hz harmonic, which has medium amplitude and applicability. The 100 Hz harmonic method can be used when *q*-axis current greater than 1 A, while the 200 Hz harmonic method requires a *q*-axis current greater than 2 A. The bandwidth of the LPF in the demodulation process is lower for 100 Hz harmonic and medium for 200 Hz harmonic. Static performance is better for the 100 Hz harmonic, while dynamic performance is better for the 200 Hz harmonic. However, regardless of whether 100 Hz or 200 Hz harmonic is used, both can provide robust solutions for position sensorless control and magnetic polarity detection under significant dc-link voltage fluctuation.

TABLE 5.1

COMPARISON OF PROPOSED SENSORLESS CONTROL METHOD BASED ON 100 HZ AND 200 HZ HARMONICS

Attribute	**100 Hz Harmonic**	**200 Hz Harmonic**
Amplitude	High	Medium
Applicability	Wide	Medium
Lowest q-axis current required	1 A	2 A
Bandwidth of LPF	Low	Medium
Static performance	Good	Medium
Dynamic performance	Medium	Good
SNR	High	Medium
Polarity detection	Good	Medium

5.4 Conclusion

This chapter proposed a robust sensorless control method utilizing the inherent current harmonics caused by small dc-link capacitor which is immune to the motor parameter mismatch. Then a comparison study of using different harmonics reveals that the 100 Hz harmonic-based methods have a broader applicability and better static performance, and the 200 Hz harmonic-based methods have a better dynamic performance which provide a valuable insight for optimizing sensorless control strategies.

Finally, the experiment results illustrate the effectiveness and robustness of the proposed methods, particularly under heavy load conditions. The utilization of inherent dc-link voltage fluctuation for rotor position estimation and magnetic polarity detection, combined with the conventional HFSI-based sensorless control method, achieves a reliable and accurate sensorless operation in zero and low-speed ranges for small dc-link capacitor-based IPMSM drive systems under full operation conditions.

CHAPTER 6

ANALYSIS AND MITIGATION STRATEGIES OF ENERGY BACKFLOW IN IPMSM DRIVE SYSTEM WITH SMALL DC-LINK CAPACITOR

This chapter first identifies and investigates the unavoidable energy backflow phenomenon in small dc-link capacitor-based PMSM drive systems. This phenomenon arises when the amplitude of the back-EMF exceeds the minimum value of the fluctuating dc-link voltage due to severe voltage fluctuations. To address this issue, the FW control method can effectively reduce the back-EMF by adjusting the *d*-axis current, thereby mitigating the energy backflow phenomenon. However, the dc-link voltage fluctuation can introduce several challenges to the conventional FB-FW control method. For instance, the *dq*-axis voltages also fluctuate due to dc-link voltage fluctuation, which can degrade the performance of the FW control method. Specifically, a dc offset is identified in the calculated *d*-axis reference current due to the dc-link voltage and *dq*-axis voltages fluctuation. Then, an analysis of the small-signal model of FB-FW control reveals that severe fluctuations in the *q*-axis voltage, particularly when it becomes negative, can cause the system to enter a positive feedback mode, leading to inherent instability. Moreover, the commonly used PI controller in conventional FB-FW control cannot adequately control the ac component introduced by these fluctuations, further degrading system performance. Therefore, this chapter proposes a novel FW control method based on a quasi-PIR controller and dc offset compensation to obtain the optimal amplitude of the *d*-axis reference current. Furthermore, an optimal phase angle selection method for the *d*-axis reference current, based on the least mean square algorithm and gradient descent algorithm, is introduced to suppress current ripple caused by the fluctuating dc-link voltage.

This chapter is based on the paper submitted in:

J. Yan, Z. Q. Zhu, X. M. Wu, H. Yang, L. H. Yang, and C. H. Liu, “Analysis and mitigation strategies of energy backflow phenomenon in IPMSM drive system with the small dc-link capacitor,” submitted to *IEEE Trans. Energy Convers.*, submitted and under review.

6.1 Introduction

PMSMs are extensively used in various industrial and automotive applications due to their high torque density, high efficiency, and robust performance [JAH99] [ZHU07]. The small dc-link capacitor-based PMSM drive systems have garnered significant attention for their cost-effectiveness, compactness, and extended lifespan [TAK01] [JUN14] [WAN20B]. Furthermore, the dc-link voltage fluctuation caused by a small dc-link capacitor can increase the conduction angle of the diodes in an uncontrolled rectifier bridge, thereby providing conditions for improving the grid side PF [SON17] [ZHA18A]. Therefore, the small dc-link capacitor-based PMSM drive systems are widely used in household appliances or areas with low control accuracy requirements [ZHO16]. However, small dc-link capacitors can inevitably lead to dc-link voltage fluctuation, particularly under high-speed or heavy load conditions. The dc-link voltage fluctuation could introduce harmonic disturbances, which deteriorate the stability, efficiency, and control performance of a PMSM drive system. To better understand and solve these issues caused by small dc-link capacitors, three scenarios for small dc-link capacitor-based PMSM drive systems are categorized in this chapter based on different operation conditions, i.e.

- No disturbance.
- Considerable harmonics in the system, such as in dc-link voltage, dc-link current, *dq*-axis voltages and currents, and torque.
- Energy backflow phenomenon.

The machine usually operates at low speed and light load in the first scenario. The dc-link voltage fluctuation is small, and the harmonics caused by fluctuating dc-link voltage are negligible. Thus, there is no need for optimization or intervention for the system. In the second scenario, the dc-link voltage fluctuation becomes more serious with speed and/or load increases. This results in nonnegligible harmonics in dc-link voltage and current, *dq*-axis voltages, currents, and torque. Therefore, it is necessary to optimize the control strategy and mitigate the effects of these harmonics. The predominant emphasis in existing research is the second scenario. Numerous effective control strategies have been proposed to mitigate the influence of small dc-link capacitors, leading to significant improvements in system stability, efficiency, and overall control performance. For instance, to achieve higher voltage utilization, a robust dc-link voltage control method is developed to eliminate the double-frequency voltage harmonics in the single-phase grid-connected dc/ac converters in [TAG19]. In [WAN20C], a

voltage boundary optimization-based overmodulation method for electrolytic capacitorless PMSM drives is proposed to optimize the overmodulation region and improve dc-link voltage utilization. In [GAO23], a voltage vector angle regulation strategy is proposed to expand the linear modulation region to improve the dc-link voltage utilization and transition performance.

For the poor grid quality caused by LC resonance, the active damping-based mitigation methods are implemented to overcome the instability problem and grid current harmonics due to LC resonance and constant power load effects [MAH13] [LEE14] [MAT17] [WAN18A] [ZHA19C] [HUO22A] [LI22B] [LIU23] [REN24]. A grid current control method is developed to improve the grid current quality by eliminating the sixth harmonics in the rectifier current in [LI22C]. In [TAG19], a grid current harmonics suppression method is proposed based on rectifier current regulation combined with dc-link voltage decoupling method.

For the FW control strategies optimization, in [JUN14], a new concept of "average voltage constraint", combined with FW control, is proposed to mitigate the dc-link voltage fluctuation issues caused by small dc-link capacitor. In [DIN19], an enhanced FW control method is presented, by which the minimized torque ripple and the enhanced dc-link voltage utilization can be achieved by switching between the minimum dc-link voltage control mode and the extended dc-link voltage control mode. The small-signal model of FB-FW control is implemented in [HUO22B]. It is found that significant fluctuations in the *q*-axis voltage caused by the small dc-link capacitor, especially when it turns negative, can push the system into a positive feedback mode, resulting in inherent instability. Therefore, a *q*-axis voltage control strategy is proposed to avoid the positive feedback mode. In [JIN24A], an FW control strategy based on active damping with a voltage angle adjustment method is implemented to reduce the current harmonics caused by voltage angle disturbance. However, in PMSM drive systems with small dc-link capacitors, both the dc-link voltage and *dq*-axis voltages are prone to fluctuations. Conventional PI controllers of voltage loops in FB-FW control struggle to effectively manage ac harmonics. Moreover, the presence of ac components in the voltage signals can create inherent calculation errors in the *d*-axis reference current. This issue has not been adequately addressed in the previous studies.

In the third scenario, the dc-link voltage fluctuation becomes more serious, and the back-EMF also increases. The amplitude of back-EMF would inevitably exceed the fluctuating dc-link voltage during one fluctuation cycle. In this case, the PMSMs would act as a generator charging the dc-link. The energy backflow phenomenon occurs, especially when the machine with small

inductance and high-speed operation. The energy backflow could not only deteriorate the system's stability and efficiency but also can even damage power devices. Therefore, this phenomenon should be prohibited. In [JAH99], the UCG operation of IPMSM following a high-speed inverter shutdown is investigated. The study reveals that IPM machines with high inductance saliency ratios are particularly vulnerable to UCG, which can lead to significant phase currents and braking torque. In [LEE09], a protection scheme for electrolytic capacitorless AC drives to prevent the overvoltage breakdown of semiconductor switches during grid interruptions is proposed. The strategy transfers energy from the *q*-axis to the *d*-axis inductance, maintaining the dc-link voltage within safe limits. In [GON20B], an enhanced model for mitigating uncontrolled generation (UCG) in IPMSM-based electric vehicles during emergencies is presented. By increasing the *d*-axis inductance through changing the rotor structure, the proposed method effectively reduces UCG feedback current, ensuring safer operation. However, existing literature primarily addresses the phenomenon of energy feedback occurring during motor braking or inverter shutdown, assuming the motor is no longer operating normally. In contrast, in small dc-link capacitor-based PMSM drive systems, energy feedback can still occur during normal motor operation, a scenario which has hardly been analyzed and/or mitigated.

Therefore, this chapter first identifies and comprehensively analyzes the energy backflow issue in the small dc-link capacitor-based IPMSM drive system. The mechanisms and possible conditions for energy backflow are then discussed in detail. The principle of energy backflow under different speed or load conditions is investigated. Furthermore, the conventional FW control method has been investigated and found to have some drawbacks due to dc-link voltage fluctuation. Therefore, a quasi-PIR-based FW control method with dc offset compensation method is proposed to eliminate the energy backflow phenomenon. In addition, an optimal phase angle selection strategy is proposed to further reduce the harmonics and improve the control performance of the system. The analysis of the energy backflow phenomenon and the effectiveness of the proposed mitigation methods are validated by experiments.

6.2 Analysis of Energy Backflow in Small DC-Link Capacitor-Based PMSM Drive Systems

6.2.1 DC-link voltage fluctuation issues in small dc-link capacitor-based PMSM drive systems

The small dc-link capacitor-based PMSM drive system is composed of a single-phase uncontrolled rectifier, a small dc-link capacitor, and an inverter as shown in Fig. 6.1.

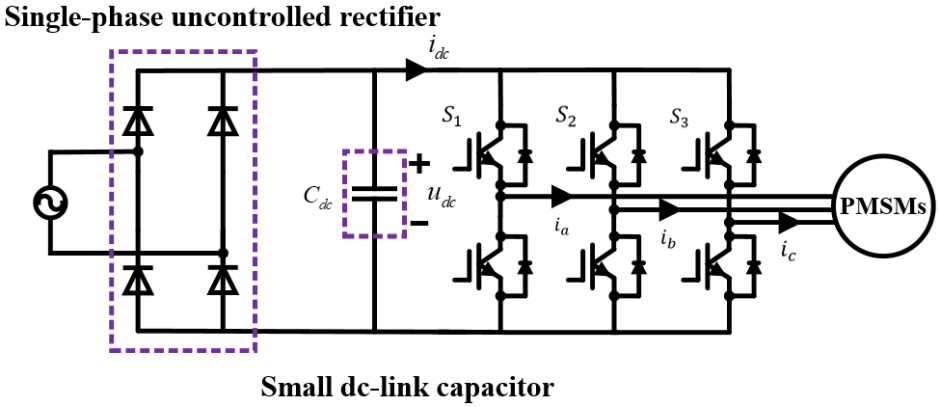

Fig. 6.1. Block diagram of PMSM drive system.

Due to single-phase uncontrolled rectifier and small dc-link capacitor, the dc-link voltage can be expressed as

$$u_{dc} = u_{dc,0} + \sum_{k=1}^{n} u_{dc,k} \sin(2k\omega_g t + \varphi_g) \tag{6.1}$$

where $u_{dc,0}$, $u_{dc,k}$, ω_g,and φ_g are the average value, the kth order harmonic, the phase angle, and the kth order harmonic of fluctuating dc-link voltage.

6.2.2 Principle of Energy Backflow iin Small DC-Link Capacitor-Based PMSM Drive Systems

In the conventional PMSM drive system, a classic three-phase inverter is used to drive the PMSMs as shown in Fig. 6.2(a). Due to the small dc-link capacitor, the dc-link voltage fluctuation could cause the dc-link voltage less than the amplitude of back-EMF, especially when the speed is high and the dc-link voltage fluctuation is severe. During each dc-link voltage fluctuation cycle, when the amplitude of back-EMF is higher than the dc-link voltage, the current could flow back to the dc-link through the freewheel diodes in the inverter. The machine acts as a generator to charge the dc-link capacitor as shown in Fig. 6.2(b). In this case, the

three-phase inverter can be regarded as a three-phase uncontrolled rectifier, and this situation is called energy backflow. The equivalent energy backflow mode is shown in Fig. 6.2(c). Fig. 6.3 shows the corresponding *dq*-axis equivalent circuits for the IPMSM work as the generator.

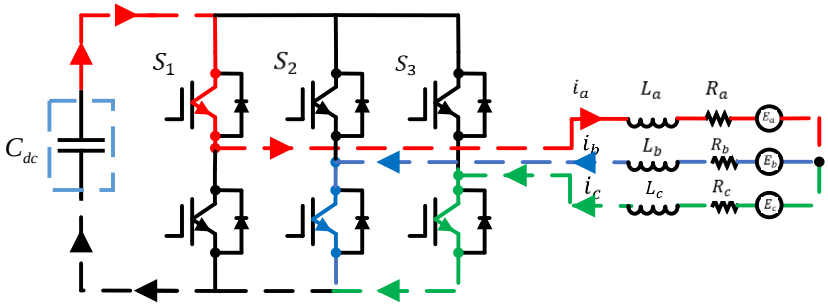

(a) Motor mode

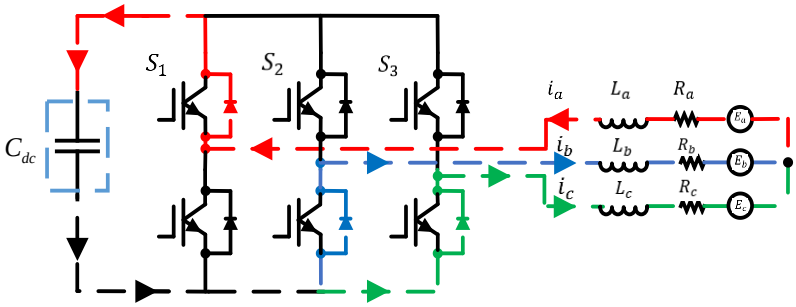

(b) Generator mode

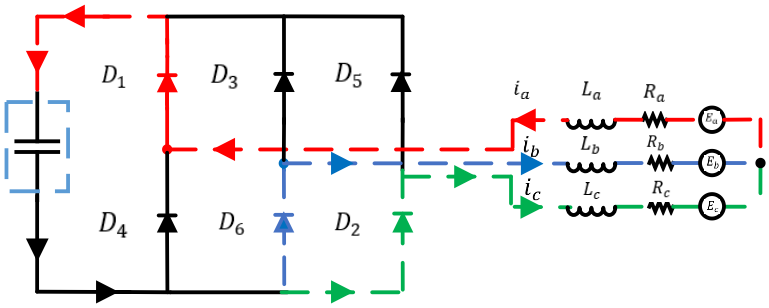

(c) Equivalent energy backflow mode

Fig. 6.2. Different operating modes. (a) Motor mode. (b) Generator mode. (c) Equivalent energy backflow mode.

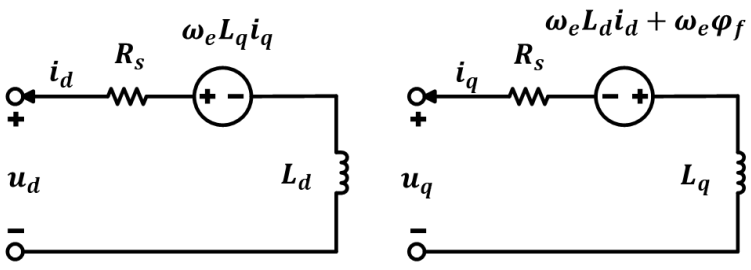

Fig. 6.3. Equivalent circuits of the PMSMs act as the generator.

6.2.3 Mathematical Mode of Energy Backflow

In this chapter, an IPMSM is used to investigate the energy backflow. The machine voltages in the *dq*-axis synchronous frame are expressed by

$$\begin{cases} u_d = R_s i_d + L_d \dfrac{di_d}{dt} - \omega_e L_q i_q \\ u_q = R_s i_q + L_q \dfrac{di_q}{dt} + \omega_e L_d i_d + \omega_e \varphi_f \end{cases} \tag{6.2}$$

where R_s, ω_e, L_d, L_q, and φ_f are the stator resistance, the motor electrical speed, the *dq*-axis inductances, and the flux linkage of PM, respectively.

In the energy backflow process, the PMSMs act as a generator and charge the dc-link capacitor through the three-phase uncontrolled rectifier as shown in Fig. 6.2(c). The back-EMF of the machine can be represented as follows:

$$\begin{cases} E_a = u_{EMF} \sin(\omega_e t + \varphi_{\text{con}}) \\ E_b = u_{EMF} \sin(\omega_e t + \varphi_{\text{con}} + \dfrac{2\pi}{3}) \\ E_c = u_{EMF} \sin(\omega_e t + \varphi_{\text{con}} - \dfrac{2\pi}{3}) \end{cases} \tag{6.3}$$

$$u_{EMF} = \omega_e \sqrt{\left(\varphi_f + L_d i_d\right)^2 + \left(L_q i_q\right)^2} \tag{6.4}$$

where E_a, E_b, E_c are the three-phase back-EMFs. φ_{con} is the conduction angle. u_{EMF} is the amplitude of the back-EMF.

According to the amplitudes of dc-link voltage and back-EMF, the dynamic model of the phase uncontrolled rectifier as shown in Fig. 6.2 (c) can be expressed as

$$\begin{cases} u_{out} = u_{EMF} - u_{dc}, & if\ u_{EMF} > u_{dc} \\ u_{out} = u_{dc} - u_{EMF}, & if\ u_{EMF} \le u_{dc} \end{cases} \tag{6.5}$$

where u_{out}, u_{EMF}, and u_{dc} are the rectifier voltage, the voltages generated by the machine and the dc-link voltage.

6.2.4 Three Scenarios with Fluctuating DC-Link Voltage

In the small dc-link capacitor-based IPMSM drive system, the dc-link voltage is always fluctuating. The peak-to-peak value of the fluctuating dc-link voltage and the amplitude of the back-EMF depend on the machine speed and load conditions. Under low speed and light-load

conditions, both the dc-link voltage fluctuation and the back-EMF are small. Consequently, the back-EMF may not exceed the minimum value of dc-link voltage, and the energy backflow does not occur. However, the dc-link voltage fluctuation and the back-EMF become larger with increasing speed and/or load. The back-EMF could exceed the dc-link voltage. Based on the relationship between the dc-link voltage and the amplitude of back-EMF, three scenarios can be classified: the back-EMF is smaller than the minimum value of dc-link voltage, the back-EMF is equal to the minimum value of dc-link voltage, and the back-EMF is greater than the minimum value of dc-link voltage. Therefore, three operation scenarios which can be expressed by

$$\begin{cases} u_{EMF} - u_{dc,min} < 0, & i_{inv,min} > 0 \\ u_{EMF} - u_{dc,min} = 0, & i_{inv,min} = 0 \\ u_{EMF} - u_{dc,min} > 0, & i_{inv,min} < 0 \end{cases} \tag{6.6}$$

where $u_{dc,min}$ and $i_{inv,min}$ are the minimum value of the dc-link voltage and the inverter current in each fluctuation cycle.

When the amplitude of back-EMF is smaller than the minimum value of fluctuating dc-link voltage, there is no energy backflow. In this scenario, the harmonics in the system remain relatively small. The control performance and the system stability may not be influenced. Secondly, when the amplitude of back-EMF equals the minimum dc-link voltage. Although there is no energy backflow, the harmonics in the dc-link current and *dq*-axis currents increase, with their minimum values reaching zero. The control performance and the system stability could be influenced, and appropriate control strategies are needed to maintain stable operation. Finally, when the back-EMF exceeds the minimum value of the fluctuating dc-link voltage in one dc-link voltage fluctuation cycle. The machine operates as a generator, resulting in a negative dc-link current. This negative current signifies that the energy is being transferred from the machine back into the dc-link through the three-phase uncontrolled rectifier. This phenomenon is the characteristic of energy backflow, resulting in the small dc-link capacitor storing the excess energy. However, the energy backflow is generally considered a fault condition and should be prohibited in PMSM drives. Furthermore, the energy backflow may lead to instability in the dc-link voltage, resulting in severe fluctuations in the system as shown in Fig. 6.4. The serious dc-link fluctuation and energy backflow in the system is a concern, as it can reduce the system's efficiency and lead to potential operational hazards. To maintain the system stability and achieve better control performance, an effective mitigation method based on FW control is proposed in the next section.

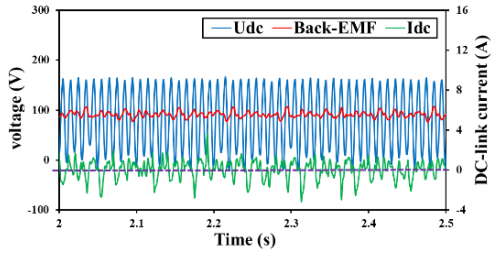

(a) dc-link voltage, back-EMF, and dc-link current

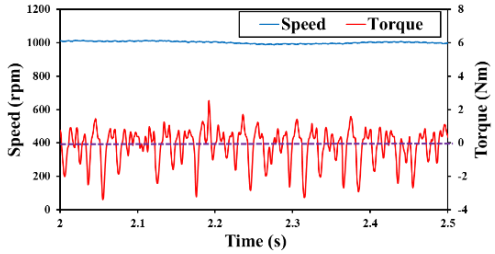

(b) Speed and torque

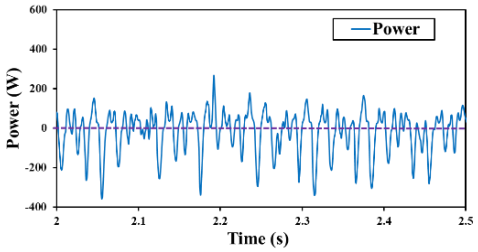

(c) Inverter power

Fig. 6.4. Measured results of energy backflow in small dc-link capacitor-based IPMSM drive system. (a) dc-link voltage, back-EMF, and dc-link current. (b) Speed and torque. (c) Inverter power.

6.2.5 Energy Backflow Accounting for Different Speed and Load Conditions

In the small dc-link capacitor-based PMSM drive system, the speed changes primarily cause back-EMF variation. Load changes mainly lead to noticeable fluctuations in dc-link voltage. This section aims to provide a comprehensive understanding of this phenomenon and analyze the effect of speed and load changes on energy backflow. The minimum value of the inverter power is used to represent whether the machine exhibits the energy backflow phenomenon. If the minimum inverter power is negative, it represents the machine entering energy backflow mode in the dc-link voltage fluctuation cycle.

The increased speed can increase the amplitude of back-EMF and slightly aggravate the dc-link voltage fluctuation. Thus, the increase in the speed might be more likely to make the

PMSMs work in generation mode.

$$\omega_e \uparrow \Rightarrow \begin{matrix} \text{back} - \text{EMF} \uparrow \\ u_{dc} \text{ fluctaution} \uparrow \end{matrix} \Rightarrow \text{Chance of energy backflow} \uparrow \tag{6.7}$$

With the speed increasing from 0 to rated value, the inverter power would increase first with the increase of the speed according to the principle of power balance if ignoring machine losses. When the speed is large enough and the back-EMF is greater than the fluctuating dc-link voltage in a certain period, the energy backflow occurs, and the minimum value of inverter power reduces and could be negative as shown in Fig. 6.5(a).

When the load increases from zero, the dc-link voltage fluctuation becomes larger, but the minimum value of the dc-link voltage at first is enough to keep the system stable. Thus, the minimum value of inverter power increases as the load increases. When the load continues to increase, the dc-link voltage fluctuation becomes severe, and the back-EMF may exceed the minimum value of the dc-link voltage, and the energy backflow phenomenon occurs. The minimum value of the inverter power decreases. As the load continues to increase, the average value of the inverter power increases, and the stator current increases as well. Even if the back-EMF is greater than the dc-link voltage, the inverter power would not be negative easily due to the large stator current and the existence of inductance as shown in Fig. 6.5(b).

$$T_{load} \uparrow \Rightarrow \begin{matrix} u_{dc} \text{ fluctaution} \uparrow \\ i_{dc} \uparrow \end{matrix} \Rightarrow \text{Chance of energy backflow} \uparrow/\downarrow \tag{6.8}$$

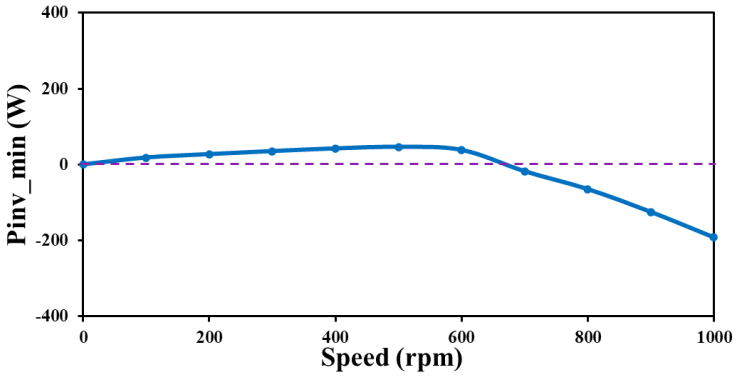

(a) With increasing speed and 1 Nm load

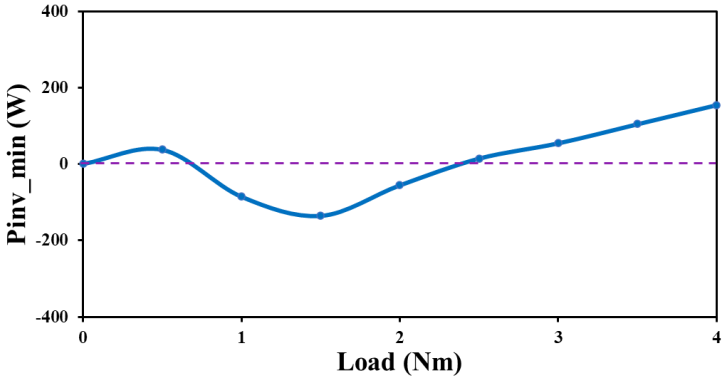

(b) With increasing load and 700 r/min

Fig. 6.5. Energy backflow with increasing speed and load conditions. (a) With increasing speed and 1 Nm load. (b) With increasing load and 700 r/min.

Fig. 6.6 shows the measured results of the influence of different speed and load on the energy backflow phenomenon. As the speed increases, the minimum value of the inverter power increases first. When the speed reaches a certain value, the back-EMF exceeds the dc-link voltage, and the minimum value of the inverter power decreases, eventually becoming negative. As the load increases, the minimum value of the inverter power increases first. When the load continues to increase, the dc-link voltage fluctuation becomes larger, and the minimum value of the inverter power decreases. As the load continues to increase, the minimum value of the inverter power increases even if the back-EMF is greater than the dc-link voltage.

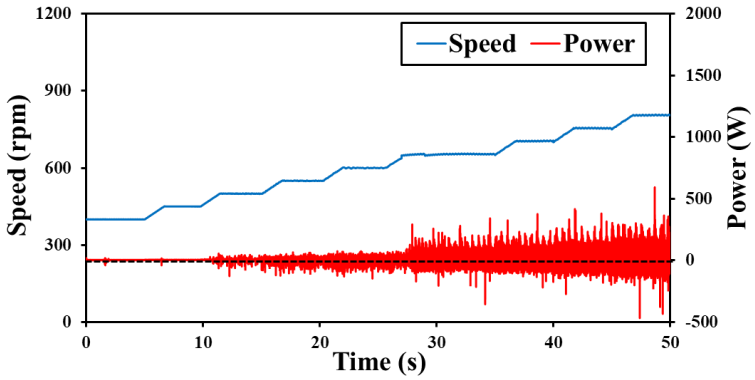

(a) With increasing speed

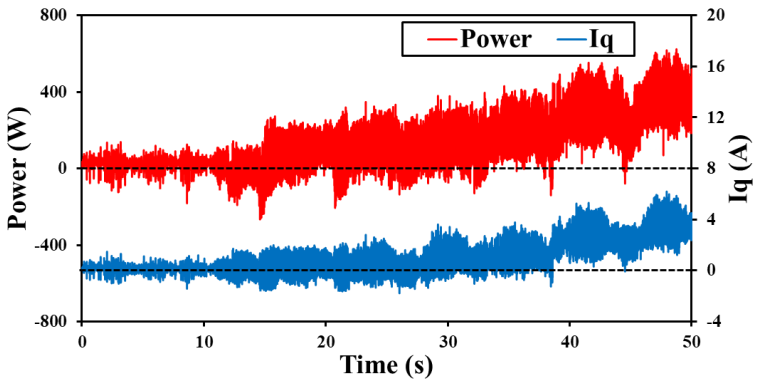

(b) With increasing load

Fig. 6.6. Measured results of energy backflow with increasing speed and load. (a) With increasing speed. (b) With increasing load.

Fig. 6.7 shows the measured results of energy backflow under various operating conditions. As shown in Fig. 6.7, the energy backflow is predominantly observed at speeds ranging from 800 r/min to 1000 r/min, particularly when the load is between 0.5 Nm and 1.5 Nm. The right side is the zoomed version of the speed ranging from 800 r/min to 1000 r/min and load from 0.5 Nm to 1.5 Nm. As can be seen, the energy backflow is most serious when the speed is 1000 r/min, and the load is 1 Nm. In this case, the minimum value of the inverter power is -200 W, and the minimum value of the dc-link current is -2 A. The energy backflow could damage the power devices and deteriorate the control performance of the system. Thus, a mitigation method for the energy backflow is critical to improve the system stability and efficiency and prevent potential damage to power electronic components due to undesirable energy backflow caused by the small dc-link capacitors.

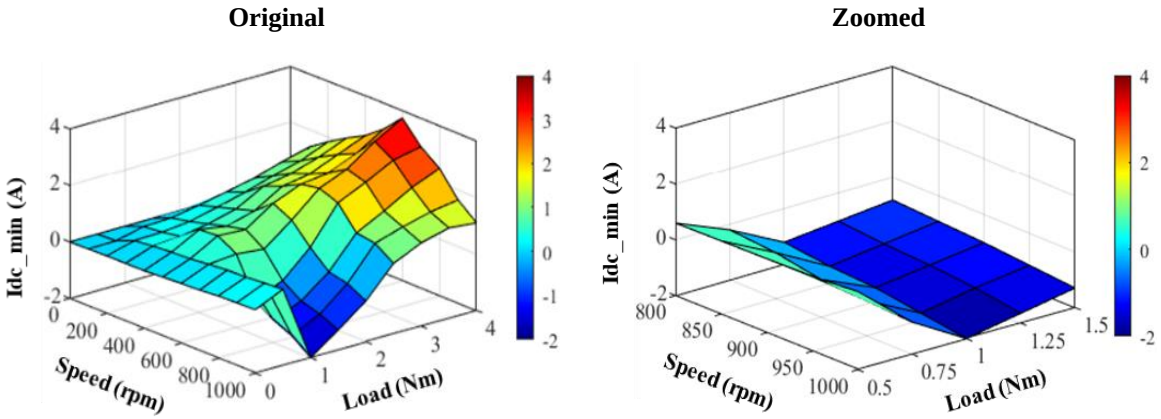

(a) Minimum value of dc-link current

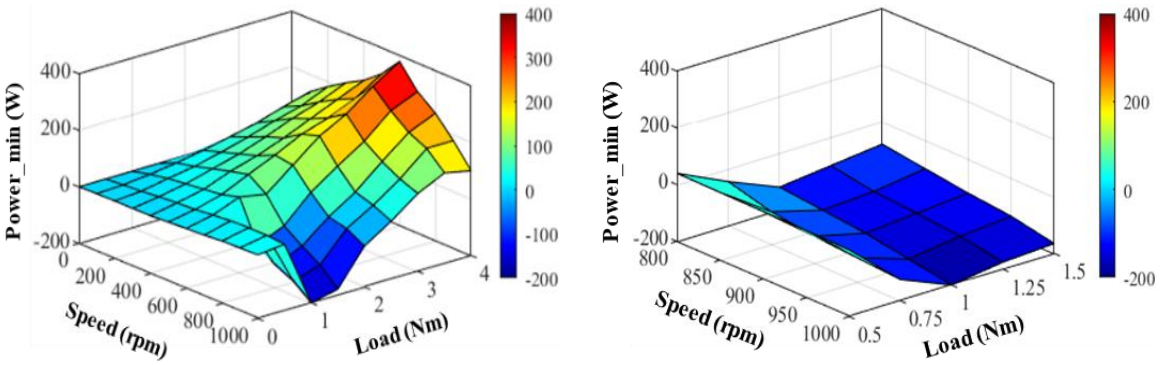

(b) Minimum value of inverter power

Fig. 6.7. Energy backflow accounting for different speed and load conditions. (a) Minimum value of dc-link current. (b) Minimum value of inverter power.

6.3 Energy Backflow Mitigation Method

6.3.1 Limitation of Conventional FW Control Scenarios with Fluctuating DC-Link Voltage

The FW control method can extend the speed range and maintain the performance of PMSM under low dc-link voltage conditions by reducing the magnetic flux. Therefore, the FW control method can effectively mitigate the challenges posed by fluctuating dc-link voltage without introducing additional current and torque harmonics. The block diagram of the conventional FB-FW control method is shown in Fig. 6.8. The voltage constraints ellipse can be expressed as

$$u_s = \sqrt{u_d^2 + u_q^2} \leq u_{max} = \frac{u_{dc}}{\sqrt{3}} \tag{6.9}$$

If the motor speed is high enough and the stator resistance voltage drop is small enough, then the voltage drop by the stator resistance can be neglected. Hence, (6.9) can be approximated as

$$(L_d i_d + \varphi_f)^2 + (L_q i_q)^2 \leq \frac{u_{max}^2}{\omega_e^2} \tag{6.10}$$

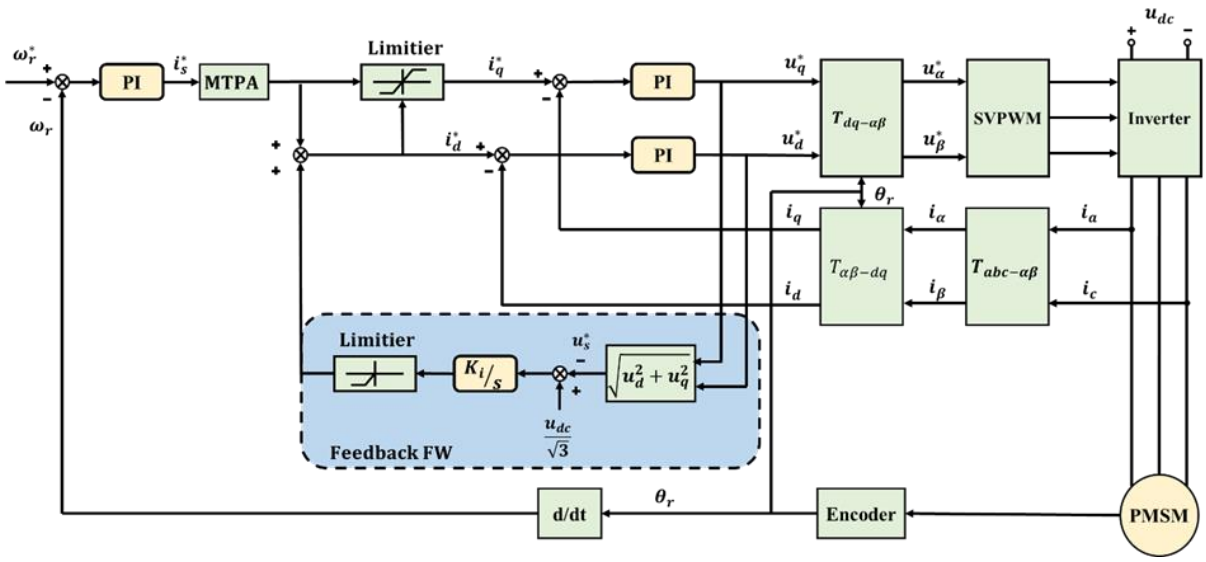

Fig. 6.8. Block diagram of the FB-FW control.

However, FW control poses certain challenges in the presence of fluctuating dc-link voltage. Specifically, these voltage fluctuations induce corresponding fluctuations in the *dq*-axis voltages, which can degrade the control performance in the FB-FW control method. Moreover, an analysis of the small-signal model of FB-FW control in [HUO22B] reveals that severe fluctuations in the *q*-axis voltage, particularly when it becomes negative, can cause the system to enter a positive feedback mode, leading to inherent instability. In addition, the PI controller commonly used in conventional FB-FW control methods is unable to adequately compensate for the AC component introduced by fluctuating dc-link voltage. These challenges underline the complexity and potential instability in the application of FW control in small dc-link capacitor-based PMSM drive systems.

- **Saturation issues due to integral operation**

As shown in Fig. 6.8, the FB-FW control method can be expressed as

$$\begin{cases} u_s^* = \sqrt{u_d^2 + u_q^2} \\ i_d^* = \dfrac{K_i}{s}(u_{max} - u_s^*) \end{cases} \tag{6.11}$$

Ignoring the higher-order harmonics (2nd order and above) of fluctuating dc-link voltage and *dq*-axis voltages, the dc-link voltage and *dq*-axis voltages can be expressed by [HUA17] [YAN22A]

$$u_{dc} = u_{dc,0} + u_{dc,1}\sin(2k\omega_g t + \varphi_g) \tag{6.12}$$

$$\begin{cases} u_d = \mathrm{u}_{d,0} + u_{d,1}\sin(2k\omega_g t + \varphi_{d,1}^u) \\ u_q = u_{q,0} + u_{q,1}\sin(2k\omega_g t + \varphi_{q,1}^u) \end{cases} \tag{6.13}$$

Combining (6.11), (6.12) and (6.13), the *d*-axis reference current can be expressed as

$$\begin{aligned} & i_d^* \\ &= \frac{K_i}{s}\left(\frac{u_{dc,0} + u_{dc,1}\sin(2k\omega_{\mathrm{g}} t + \varphi_{\mathrm{g}})}{\sqrt{3}}\right. \\ &\left. - \sqrt{\left[u_{d,0} + u_{d,1}\sin(2k\omega_g t + \varphi_{d,1}^u)\right]^2 + \left[u_{q,0} + u_{q,1}\sin(2k\omega_g t + \varphi_{q,1}^u)\right]^2}\right) \\ &= \frac{K_i}{s}\left(\frac{u_{dc,0} + u_{dc,1}\sin(2k\omega_{\mathrm{g}} t + \varphi_{\mathrm{g}})}{\sqrt{3}}\right. \\ &\left. - \sqrt{\begin{array}{c}\left(u_{d,0}^2 + u_{q,0}^2\right) + 2\left[u_{d,0}u_{d,1}\sin(2k\omega_g t + \varphi_{d,1}^u) + u_{q,0}u_{q,1}\sin(2k\omega_g t + \varphi_{q,1}^u)\right] \\ + u_{d,1}^2\sin^2(2k\omega_g t + \varphi_{d,1}^u) + u_{q,1}^2\sin^2(2k\omega_g t + \varphi_{q,1}^u)\end{array}}\right) \end{aligned} \tag{6.14}$$

In conventional PMSM drive systems where the dc-link voltage and *dq*-axis voltages have no AC harmonics, the *d*-axis reference current is obtained by

$$i_d^* = \frac{K_i}{s}\left(\frac{u_{dc,0}}{\sqrt{3}} - \sqrt{u_{d,0}^2 + u_{q,0}^2}\right) \tag{6.15}$$

However, with the fluctuating dc-link voltage, the *dq*-axis voltages also fluctuate. The *d*-axis reference current is shown as (6.15), it is shown that there is a dc offset in the *d*-axis reference current due to the squared sinusoidal terms $u_{d,1}^2\sin^2(2k\omega_g t + \varphi_{d,1}^u)$ and $u_{q,1}^2\sin^2(2k\omega_g t + \varphi_{q,1}^u)$, which can be expressed as

$$\begin{aligned} & \sqrt{u_{d,1}^2\sin^2(2k\omega_g t + \varphi_{d,1}^u) + u_{q,1}^2\sin^2(2k\omega_g t + \varphi_{q,1}^u)} \\ &= \sqrt{u_{d,1}^2\left(\frac{1 - \cos 2\left(2k\omega_g t + \varphi_{d,1}^u\right)}{2}\right) + u_{q,1}^2\left(\frac{1 - \cos\ 2(2k\omega_g t + \varphi_{q,1}^u)}{2}\right)} \end{aligned} \tag{6.16}$$

These squared terms $u_{d,1}^2\sin^2(2k\omega_g t + \varphi_{d,1}^u)$ and $u_{q,1}^2\sin^2(2k\omega_g t + \varphi_{q,1}^u)$ have an average value of 0.5 over one period of the sinusoidal function, which introduces a dc offset in the obtained *d*-axis reference current. Ignoring the ac component, the *d*-axis reference current considering the *dq*-axis voltage fluctuation can be expressed as

$$i_{d,e}^{*} = \frac{K_i}{s}\left(\frac{u_{dc,0}}{\sqrt{3}} - \sqrt{u_{d,0}^2 + u_{q,0}^2 + \frac{1}{2}(u_{d,1}^2 + u_{q,1}^2)}\right) \tag{6.17}$$

where $i_{d,e}^{*}$ represents the resulting *d*-axis reference current with dc-link voltage fluctuation. Hence, when the dc-link voltage and *dq*-axis voltage fluctuations are serious, the calculated *d*-axis reference current error will also become significant. Fig. 6.9 shows the experiment results of the conventional FW control with dc-link voltage fluctuation. Due to the dc-link voltage fluctuation and the voltage error caused by voltage fluctuations, the *d*-axis reference current gradually saturates, leading to the failure of the FW control. This indicates that dc-link voltage fluctuation has a negative effect on the system stability.

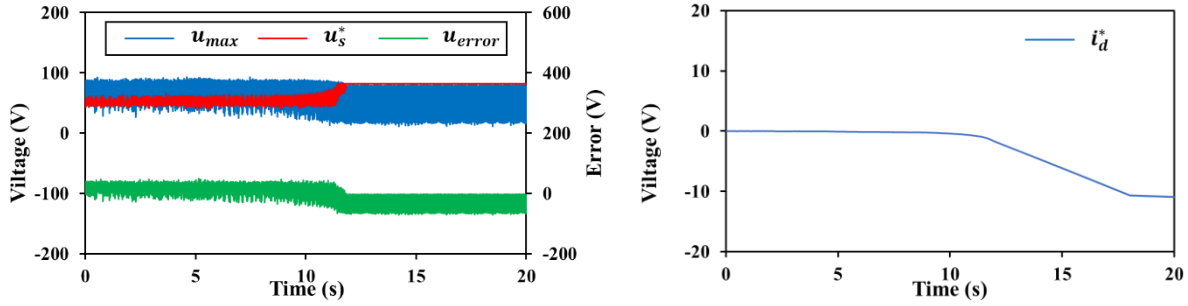

(a) Voltage (b) *D*-axis current

Fig. 6.9. Measured results of conventional FW control method with fc-link voltage fluctuation. (a) Voltage. (b) *D*-axis current.

- **Instability issues due to positive feedback mode**

According to [HUO22B], the small signal model of the conventional voltage FB-FW control method is shown in Fig. 6.10.

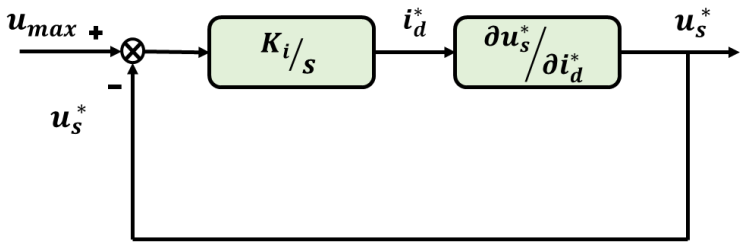

Fig. 6.10. Small signal model of FB-FW control method.

$\frac{\partial u_s^*}{\partial i_d^*}$ is the *d*-axis current change on stator voltage u_s^*.

$$\frac{\partial u_s^*}{\partial i_d^*} = \frac{\partial u_s^*}{\partial u_d^*}\frac{\partial u_d^*}{\partial i_d^*} + \frac{\partial u_s^*}{\partial u_q^*}\frac{\partial u_q^*}{\partial i_d^*} \tag{6.18}$$

According to motor voltage equations and stator voltage equations

$$\frac{\partial u_s^*}{\partial i_d^*} = \frac{u_d R_s + u_q \omega_r L_d}{\sqrt{u_d^2 + u_q^2}} \tag{6.19}$$

Therefore, when $\frac{\partial u_s^*}{\partial i_d^*} > 0$, u_s^* is the increasing function of i_d^*, and the close-loop system is negative feedback, the system is stable. However, when $\frac{\partial u_s^*}{\partial i_d^*} < 0$, u_s^* is the decreasing function of i_d^*, and the close-loop system is position feedback, which is unstable.

Therefore, the stable conditions should be

$$u_d R_s + u_q \omega_r L_d > 0 \tag{6.20}$$

In high-speed operation, the above equations can be simplified as $u_q > 0$. If $u_q < 0$, the system would be unstable as shown in Fig. 6.11.

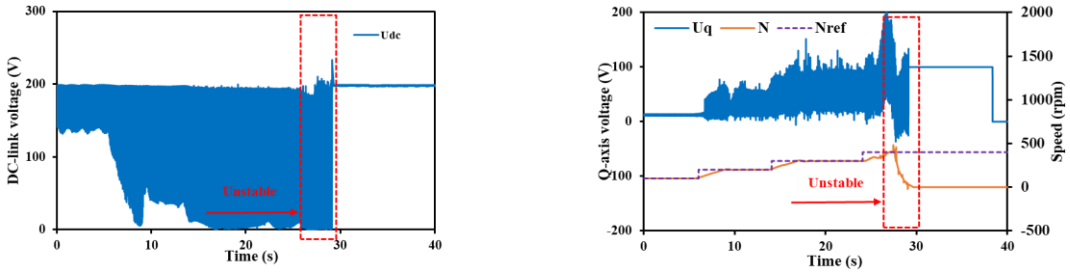

(a) dc-link voltage (b)) *Q*-axis voltage and speed

Fig. 6.11. Unstable issues with negative *q*-axis voltage. (a) dc-link voltage. (b) *Q*-axis voltage and speed.

6.3.2 Proposed FW Control Method Based on Quasi-PIR Controller

Fig. 6.12 shows the block diagram of the energy backflow mitigation method based on the proposed FW control. The primary objective of this approach is to modulate the *d*-axis current to effectively reduce the magnitude of back-EMF, and mitigate the dc-link voltage fluctuation, thereby eliminating the energy backflow issue.

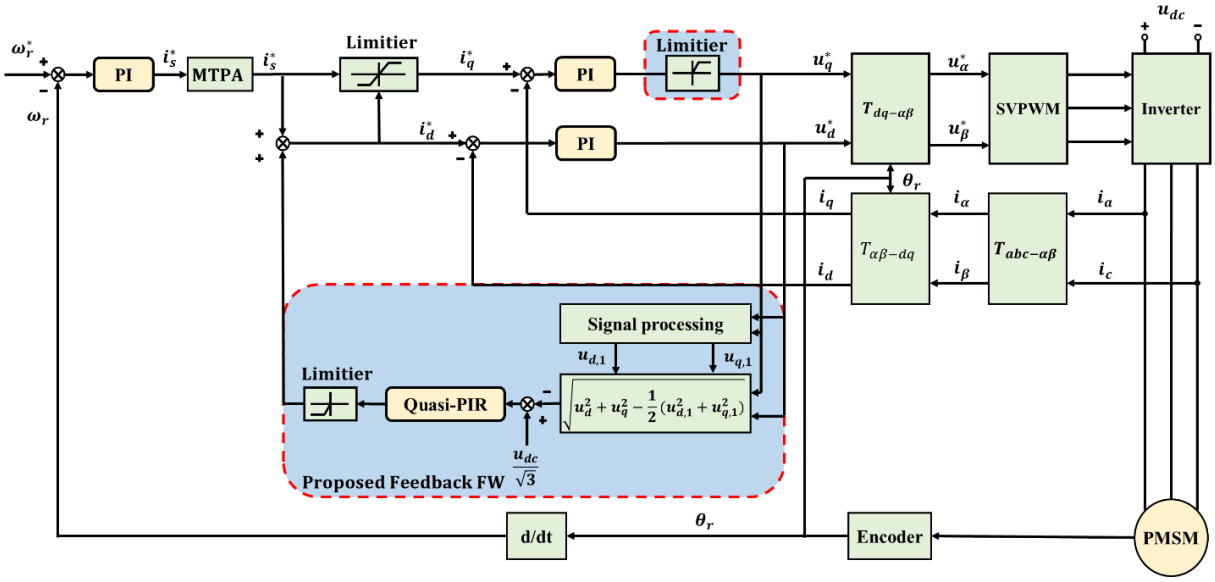

Fig. 6.12. Block diagram of proposed FW control method.

In the proposed method, a quasi-PIR controller is employed to control the harmonic components of the voltage error. Unlike the traditional PI controller, which is typically effective for steady-state error correction but may fall short in addressing periodic disturbances, the quasi-PIR controller integrates a resonant component that is fine-tuned to the frequency of the system harmonics. Compared with the traditional PIR controller, the quasi-PIR controller is designed to provide better control performance in scenarios where disturbances are not strictly limited to a single frequency. The transfer function of the quasi-PIR controller is presented by:

$$G_{PIR}(s) = K_p + \frac{K_i}{s} + \frac{2\omega_i K_r s}{s^2 + 2\omega_i s + \omega_g^2} \tag{6.21}$$

Furthermore, a dc offset compensation method is implemented to compensate for voltage calculation errors caused by voltages fluctuation, and a signal processing procedure is utilized to obtain the amplitude of the ac components of the *dq*-axis voltages as shown in Fig. 6.13. In addition, a *q*-axis voltage limiter is employed to prevent the *q*-axis voltage from becoming negative.

6.3.3 Optimal Phase Angle Selection for *D*-axis Reference Current

Since the *d*-axis reference current contains the ac component, it is essential to consider the phase angle. As optimal current angle selection enables achieving maximum output torque with minimal current, thus ensuring optimal control performance. By precisely adjusting the phase

angle, the fluctuations in the system can be suppressed. The performance of the system can be improved.

The *d*-axis reference current can be expressed by:

$$i_{\mathrm{d},2\omega_\mathrm{g}}^{\mathrm{ref}} = i_{\mathrm{d,dc},2\omega_\mathrm{g}}^{\mathrm{ref}} + i_{\mathrm{d,ac},2\omega_\mathrm{g}}^{\mathrm{ref}} \cos\left(2\omega_g t + \varphi_{\mathrm{i_{d,ac},2\omega_g}}\right) \tag{6.22}$$

where $i_{\mathrm{d},2\omega_\mathrm{g}}^{\mathrm{ref}}$ is the *d*-axis reference current, $i_{\mathrm{d,dc},2\omega_\mathrm{g}}^{\mathrm{ref}}$ is the amplitude of the dc component of *d*-axis reference current, $i_{\mathrm{d,ac},2\omega_\mathrm{g}}^{\mathrm{ref}}$, and $\varphi_{\mathrm{i_{d,ac},2\omega_g}}$ are the amplitude and phase of the 2nd order harmonic of *d*-axis reference current. The amplitude and phase angle of *dq*-axis voltages and currents can be obtained by the following signal process method as shown in Fig. 6.13.

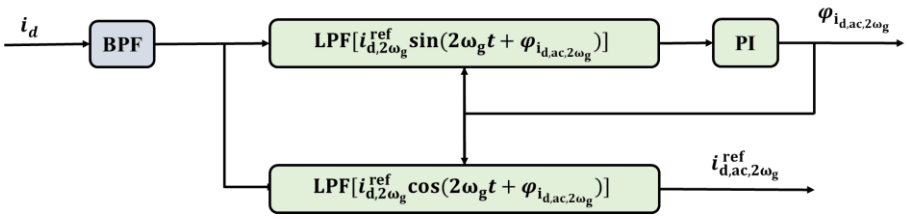

Fig. 6.13. Block diagram of the signal process.

As mentioned above, the relative alignment of the magnetic field and the rotor can be influenced to achieve precise machine control by appropriately adjusting the phase angle of the d-axis reference current. This adjustment reduces torque ripple caused by DC-link voltage fluctuations and enhances the overall system's control performance. The LMS algorithm is particularly suitable for real-time adjustments due to its fast convergence and simplicity, while the GD algorithm effectively handles complex nonlinear problems to refine the d-axis reference current phase angle. The combination of these algorithms ensures optimal phase angle selection; the LMS algorithm minimizes the q-axis current harmonic at twice the grid frequency, and the GD algorithm dynamically adjusts the LMS parameters to address system uncertainties and external disturbances, enabling high-precision control.

The structure of the optimal phase angle selection is shown in Fig. 6.14. The 100Hz ac component of *q*-axis current $i_{\mathrm{q,ac},2\omega_\mathrm{g}}(n)$ is the input signal. The phase angle of *d*-axis reference current $\varphi_{\mathrm{i_{d,ac},2\omega_g}}(n)$ is considered as the weight factor.

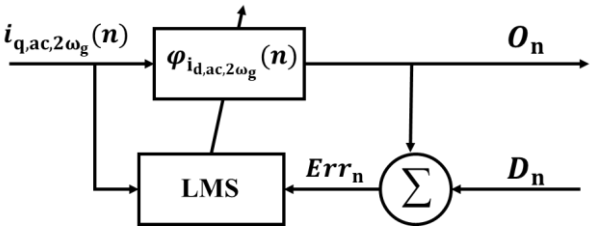

Fig. 6.14. Block diagram of LMS algorithm.

The output signal O_n is presented by

$$O_n = i_{q,ac,2\omega_g}(n) \times \varphi_{i_{d,ac,2\omega_g}}(n) \tag{6.23}$$

where $i_{\mathrm{q,ac,2\omega_g}}(n)$ is the 100Hz ac component of q-axis current.

The error $\mathrm{Err_n}$ between the desired response D_n and the output signal O_n can be expressed as:

$$Err_n = D_n - O_n = 0 - i_{\mathrm{q,ac,2\omega_g}}(n) \times \varphi_{\mathrm{i_{d,ac,2\omega_g}}}(n) \tag{6.24}$$

where the desired response D_n is set to zero. The objective of the LMS algorithm is to find the optimal weight factor/phase angle of the d-axis reference current to produce the minimum Err_n, and then, $i_{\mathrm{q,ac,2\omega_g}}(n)$ will be minimized.

The objective function of the LMS algorithm J_n can be defined as half of the squared error criterion as expressed by

$$J_n = 0.5(Err_n)^2 = 0.5[-i_{\mathrm{q,ac,2\omega_g}}(n) \times \varphi_{i_{d,ac,2\omega_g}}(n)]^2 \tag{6.25}$$

The optimal phase angle $\varphi_{\mathrm{i_{d,ac,2\omega_g}}}$ can be trained by the GD algorithm to minimize the objective function as presented by

$$\varphi_{i_{\mathrm{d,ac,2\omega_g}}}(n+1) = \varphi_{\mathrm{i_{d,ac,2\omega_g}}}(n) + \xi[-\nabla J_{(n)}] \tag{6.26}$$

where $\nabla J_{(\mathrm{n})}$ represents the gradient, ξ is the training constant, determining the convergence speed.

The flow chart of the GD algorithm is shown in Fig. 6.15.

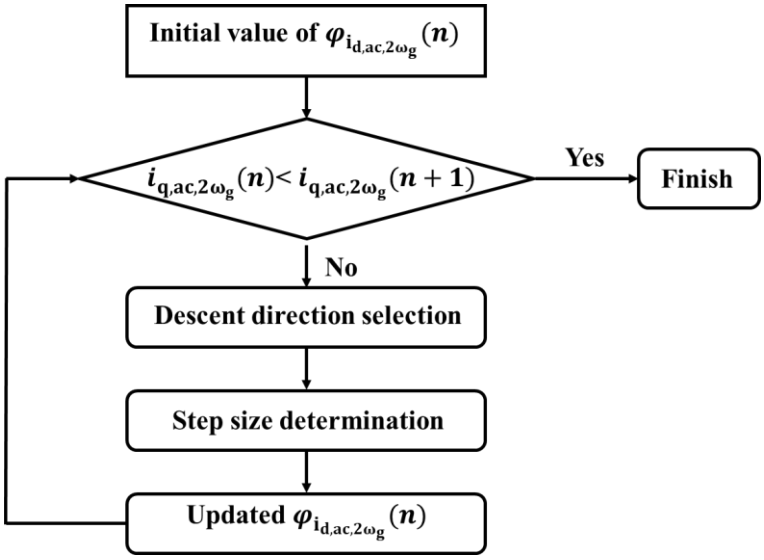

Fig. 6.15. Flow chart of GD algorithm.

The weight factors are updated in the opposite direction of the gradient $\nabla J_{(n)}$ as the goal is to minimize the 100Hz q-axis current harmonics. Consequently, with the help of the LMS algorithm, $\varphi_{i_{d,ac,2\omega_g}}(n)$ can be trained to an optimized value.

If $i_{q,ac,2\omega_g}(n) > i_{q,ac,2\omega_g}(n+1)$, the descent direction is right;

If $i_{q,ac,2\omega_g}(n) < i_{q,ac,2\omega_g}(n+1)$, the descent direction is wrong.

Then, the optimal phase angle can be obtained by minimizing the q-axis current harmonics. The block diagram of the proposed energy backflow mitigation method, together with the optimal phase angle selection method, is shown in Fig. 6.16.

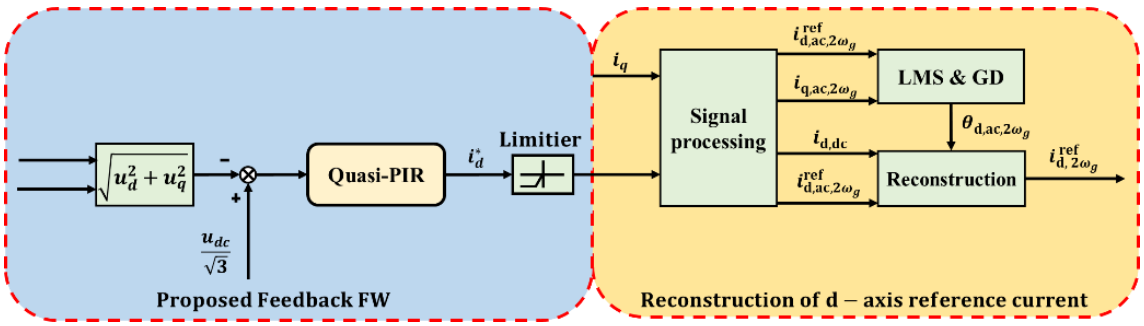

Fig. 6.16. Block diagram of proposed energy backflow suppression method with optimal phase angle selection method.

6.4 Experimental Validation

6.4.1 Proposed FW Control Method Based on Quasi-PIR Controller

Fig. 6.17 to Fig. 6.19 show the measured results of the proposed FW method under different operation conditions (from Fig. 6.17 to Fig. 6.19, 800 r/min with 0.5 Nm load, 800 r/min with 1 Nm load, 1000 r/min with 0.5 Nm load). When the machine operates at 800 r/min with 0.5 Nm load, it can be observed that the back-EMF exceeds the minimum value of the dc-link voltage before 5 s, leading to the occurrence of the energy backflow phenomenon. In this case, the dc-link current, torque, and inverter power exhibit both positive and negative values. The dc-link cannot handle the backflow energy, resulting in an increase in the dc-link voltage amplitude from 160 V to 170 V. After 5 s, the proposed FW method is applied. The negative dc-link current, torque, and inverter power are almost eliminated. Additionally, current harmonics in the system are reduced. When the load is increased to 1 Nm as shown in Fig. 6.18, the energy backflow phenomenon is effectively suppressed by the proposed FW method after 5 s. When the machine operates at 1000 r/min and 0.5 Nm load as shown in Fig. 6.19, the energy backflow is evidenced before 5 s. After 5 s, the proposed FW method is used, and the system exhibits an effective elimination of the energy backflow phenomenon. Fig. 6.20 shows the effectiveness of the proposed FW method under different operating conditions. By the proposed methods, the maximum backflow current is reduced from -2 A to 0 A, and the maximum backflow power from -200 W to close to 0 W. Fig. 6.17 and Fig. 6.20 demonstrate the effectiveness of the proposed FW control method in eliminating the energy backflow phenomenon and improving the stability of the small dc-link capacitor based-PMSM drive systems.

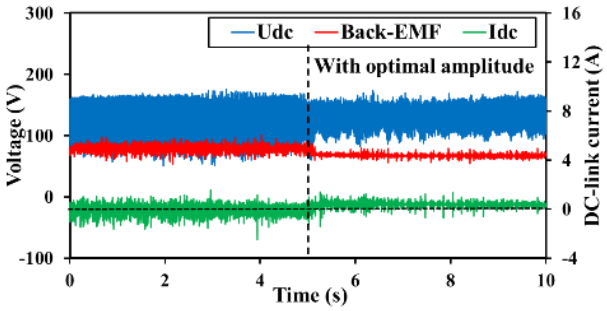

(a) dc-link voltage, back-EMF, and dc-link current

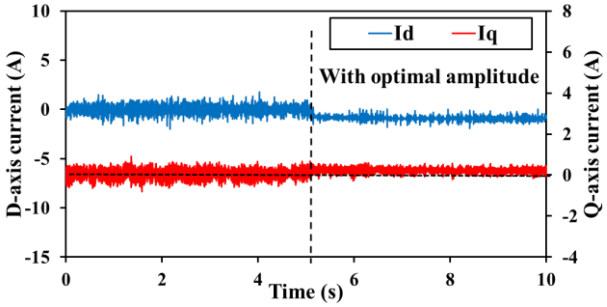

(b) *dq*-axis current

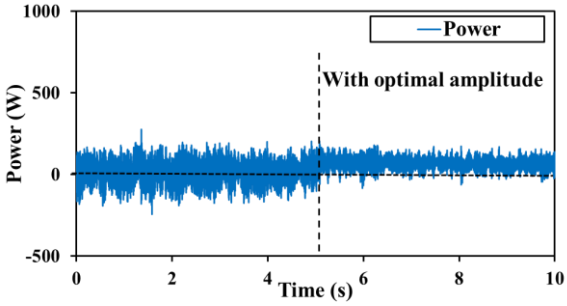

(c) Inverter output power

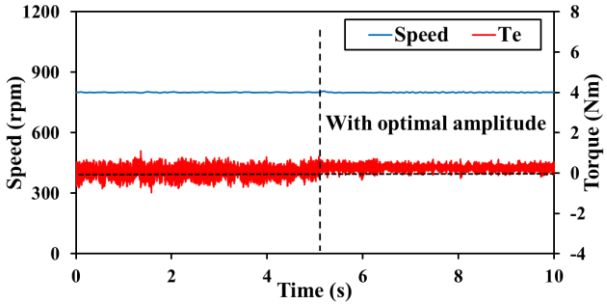

(d) Speed and torque

Fig. 6.17. Measured results without and with the proposed FW method at 800 r/min and under 0.5 Nm condition. (a) dc-link voltage, back-EMF, and dc-link current. (b) *dq*-axis current. (c) Inverter output power. (d) Speed and torque.

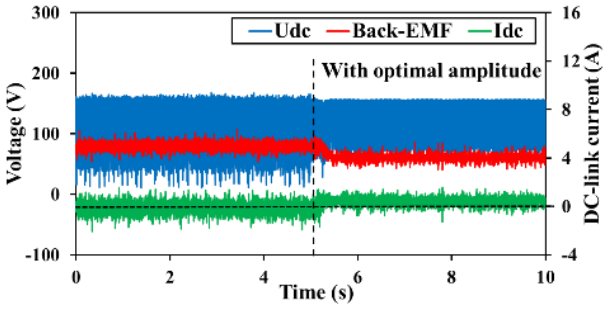

(a) dc-link voltage, back-EMF, and dc-link current

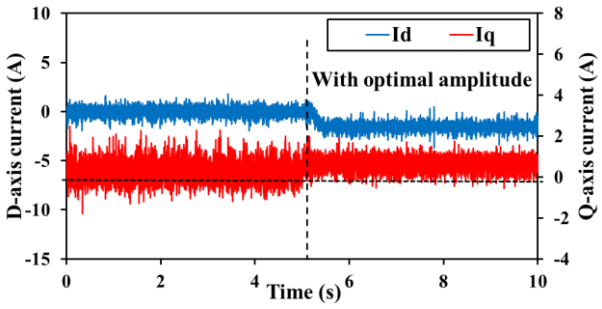

(b) *dq*-axis current

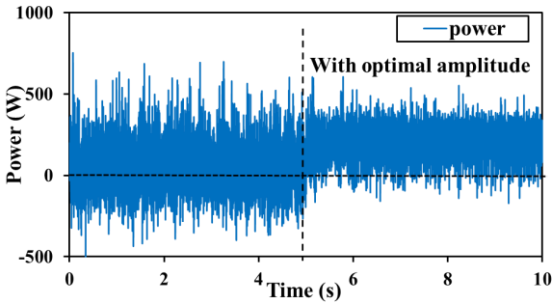

(c) Inverter output power

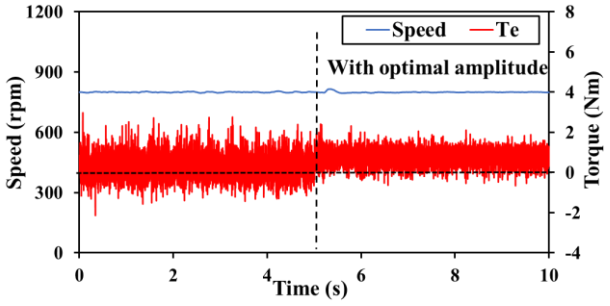

(d) Speed and torque

Fig. 6.18. Measured results without and with the proposed FW method at 800 r/min and under 1 Nm condition. (a) dc-link voltage, back-EMF, and dc-link current. (b) *dq*-axis current. (c) Inverter output power. (d) Speed and torque.

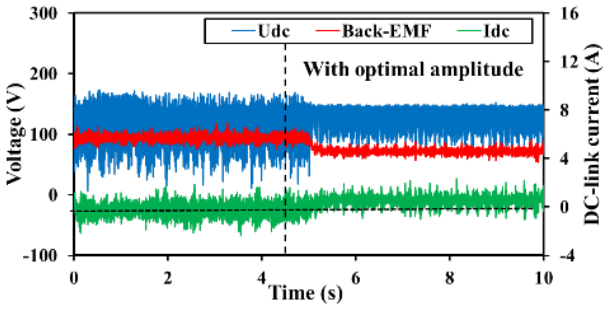

(a) dc-link voltage, back-EMF, and dc-link current

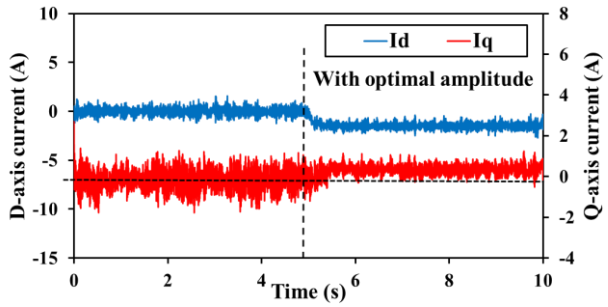

(b) *dq*-axis current

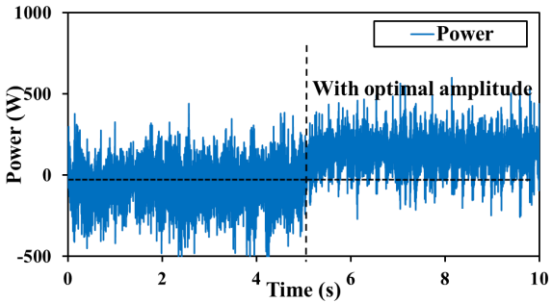

(c) Inverter output power

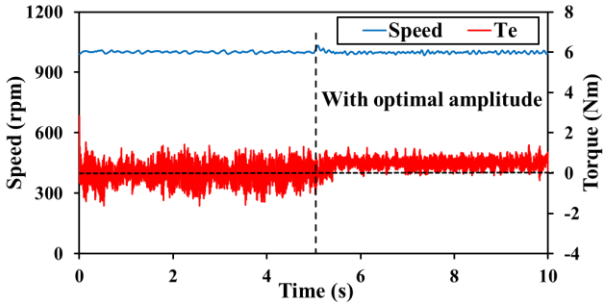

(d) Speed and torque

Fig. 6.19. Experimental results without and with the proposed FW method at 1000 r/min and under 0.5 Nm condition. (a) dc-link voltage, back-EMF, and dc-link current. (b) *dq*-axis current. (c) Inverter output power. (d) Speed and torque.

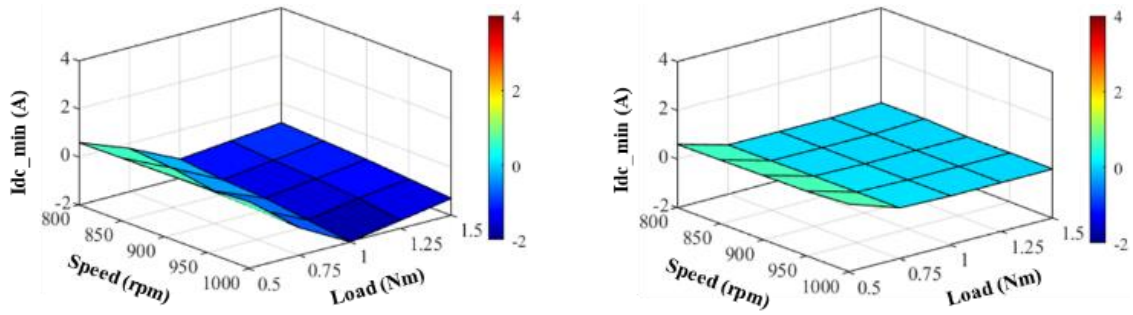

(a) Minimum value of dc-link current

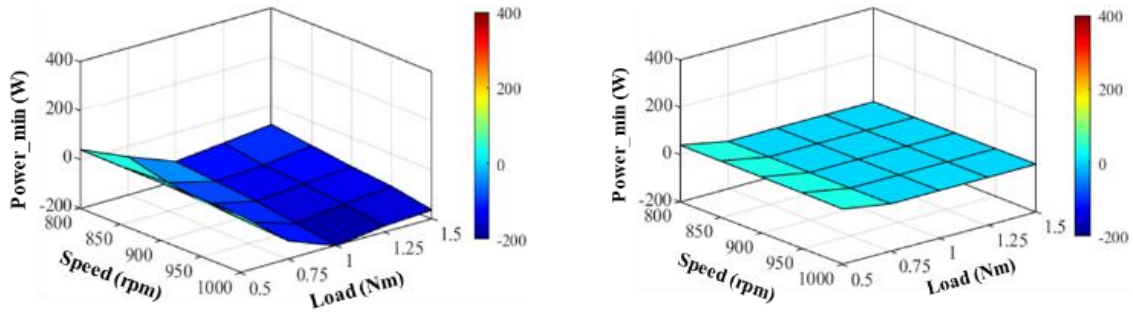

(b) Minimum value of inverter power

Fig. 6.20. Comparison of energy backflow issues without and with the proposed FW method. (a) Minimum value of dc-link current. (b) Minimum value of inverter power.

6.4.2 Optimal Phase Angle Selection of *D*-axis Reference Current

Fig. 6.21 to Fig. 6.23 show the measured results without and with optimal phase angle selection method under different operation conditions (from Fig. 6.21 to Fig. 6.23, 800 r/min with 0.5 Nm load, 800 r/min with 1 Nm load, 1000 r/min with 0.5 Nm load). In Fig. 6.21, when without optimal phase angle selection before 4s, an obvious 100 Hz harmonic in the system is caused by the small dc-link capacitor. After 4s, the *d*-axis reference current is reconstructed by the phase angle selection method, and the system shows a significant reduction in 100 Hz harmonic from 0.25 A to 0.12 A. When the load is increased to 1 Nm as shown in Fig. 6.22, the 100 Hz harmonic of the *q*-axis current is reduced from 0.5 A to 0.3 A by selecting the optimal phase angle, proving the effectiveness of the optimal phase angle selection method. In Fig. 6.23, after 4s, the 100 Hz harmonica of the *q*-axis current is greatly reduced from 0.38 A to 0.15 A by selecting the optimal phase angle of the *d*-axis reference current. The measured results show better control performance of the system by optimizing the phase angle of the *d*-axis reference current.

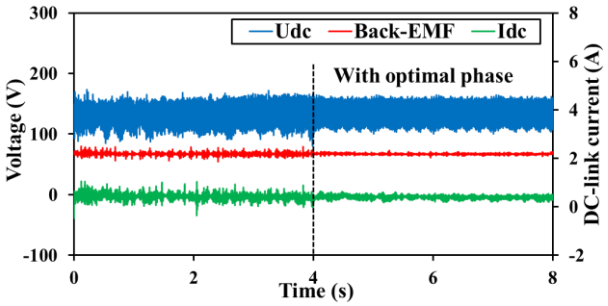

(a) dc-link voltage, back-EMF, and dc-link current

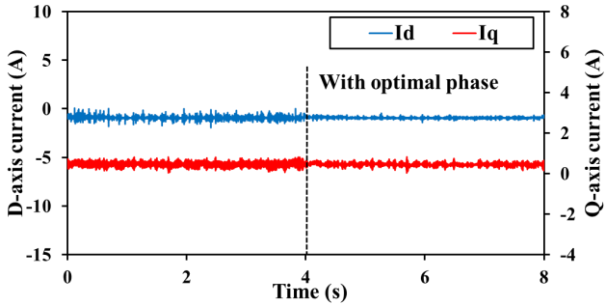

(b) *dq*-axis current

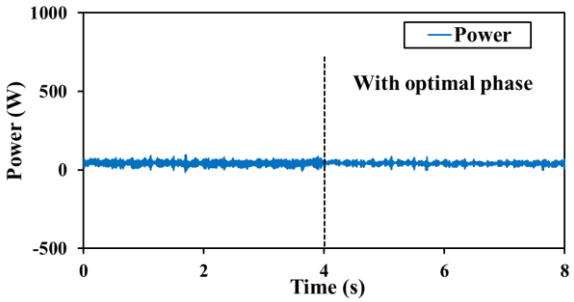

(c) Inverter output power

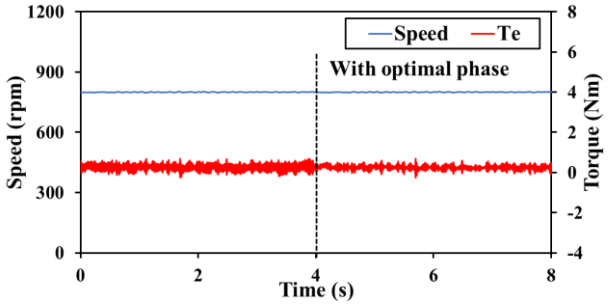

(d) Speed and torque

Fig. 6.21. Measured results without and with the proposed optimal phase angle selection method at 800 r/min and under 0.5 Nm condition. (a) dc-link voltage, back-EMF, and dc-link current. (b) *dq*-axis current. (c) Inverter output power. (d) Speed and torque.

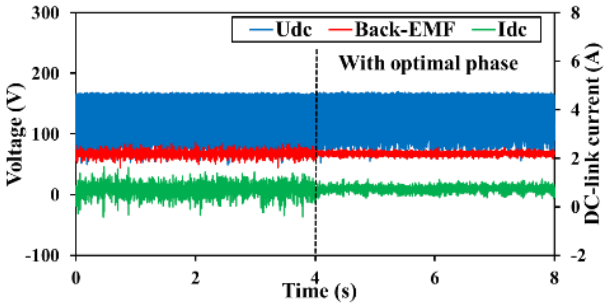

(a) dc-link voltage, back-EMF, and dc-link current

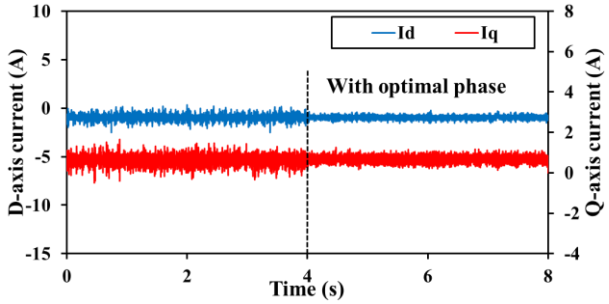

(b) *dq*-axis current

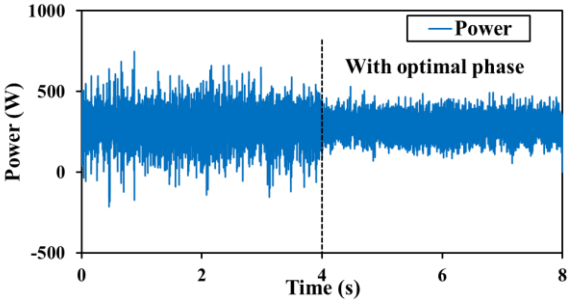

(c) Inverter output power

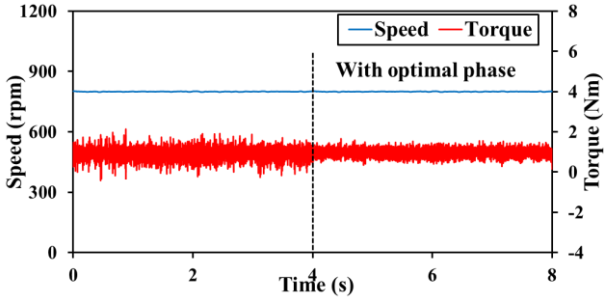

(d) Speed and torque

Fig. 6.22. Measured results without and with the proposed optimal phase angle selection method at 800 r/min and under 1 Nm condition. (a) dc-link voltage, back-EMF, and dc-link current. (b) *dq*-axis current. (c) Inverter output power. (d) Speed and torque.

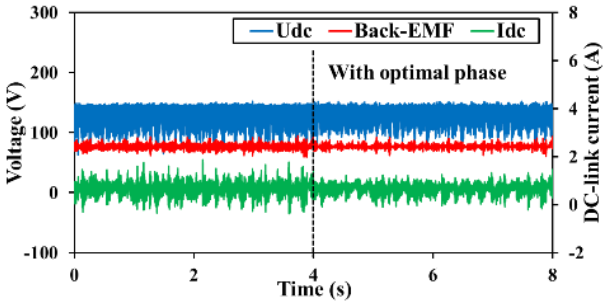

(a) dc-link voltage, back-EMF, and dc-link current

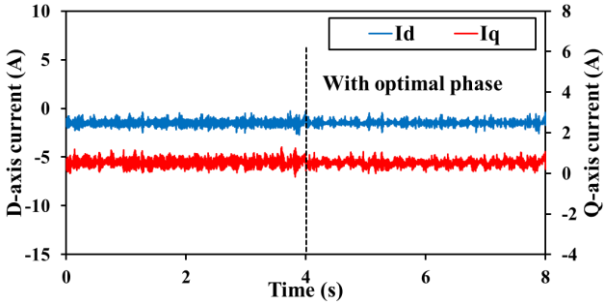

(b) *dq*-axis current

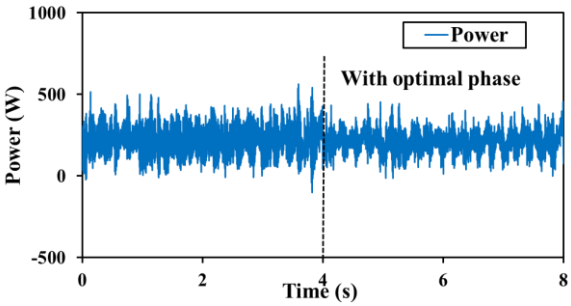

(c) Inverter output power

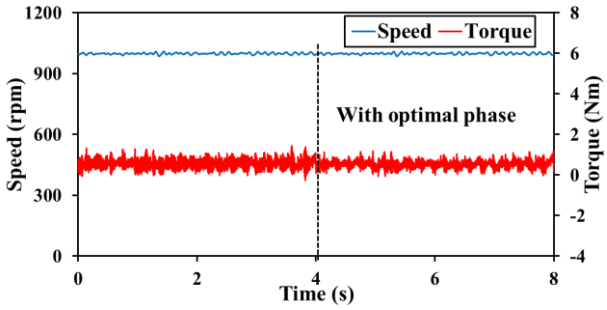

(d) Speed and torque

Fig. 6. 23. Measured results without and with the proposed optimal phase angle selection method at 1000 r/min and under 0.5 Nm condition. (a) dc-link voltage, back-EMF, and dc-link current. (b) *dq*-axis current. (c) Inverter output power. (d) Speed and torque.

Fig. 6.24 and Fig. 6.25 show the spectra of the *q*-axis current without and with the proposed optimal phase angle selection method under different operation conditions. These measured

results show that the control performance is improved under various speed and load conditions by selecting the optimal phase angle of *d*-axis reference current.

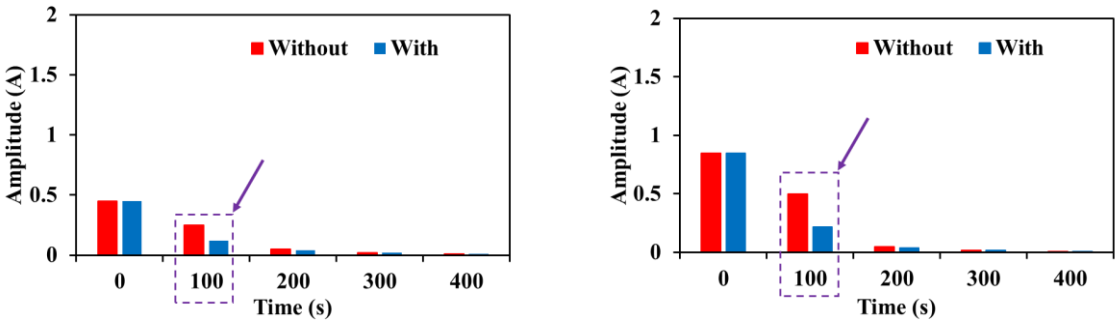

(a) 0.5 Nm (b) 1 Nm

Fig. 6.24. Spectra of *q*-axis current without and with proposed optimal phase angle selection method. (a) 0.5 Nm. (b) 1 Nm.

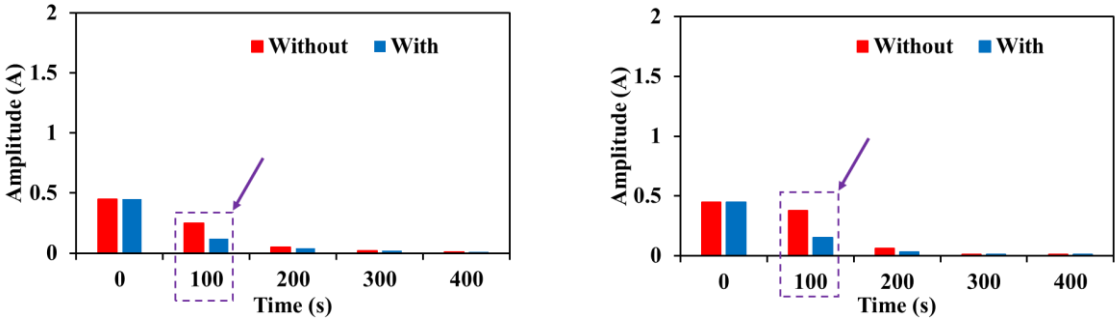

(a) 800 r/min (b) 1000 r/min

Fig. 6.25. Spectra of *q*-axis current without and with proposed optimal phase angle selection method. (a) 800 r/min. (b) 1000 r/min.

Fig. 6.26 and Fig. 6.27 show the measured results of the dynamic control performance of the proposed mitigation methods. In Fig. 6.26, the speed is increased from 600 r/min to 700 r/min with a load of 0.5 Nm. In the left column, without the implementation of the proposed methods, the dc-link voltage experiences significant fluctuations during the speed ramp-up period, which causes the amplitude back-EMF to exceed the dc-link voltage, leading to the energy backflow phenomenon. The dc-link current reaches a negative peak of nearly 2 A, maximum negative power approaching 200 W, and maximum negative torque close to 2.5 Nm. In contrast, when the proposed method is applied as shown in the right column, the energy backflow phenomenon is effectively eliminated, and the harmonics in dc-link current, power, and torque are significantly reduced. In Fig. 6.27, the load increases from 0.2 Nm to 1.5 Nm at a constant speed of 600 r/min. In the left column, the energy backflow phenomenon occurs without the proposed method, and the system demonstrates instability due to significant dc-link voltage

fluctuation. In the right column, with the implementation of the proposed method, the energy backflow phenomenon is completely suppressed, and the harmonics in dc-link voltage, dc-link current, and torque are greatly reduced.

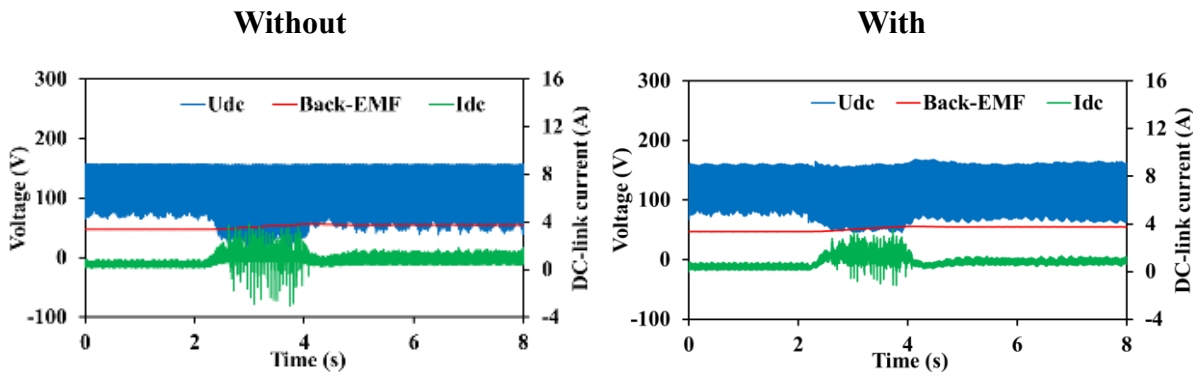

(a) dc-link voltage, back-EMF, and dc-link current

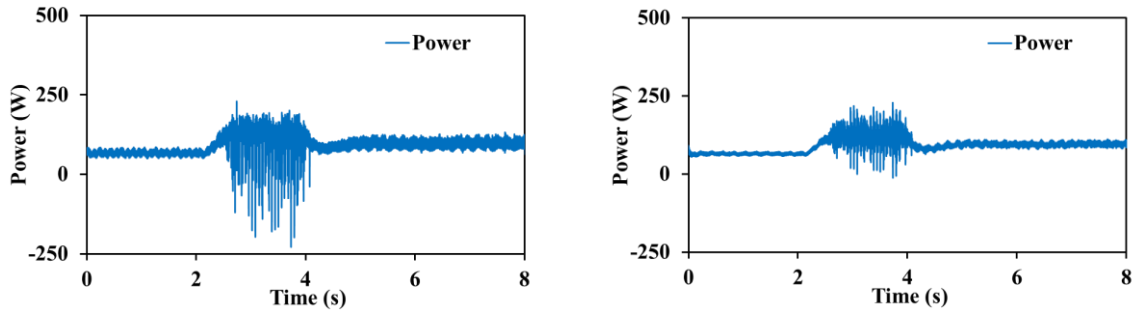

(b) Inverter output power

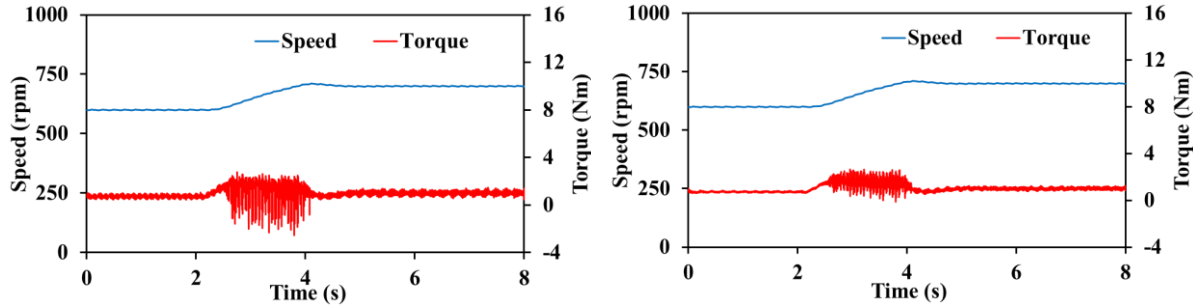

(c) Speed and torque

Fig. 6.26. Measured results with speed increased from 600 r/min to 700 r/min without and with the proposed methods. (a) dc-link voltage, back-EMF, and dc-link current. (b) Inverter output power. (c) Speed and torque.

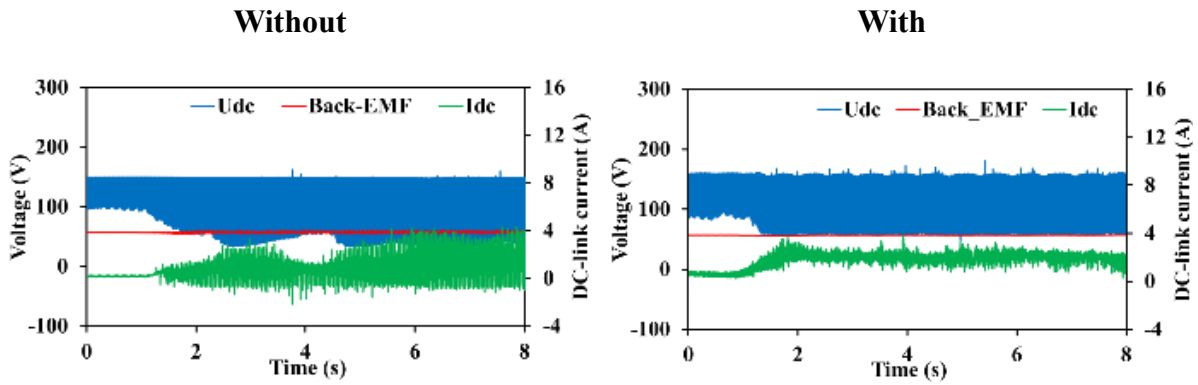

(a) dc-link voltage, back-EMF, and dc-link current

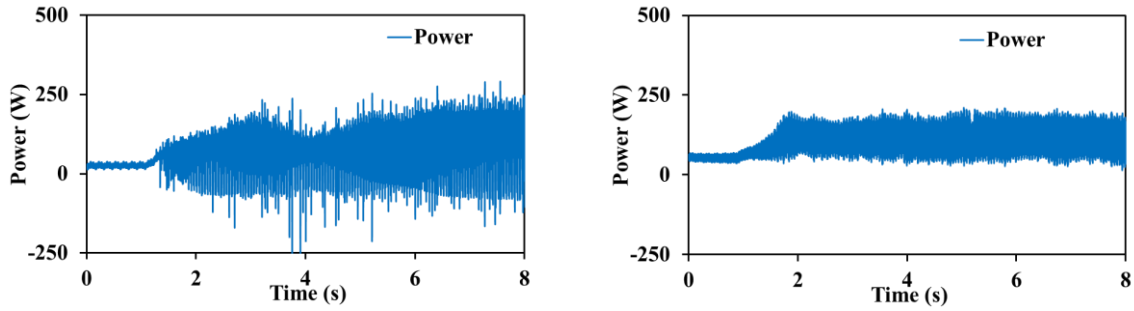

(b) Inverter output power

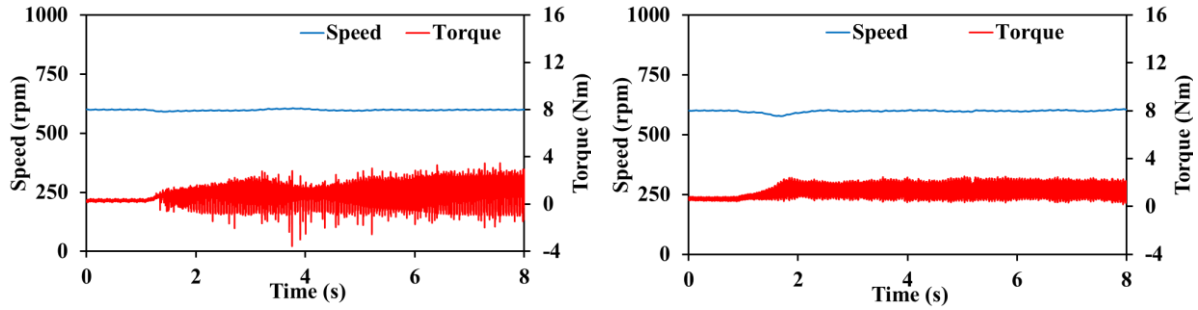

(c) Speed and torque

Fig. 6.27. Measured results with load increased from 0.2 Nm to 1.5 Nm without and with the proposed methods. (a) dc-link voltage, back-EMF, and dc-link current. (b) Inverter output power. (c) Speed and torque.

6.5 Conclusion

This chapter systematically analyzes the potential energy backflow phenomenon in small dc-link capacitor-based IPMSM drive systems. This chapter also investigates the influence of dc-link voltage fluctuations on the conventional FW control strategies. A quasi-PIR-based FW control method with dc offset compensation is proposed to achieve the optimal amplitude of the *d*-axis reference current. Furthermore, an optimal phase angle selection method, based on

LMS and GD algorithms, is introduced to further suppress *q*-axis current harmonics and enhance system control performance. Experimental validation confirms the accuracy of the energy backflow phenomenon analysis and demonstrates the effectiveness of the proposed methods in eliminating energy backflow, as well as improving control performance and stability in small dc-link capacitor-based IPMSM drive systems.

CHAPTER 7

GENERAL CONCLUSION AND FUTURE WORK

7.1 Introduction

This thesis has presented a comprehensive investigation into the small dc-link capacitor-based PMSM drive systems, focusing on improving machine side control performance, which was often overlooked in the previous studies. It includes sensorless control strategies (both at low and high speeds) and FW control, and addresses issues related to dc-link voltage sensor faults.

The key contributions of this thesis can be summarized as follows:

- For middle and high-speed sensorless control, the effects of fluctuating dc-link voltage on EEMF-based sensorless control are examined, and a back-EMF harmonic suppression method is proposed to eliminate the estimated position error harmonics.
- For zero and low-speed sensorless control, two different sensorless control methods that do not require additional voltage signal injection to estimate rotor position are proposed. Furthermore, a magnetic polarity detection method based on inherent current harmonics is proposed to determine the magnetic polarity. In addition, a comparison of harmonic-based sensorless methods reveals that 100 Hz harmonics offer better static performance, while 200 Hz harmonics excel in dynamic performance.
- For the dc-link voltage sensor faults, the influence of sensor faults on the EEMF-based sensorless control method is investigated, and a dc-link voltage observer is proposed. Practical challenges such as parameter mismatches, coupling issues between estimated dc-link voltage and rotor position, sampling delays, and power losses are comprehensively analyzed and mitigated.
- The unavoidable energy backflow phenomenon is thoroughly analyzed. A novel FW control method that optimizes the amplitude and phase of the *d*-axis reference current is proposed to enhance control performance.

Several novel control strategies are proposed for the first time. Some findings and conclusions are detailed below. The summary of this thesis is shown in Fig. 7.1.

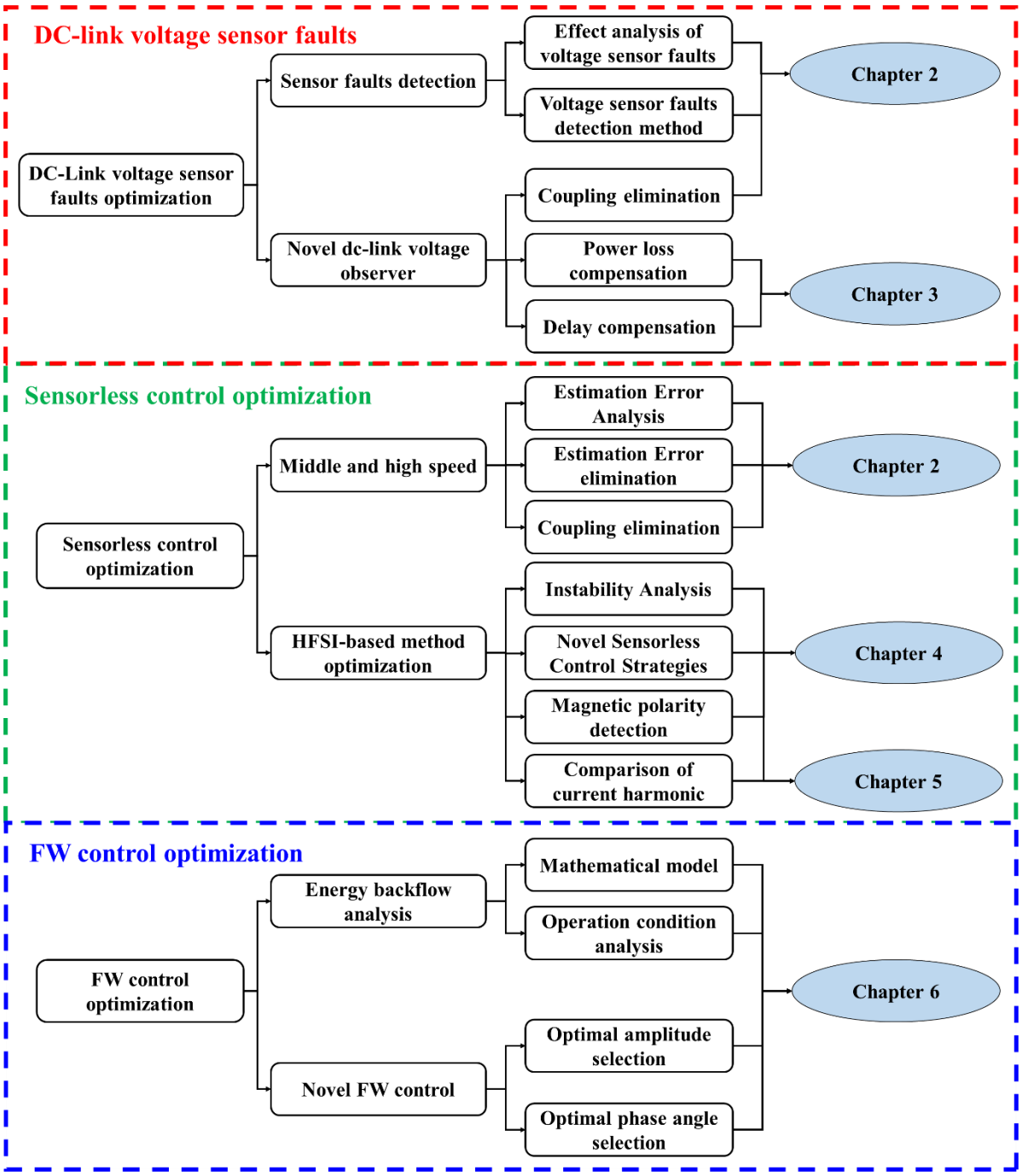

Fig. 7.1. Summary of the research in this thesis.

7.2 General Conclusions

7.2.1 DC-Link Voltage Sensor Faults Issues

In small dc-link capacitor-based PMSM drive systems, where dc-link voltage is constantly fluctuating (always changing), accurate voltage information is crucial for ensuring stable operation. This thesis investigates the effects of dc-link voltage sensor faults on the control performance of PMSM drive systems, particularly focusing on the EEMF-based sensorless

control method. The analysis shows that dc-link voltage sensor error, such as dc-link voltage measurement error can introduce a dc offset in the estimated rotor position error. To address this issue, a novel dc-link voltage observer which is immune to estimated rotor position error is proposed to effectively mitigate the effects on the EEMF-based sensorless control method caused by sensor faults. Additionally, the motor parameters mismatch caused by magnetic saturation is investigated using FEA, and it is evident that the parameter mismatches have minimal effect on the proposed observer. To further address the coupling issue related to using estimated dc-link voltage in the EEMF-based sensorless control, a back-EMF harmonic suppression method is proposed to reduce the harmonics in the estimated back-EMF, speed, position error, and dc-link voltage, thereby eliminating the coupling issues. Moreover, this thesis explores challenges related to time delay and power loss on the proposed observer and the EEMF-based control method. To overcome these, a time delay compensation method based on dc-link voltage reconstruction is introduced, along with a power compensation method to cancel the effects of power losses, enhancing the accuracy and applicability of the proposed observer in more complex operational environments.

TABLE 7.1

COMPARED OF DIFFERENT TECHNIQUES OF DC-LINK VOLTAGE SENSOR FAULT DETECTION

	Methodology	**Target system**	**Post-Fault remediation**	**Deal with dc-link voltage fluctuation**
[TEN17]	Sliding-mode observer	PMSM	No	No
[SKO22]	Neural network fault classification	IM	Yes	No
[WAN19C]	Stator flux observer combination	DTP PMSM	Yes	No
[TRI19]	Adaptive observer	PMSM	Yes	No
[XIA23]	Unknown input SMO and adaptive FTC	Single-phase grid converters	Yes	No
Proposed method	PIR-based voltage observer with optimization methods	PMSM	Yes	**Yes**

In comparison to the existing methodologies, the proposed PIR-based voltage observer with optimization methods offers some important advantages, particularly in its capability to accurately observe and compensate for ac signals. Traditional methods, while effective in identifying specific faults or optimizing control under stable conditions, cannot generally

monitor and adjust for the complexities introduced by fluctuating ac signals. For instance, the extreme learning method and neural network fault classification are proficient in fault detection but do not inherently support the observation of ac signals. Similarly, while SMO and adaptive observers are robust in certain dynamic scenarios, they are typically optimized for dc signals and may not adequately address ac variations. The stator flux observer combination and unknown input SMO approach, although more advanced, primarily targets fault detection and mitigation, without focus on ac signal fluctuations. In contrast, the PIR-based observer not only enhances fault detection and post-fault remediation but also integrates optimization strategies that enable precise observation and compensation for ac quantities, which is crucial in small dc-link capacitor-based PMSM systems. This makes the proposed methods more versatile and effective in ensuring robust system performance under varying operational conditions. The comparison of each method is shown in Table 7.2.

TABLE 7.2
COMPARED OF DIFFERENT TECHNIQUES OF DC-LINK VOLTAGE OBSERVER

	Primary Focus	**AC signal Observation**	**Strengths**
Extreme Learning Method	Fault Detection	No	Effective in fault detection
Sliding-Mode Observer	Dynamic Fault Detection	Limited	Robust in dynamic scenarios
Neural Network Classification	Fault Classification	No	Advanced fault classification
Stator Flux Observer	Fault Detection & Compensation	Limited	Effective in flux estimation
Adaptive Observer	Adaptive Fault Detection	Limited	Adapts to dynamic changes
Unknown Input SMO with FTC	Fault Detection & Mitigation	Limited	Advanced fault tolerance
Quasi-PIR-based Voltage Observer	Fault Detection & Compensation	**Yes**	AC signal observation

7.2.2 DC-Link Voltage Fluctuation on Sensorless Control Method

In small dc-link capacitor-based PMSM drive systems, severe fluctuations in the dc-link voltage can not only introduce harmonics into the system but also result in insuffient dc-link voltage conditions in certain scenarios, further deteriorating control system performance. For

instance, the conventional HF signal injection-based sensorless control methods normally used in zero and low-speed regions always need the extra HF voltage sensor to extract rotor position information. However, the dc-link voltage fluctuation, particularly when the minimum dc-link voltage is low, can severely deteriorate control performance in zero and low-speed regions due to insufficient dc-link voltage. Additionally, these extra HF signal injection methods tend to increase losses, torque ripples, and acoustic noise. To overcome these challenges, two novel sensorless control methods are introduced, which utilize inherent current harmonics caused by dc-link voltage fluctuations to determine rotor position, eliminating the need for additional HF voltage injection. These unavoidable current harmonics are also utilized for magnetic polarity detection in this thesis, providing better performance than the conventional secondary harmonic-based methods, especially under heavy load conditions. To address the sensitivity of the proposed method-I to motor parameter mismatches, a lookup table derived from FEA was initially employed in Chapter 4. However, this approach has limitations, such as reliance on precomputed data and the requirement for additional memory resources. Estimated position error could introduced if input data do not precisely match the stored values, potentially affecting rotor position estimation accuracy. Moreover, the method's dependence on multiple variables, including both *dq*-axis current signals and the amplitude and phase of the *dq*-axis voltages, can limit the precision and overall system performance. Consequently, the novel sensorless control method-II is introduced, which is immune to motor parameter mismatches and reduces dependency by requiring only the *q*-axis current and the phase angle of the *dq*-axis voltages. The proposed sensorless control methods based on 100 Hz and 200 Hz harmonics are also compared, providing a robust solution for HF signal injection-based sensorless control under severe dc-link voltage fluctuations. The comparison of the proposed novel sensorless control methods and the conventional HFSI-based sensorless control methods is shown in Table 7.3.

TABLE 7.3

COMPARED OF CONVENTIONAL HFSI-BASED METHODS AND PROPOSED SENSORLESS METHODS

	Conventional HFSI-based methods	**Proposed method-I**	**Proposed method-II**
Bandwidth	High	Medium	Medium
Static performance	Medium	Good	Good
Dynamic performance	Good	Worse	Medium
SNR	Medium	Worse	**Good**
Parameter sensitivity	No	**Yes**	No
System complexity	Medium	High	Medium
Feasibility under fluctuating dc-link voltage	Worse	**Good**	**Good**
Losses	Medium	**Low**	**Low**
Torque ripples	Medium	**Low**	**Low**
Acoustic noise	Medium	**Low**	**Low**

For middle and high-speed sensorless control, the influence of fluctuating dc-link voltage on EEMF-based sensorless control is firstly investigated. To address this, a back-EMF harmonic suppression technique utilizing notch filters is proposed to eliminate rotor position error harmonics, thereby enhancing the performance of the EEMF-based sensorless control method.

7.2.3 DC-Link Voltage Fluctuation on FW Control Method

The energy backflow phenomenon in small dc-link capacitor-based PMSM drive systems is firstly identified and investigated in this thesis. The large amplitude of back-EMF could exceed the minimum value of fluctuating dc-link voltage, leading to notable energy backflow. This unintended energy backflow not only poses risks to power devices but also introduces challenges to system stability and efficiency. The FW control strategy can effectively mitigate energy backflow by controlling the *d*-axis current to reduce the back-EMF. However, FW control faces challenges in systems with fluctuating dc-link voltage, as the *dq*-axis voltages also fluctuate, potentially causing voltage calculation errors that lead to *d*-axis reference current errors which are first identified in this thesis. Additionally, an analysis of the small-signal model of FB-FW control reveals that severe *q*-axis voltage fluctuations, particularly when the voltage becomes negative, can induce a positive feedback mode, resulting in inherent instability.

To address these issues, this thesis proposes a quasi-PIR-based FW control with dc offset compensation method. Furthermore, an optimal phase angle selection method based on the LMS algorithm and GD algorithm for *d*-axis reference current is introduced to suppress current ripple caused by the fluctuating dc-link voltage. This approach enhances the control performance and stability of the PMSM drive system. An overall summary of the existing works about FW control optimaziont in case of dc-link voltage fluctuation is shown below.

- In [JUN14], a concept of "average voltage constraint" is introduced to reduce the *d*-axis reference current ripple caused by dc-link voltage fluctuation in the FW control method.
- In [DIN19], by switching different FW control modes (minimum dc-link voltage control mode and extended dc-link voltage control mode) to improve dc-link voltage utilization and reduce torque ripple.
- In [HUO22B], a *q*-axis voltage control method is proposed to avoid positive feedback mode and improve the stability of the FW control.
- In [JIN24A], an active damping and voltage angle control-based FW control is proposed to reduce current harmonics.
- The proposed quasi-PIR and optimal phase angle selection-based FW control with dc offset compensation is proposed to eliminate the energy backflow issues, reduce current harmonics, and improve the performance and stability of the FW method. The comparison of proposed FW method and other works are systematically compared as shown in Table 7.4.

TABLE 7.4

COMPARED OF OTHER OPTOMAZED FW METHODS AND PROPOSED FW METHOD

	[JUN14]	**[DIN19]**	**[HUO22B]**	**[JIN24A]**	**Proposed methods**
Dynamic Performance	Medium	Medium	Medium	Good	Good
Static Performance	Medium	Medium	Medium	Good	Good
Computational burden	Low	Medium	Low	High	High
D-axis reference current error	Yes	Yes	Yes	Yes	**No**
Positive feedback mode suppression	No	No	Yes	No	**Yes**
Torque ripple	High	Medium	Medium	Low	Low

7.3 Future Work

Based on the analysis and conclusions, the future work can be summarized as follows:

1. Investigating a lookup table to further reduce the influence of motor parameter mismatch on the proposed dc-link voltage observer, or designing a new observer that is completely immune to motor parameter variations.
2. Investigating the influence of dc-link voltage sensor faults on FW control and adapting the proposed dc-link voltage observer for use in FW control strategies.
3. Investigating bandwidth enhancement strategies to address the low bandwidth issue in the proposed sensorless control methods.
4. Investigating the influence of *dq*-axis current fluctuations caused by small dc-link capacitor on the magnetic polarity detection strategy, a potential dc offset in the *d*-axis secondary harmonic response current need to be analyzed and suppression.
5. Investigating the optimal efficiency control strategies optimization method for small dc-link capacitor-based PMSM drive systems to maximize performance while minimizing energy losses.
6. Investigating grid side optimization strategies, such as high PF control, LC resonance suppression, and grid current quality improvement. Then, investigate strategies for simultaneous optimization of both grid side and machine side control.

REFERENCES

[ABE17] K. Abe, H. Haga, K. Ohishi, and Y. Yokokura, “Fine current harmonics reduction method for electrolytic capacitor-less and inductor-less inverter based on motor torque control and fast voltage feedforward control for IPMSM,” *IEEE Trans. Ind. Electron.*, vol. 64, no. 2, pp. 1071-1080, Feb. 2017.

[ABE18] K. Abe, H. Haga, K. Ohishi, and Y. Yokokura, “Direct dc-link current control considering voltage saturation for realization of sinusoidal source current waveform without passive components for IPMSM drives,” *IEEE Trans. Ind. Electron.*, vol. 65, no. 5, pp. 3805-3814, May 2018.

[ALM17] A. H. Almarhoon, Z. Q. Zhu, and P. Xu, “Improved pulsating signal injection using zero-sequence carrier voltage for sensorless control of dual three-phase PMSM,” *IEEE Trans. Energy Convers*, vol. PP, no. 99, pp. 1–1, 2017.

[ALZ17] R. P.-Alzola, D. C.-Gaona, P. F. Ksiazek, and M. Ordonez, “DC-link control filtering options for torque ripple reduction in low-power wind turbines,” *IEEE Trans. Power Electron.*, vol. 32, no. 6, pp. 4812-4826, Jun. 2017.

[BAE03] B. Bae and S. Sul, “A compensation method for time delay of full-digital synchronous frame current regulator of PWM AC drives,” *IEEE Trans. Ind. Appl.*, vol. 39, no. 3, pp. 802-810, May-Jun. 2003.

[BAI14] Z. Bai, H. Ma, D. Xu, B. Wu, Y. Fang, and Y. Yao, “Resonance damping and harmonic suppression for grid-connected current-source converter,” *IEEE Trans. Ind. Electron.*, vol. 61, no. 7, pp. 3146-3154, Jul. 2014.

[BAO19] D. Bao, X. Pan, and Y. Wang, “A novel hybrid control method for single-phase-input variable frequency speed control system with a small dc-link capacitor,” *IEEE Trans. Power Electron.*, vol. 34, no. 9, pp. 9016-9032, Sept. 2019.

[BAO20] D. Bao, X. Pan, Y. Wang, H. Huang, and B. Wu, “Integrated-power-control-strategy-based electrolytic capacitor-less back-to-back converter for variable frequency speed control system,” *IEEE Trans. Ind. Electron.*, vol. 67, no. 12, pp. 10065-10074, Dec. 2020.

[BAS11] D. Basic, F. Malrait, and P. Rouchon, “Current controller for low-frequency

signal injection and rotor flux position tracking at low speeds," *IEEE Trans. Ind. Electron.*,vol. 58, no. 9, pp. 4010–4022, Sep. 2011.

[BER01] F. F. Bernal, A.G. Cerrada, and R. Faure, "Determination of parameters in interior permanent-magnet synchronous motors with iron losses without torque measurement," *IEEE Trans. Ind. Appl.*, vol. 37, no. 5, pp. 1265–1272, Sept.-Oct. 2001.

[BIA01] N. Bianchi, S. Bolognani, and M. Zigliotto, "High performance PM synchronous motor drive for an electric scooter," *IEEE Trans. Ind. Appl*.,vol. 37, no. 5, pp. 1348–1355, Sep./Oct. 2001

[BIA05] N. Bianchi, and S. Bolognani, "Influence of rotor geometry of an interior PM motor on sensorless control feasibility," *Conf. Rec. IEEE-IAS Annu. Meeting*, vol. 4, pp. 2553-2560, 2005.

[BIE09] M. H. Bierhoff and F. W. Fuchs, "Active damping for three-phase PWM rectifiers with high-order line-side filters," *IEEE Trans. Ind. Electron.*, vol. 56, no. 2, pp. 371-379, Feb. 2009.

[BOL08] I. Boldea, M. C. Paicu, and G.-D. Andreescu, "Active flux concept for motion-sensorless unified AC drives," *IEEE Trans. Power Electron.*, vol. 23, no. 5, pp. 2612–2618, Sep. 2008.

[BOL09] I. Boldea, M. C. Paicu, G.-D. Andreescu, and F. Blaabjerg, "Active flux" DTFC-SVM sensorless control of IPMSM," *IEEE Trans. Energy Convers.*, vol. 24, no. 2, pp. 314–322, Jun. 2009.

[BOL14] S. Bolognani, S. Calligaro, and R. Petrella, "Adaptive flux-weakening controller for interior permanent magnet synchronous motor drives," *IEEE J. Emerg. Sel. Topics Power Electron.*, vol. 2, no. 2, pp. 236–248, Jun. 2014.

[BOZ17] S. Bozhko, M. Rashed, C. I. Hill, S. S. Yeoh, and T. Yang, "Flux-weakening control of electric starter-generator based on permanent-magnet machine," *IEEE Trans. Transport. Electrific*., vol. 3, no. 4, pp. 864-877, 2017.

[BRI05] F. Briz, M. W. Degner, P. Garcia, and J. M. Guerrero, "Rotor position estimation of AC machines using the zero-sequence carrier-signal voltage," *Trans. Ind. Appl.*, vol. 41, no. 6, pp. 1637–1646, Nov. 2005

[BRO21] A. Brosch, O. Wallscheid, and J. Böcker, “Model predictive control of permanent magnet synchronous motors in the overmodulation region including six-step operation,” *IEEE Open J. Ind. Appl.*, vol. 2, pp. 47-63, 2021.

[CES11] M. Cespedes, L. Xing, and J. Sun, “Constant-power load system stabilization by passive damping,” *IEEE Trans. Power Electron.*, vol. 26, no. 7, pp. 1832-1836, Jul. 2011.

[CHE03] Z. Chen, M. Tomita, S. Doki, and S. Okuma, “An extended electromotive force model for sensorless control of interior permanent-magnet synchronous motors,” *IEEE Trans. Ind. Electron.,* vol. 50, no. 2, pp. 288–295, Apr. 2003.

[CHE16] L. Chen, G. Götting, S. Dietrich, and I. Hahn, “Self-sensing control of permanent-magnet synchronous machines with multiple saliencies using pulse-voltage-injection,” *IEEE Trans. Ind. Appl.*, vol. 52, no. 4, pp. 3480–3491, Jul./Aug. 2016.

[CHE22] D. X. Chen, “Research on control strategy of permanent magnet synchronous motor drive system without electrolytic capacitor,” thesis, Huazhong University of Science and Technology, 2022.

[CHE99] Y. S. Chen, “Motor topologies and control strategies for permanent magnet brushless AC drives,” PhD Thesis, University of Sheffield, 1999.

[CHO12] C. Choi and W. Lee, “Analysis and compensation of time delay effects in hardware-in-the-loop simulation for automotive PMSM drive system,” *IEEE Trans. Ind. Electron.*, vol. 59, no. 9, pp. 3403-3410, Sept. 2012.

[CHU13] W. Q. Chu, “Investigation of torque characteristics of permanent magnet and electrically excited machines,” PhD thesis, University of Sheffield, 2013.

[COR12] P. Cortes, J. Rodriguez, C. Silva, and A. Flores, “Delay compensation in model predictive current control of a three-phase inverter,” *IEEE Trans. Ind. Electron.*, vol. 59, no. 2, pp. 1323–1325, Feb. 2012.

[CUP12] F. Cupertino, A. Guagnano, A. Altomare, and G. Pellegrino, “Position estimation delays in signal injection-based sensorless PMSM drives,” *3rd lEEE International Symposium on Sensorless Control for Electrical Drives (SLED 2012)*, pp. 1-6, 2012.

[DE10] F. M. L. De Belie, P. Sergeant, and J. A. Melkebeek, “A sensorless drive by applying test pulses without affecting the average-current samples,” *IEEE Trans. Power Electron.*,vol. 25, no. 4, pp. 875–888, Apr. 2010.

[DEN19] T. Deng, Z. Su, J. Lin, P. Tang, X. Chen, and P. Liu, “Advanced angle field weakening control strategy of permanent magnet synchronous motor,” *IEEE Trans. Veh. Technol.*, pp. 1-1, 2019.

[DEG98] M. W. Degner and R. D. Lorenz, “Using multiple saliencies for the estimation of flux, position, and velocity in AC machines,” *IEEE Trans. Ind. Appl.*, vol. 34, no. 5, pp. 1097–1104, Sep. 1998.

[DIN16] X. Ding, G. Liu, M. Du, H. Guo, C. Duan, and H. Qian, “Efficiency improvement of overall PMSM-inverter system based on artificial bee colony algorithm under full power range,” *IEEE Trans. Magn.*, vol. 52, no. 7, pp. 1-4, Jul. 2016.

[DIN19] D. Ding, G. Wang, N. Zhao, G. Zhang, and D. Xu, “Enhanced flux-weakening control method for reduced dc-link capacitance IPMSM drives,” *IEEE Trans. Power Electron.*, vol. 34, no. 8, pp. 7788-7799, Aug. 2019.

[DIN20] D. Ding, G. Zhang, G. Wang, and D. Xu, “Dual antiovervoltage control scheme for electrolytic capacitorless IPMSM drives with coefficient autoregulation,” *IEEE Trans. Power Electron.*, vol. 35, no. 3, pp. 2895-2907, Mar. 2020.

[DIN22A] D. Ding et al., “Impedance reshaping for inherent harmonics in PMSM drives with small DC-link capacitor,” *IEEE Trans. Power Electron.*, vol. 37, no. 12, pp. 14265-14279, Dec. 2022.

[DIN22B] D. Ding et al., “Suppression of beat phenomenon for electrolytic capacitorless motor drives accounting for sampling delay of DC-link voltage,” *IEEE Trans. Ind. Electron.*, vol. 69, no. 2, pp. 1167-1176, Feb. 2022.

[DIN24A] W. Ding, L. Huo, and S. Chen, “A novel suppression method for position estimation error in sensorless control of electrolytic capacitor-less PMSM drives,” *IEEE J. Emerg. Sel. Topics Power Electron.*, vol. 12, no. 1, pp. 618-630, Feb. 2024.

[DIN24B] D. Ding et al., “Harmonic suppression based on rectified current regulation with dc-link voltage decoupling for electrolytic capacitorless PMSM drives,” *IEEE Trans. Power Electron.*, vol. 39, no. 2, pp. 2213-2225, Feb. 2024.

[DRA18] T. Dragičević, “Dynamic stabilization of dc microgrids with predictive control of point-of-load converters,” *IEEE Trans. Power Electron.*, vol. 33, no. 12, pp. 10872-10884, Dec. 2018.

[ERT94] N. Ertugrul and P. Acarnley, “A new algorithm for sensorless operation of permanent magnet motors,” *IEEE Trans. Ind. Appl.*, vol. 30, no. 1, pp. 126–133, Jan. 1994.

[FIS14] J. R. Fischer, S. A. González, M. A. Herrán, M. G. Judewicz, and D. O. Carrica, “Calculation-delay tolerant predictive current controller for three phase inverters,” *IEEE Trans. Ind. Inform.*, vol. 10, no. 1, pp. 233–242, Feb. 2014.

[FOO15] G. H. B. Foo, X. Zhang, and D. M. Vilathgamuwa, “Sensor fault-resilient control of interior permanent-magnet synchronous motor drives,” *IEEE Trans. Mech.*, vol. 20, no. 2, pp. 855-864, Apr. 2015.

[GAB13] F. Gabriel, F. De Belie, X. Neyt, and P. Lataire, “High-frequency issues using rotating voltage injections intended for position self-sensing,” *IEEE Trans. Ind. Electron.*, vol. 60, no. 12, pp. 5447–5457, Dec. 2013.

[GAR07] P. Garcia, F. Briz, M. W. Degner, and D. D. Reigosa, “Accuracy, bandwidth, and stability limits of carrier-signal-injection-based sensorless control methods,” *IEEE Trans. Ind. Appl.*, vol. 43, no. 4, pp. 990–1000, Jul./Aug. 2007.

[GAO23] R. Gao, D. Ding, G. Wang, Q. Wang, G. Zhang, and D. Xu, “Linear modulation region expansion strategy based on voltage vector angle regulation for PMSM drives with small dc-link capacitor,” *IEEE Trans. Power Electron.*, vol. 38, no. 7, pp. 8327-8339, Jul. 2023.

[GON12] L. M. Gong, “Carrier signal injection based sensorless control of permanent magnet brushless AC machines,” PhD thesis, University of Sheffield, 2012.

[GON13] L. M. Gong and Z. Q. Zhu, “Robust initial rotor position estimation of permanent-magnet brushless AC machines with carrier-signal-injection-based

sensorless control," *IEEE Trans. Ind. Appl.*, vol. 49, no. 6, pp. 2602–2609, Nov. 2013.

[GON20A] C. Gong, Y. Hu, J. Gao, Y. Wang, and L. Yan, "An improved delay-suppressed sliding-mode observer for sensorless vector-controlled PMSM," *IEEE Trans. Ind. Electron.*, vol. 67, no. 7, pp. 5913-5923, Jul. 2020.

[GON20B] C. Gong, Y. Hu, C. Gan, G. Chen, and M. Alkahtani, "Modeling, analysis, and attenuation of uncontrolled generation for IPMSM-based electric vehicles in emergency," *IEEE Trans. Ind. Electron.*, vol. 67, no. 6, pp. 4453-4462, Jun. 2020.

[GON23] C. Gong, L. Ding, Y. Li, and J. Li, "Improved sensorless FCS-MPCC with current pre-estimation-based delay compensation integrated for PMSMs over high-speed range," *IEEE Trans. Ind. Appl.*, vol. 59, no. 6, pp. 6756-6765, Nov.-Dec. 2023.

[GUG06] P. Guglielmi, M. Pastorelli, and A. Vagati, "Cross-saturation effects in IPM motors and related impact on sensorless control," *IEEE Trans. Ind. Appl.*, vol. 42, no. 6, pp. 1516 – 1522, 2006.

[HAG03] H. Haga, I. Takahashi, and K. Ohishi, "Direct torque IPM motor control method to obtain unity power factor using a single-phase diode rectifier," *Proc. IEEE Int. Electr. Mach. Drives Conf. (IEMDC)*, vol. 2, pp. 1078-1083, Jun. 2003.

[HAS12] W. Hassan and Bingsen Wang, "Efficiency optimization of PMSM based drive system," *in Proc. 7th Int. Power Electron. Motion Control Conf.*, vol. 2, pp. 1027-1033, Jun. 2012.

[HE22] T. He, Z. Q. Zhu, F. Xu, Y. Wang, H. Bin, and L. Gong, "Electromagnetic performance analysis of 6-slot/2-pole high-speed permanent magnet motors with coil-pitch of two slot-pitches," *IEEE Trans. Energy Convers.*, vol. 37, no. 2, pp. 1335-1345, Jun. 2022.

[HEI23] P. Heil and A. Ali, "Analysis, diagnosis and reconfiguration of a synchronous motor control with faulty dc link voltage measurement," *IEEE Access*, vol. 11, pp. 37243-37252, 2023.

[HOS16] R. Hosooka, S. Shinnaka, and N. Nakamura, “New sensorless vector control of PMSM by discrete-time voltage injection of PWM carrier frequency–sine- and cosine-form amplitudes extraction method,” *in Proc. 42nd Annu. Conf. IEEE Ind. Electron. Soc.*, pp. 2862–2867, 2016.

[HU98] J. Hu and B. Wu, “New integration algorithms for estimating motor flux over a wide speed range,” *IEEE Trans. Power Electron.*, vol. 13, no. 5, p. 9, 1998.

[HUA17] Y. Huang, Y. Xu, Y. Li, and J. Zou, “A modified sensorless method for PMSM drive with small dc-link capacitor,” *2017 IEEE Trans. Electrif. Conf. Expo, Asia-Pacific*, pp. 1-5, Sep. 2017.

[HUA19] K. -P. Huang, Y. Wang, and R. -J. Wai, “Design of power decoupling strategy for single-phase grid-connected inverter under nonideal power grid,” *IEEE Trans. Power Electron.*, vol. 34, no. 3, pp. 2938-2955, Mar. 2019.

[HUA21] X. Huang, X. Ruan, J. Fang, and S. Kan, “A virtual impedance based control scheme for modular electrolytic capacitor-less second harmonic current compensator,” *IEEE Trans. Ind. Electron.*, vol. 68, no. 1, pp. 198-209, Jan. 2021.

[HUO22A] J. Huo, N. Zhao, G. Wang, G. Zhang, L. Zhu, and D. Xu, “An active damping control method for reduced dc-link capacitance PMSM drives with low line inductance,” *IEEE Trans. Power Electron.*, vol. 37, no. 12, pp. 14328–14342, Dec. 2022.

[HUO22B] J. Huo, D. Ding, Z. Ren, G. Wang, N. Zhao, L. Zhu, and D. Xu, “A novel flux-weakening control method with quadrature voltage constrain for electrolytic capacitorless PMSM drives,” *CES Trans. Elect. Mach. Syst.*, vol. 6, no. 3, pp. 279-287, Sept. 2022.

[HUO23] J. Huo, N. Zhao, R. Gao, G. Zhang, G. Wang, and D. Xu, “Analysis and compensation of position estimation error for sensorless reduced dc-link capacitance IPMSM drives,” *IEEE Trans. Ind. Electron.*, vol. 70, no. 3, pp. 3213-3221, Mar. 2023.

[HWA10] S. Hwang and J. Kim, “Dead time compensation method for voltage-fed PWM inverter,” *IEEE Trans. Energy Convers.*, vol. 25, no. 1, pp. 1-10, Mar. 2010.

[INA11] K. Inazuma, K. Ohishi, and H. Haga, “High-power-factor control for inverter output power of IPM motor driven by inverter system without electrolytic capacitor,” *Proc. IEEE Int. Symp. Ind. Electron.*, pp. 619-624, Jun. 2011.

[INA13] K. Inazuma, H. Utsugi, K. Ohishi, and H. Haga, “High-power-factor single-phase diode rectifier driven by repetitively controlled IPM motor,” *IEEE Trans. Ind. Electron.*, vol. 60, no. 10, pp. 4427-4437, Oct. 2013.

[JAN95] P. L. Jansen and R. D. Lorenz, “Transducerless position and velocity estimation in induction and salient ac machines,” *IEEE Trans. Ind. Appl.*, vol. 31, no. 2, pp. 240–247, Mar./Apr. 1995.

[JAH99] T. M. Jahns and V. Caliskan, “Uncontrolled generator operation of interior PM synchronous machines following high-speed inverter shutdown,” *IEEE Trans. Ind. Appl.*, vol. 35, no. 6, pp. 1347-1357, Nov.-Dec. 1999.

[JAN06] M. Jansson, L. Harnefors, O. Wallmark, and M. Leksell, “Synchronization at startup and stable rotation reversal of sensorless nonsalient PMSM drives,” *IEEE Trans. Ind. Electron.*, vol. 53, no. 2, pp. 379–387, Apr. 2006.

[JEO05A] Y. Jeong, S. Sul, S. Schulz, and N. Patel, “Fault detection and fault-tolerant control of interior permanent-magnet motor drive system for electric vehicle,” *IEEE Trans. Ind. Appl.*, vol. 41, no. 1, pp. 46-51, Jan.-Feb. 2005.

[JEO05B] Y. Jeong, R. D. Lorenz, T. M. Jahns, and S. K. Sul, "Initial rotor position estimation of an interior permanent-magnet synchronous machine using carrier-frequency injection methods," *IEEE Trans. Ind. Appl.*, vol. 41, no. 1, pp. 38-45, Jan.-Feb. 2005.

[JIA18] K. Jiang, C. Zhang, and X. Ge, “Low-frequency oscillation analysis of the train-grid system based on an improved forbidden-region criterion,” *IEEE Trans. Ind. Appl.*, vol. 54, no. 5, pp. 5064-5073, Sept.-Oct. 2018.

[JIN18] X. Jin, R. Ni, W. Chen, F. Blaabjerg, and D. Xu, “High-frequency voltage-injection methods and observer design for initial position detection of permanent magnet synchronous machines,” *IEEE Trans. Power Electron.*, vol. 33, no. 9, pp. 7971-7979, Sept. 2018.

[JIN19] T. Jin, X. Shen, T. Su, and R. C. C. Flesch, “Model predictive voltage control based on finite control set with computation time delay compensation for PV

systems," *IEEE Trans. Energy Convers.*, vol. 34, no. 1, pp. 330–338, Mar. 2019.

[JIN24A] R. Jing, D. Ding, G. Zhang, Q. Wang, G. Wang, and D. Xu, "Active-damping-based field-weakening control strategy with voltage angle regulation for high-speed SPMSM drive," *IEEE Trans. Ind. Electron.*, vol. 71, no. 2, pp. 1421-1431, Feb. 2024.

[JIN24B] R. Jing, Q. Wang, G. Wang, L. Zhu, G. Zhang and D. Xu, "Overmodulation voltage boundary adaptation-based field weakening strategy for high-speed SPMSM drives," *IEEE Trans. Ind. Electron.*, *IEEE access*, 2024.

[JUN14] H. S. Jung, S. J. Chee, S. K. Sul, Y. J. Park, H. S. Park, and W. K. Kim, "Control of three-phase inverter for ac motor drive with small dc-link capacitor fed by single-phase ac source," *IEEE Trans. Ind. Appl.*, vol. 50, no. 2, pp. 1074-1081, Mar.-Apr. 2014.

[KIM97] J. M. Kim and S. K. Sul, "Speed control of interior permanent magnet synchronous motor drive for the flux weakening operation," *IEEE Trans.Ind. Appl.*, vol. 33, no. 1, pp. 43–48, Jan./Feb. 1997.

[KIM12] S. Kim, J. I. Ha, and S. K. Sul, "PWM switching frequency signal injection sensorless method in IPMSM," *IEEE Trans.Ind. Appl.*, vol. 48, no.5, pp. 1576–1587, Sep./Oct. 2012.

[KIM16] S. I. Kim, J. H. Im, E. Y. Song, and R. Y. Kim, "A new rotor position estimation method of IPMSM using all-pass filter on high-frequency rotating voltage signal injection," *IEEE Trans. Ind. Electron.*,vol. 63, no. 10, pp. 6499–6509, Oct. 2016.

[KOM18] S. K. Kommuri, S. B. Lee, and K. C. Veluvolu, "Robust sensors-fault-tolerance with sliding mode estimation and control for PMSM drives," *IEEE/ASME Trans. Mechatron.*, vol. 23, no. 1, pp. 17-28, Feb. 2018.

[KOW22] T. O.-Kowalska et al., "Fault diagnosis and fault-tolerant control of PMSM drives–state of the art and future challenges," *IEEE Access*, vol. 10, pp. 59979-60024, 2022.

[LAI20] C. Lai et al., "PMSM drive system efficiency optimization using a modified gradient descent algorithm with discretized search space," *IEEE Trans.*

Transport. Electrific., vol. 6, no. 3, pp. 1104-1114, Sept. 2020.

[LAM09] H. Lamsahel and P. Mutschler, "Permanent magnet drives with reduced DC-link capacitor for home appliances," *Proc. IEEE 35th Annu. Conf. Ind. Electron.*, pp. 725-730, 2009.

[LEE09] J. Lee, K. Nam, S. Choi, and S. Kwon, "Loss-minimizing control of PMSM with the use of polynomial approximations," *IEEE Trans. Power Electron.*, vol. 24, no. 4, pp. 1071-1082, Apr. 2009.

[LEE14] W. J. Lee and S. K. Sul, "DC-link voltage stabilization for reduced dc-link capacitor inverter," *IEEE Trans. Ind. Appl.*, vol. 50, no. 1, pp. 404-414, Jan.-Feb. 2014.

[LEE15] Y. Lee, Y.-C. Kwon, and S.-K. Sul, "Comparison of rotor position estimation performance in fundamental-model-based sensorless control of PMSM," *in Proc. 2015 IEEE Energy Convers. Congr. Expo.*, pp. 5624–5633, 2015.

[LI09] Y. Li, Z. Q. Zhu, D. Howe, C. M. Bingham, and D. A. Stone, "Improved rotor-position estimation by signal injection in brushless AC motors, accounting for cross-coupling magnetic saturation," *IEEE Trans. Ind. Appl.*, vol. 45, no. 5, pp. 1843-1850, Sept.-Oct. 2009.

[LI22A] H. C. Li, "Research on control strategy for electrolytic capacitor-less permanent magnet compressor drive system," PhD thesis, Huazhong University of Science and Technology, 2022.

[LI22B] H. Li, Q. Yin, Q. Wang, H. Luo, and Y. Hou, "A novel dc-link voltage feedback active damping control method for IPMSM drives with small dc-link capacitors," *IEEE Trans. Ind. Electron.*, vol. 69, no. 3, pp. 2426-2436, Mar. 2022.

[LI22C] K. Li, T. Sun, H. Li, Y. Wang, W. Li, and L. Gong, "Grid current quality improvement for three-phase diode rectifier-fed small dc-link capacitance IPMSM drives," *IEEE Trans. Energy Convers.*, vol. 37, no. 4, pp. 2310-2320, Dec. 2022.

[LI24] Y. Li, Z. Yin, Y. Zhang, Y. Gao, J. Liu, and P. Zhang, "A harmonic suppression strategy based on adaptive synchronous rotating frame transformation for improving the estimation accuracy of sensorless drivers with small

capacitors," *IEEE Trans. Power Electron.*, vol. 39, no. 3, pp. 3521-3532, Mar. 2024.

[LIA24] D. Liang, Z. Q. Zhu, T. He, and F. Xu, "Analytical multi-element rotor thermal modelling of high-speed permanent magnet motors accounting for retaining sleeve," *IEEE Trans. Ind. Appl.*, vol. 60, no. 3, pp. 3920-3933, May-Jun. 2024.

[LIS05] M. Liserre, F. Blaabjerg, and S. Hansen, "Design and control of an LCL-filter-based three-phase active rectifier," *IEEE Trans. Ind. Appl.*, vol. 41, no. 5, pp. 1281-1291, Sept.-Oct. 2005.

[LIU14] J. M. Liu and Z. Q. Zhu, "Novel sensorless control strategy with injection of high-frequency pulsating carrier signal into stationary reference frame," *IEEE Trans. Ind. Appl.*, vol. 50, no. 4, pp. 2574-2583, July-Aug. 2014.

[LIU22] J. Liu and Y. Zhang, "Current pulsation suppression method based on power current closed-loop control for a PMSM under fluctuating dc-link voltage," *IEEE Trans. Power Electron.*, vol. 37, no. 1, pp. 761-770, Jan. 2022.

[LIU23] Z. Liu, W. Ding, S. Chen, R. Hu, and S. Shi, "Grid side current harmonic suppression and power factor improvement using q-axis damping current injection for PMSM drives without electrolytic capacitor," *IEEE J. Emerg. Sel. Topics Power Electron.*, vol. 11, no. 3, pp. 3371–3384, Jun. 2023.

[LU18] M. Lu, X. Wang, P. C. Loh, F. Blaabjerg, and T. Dragicevic, "Graphical evaluation of time-delay compensation techniques for digitally controlled converters," *IEEE Trans. Power Electron.*, vol. 33, no. 3, pp. 2601–2614, Mar. 2018.

[LUO24] P. Luo, Z. Yin, Z. Zhang, Y. Zhang, P. Zhang, and J. Liu, "Diversified diagnosis strategy for PMSM inter-turn short-circuit fault via novel sliding mode observer," *IEEE Trans. Power Electron.*, vol. 39, no. 4, pp. 4149-4159, Apr. 2024.

[MAG12] P. Magne, D. Marx, B. Nahid-Mobarakeh, and S. Pierfederici, "Large-signal stabilization of a DC-link supplying a constant power load using a virtual capacitor: Impact on the domain of attraction," *IEEE Trans. Ind. Appl.*, vol. 48, no. 3, pp. 878-887, May-Jun. 2012.

[MAH13] R. Maheshwari, S. Munk-Nielsen, and K. Lu, “An active damping technique for small DC-link capacitor based drive system,” *IEEE Trans. Ind. Inform.*, vol. 9, no. 2, pp. 848-858, May 2013.

[MAI21] Z. Mai et al., “HF pulsating carrier voltage injection method based on improved position error signal extraction strategy for PMSM position sensorless control,” *IEEE Trans. Power Electron.*, vol. 36, no. 8, pp. 9348-9360, Aug. 2021.

[MAT17] L. Mathe, L. Török, D. Wang, and D. Sera, “Resonance reduction for ac drives with small capacitance in the dc link,” *IEEE Trans. Ind. Appl.*, vol. 53, no. 4, pp. 3814-3820, Jul.-Aug. 2017.

[MED15] S. Medjmadj, D. Diallo, M. Mostefai, C. Delpha, and A. Arias, “PMSM drive position estimation: contribution to the high-frequency injection voltage selection issue,” *IEEE Trans. Energy Convers.*, vol. 30, no. 1, pp. 349–358, Mar. 2015.

[MIK00] I. Miki, Y. Inagaki, and S. Nakashima, “Sensorless initial rotor position estimation of surface permanent-magnet synchronous motor,” *IEEE Trans. Ind. Appl.*,vol. 36, no. 6, pp. 1598–1603, Nov.-Dec. 2000.

[MOR02] S. Morimoto, K. Kawamoto, M. Sanada, and Y. Takeda, “Sensorless control strategy for salient-pole PMSM based on extended EMF in rotating reference frame,” *IEEE Trans. Ind. Appl.*, vol. 38, no. 4, pp. 1054–1061, Jul. 2002.

[MOR21] S. Morimoto, K. Shimamoto, M. Kakihara, and T. Hanamoto, “Improving position estimation accuracy of magnetic saliency based sensorless control by considering cross-coupling factor,” *IEEJ J. Ind. Appl.,*vol. 10, no. 1, pp. 18–26, Jan. 2021.

[MOR90] S. Morimoto, Y. Takeda, and T. Hirasa, “Expansion of operating limits for permanent magnet motor by current vector control considering inverter capacity,” *IEEE Trans. Ind. Appl*., vol. 26, no. 5, pp. 866–871, Sep./Oct. 1990.

[MOR94] S. Morimoto, M. Sanada, and Y. Takeda, “Wide-speed operation of interior permanent magnet synchronous motors with high-performance current regulator,” *IEEE Trans. Ind. Appl.,* vol. 30, no. 4, pp. 920-926, Jul.-Aug. 1994.

[MUR12] S. Murakami, T. Shiota, M. Ohto, K. Ide, and M. Hisatsune, “Encoderless servo drive with adequately designed IPMSM for pulse-voltage-injection-based position detection,” *IEEE Trans. Ind. Appl.*,vol. 48, no. 6, pp. 1922–1930, Nov.-Dec. 2012.

[NAD24] M. Naderian, G. A. Markadeh, M. Karimi-Ghartemani and M. Mojiri, “Improved sensorless control strategy for IPMSM using an ePLL approach with high-frequency injection,” *IEEE Trans. Ind. Electron.*, vol. 71, no. 3, pp. 2231-2241, Mar. 2024.

[NI15] R. Ni, D. Xu, G. Wang, L. Ding, G. Zhang, and L. Qu, “Maximum efficiency per ampere control of permanent-magnet synchronous machines,” *IEEE Trans. Ind. Electron.*, vol. 62, no. 4, pp. 2135-2143, Apr. 2015.

[NIM14] T. Nimura, S. Doki and M. Fujitsuna, “Position sensorless control of PMSM with a low-frequency signal injection,” *2014 International Power Electronics Conference (IPEC-Hiroshima 2014 ECCE ASIA),* Hiroshima, Japan, pp. 3079-3084, 2014.

[OUY11] H. Ouyang, K. Zhang, P. Zhang, Y. Kang, and J. Xiong. “Repetitive compensation of fluctuating dc link voltage for railway traction drives,” *IEEE Trans. Power Electron.*, vol. 26, no. 8, pp. 2160-2171, Aug. 2011.

[PAI23] H. Pairo and B. Nikmaram, “Initial rotor position estimation of SynRM based on pulsating voltage injection combined with finite position set algorithm,” *IEEE J. Emerg. Sel. Topics Power Electron.*, vol. 11, no. 4, pp. 4321-4331, Aug. 2023.

[PES23] P. Pescetto, A. S.-Gonzalez, F. A.-Gonzalez, H. Kapeller, E. Trancho, and G. Pellegrino, “Active control of variable dc-link for maximum efficiency of traction motor drives,” *IEEE Trans. Ind. Appl.*, vol. 59, no. 4, pp. 4120-4129, pp. 4120-4129, Jul.-Aug. 2023.

[QU23] J. Qu, P. Zhang, J. Jatskevich, and C. Zhang, “Torque-ripple reduction of permanent magnet synchronous machine drives based on novel speed harmonic control at low-speed operation,” *IEEE Trans. Ind. Electron.*, vol. 70, no. 8, pp. 7683-7694, Aug. 2023.

[RAC08] D. Raca, M. C. Harke, and R. D. Lorenz, “Robust magnet polarity estimation

for initialization of PM synchronous machines with near-zero saliency," *IEEE Trans. Ind. Appl.*,vol. 44, no. 4, pp. 1199–1209, Jul./Aug. 2008.

[RAC10] D. Raca, P. Garcia, D. D. Reigosa, F. Briz, and R. D. Lorenz, "Carrier-signal selection for sensorless control of PM synchronous machines at zero and very low speeds," *IEEE Trans. Ind. Appl.*,vol. 46, no. 1, pp. 167–178, Jan.-Feb. 2010.

[REI08] D. D. Reigosa, P. Garcia, D. Raca, F. Briz, and R. D. Lorenz, "Measurement and adaptive decoupling of cross-saturation effects and secondary saliencies in sensorless controlled IPM synchronous machines," *IEEE Trans. Ind. Appl.*,vol. 44, no. 6, pp. 1758–1767, Nov./Dec. 2008.

[REN24] Z. Ren, et al., "Adaptive virtual admittance reshaping-based resonance suppression strategy for PMSM drives with small dc-link capacitor," *IEEE Trans. Power Electron.*, vol. 39, no. 3, pp. 3109-3121, Mar. 2024.

[SAL10] F. Salmasi, T. Najafabadi, and P. Maralani, "An adaptive flux observer with online estimation of dc-link voltage and rotor resistance for VSI-based induction motors," *IEEE Trans. Power Electron.*, vol. 25, no. 5, pp. 1310-1319, May 2010.

[SAR05] H. Saren, O. Pyrhonen, K. Rauma, and O. Laakkonen, "Overmodulation in voltage source inverter with small dc-link capacitor," *Proc. IEEE 36th Power Electron. Spec. Conf.*, pp. 892–898, 2005.

[SCH97] P. B. Schmidt, M. L. Gasperi, G. Ray, and A. H. Wijenayake, "Initial rotor angle detection of a nonsalient pole permanent magnet synchronous machine," *in Proc. IEEE-IAS Annual Meeting*, 1997, pp. 459–463.

[SEP16] L. Sepulchre, M. Fadel, and M. Pietrzak-David, "Improvement of the digital control of a high speed PMSM for vehicle application," *in Proc. 11th Int. Conf. Ecol. Veh. Renewable Energies* (EVER), Monte Carlo, Monaco, pp. 1-9, 2016.

[SHI04] Y. F. Shi, Z. Q. Zhu, Y. S. Chen, and D. Howe, "Investigation of flux-weakening performance and current oscillation of permanent magnet brushless AC drives," *4th Int. Conf. Power Electr. Motion Control*, pp. 1257-1262, 2004.

[SHI17] H. Shin, Y. Son, and J. I. Ha, “Grid current shaping method with dc-link shunt compensator for three-phase diode rectifier-fed motor drive system,” *IEEE Trans. Power Electron.*, vol. 32, no. 2, pp. 1279-1288, Feb. 2017.

[SHU21] B. Shuang and Z. Q. Zhu, “A novel method for estimating the high frequency incremental *dq*-axis and cross-coupling inductances in interior permanent magnet synchronous machines,” *IEEE Trans. Ind. Appl.*, vol. 57, no. 5, pp. 4913-4923, Sept.-Oct. 2021.

[SHU22] B. Shuang, Z. Q. Zhu, and X. Wu, “Improved cross-coupling effect compensation method for sensorless control of IPMSM with high frequency voltage injection,” *IEEE Trans. Energy Convers.*, vol. 37, no. 1, pp. 347-358, Mar. 2022.

[SKO22] M. Skowron, K. Teler, M. Adamczyk, and T. O.-Kowalska. “Classification of single current sensor failures in fault-tolerant induction motor drive using neural network approach,” *Energies*, vol. 15, no. 18, pp. 1-17, 2022.

[SOM23] S. Somkun, S. Srita, T. Kaewchum, A. Pannawan, C. Saeseiw, and P. Pachanapan, “Adaptive notch filters for bus voltage control and capacitance degradation prognostic of single-phase grid-connected inverter,” *IEEE Trans. Ind. Electron.*, vol. 70, no. 12, pp. 12190-12200, Dec. 2023.

[SON96] H. Song, J. M. Kim, and S. K. Sul, “A new robust SPMSM control to parameter variations in flux weakening region,” *in Proc. IEEE Ind. Electron.Soc. Annu. Conf.*, pp. 1193–1198, 1996.

[SON15] Y. Son and J. I. Ha, “Direct power control of a three-phase inverter for grid input current shaping of a single-phase diode rectifier with a small dc-link capacitor,” *IEEE Trans. Power Electron.*, vol. 30, no. 7, pp. 3794-3803, Jul. 2015.

[SON17] Y. Son and J. I. Ha, “Discontinuous grid current control of motor drive system with single-phase diode rectifier and small dc-link capacitor,” *IEEE Trans. Power Electron.*, vol. 32, no. 2, pp. 1324-1334, Feb. 2017.

[STA14] C. S. Staines, C. Caruana, and R. Raute, “A review of saliency-based sensorless control methods for alternating current machines,” *IEEJ J. Ind. Appl.*, vol. 3, no. 2, pp. 86–96, 2014.

[TAG19] S. Taghizadeh, M. Karimi-Ghartemani, M. J. Hossain, and J. Lu, “A fast and robust dc-bus voltage control method for single-phase voltage-source dc/ac converters,” *IEEE Trans. Power Electron.*, vol. 34, no. 9, pp. 9202-9212, Sept. 2019.

[TAK01] I. Takahashi and H. Haga. “Power factor improvement of single-phase diode rectifier by fast field-weakening of inverter driven IPM motor,” *IEEE 4th Int. Conf. Power Electron. Drive Syst.*, vol. 2, no. 1, pp. 241–246, 2001.

[TAK02] I. Takahashi and H. Haga, “Inverter control method of IPM motor to improve power factor of diode rectifier,” *Proc. Power Convers. Conf.*, Osaka, pp. 142-147, 2002.

[TEN17] Q. Teng, J. Tian, J. Duan, H. Cui, J. Zhu, and Y. Guo, “Sliding-mode MRA observer-based model predictive current control for PMSM drive system with dc-link voltage sensorless,” *2017 20th Int. Conf. Electr. Mach. Syst. (ICEMS)*, pp. 1-6, 2017.

[TRI19] Q. N. Trinh, F. H. Choo, Y. Tang, and P. Wang, “Control strategy to compensate for current and voltage measurement errors in three-phase PWM rectifiers,” *IEEE Trans. Ind. Appl.*, vol. 55, no. 3, pp. 2879-2889, May-Jun. 2019.

[WAI01] J. Wai and T. M. Jahns, “A new control technique for achieving wide constant power speed operation with an interior PM alternator machine,” *in Proc. IEEE 36th IAS Annu. Meeting, Conf. Rec. Ind. Appl. Conf.*,vol. 2. pp. 807–814, Oct. 2001.

[WAN14] G. Wang, H. Zhan, G. Zhang, X. Gui, and D. Xu, “Adaptive compensation method of position estimation harmonic error for EMF-based observer in sensorless IPMSM drives,” *IEEE Trans. Power Electron.*, vol. 29, no. 6, pp. 3055-3064, Jun. 2014.

[WAN16] G. Wang, L. Yang, B. Yuan, B. Wang, G. Zhang, and D. Xu, “Pseudo-random high-frequency square-wave voltage injection based sensorless control of IPMSM drives for audible noise reduction,” *IEEE Trans. Ind. Electron.,* vol. 63, no. 12, pp. 7423-7433, Dec. 2016.

[WAN17A] G. Wang, L. Yang, G. Zhang, X. Zhang, and D. Xu, “Comparative investigation of pseudorandom high-frequency signal injection schemes for

sensorless IPMSM drives," *IEEE Trans. Power Electron.*, vol. 32, no. 3, pp. 2123–2132, Mar. 2017.

[WAN17B] G. Wang, D. Xiao, N. Zhao, X. Zhang, W. Wang, and D. Xu, "Low-frequency pulse voltage injection scheme-based sensorless control of IPMSM drives for audible noise reduction," *IEEE Trans. Ind. Electron.*, vol. 64, no. 11, pp. 8415-8426, Nov. 2017.

[WAN18A] D. Wang, K. Lu, P. O. Rasmussen, L. Mathe, Y. Feng, and F. Blaabjerg, "Voltage modulation using virtual positive impedance concept for active damping of small DC-link drive system," *IEEE Trans. Power Electron.*, vol. 33, no. 12, pp. 10611-10621, Dec. 2018.

[WAN18B] D. Wang and K. Lu, "Analysis of system interharmonics of VSI-Fed small dc-link drive with varying power load," *2018 IEEE Energy Convers. Congr. Expo., (ECCE)*, Portland, OR, USA, pp. 3347-3354, 2018.

[WAN19A] C. Wang, "Novel flux-weakening control of permanent magnet synchronous machines with particular reference to stability issues," PhD thesis, University of Sheffield, 2019.

[WAN19B] G. Wang, D. Xiao, G. Zhang, C. Li, X. Zhang, and D. Xu, "Sensorless control scheme of IPMSMs using HF orthogonal square-wave voltage injection into a stationary reference frame," *IEEE Trans. Power Electron.*, vol. 34, no. 3, pp. 2573–2584, Mar. 2019.

[WAN19C] X. Wang, Z. Wang, Z. Xu, M. Cheng, W. Wang, and Y. Hu, "Comprehensive diagnosis and tolerance strategies for electrical faults and sensor faults in dual three-phase PMSM drives," *IEEE Trans. Power Electron.*, vol. 34, no. 7, pp. 6669-6684, Jul. 2019.

[WAN20A] G. Wang, M. Valla and J. Solsona, "Position sensorless permanent magnet synchronous machine drives—a review," *IEEE Trans. Ind. Electron.*, vol. 67, no. 7, pp. 5830-5842, Jul. 2020.

[WAN20B] G. Wang, N. Zhao, G. Zhang, and D. Xu, "Reduced dc-link capacitance AC motor drives," Singapore, Springer Nature, 2020.

[WAN20C] G. Wang, H. Hu, D. Ding, N. Zhao, Y. Zou, and D. Xu, "Overmodulation strategy for electrolytic capacitorless PMSM drives: voltage distortion

analysis and boundary optimization," *IEEE Trans. Power Electron.*, vol. 35, no. 9, pp. 9574-9585, Sep. 2020

[WAN20D] W. Wang and Z. Lu, "Analysis of model predictive current-controlled permanent magnet synchronous motor drives with inaccurate dc bus voltage measurement," *Energies*, vol. 13, no. 2, pp. 1-15, 2020.

[WAN23] C. Wang, Z.Q. Zhu, L. Xu, and X. Wu, "Comparative stability study of two feedback flux-weakening control methods of permanent magnet synchronous machine," *Trans. China Electrotech. Soc.*, vol.38, no.14, pp.3689-3707, Jul. 2023.

[WU17] X. Wu et al., "Initial rotor position detection for sensorless interior PMSM with square-wave voltage injection," *IEEE Trans. Magn.*, vol. 53, no. 11, pp. 1-4, Nov. 2017.

[WU20] X. M. Wu, "Novel sensorless control of surface-mounted permanent magnet synchronous machines," PhD thesis, University of Sheffield, 2020.

[WU22] T. Wu, D. Luo, X. Wu, K. Liu, S. Huang, and X. Peng, "Square-wave voltage injection based PMSM sensorless control considering time delay at low switching frequency," *IEEE Trans. Ind. Electron.*, vol. 69, no. 6, pp. 5525-5535, Jun. 2022.

[WU23A] Z. Wu, C. Cheng, W. Hua, Y. Wang, H. Zhang, and W. Wang, "A frequency-adaptive delay signal cancelation-based filter to reduce position estimation error for sensorless IPMSM drives," *IEEE Trans. Power Electron.*, vol. 38, no. 2, pp. 1662-1671, 2023.

[WU23B] L. Wu and Z. Lyu, "Harmonic injection-based torque ripple reduction of PMSM with improved dc-link voltage utilization," *IEEE Trans. Power Electron.*, vol. 38, no. 7, pp. 7976-7981, Jul. 2023.

[XIA17] J. Xia, Y. Guo, B. Dai, and X. Zhang, "Sensor fault diagnosis and system reconfiguration approach for an electric traction PWM Rectifier based on sliding mode observer," *IEEE Trans. Ind. Appl.*, vol. 53, no. 5, pp. 4768-4778, Sept.-Oct. 2017.

[XIA23] J. Xia, Z. Li, X. Gao, Y. Guo, and X. Zhang, "Real-Time sensor fault identification and remediation for single-phase grid-connected converters

using hybrid observers with unknown input adaptation," *IEEE Trans. Ind. Electron.*, vol. 70, no. 3, pp. 2407-2418, Mar. 2023.

[XU14] W. Xu and R. D. Lorenz, "High-frequency injection-based stator flux linkage and torque estimation for DB-DTFC implementation on IPMSMs considering cross-saturation effects," *IEEE Trans. Ind. Appl.*, vol. 50, no. 6, pp. 3805–3815, Nov.-Dec. 2014.

[XU16A] P. L. Xu and Z. Q. Zhu, "Novel carrier signal injection method using zero-sequence voltage for sensorless control of PMSM drives," *IEEE Trans. Ind. Electron.*, vol. 63, no. 4, pp. 2053–2061, Apr. 2016.

[XU16B] P. L. Xu, Z. Q. Zhu, and D. Wu, "Carrier signal injection-based sensorless control of permanent magnet synchronous machines without the need of magnetic polarity Identification", *IEEE Trans. Ind. Appl.*, vol. 52, no. 5, pp. 3916–3926, Sept.-Oct., 2016.

[XU17] P. Xu and Z. Zhu, "Carrier signal injection-based sensorless control for permanent magnet synchronous machine drives with tolerance of signal processing delays," *IET Elect. Power Appl.*, vol. 11, no. 6, pp. 1140–1149, 2017.

[YAN17] S. C. Yang and Y. L. Hsu, "Full speed region sensorless drive of permanent-magnet machine combining saliency-based and back-EMF-based drive," *IEEE Trans. Ind. Electron.*, vol. 64, no. 2, pp. 1092-1101, Feb. 2017.

[YAN21] J. Yang, R. Song, L. Zhao, X. Zhang, S. Hussain, G. Liu, Z. Shi, and G. Qiao, "Magnetic Ni doping induced high power factor of Cu2GeSe3-based bulk materials," *Journal of the European Ceramic Society*, vol. 41, no. 6, pp. 3473-3479, 2021.

[YAN22A] J. Yan, X. Wu, and Z. Q. Zhu, "Analysis of extended EMF based sensorless control with dc-link voltage fluctuation," *2022 11th Int. Conf. Power Electro., Mach. Drives (PEMD)*, pp. 327-334, Jun. 2022.

[YAN22B] J. Yan, X. Wu, Z. Q. Zhu, and C. Liu, "Influence of dc-link voltage measurement error on extended EMF based sensorless control with reduced dc-link capacitor," *2022 25th Int. Conf. Electr. Mach. and Syst. (ICEMS)*, Thailand, pp. 1-6. 2022.

[YAN22C] J. Yan, X. Wu, Z. Q. Zhu, and C. Liu, “A novel dc-link voltage observer with time delay compensation for small dc-link capacitor-based IPMSM with EEMF-based sensorless control,” *in Proc. IEEE 2nd Int. Conf. Sustain. Mobility Appl., Renewables Technol.* (SMART)., pp. 1-6, Nov. 2022.

[YAN22D] L. Yan, Z. Q. Zhu, J. Qi, Y. Ren, C. Gan, S. Brockway, and C. Hilton, “Multiple synchronous reference frame current harmonic regulation of dual three phase PMSM with enhanced dynamic performance and system stability,” *IEEE Trans. Ind. Electron.*, vol. 69, no. 9, pp. 8825-8838, Sept. 2022.

[YAN24] J. Yan, X. Wu, Z. Q. Zhu and C. Liu, “Improved extended EMF-based sensorless control for IPMSMs with small dc-link capacitor considering dc-link voltage measurement error,” *IEEE Trans. Ind. Appl.*,, vol. 60, no. 4, pp. 6299-6313, Jul.-Aug. 2024.

[YOO11] Y. Yoon, S. K. Sul, S. Morimoto, and K. Ide, “High-bandwidth sensorless algorithm for ac machines based on square-wave-type voltage injection,” *IEEE Trans. Ind. Appl.*, vol. 47, no. 3, pp. 1361-1370, May-Jun. 2011.

[YU13] C. -Y. Yu, J. Tamura, and R. D. Lorenz, “Optimum dc bus voltage analysis and calculation method for inverters/motors with variable dc bus voltage,” *IEEE Trans. Ind. Appl.,* vol. 49, no. 6, pp. 2619-2627, Nov.-Dec. 2013.

[ZHA04] H. Zhao, Q. M. J. Wu, and A. Kawamura, “An accurate approach of nonlinearity compensation for VSI inverter output voltage,” *IEEE Trans. Power Electron.*, vol. 19, no. 4, pp. 1029-1035, Jul. 2004.

[ZHA17] G. Zhang, G. Wang, and D. Xu, “Saliency-based position sensorless control methods for PMSM drives—A review,” *Chin. J. Elect. Eng.*, vol. 3, no. 2, pp. 14–23, Sep. 2017.

[ZHA18A] N. Zhao, G. Wang, D. Xu, L. Zhu, G. Zhang, and J. Huo, “Inverter power control based on DC-link voltage regulation for IPMSM drives without electrolytic capacitors,” *IEEE Trans. Power Electron.*, vol. 33, no. 1, pp. 558-571, Jan. 2018.

[ZHA18B] X. Zhang, H. Li, S. Yang, and M. Ma, “Improved initial rotor position estimation for PMSM drives based on HF pulsating voltage signal injection,”

IEEE Trans. Ind. Electron., vol. 65, no. 6, pp. 4702–4713, Jun. 2018.

[ZHA19A] N. Zhao, G. Wang, R. Zhang, B. Li, Y. Bai, and D. Xu, "Inductor current feedback active damping method for reduced DC-link capacitance IPMSM drives," *IEEE Trans. Power Electron.*, vol. 34, no. 5, pp. 4558-4568, May 2019.

[ZHA19B] N. Zhao, G. Wang, B. Li, R. Zhang, and D. Xu, "Beat phenomenon suppression for reduced dc-link capacitance IPMSM drives with fluctuated load torque," *IEEE Trans. Ind. Electron.*, vol. 66, no. 11, pp. 8334-8344, Nov. 2019.

[ZHA19C] N. Zhao, G. Wang, D. Ding, G. Zhang, and D. Xu, "Impedance based stabilization control method for reduced dc-link capacitance IPMSM drives," *IEEE Trans. Power Electron.*, vol. 34, no. 10, pp. 9879-9890, Oct. 2019.

[ZHA19D] G. Zhang, G. Wang, H. Wang, D. Xiao, L. Li, and D. Xu, "Pseudo random frequency sinusoidal injection based sensorless IPMSM drives with tolerance for system delays," *IEEE Trans. Power Electron.*, vol. 34, no. 4, pp. 3623–3632, Apr. 2019.

[ZHA20] S. Zhao, X. Huang, Y. Fang, and H. Zhang, "DC-link-fluctuation-resistant predictive torque control for railway traction permanent magnet synchronous motor in the six-step operation," *IEEE Trans. Power Electron.*, vol. 35, no. 10, pp. 10982-10993, Oct. 2020.

[ZHA21] C. Zhang, L. Xu, X. Zhu, Y. Du, and L. Quan, "Torque ripple reduction of PMSM with small capacitor drive systems based on combined control method," *IEEE Access*, vol. 9, pp. 98874-98882, 2021.

[ZHA24] J. Zhang, X. Zhang, Y. Yu, B. Wang, and D. Xu, "Optimization of current dynamic performance and torque harmonic for induction motor field-weakening control under hexagon voltage extension," *IEEE Trans. Power Electron.*, vol. 39, no. 6, pp. 7329-7342, Jun. 2024.

[ZHO16] Y. Zhou, W. Huang, and F. Hong, "Single-phase input variable-speed AC motor system based on an electrolytic capacitor-less single-stage boost three-phase inverter," *IEEE Trans. Power Electron.*, vol. 31, no. 10, pp. 7043-7052, Oct. 2016.

[ZHU02] Z. Q. Zhu, Y. S. Chen, and D. Howe, “Iron loss in permanent-magnet brushless AC machines under maximum torque per ampere and flux weakening control,” *IEEE Trans. Magn.*, vol. 38, no. 5, pp. 3285-3287, Sept. 2002.

[ZHU07] Z. Q. Zhu and D. Howe, “Electrical machines and drives for electric, hybrid, and fuel cell vehicles,” *Proc. IEEE*, vol. 95, no. 4, pp. 746–765, Apr. 2007.

[ZHU11A] Z. Q. Zhu and L. M. Gong, “Improved sensorless operation of permanent magnet brushless AC motors based on online optimal efficiency control,” *in Proc. IEEE Int. Electr. Mach. Drives Conf.* (IEMDC), Niagara Falls, Canada, pp. 1591–1596, May 2011.

[ZHU11B] Z. Q. Zhu and L. M. Gong, “Investigation of effectiveness of sensorless operation in carrier-signal-injection-based sensorless-control methods,” *IEEE Trans. Ind. Electron.*, vol. 58, no. 8, pp. 3431-3439, Aug. 2011.

[ZHU23] Z. Q. Zhu and X. M. Wu, “Sensorless control of permanent magnet synchronous machine drives,” New York, US, *Wiley-IEEE Press*, 2023.

APPENDIX

Appendix 1 Experimental Platform

In this thesis, the experimental platform is designed using a variable transformer and an isolation transformer connected to the main power, providing an adjustable and isolated AC input source. The platform is built around the Infineon EVAL-M1-CTE610N3 evaluation board, which is used to control and interface with the system. The dSPACE1006 control system is employed to manage the operations. The platform includes both a test motor and a load motor, as shown in Fig. A.1.

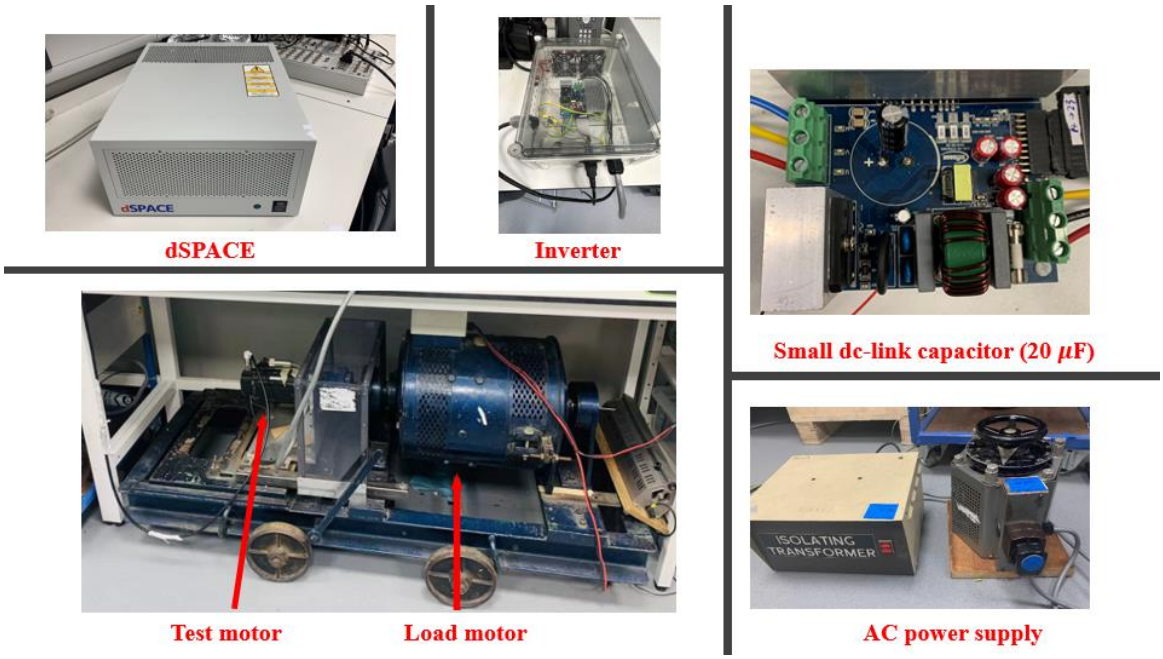

Fig. A.1. Experiment platform.

The variable transformer allows for precise adjustment of the input voltage, while the isolation transformer ensures safety by electrically isolating the system from the mains supply.

The dPACE1006 processor board, which serves as the core of the real-time control system, is powered by a 2.4 GHz multi-core AMD Opteron CPU. In this setup, the analog signals from the current and voltage sensors are digitized by the DS2004 ADC board before being sent to the DS1006 processor board. The incremental encoder's output is routed through the DS3001 incremental encoder board, which then forwards the data to the DS1006 processor.

Upon processing, the DS1006 processor board sends PWM duty cycle information to the DS5101 board, which generates six-channel PWM signals for the inverter module. Then, the

Infineon EVAL-M1-CTE610N3 evaluation board is responsible for managing the power electronics and control functions of the test motor.

The test motor is equipped with sensors to measure three-phase stator currents. The rotor position and speed are tracked using an incremental encoder mounted on the motor shaft. Additionally, the output torque of the test motor can be optionally measured using a torque transducer connected to the shaft. The parameters of the test motor are given in TABLE A.1.

TABLE A1.1

PARAMETERS OF THE TEST MOTOR OF THE IPMSM [CHE99]

Rated voltage (peak)	158V
Rated current (peak)	4.0A
Rated power	0.6 kW
Rated torque	4.0 Nm
Number of pole pairs	6
Slot number	18
Number of series connected conductors/pole/phase	152 turns
Wire diameter (2 wires stranded)	0.36mm+0.51mm
Winding coil pitch	3 slots
Winding resistance per phase	6.0 Ω (20°C)
Skew	1 slot-pitch
Stator outer radius	53.3 mm
Stator inner radius	31.00 mm
Stator outer radius	30.25 mm
Core length (stator)	32.00 mm
Core length (rotor)	30.00 mm
Shaft diameter	25.00 mm
Air gap length	0.75 mm
Magnet	UGIMAX 35HC1 (B_r=1.17T, μ_r=1.07)
Stator steel	Transil 310-50
Rotor Steel	Transil 300-35

Appendix 2 Publications during PhD Study

Published and Submitted Journal Papers:

[1] J. Yan, X. Wu, Z. Q. Zhu, and C. Liu, “Improved extended EMF-based sensorless control for IPMSMs with small dc-link capacitor considering dc-link voltage measurement error,” *IEEE Trans. Ind. Appl.*, vol. 60, no. 4, pp. 6299-6313, Jul.-Aug. 2024.

[2] J. Yan, Z. Q. Zhu, X. M. Wu, Y. Chen, H. Yang, L. H. Yang, and C. H. Liu, “A novel position sensorless control strategy for IPMSM drives with small dc-link capacitor,” submitted to *IEEE Trans. Power Electron*., submitted and under review.

[3] J. Yan, Z. Q. Zhu, X. M. Wu, H. Yang, L. H. Yang, and C. H. Liu, “Analysis and mitigation strategies of energy backflow phenomenon in IPMSM drive system with the small dc-link capacitor,” submitted to *IEEE Trans. Energy Convers.*, submitted and under review.

[4] Y. Zheng, Z. Q. Zhu, H. Xu, J. Yan, and D. Liang, “Optimal multi-tooth numbers for vernier PM synchronous machines," *IEEE Access*, vol. 12, pp. 89599-89612, 2024.

[5] Y. Zheng, D. Liang, Z. Q. Zhu, J. Yan, Y. Zhou, H. Liu, and H. Xu, “Asymmetric PM eddy current loss and temperature distributions of SPMSMs,” *IEEE Trans. Ind. Appl.*, under revision.

[6] D. Liang, Z. Q. Zhu, J. Yan, “Thermal protective control for permanent magnet synchronous machines,” drafted and to be submitted.

Published Conference Papers:

[7] J. Yan, X. Wu, and Z. Q. Zhu, “Analysis of extended EMF based sensorless control with dc-link voltage fluctuation,” *Proc. Int. Conf. on Power Electronics, Machines. and Drives (PEMD)*, Newcastle, UK, 2022, pp. 327-334.

[8] J. Yan, X. Wu, Z. Q. Zhu, and C. Liu, “A novel dc-link voltage observer with time delay compensation for small dc-link capacitor-based IPMSM with EEMF-based sensorless control,” *2nd Int. Conf. Sustain. Mobility Appl. Renew. Technol. (SMART)*, Cassino, Italy, 2022, pp. 1-6, 2022.

[9] J. Yan, X. Wu, Z. Q. Zhu, and C. Liu “Influence of dc-link voltage measurement error on extended EMF based sensorless control with reduced dc-link capacitor,” *25th Int. Conf. Electr. Mach. Syst. (ICEMS)*, Chiang Mai, Thailand, 2022, pp. 1-6, 2022.